Dye Sensitized Solar Cells – Investigation of bis(diimine)copper(I) Dyes

Inauguraldissertation

zur

Erlangung der Würde eines Doktors der Philosophie

vorgelegt der

Philosophisch-Naturwissenschaftlichen Fakultät

der Universität Basel

von

Annika Büttner

aus Bad-Säckingen (D)

Basel, 2018

Genehmigt von der Philosophisch-Naturwissenschaftlichen Fakultät

auf Antrag von

Prof. Dr. Edwin C. Constable und Prof. Dr. Anders Hagfeldt

Basel, den 26. Juni 2018

Prof. Dr. Martin Spiess

Dekan

Acknowledgements

First of all, I would like to thank Prof. Dr. Catherine E. Housecroft and Prof. Dr. Edwin C. Constable for giving me the opportunity to do my PhD in their group, working on this very exciting topic. I am also very thankful for the freedom they gave me during my research and their confidence in me supervising the inorganic practical course. Furthermore I want to thank Catherine and Ed for all their support and the time they invested for proof-reading my thesis.

I thank Prof. Dr. Anders Hagfeldt for being my co-examiner and co-referee, investing his precious time to come to Basel.

I thank all the supporting staff of the department, namely Dr. Heinz Nadig and Sylvie Mittelheisser for recording HR-MS and elemental analysis, Markus Hauri, Roy Lips, Oliver Ilg and Susanne Foley for material supply. Markus Hauri in particular for all his help ordering tones of chemicals for the practical course. Furthermore Andres Koller, Markus Ast, Andreas Sohler, Meha Hisni and Pascal Andrek are acknowledged for keeping the building running, for their help in maintaining instruments and their support during the move.

Many thanks to the people of the NMR group, namely PD Dr. Daniel Häussinger, Thomas Müntener and Daniel Joss for their great job maintaining the NMR instruments in the department.

Big thanks got to all the current and former members of the Constable/Housecroft group, for the nice working atmosphere and the good time I had with you all, in and outside the lab and at conferences. It was a pleasure to work with you. In particular I want to thank Mariia Karpacheva, Cedric Wobil and Frederik J. Malzner for our cooperation on the ´Cuprophilia´. Special thanks go to Nathalie Marinakis for our nice collaboration building tandem DSCs and the enthusiastic and interesting discussions we had.

Beatrice Erismann I would like to thank for all her administrative work and the entertaining coffee breaks we had together.

Special thanks got to Dr. Nik Hostettler, Dr. Sebastian Fürer, Dr. Collin Morris, Dr. Ewald Schönhofer, Dr. Sven Brauchli, Dr. Jonas Schönle, Dr. Markus Willgert and Beatrice Erismann for the good time we had together in and outside the lab and their friendship. I enjoyed it a lot.

Furthermore I want to thank my friends for their constant support outside of the lab. In particular Dr. Stefanie Geigle for her friendship and the amazing times we had together discussing about life. I deeply thank Dr. Florian Weiss for his friendship and all the great trips we had.

Special thanks go to Dr. Ina Bodoky for her motivational visits keeping me up to date what´s happening in the world. I am very thankful for our deep friendship, all the stunning memories we share and all the awesome conversation we had on ´karma´.

Furthermore I thank Andreas for his love and friendship and his patience enduring all the ups and downs of my emotions in the last few months.

Finally I thank my mother and my sister who constantly motivated and supported me during all stages of my life and for enduring all my nerviness and moods during the last few months.

Abstract

Our society with its modern lifestyle based on the dependency of technology is facing an energy problem associated with a climate crisis. With the extensive use of electronic devices the world´s energy demand increased tremendously. The limited availability of fossil fuels, which are mainly used to provide the energy needed cause the pollution of the environment. The urgent need to find a new, sustainable energy source focussed on harnessing the sun light the unlimited energy source. Silicon based photovoltaic devices are still the most established choice to capture solar energy but the requirement on highly pure materials for this devices is a drawback for cost efficient energy. Dye sensitized solar cells turn out to be a beneficial alternative since their manufacturing is much simpler and non-depending on the pureness of the material. However the best performing dye sensitized solar cells are based on ruthenium sensitizers. Replacing the rare and expensive ruthenium by more earth abundant and sustainable metals is the challenge and goal of our research group. This thesis describes the use of heteroleptic bis(diimine)copper(I) dyes to harvest sunlight.

Chapter 1 gives a short overview on the energy problem and introduces photovoltaic devices including the design and important device components of dye sensitized solar cells.

Chapter 2 describes general analytical methods, the preparation of solar cell devices and their characterization methods.

Chapter 3 shows the synthesis of different anchoring ligand and their application in dye sensitized solar cells in combination with different ancillary ligands.

Chapter 4 compares the device performance using two different anchoring ligands combined with asymmetric ancillary ligands. Furthermore the dye bleaching and regeneration is investigated.

Chapter 5 investigates the effects of ancillary ligands with different numbers of methoxy groups in bis(diimine)copper(I) dyes.

Chapter 6 the enhanced cell performance of substituents in the 4,4´-positions of the phenyl spacer in the ancillary ligands is further explored.

Chapter 7 shows the synthesis and device performance of 4-methoxycarbonyl phenyl and 4-ethylphenyl functionalized ancillary ligands.

Chapter 8 describes a preliminary study of all copper dye sensitized solar cells.

Chapter 9 reports a preliminary investigation of tandem dye sensitized solar cells.

Chapter 10 gives a short summary over the thesis.

Chapter 11 concludes the thesis and gives a short outlook for future investigations.

Parts of this work have been published

Annika Büttner, Sven Y. Brauchli, Raphael Vogt, Edwin C. Constable and Catherine E. Housecroft, "Combining phosphonic acid-functionalized anchoring ligands with asymmetric ancillary ligands in bis(diimine)copper(I) dyes for dye-sensitized solar cells", *RSC Adv.*, 2016, **6**, 5205.

Annika Büttner, Sven Y. Brauchli, Edwin C. Constable and Catherine E. Housecroft, "Effects of Introducing Methoxy Groups into the Ancillary Ligands in Bis(diimine) Copper(I) Dyes for Dye-Sensitized Solar Cells", *Inorganics*, 2018, **6**, article 40.

Mariia Karpacheva, Frederik J. Malzner, Cedric Wobill, Annika Büttner, Edwin C. Constable and Catherine E. Housecroft, "Cuprophilia: Dye-sensitized solar cells with copper(I) dyes and copper(I)/(II) redox shuttles", *Dyes Pigm.*, 2018, **156**, 410.

Abbreviations

%	per cent
$[Cu(MeCN)_4][PF_6]$	tetrakis(acetonitrile)copper(I) hexafluoridophosphate
$[Ni(acac)_2]$	nickel(II) acetylacetonate
$[Pd(PPh_3)_4]$	tetrakis(triphenylphosphine)palladium(0)
°C	degree celsius
2D	two dimensional
A	ampere
ALP1	((6,6´-dimethyl-[2,2´-bipyridine]-4,4´-diyl)bis(4,1-phenylene)) bis(phosphonic acid)
AM	air mass
asym. ALP1	6-methyl-[2,2´bipyridine]-4,1-phenyl-4-phosphonic acid
black dye	$[Ru(4,4´,4´´\text{-tricarboxylic acid-}2,2´:6´,2´´\text{-terpyridine})(NCS)_3]$
bpy	2,2´-bipyridine
calc.	calculated
CdTe	cadmium telluride
CH_2Cl_2	dichlormethane or DCM
CIGS	copper indium gallium selenide
cm	centimetre
CO_2	carbon dioxide
CO_2H	carboxyl
CoS	cobalt sulfid
COSY	correlation spectroscopy
Cs_2CO_3	caesium carbonate
D	deuterium
dm^3	cubic decimetre
dmbpy	6,6´-dimethyl-2,2´-bipyridine
dmphen	2,9-dimethyl-1,10-phenanthroline
DMSO	dimethl sulfoxide
DSC	dye sensitized solar cell
eq.	equivalent
EQE	external quantum efficiency
EQE_{max}	maximum external quantum efficiency
ESI	electrospray ionisation
Et	ethyl

Et_2O	diethyl ether
EtOH	ethanol
ff	fill factor
FTO	fluorine doped tin oxide
g	gram
h	hour
H_2SO_4	sulfuric acid
HCl	chloric acid
HMBC	heteronuclear multiple bond correlation
HMQC	heteronuclear multiple quantum coherence
HPLC	high performance liquid chromatography
Hz	hertz
I	current
I^-	iodide
I_3^-	triiodide
IEA	international energy agency
IPCE	incident photon to electrical conversion efficiency
IQE	internal quantum efficiency
IR	infrared
I_S	incident light
I_{SC}	short-circuit current
IV	current voltage
J	coupling constant
J_{MPP}	current density measured at maximum power point
J_{SC}	current density measured at short-circuit
J-V	current density versus potential
K_2CO_3	potassium carbonate
KOH	potassium hydroxide
LiI	lithium iodide
$LiPF_6$	lithium hexafluorophosphate
M	mol L^{-1} or parent ion
m/z	mass to charge ratio
mA	milliampere
MALDI-TOF	matrix assisted laser desorption ionisation-time of flight
Me	methyl

Me_3SiBr	bromotrimethyl silane
MeCN	acetonitrile
MeO	methoxy also abbreviated as OMe
MeOH	methanol
mg	milligram
$MgSO_4$	magnesium sulfate
MHz	megahertz
min	minute
MLCT	metal to ligand charge transfer
mm	millimeter
mM	milli molar
mmol	millimole
mol	mole
MPP	maximum power point
MS	mass spectrometry
Mtoe	million tons oil
mV	millivolt
mW	milliwatt
N^N	diimine
N3	$[Ru(4,4´\text{-}(dicarboxylicacid)\text{-}2,2´\text{-}bipyridine)_2(NCS)_2]$
N719	$[Ru(4,4´\text{-}(dicarboxylicacid)\text{-}2,2´\text{-}bipyridine)_2(NCS)_2][TBA]_2$
NaOH	sodium hydroxide
NH_2	amine
NH_4OAc	amonium acetate
NHAc	acetamido
NiO	nickel oxide
NIR	near infrared
nm	nanometre
NMR	nuclear magnetic resonance, with the signals being identified as singlet (s), doublet (d), triplet (t), quartet (q), multiplet (m)
NOESY	nuclear overhauser enhancement spectroscopy
P	power
P1	4-(bis-{4-[5-(2,2-dicyano-vinyl)-thiophene-2-yl]-phenyl}-amino)-benzoic acid
PCE	photon to power conversion efficiency
PEDOT	poly(3,4-ethylene dioxy-thiophene polystylenesulfonate)
PF_6	hexafluoridophosphate

pH	potential of hydrogen
Ph	phenyl
PhALP1	((6,6´-diphenyl-[2,2´-bipyridine]-4,4´-diyl)bis(4,1-phenylene)) bis(phosphonic acid)
P_{in}	power input
$PO(OH)_2$	phosphonic acid group
ppm	parts per million
Pt	platinum
PV	photovoltaic
Ru	ruthenium
S	ground state of the dye
S*	excited state of the dye
SALSAC	surface-as-ligand, surface-as-complex
Si	silicon
SnO_2	tin(IV) oxide
SW	stepwise
T	transmission
TBP	4-*tert*-butylpyridine
THF	tetrahydrofuran
$TiCl_4$	titanium tetrachloride
TiO_2	titanium dioxide
TMS	tetramethylsilane
TW	terawatt
TWh	terawatt hour
UV-O_3	ultraviolet-ozone
UV-Vis	ultraviolet-visible
V	potential
V_2O_5	vanadium pentoxide
V_{MPP}	voltage at maximum power point
V_{OC}	open-circuit voltage
W	watt
WO_3	tungsten trioxide
Z907	cis-Bis(isothiocyanato)(2,2´-bipyridyl-4,4´-dicarboxylato)(4,4´-di-nonyl-2´-bipyridyl)ruthenium(II)
ZnO	zinc oxide
ZnS	zinc sulfide
δ	chemical shift [ppm]

ε	molar absorption coefficient
ε_{max}	maximum molar absorption coefficient
η	overall conversion efficiency from solar to electrical energy for a photovoltaic device
λ_{max}	maximum absorption
μm	micrometre
Ω	electrical resistance; ohm

Structure of ligands used in this thesis

Anchoring ligands

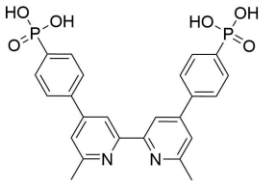

1

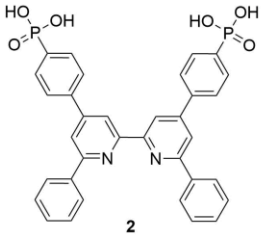

2

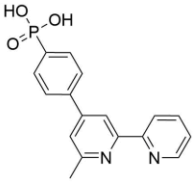

3

Ancillary ligands

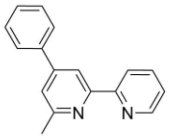

4

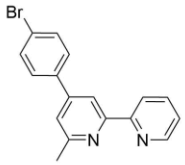

5

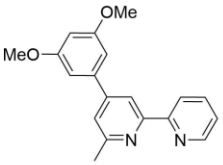

6

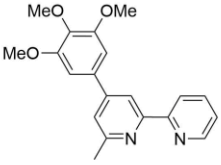

7

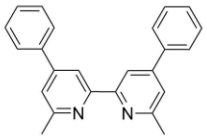

8

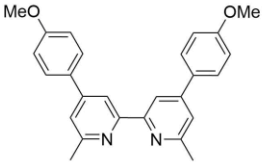

9

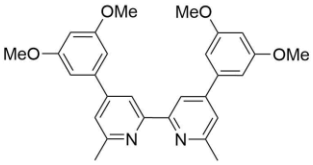

10

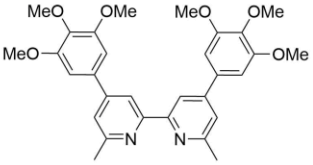

11

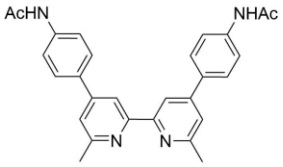

12

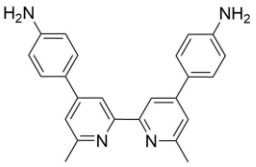

13

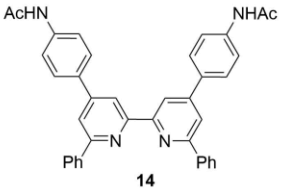

14

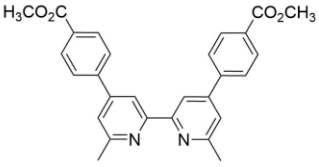

15

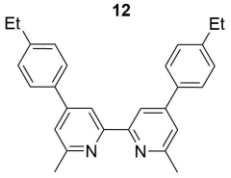

16

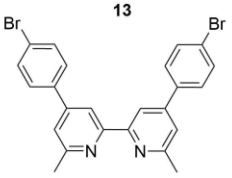

17

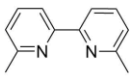

18

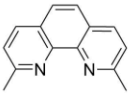

19

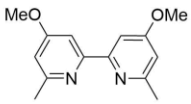

20

p-Type dyes

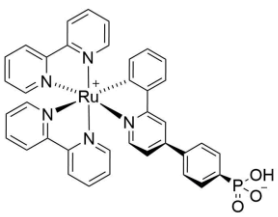

21

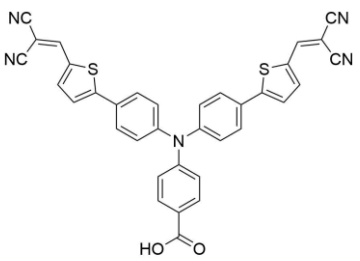

P1 (22)

Reference dye

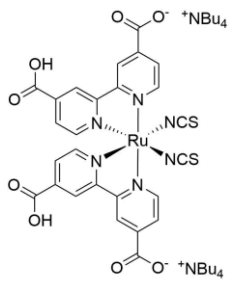

N719

Table of contents

Chapter 1

Chapter 1 Introduction

1.1 Motivation

During the last century, the technical progress has changed our lifestyle tremendously. The dependency on the use of electronic devices and the growth of the population[1] lead to an incredible increase in energy consumption. In 2016 the total global energy consumption for around 7.5 billion people[1] was 13 276.3 Mtoe (million tons oil), which is equivalent to 154 403 TWh (terra watt hours).[2] The IEA (International Energy Agency) estimated a growth of the global energy demand by 2.1% in 2017, more than twice the growth rate in 2016, reaching an estimated energy consumption of over 14 000 Mtoe.[3] The future prognosis for the energy demand is alarming[4], especially as the main energy requirement is still gained from fossil fuels (Figure 1) and the world population is predicted to grow by another two billions until 2050[1].

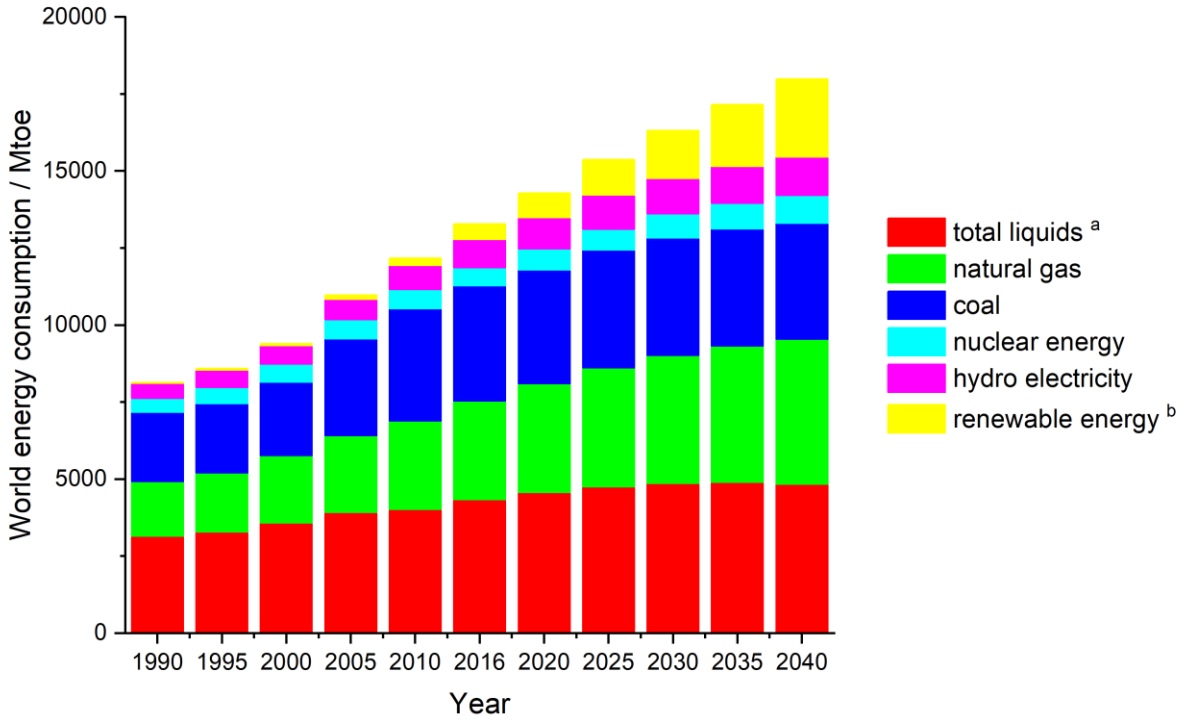

Figure 1: Global energy consumption by energy source from 1990 to2040; history (1990-2016) and prediction (2020-2040). (a) includes oil, biofuels, gas-to-liquids and oil-to-liquids. (b) includes wind power and solar electricity.[4]

The limited availability of fossil fuels not only leads to the importance of changing to renewable energy sources but also the concern about the pollution of the environment. Only 3.16% of the worldwide energy consumption was gained from renewable energies, 6.86% from hydroelectricity and 4.46% from nuclear energy (Figure 2). In total not even one sixth of the global energy consumption was produced CO_2 neutral. From 2005 to 2015 the global CO_2 emission caused by use of fossil fuels to

gain energy increased yearly by 1.6%.[2] This development is alarming as CO_2 is known to be the dominant greenhouse gas causing global warming and climate change.

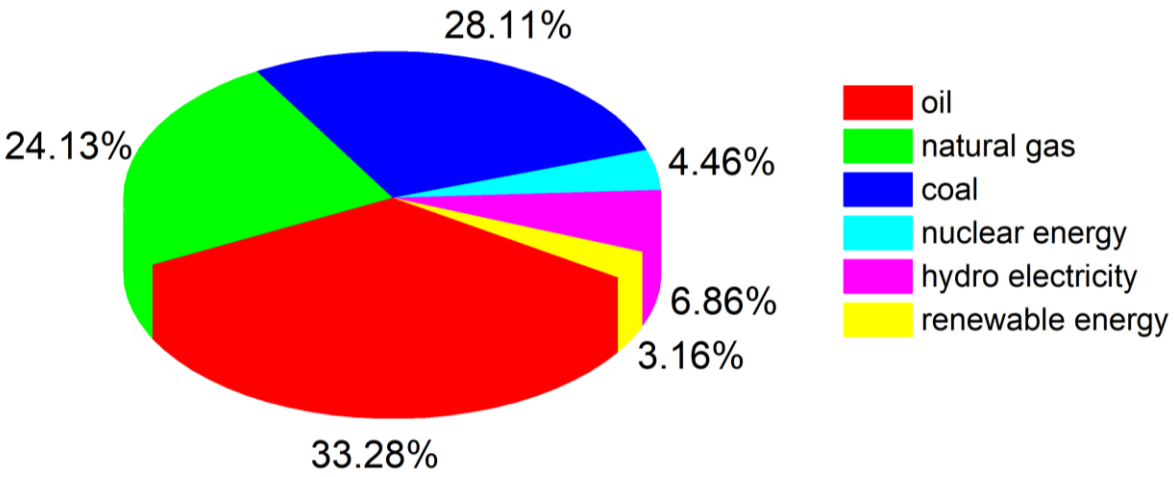

Figure 2: Worldwide total primary energy production in 2016 by energy source; global fuel consumption in 2016: 13276.3 Mtoe.[2]

There are several requirements an alternative energy source needs to fulfil. It must be ecologically friendly, cheap and efficient. Nuclear power was meant to be a good solution to afford the high energy demand, delivering cheap energy without producing greenhouse gases. Nevertheless there is still no solution for the radioactive waste disposal. Moreover the breakdown in Chernobyl in 1986 and more recently the accident in Fukushima in 2011 showed that nuclear power can provoke disastrous environmental catastrophes, still not knowing all the future consequences.[5]

In order to fulfil the requirements of today´s lifestyle the sun as a renewable energy supplier becomes very attractive. Not only is the sun an abundant, unlimited and environmentally friendly energy source, it is also free of charge. With around 100000 TW of solar energy per hour[6] hitting the earth´s surface harvesting sun light could be sufficient to provide the energy demand of mankind. Hence the conversion of solar photons into electrical energy is the obvious choice for a renewable energy source. To achieve this high potential becoming the future energy supplier highly efficient photoconversion by cheap solar cells produce with earth abundant materials is requested. A promising technology for the future are dye sensitized solar cells (DSCs) having an enormous potential becoming a commercial low-cost solar energy provider.

1.2 Photovoltaic technology

The word ´photovoltaic´ is derived from the Greek word φῶς (phōs) which means ´light´, and from the word ´volt´ the unit of the electric potential. Photovoltaics, often abbreviated as PVs, are defined as the technology of direct sunlight conversion into electricity using a semiconductor material.[7,8] Depending of the material used, the maximum solar to power conversion efficiency and the production costs, Martin A. Green categorized solar cells into three main groups, namely the first, second and third generation devices.[7,8,9]

1.2.1 First Generation

The first generation solar cells are based on crystalline silicon and include the conventional solar cells of today. The material used for these first generation solar cells have to be highly pure. The main part of the first generation PVs are single-junction solar cells based on silicon wafers with single crystal or multi-crystalline silicon. A drawback of the PVs is the high cost for both, the material itself and the production.[9,10,11]

1.2.2 Second Generation

The second generation solar cells are based on thin film technologies being single-junction devices. The materials are applied as a thin film on a glass or ceramics as a supporting material, which have the advantage of using less material therefore being more price efficient compared to the first generation PVs.[7,9,11] Solar cells made from amorphous Si, CdTe and CIGS (Cd-In-Ga-Se) yield the highest solar to power conversion efficiencies. [7,9,11]

1.2.3 Third Generation

The first and second generation PVs, both being single junction devices are restricted by the Shockley-Queisser limit [12], which defines the maximum power conversion efficiency of a solar cell being 31% at 1 sun illumination. The Shockley-Queisser limit is a theoretical calculation for an ideal case, which describes the formation of a single electron-hole pair upon absorption of one photon. The first and second generation PVs are limited by a thermodynamic energy loss of the excess energy of incident photons above the band-gap of the semiconductor.[12] All devices that can overcome the Shockley-Queisser limit are called third generation photovoltaics, as for example tandem cells, hot carrier cells, multiexcitaion generation, multiband cells or thermophotovoltaics.[7,11] The challenge for the third generation solar cells is being highly efficient and on the same time having low production costs.

1.3 Dye-sensitized solar cells

Dye-sensitized solar cells (DSCs) are something in between the second and the third generation PVs. Some advantages of DSCs are easy device structure offering a variation of design possibilities like transparency or multi-colour options and the low production costs. Furthermore DSCs can be flexible and lightweight and have a shorter energy payback compared to conventional PVs.[11] The first dye-

sensitized solar cell also known as Grätzel-type DSC[13] was first discovered in the early 1990s. The Grätzel DSC is built up with a transparent, TiO_2 semiconductor which is sensitized with a dye adsorbed on the surface, being able to absorb the incident photons.[13,14,15]

1.3.1 Design and working principle

1.3.1.1 n-Type DSCs

In Figure 3 the schematic presentation of the design and working principle of a n-type DSC is shown.[16] Upon irradiation the dye is excited from its ground state (S) by absorption of an incident photon. This process is followed by the injection of an electron from the excited dye (S*) into the conduction band of the semiconductor, in this case microcrystalline TiO_2. The injected electron migrates through the semiconductor and is released to the external circuit at the FTO glass covered back electrode. The electron travels through the external circuit to the counter electrode, a Pt covered FTO glass plate where it reduces the oxidized redox mediator of the electrolyte, which regenerated the dye to the ground state (S).[11,13,16] The processes described here take place in a millisecond to hundred nanoseconds time scale (Figure 4).[11] In Figure 4 an overview of the time constants of the working processes is given for a Ru-dye based DSC with an I^-/I_3^- electrolyte under 1 sun illumination is given. The recombination processes are indicated by red arrows.[11]

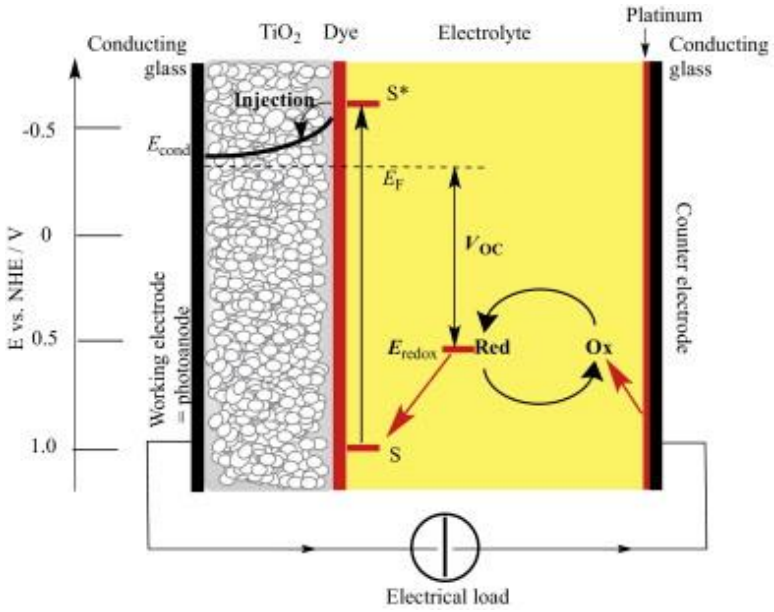

Figure 3: Schematic presentation of the design and working principle of a n-type DSC.[16]

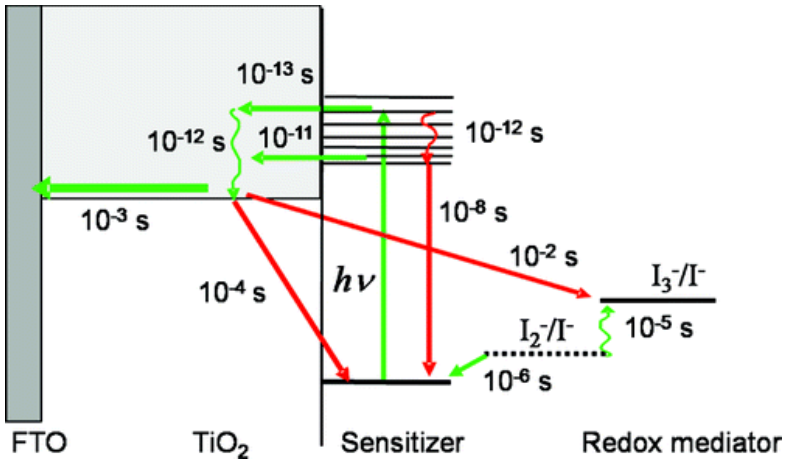

Figure 4: Schematic overview of the processes in a Ru-dye based DSC with an I^-/I_3^- electrolyte under working conditions with time constants (the recombination processes are indicated by red arrows).[11]

1.3.1.2 p-Type DSCs

In Figure 5 the schematic presentation of the design and working principle of a p-type DSC is shown.[17] Upon irradiation the dye is excited from its ground state (S) by absorption of an incident photon, followed by an electron transfer from the excited dye (S*) to the oxidized species in the electrolyte and an electron transfer from the valence band of the p-type semiconductor (NiO) to the dye (S). The generated hole in the valence band of the semiconductor diffuses through the external circuit to the counter electrode, where the oxidized species in the electrolyte is regenerated.[18,19]

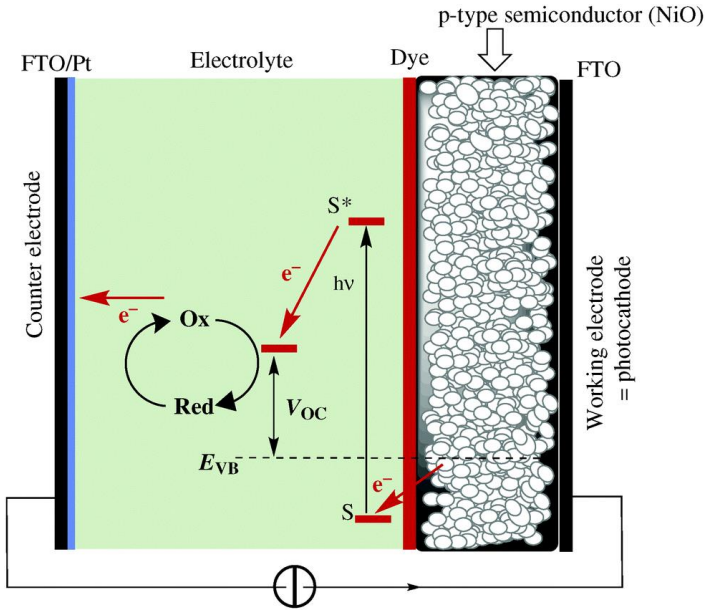

Figure 5: Schematic presentation of the design and working principle of a p-type DSC.[17]

1.3.1.3 Tandem DSCs

A tandem DSC is the combination of an n- and a p-type DSC, in which both electrodes feature a semiconducting material sensitized with a photoactive dye. The tandem DSC is irradiated from the n-

type side, were the dye is excited by the incident photons. The photons which are not absorbed on the photoanode are transmitted to the p-type side of the tandem cell exciting the p-type dye. The excited p-type dye reduces the electrolyte and a hole is injected into the valence band of the NiO from the dye. The reduced redox couple in the electrolyte can then regenerate the excited n-type dye.[11]

1.3.2 Device components

As shown in Figure 3 a DSC consists of several components, namely the working electrode with the semiconductor surface which is functionalized with a dye, the Pt counter electrode and the electrolyte. All these parts have to cooperate, resulting in a working system yielding the highest efficiency possible. Consequently all these parts are dependent on each other making the optimization of a DSC difficult.[20] For example changing the dye can influence the properties of the semiconductor or the electrolyte.

1.3.2.1 Semiconductor

A semiconductor is a solid material, which is electrically conductive and can be classified between a conductor and an insulator. This property is temperature dependent and the conductivity of a semiconductor increases with increasing temperature, caused by a small band-gap between the valence and conduction band of the material, allowing the absorption of an electron to the conduction band. In contrast to that an insulator has a large band-gap.[21] There are many metal oxides featuring semiconductor characteristics, which are therefore used in DSCs, for example TiO_2, ZnO, SnO_2, WO_3, V_2O_5, ZnS, as well as core-shell materials as ZnO-coated SnO_2 and many more.[11,22] Still the widely-used and most efficient semiconductor is TiO_2 as mesoporous electrodes in DSCs. It is nontoxic, stable and easily available. Furthermore TiO_2 nanoparticle-based thin-films have a large surface area allowing high dye-functionalization.[11,16] TiO_2 can form transparent and opaque films and can be found as white pigment in paint, sunscreen or toothpaste. There are three crystal forms of TiO_2, namely anatase, rutile and brookite, and the photocatalytical activity of the material is strongly dependent on the phase. Rutile is the thermodynamic favoured form, but anatase shows a larger bandgap and a higher conduction band energy, which makes anatase the preferential structure to use in DSCs.[11,23] For the preparation of a thin film of titanium dioxide to use as working electrodes in DSCs, TiO_2 nanoparticles are used to prepare a paste.[11,24] The paste is then applied to a conductive substrate, usually FTO coated glass by doctor blading or screen-printing (Chapter 2 Section 2.2.2) to prepare a mesoporous film with a large surface area.

1.3.2.2 Dyes

The key component of DSCs is the dye which functionalizes the TiO_2 surface. It absorbs the photon flux from the sun (Figure 6) and injects electrons to the conduction band of the semiconductor. The sensitizers applied in DSCs can be categorized in two major groups, metal complex dyes and organic dyes. There are several properties a dye needs to cover in order to yield an efficiently working DSC. It

is of high importance that the dye absorbs as much light as possible from the solar spectrum, ideally covering the whole visible spectrum as well as the near IR region (Figure 6).[11,25] Furthermore the sensitizer need a high binding affinity to the semiconductor surface, which is provided by a good anchoring group such as carboxylic acid anchoring groups (-CO_2H), phosphonic acid anchoring groups (-$PO(OH)_2$) (Figure 7) or typically for organic dyes a cyanoacrylic acid anchoring groups. In order to enable an efficient electron transfer from the dye molecule to the semiconductor, the energy bands of the dye need to fit those of the semiconductor used. This means that the excited state of the dye should be higher in energy then the conduction band edge of the semiconductor. For an efficient dye regeneration by the redox shuttle in the electrolyte, the potential of the oxidized state of the sensitizer should be more positive then the redox potential of the electrolyte. The structure of the dye should be optimized to avoid dye aggregation on the semiconductor surface as this may have a negative influence on the efficiency. One way to overcome possible dye aggregation is the use of a coadsorber as for example chenodeoxycholic acid.[26,27] Besides these properties, the dye needs to exhibit a high stability under working conditions; being thermally, electrochemically and photo stable.[11]

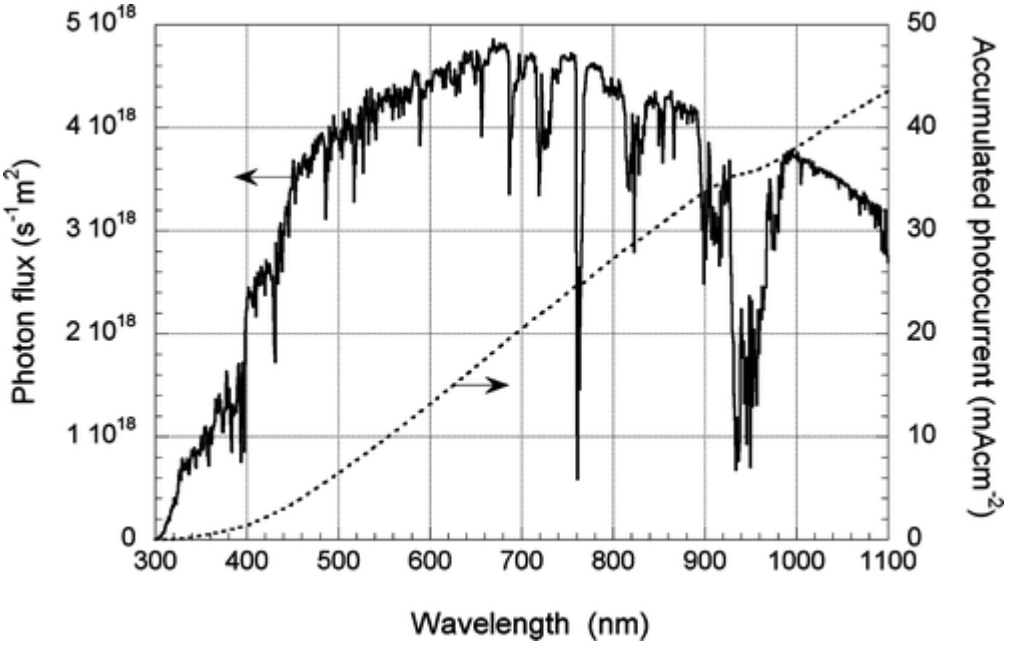

Figure 6: Photon flux of the AM 1.5 G spectrum at 100 mW/ m^2 and calculated accumulated photocurrent (dotted line).[11]

In relation to the binding affinity of the anchoring group of the dye to the semiconductor, there are different ways how a dye can interact and therefore bind to the surface. A dye can anchor to the surface via electrostatic interactions such as donor-acceptor interactions or ion exchange. Furthermore hydrogen bond interactions can sufficiently bind the sensitizer to the semiconductor surface. An interaction of hydrophobic groups such as long alkyl chains is able to bind the dye via hydrophobic interactions. Also van der Waals interactions or dye trapping in cavities on the surface are possibilities of sensitizing the semiconductor surface.[28] As an example in Figure 7 different possible anchoring

modes of carboxylated anchoring groups are shown.[29] The anchoring mode is dependent on the protonation state of the anchoring group, which can be changed by varying the pH. Nevertheless it is not possible to determine exactly through which binding mode a dye anchors to the surface. *Filippo de Angelis et. al* [30] combined FT-IR measurements with DFT calculations to find the energetically favoured anchoring mode of an acidic acid anchoring group on the TiO_2 surface. They found the bidentate bridging mode fitting closest in the FT-IR measurements, also being calculated as the most stable anchoring mode.[30]

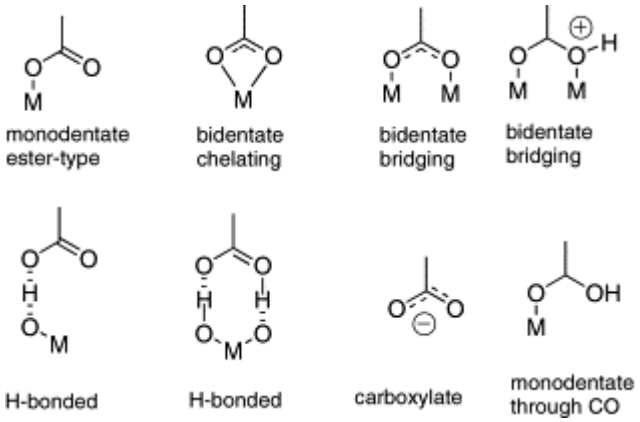

Figure 7: Different anchoring modes of carboxylated anchoring groups to a semiconductor as for example TiO_2.[29]

There is a large variety of dyes that have been tested in DSCs, as mentioned in the beginning of this section they can be grouped into metal-containing or metal-free organic dyes. Providing an overview of different dyes, a short insight into ruthenium(II) dyes, copper(I) dyes and donor-π-bridge acceptor dyes.

Ruthenium(II) based dyes have been studied intensively and represent the best dyes for DSCs.[31] In the last couple of decades, sensitizers based on ruthenium(II) have commonly been used as they feature broad absorption spectra, have long excited-state lifetimes and show a good chemical stability.[11] In 1979 the first functionalization of TiO_2 with ruthenium dyes was reported.[32] An exceptional high efficiency of 7.1-7.9% using a Ru(II) dye was achieved by *O´Regan* and *Grätzel* in 1991 as a consequence of moving to nanoparticular TiO_2.[33] Some of the best performing ruthenium(II) based photosensitizers are shown in Scheme 1. Remarkable efficiencies of over 10% have been achieved with these dyes (Scheme 1). The highest power conversion efficiency of 11.2% was obtained using the N719 dye.[34] Today N719 is still one of the best investigated and best performing dyes and is generally used as reference dye, also in this thesis. Although the N719 is one of the most efficient Ru(II) dyes there could still be improvement as for example in the long-term stability of the DSCs. The introducing alkyl chains[35] as in the **Z907** dye (Scheme 1) or the investigation of thiocyanate free ruthenium(II) sensitizers could possibly enhance the long-term stability of the devices.[36,37,38]

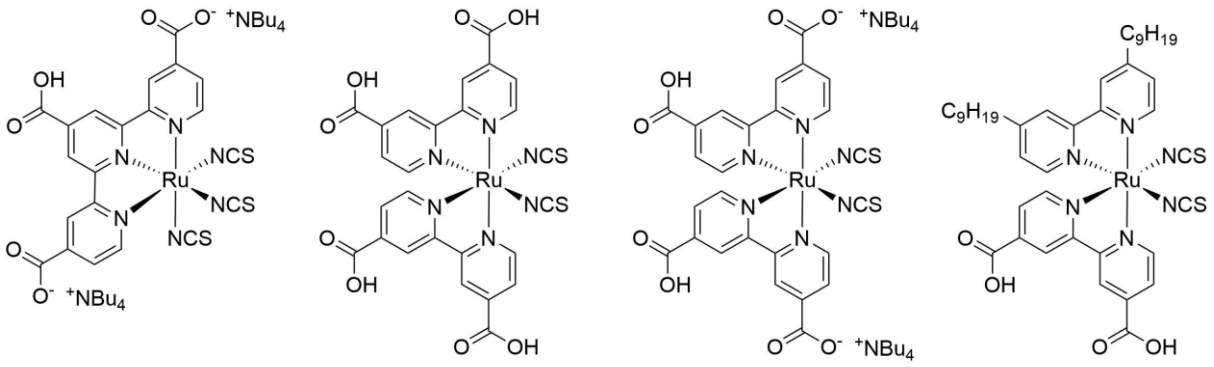

Scheme 1: Structures for examples of some of the best performing ruthenium(II) dyes.

Although the ruthenium(II) dyes are very promising as they yield exceptional high efficiencies in DSCs, the main disadvantages of these sensitizer is the use of the toxic and rare abundant ruthenium metal (Figure 8). In terms of sustainability it is therefore necessary to use cheaper and more abundant materials which can be achieved by the use copper(I) based dyes (Figure 8).

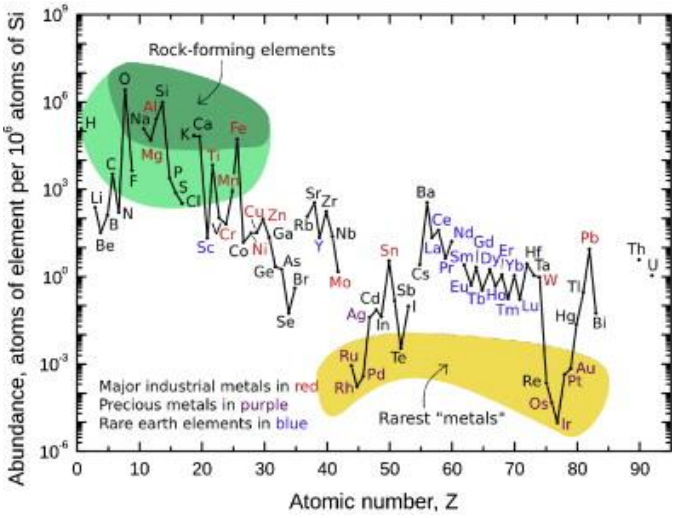

Figure 8: Abundance of the elements in the upper continental earth crust.[16,39]

The applications of copper(I) complexes as dyes in DSCs remains less investigated as those of the ruthenium(II) based dyes mentioned above. Nevertheless in terms of sustainability and their photophysical characteristics similar to those of Ru(II) dyes, copper(I) complexes are promising candidates to use as sensitizers in DSCs.[40] *Sauvage and co-workers*[41] and later *Sakaki et al.*[42] were the first to report copper(I) dyes in DSCs. In the beginning homoleptic copper(I) complexes were used to functionalize the semiconductor yielding efficiencies of up to 2.3% (for masked DSCs).[43] In order to improve performance, a change was needed to heteroleptic copper(I) dyes and this lead to the investigation by our research group of a ´surface-as-ligand, surface-as-complex´ (´SALSAC´) strategy to functionalize the surface with a heteroleptic copper(I) dye enabling an easy screening of sensitizers.[44,45,46,47] To sensitize the surface with a heteroleptic copper(I) dye the semiconductor is first functionalized with an anchoring ligand followed by a ligand exchange reaction with the homoleptic

copper(I) complex. This strategy is described in detail in Chapter 2 in Section 2.2.5 and was used to functionalize the semiconductor surface with the dyes presented in this thesis. Besides the advantage of fast and easy screening of dyes this strategy can bypass the synthesis of the heteroleptic copper(I) complex which often bears the problem of fast ligand exchange in solution.[48] The application of heteroleptic copper(I) dyes together with the ´SALSAC´ strategy yielded high efficiencies of up to 3.16% in DSCs.[49] Another approach is the HETPHEN strategy[50,51], using sterically demanding phenanthroline based ligands to synthesize heteroleptic copper(I) complexes. With this strategy it was possible to synthesize heteroleptic copper(I)bisdiimine complexes that are stable with respect to dissociation. Their application in DSCs yielded high efficiencies of up to 4.66% (with unmasked cells).[52]

The advantage of pure organic dyes over ruthenium(II) or copper(I) based sensitizers is clearly the non-use of a metal. These dyes are designed in a donor-π-bridge acceptor way. This design enables an intramolecular charge separation.[11] Arylamines are often used as the donor and cyanoacrylates as the acceptor being able to anchor to the surface. The π-bridging units are usually thiophene units. A large variety of organic dyes such as indoline dyes, coumarin dyes triarylamine dyes and many more are available.[11] Although high efficiencies for donor-π-bridge-acceptor like zinc porphyrin dyes[31] are reported the disadvantages of these organic porphyrin based sensitizers are their stability and the challenging synthesis. Nevertheless organic dyes show an attractive ability to be used as a co-sensitizer in DSCs.[53]

1.3.2.3 Electrolytes

Besides the semiconductor and the dye, the electrolyte is a crucial part of the DSC and can have a high influence on the device performance. The electrolyte is responsible for the electron transport between both electrodes and the reduction of the excited dye to its ground state. It is necessary that the electrolyte features a good contact between the semiconductor and the counter electrode enabling a fast diffusion of the charge carriers. Furthermore the electrolyte needs to be chemically, thermally, optically and electrochemically stable under working conditions and towards the dye, the semiconductor and the device in total. The ideal electrolyte should absorb as little light as possible.[54] The standard electrolyte used, also in this thesis, is based on an I^-/I_3^- redox couple. Usually the electrolyte needs to be optimized for each dye which could further improve the efficiency. For example Co^{2+}/Co^{3+}-based electrolytes are beneficial in combination with copper(I) dyes.[55] Also other redox couples in liquid electrolytes, quasi-solid state or solid electrolytes are promising alternatives to the a I^-/I_3^- based electrolyte.[54,56,57] Moreover $Cu^{+/2+}$ redox mediators in electrolytes are of high interest and are investigated and discussed in more detail in Chapter 8.[58,59] The I^-/I_3^-, the Co^{2+}/Co^{3+} and the Cu^+/Cu^{2+} based electrolytes presented here all absorb light as their colour varies from yellow to orange to red.

1.3.2.4 Counter electrodes

Usually a Pt-coated counter electrode is used in DSCs; electrical circuit is completed by catalytic reduction of the electrolyte at the platinized counter-electrode. The platinum layer can be deposited by spray pyrolysis, sputtering, electrodeposition or vapour deposition on the FTO coated glass substrate.[11,60] Other alternatives are carbon materials as for example a mixture of graphite and carbon black developed by *Kay* and *Grätzel* [61] or a counter electrode with two carbon layers as reported by *Pettersson et al*.[62] Furthermore conductive polymers as PEDOT doped with anions[63] or CoS-based[64] counter electrodes can be applied in DSCs.

Chapter 2

Chapter 2 Materials and Methods

2.1 General analytical characterization methods

^{1}H and ^{13}C NMR spectra were recorded on a Bruker Avance-III-400, III-500 or III-600 MHz NMR spectrometer. The chemical shifts of ^{1}H and ^{13}C were referenced with respect to δ(TMS) = 0 ppm. The spectra were assigned using COSY, NOESY, HMQC and HMBC techniques. Solution and solid-state absorption spectra were recorded on an Agilent Cary 5000 UV-Vis NIR spectrometer. Electrospray ionization (ESI) mass spectra were recorded on a Shimadzu LCMS-2020 instrument or on a Bruker Daltonics Inc. microflex instrument. High resolution ESI mass spectra were recorded on a Bruker maXis 4G QTOF instrument. MALDI-TOF mass spectra were recorded on a Bruker microflex and elemental analysis were measured on a Leco CHN-900 microanalyser.

A Biotage Initiator 8 reactor was used for the synthesis under microwave conditions.

The current density-voltage (*J-V*) measurements were made by irradiating the DSC from behind with a LOT Quantum Design LS0811 instruments (100 mW/ cm^2 = 1 sun, AM 1.5G conditions). The tandem DSCs were measured by irradiating from the n-type working electrodes. The power of the simulated light was calibrated with a silicon reference cell. The standard reference dye N719 was purchased from Solaronix. The external quantum efficiency (EQE) measurements of the DSCs were performed on a Spe-Quest quantum efficiency setup from Rera Systems (Netherlands) equipped with a 100 W halogen lamp (QTH) and a lambda 300 grating monochromator from Lot Oriel. The monochromatic light was modulated to 3 or 1 Hz using a chopper wheel from ThorLabs and the cell response was amplified with a large dynamic range IV converter from CVI Melles Griot and the measured with a SR830 DSP Lock-In amplifier from Stanford Research.

2.2 Materials for DSCs

Sonoswiss cleaner, SW-C L2, was used to prepare the surfactant solution to clean the glass plates. For cleaning of electrodes milliQ water and HPLC grade solvents were used exclusively. All dye and electrolyte solutions were prepared using HPLC grade solvent, except for DMSO, which was dried over molecular sieve and was 98% pure.

2.2.1 Working electrodes

TiO_2 working electrodes were either purchased from Solaronix (Solaronix Test Cell Titania Electrodes) or screen-printed in house using a DN-GPS-18TS TiO_2 paste and a DN-GPS-22OS TiO_2 paste for the scattering layer both from Dyenamo.

2.2.2 Screen-printing process

For the screen-printing of the working electrodes a custom made fixed aluminium frame and a squeegee slider were used (Figure 9 and Figure 10).

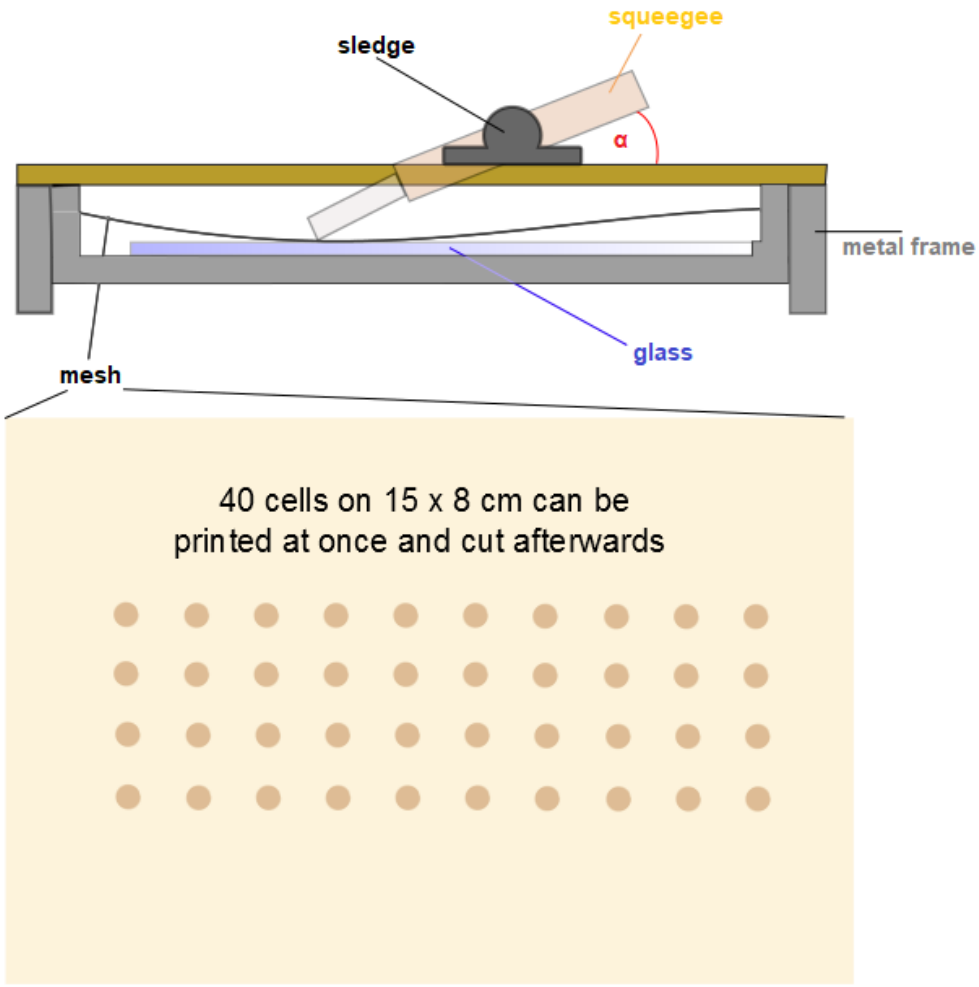

Figure 9: Schematic presentation of the screen -printing device. Figure made by Ewald Schönhofer.

The squeegee is connected to a sledge on which the angle α can be changed. Depending on the size of this angle, the TiO_2 paste is either loaded (α = 45°) into the mesh (90-48Y PET mesh from Serelith AG) of the frame or pressed through it (α = 70-80°). The mesh is attached to a metal frame and is stringed with a ´SEFAR PET gold´. With the 40 printing spots in the mesh 40 electrodes can be printed at the same time on a glass plate. TiO_2 paste is put on the mesh and disposed equally using the squeegee with the smaller angle in order to fill the pores of the mesh with the paste. The glass plate is then put under the loaded mesh and the paste is pressed through the pores onto the glass plate with the squeegee with the bigger angle. This process is repeated four times. Both, the mesh and the squeegee are cleaned with EtOH after each screen-printing cycle (Figure 9 and Figure 10).

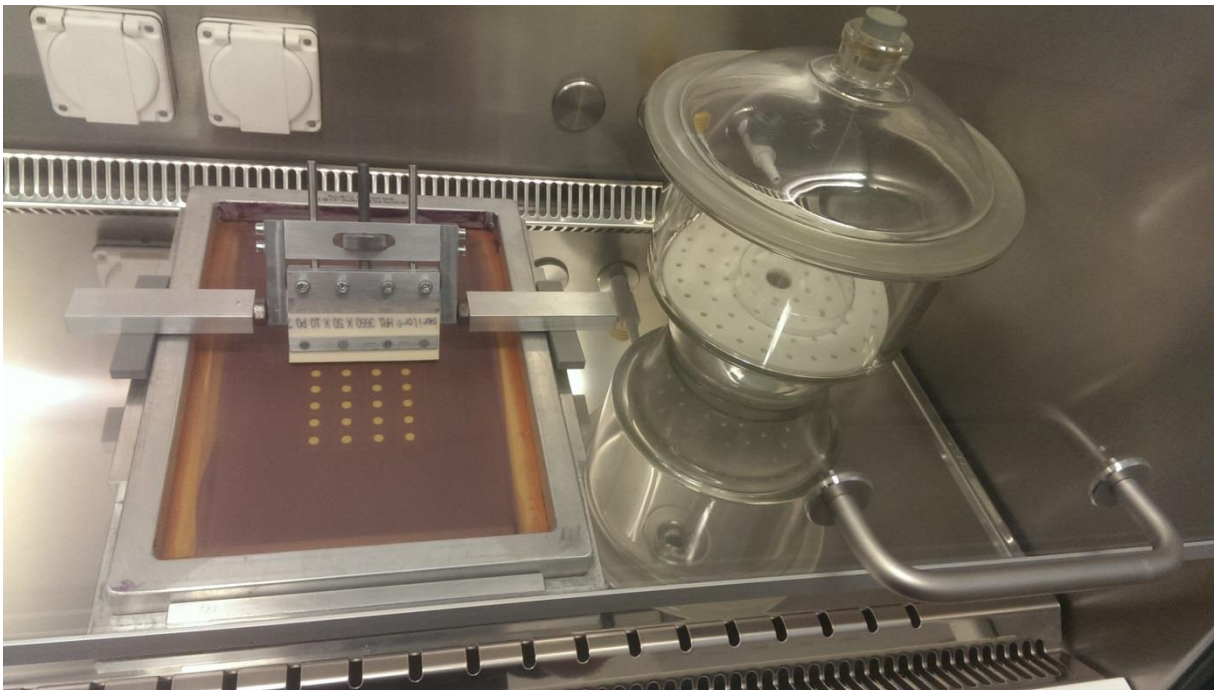

Figure 10: Photograph of the screen-printing device with the frame, the mesh, the squeegee and a desiccator with EtOH vapour inside a clean bench. Photograph taken by Ewald Schönhofer.

The FTO glass plates for screen-printing electrodes were purchased from Solaronix (Solaronix TCO22-7, 2.2 mm thickness, sheet resistance ≈ 7 Ω square^{-1}). A glass plate of 15 cm × 8 cm was cleaned by sonicating in a 2% surfactant solution in milliQ water (Sonoswiss cleaner, SW-C L2) and rinsed with milliQ water and EtOH. The surface of the glass plate was then activated using a Moedel 256-220UV-O_3 system from Jetlight Company Inc for 18 min. The FTO plate was immersed into a 40 mM aqueous $TiCl_4$ solution at 70 °C for 30 min, washed with milliQ water and EtOH and dried in a stream of nitrogen before screen-printing a layer of TiO_2 paste with the device described above (Figure 9 and Figure 10). After each printing cycle the glass plate was kept in an EtOH chamber for 3 min to reduce surface irregularities of the printed layer (Figure 10 right, desiccator with EtOH vapour) and dried at 125 °C for 6 min. The screen-printing process was repeated 4 times, and then a final scattering layer was printed on top (DN-GPS-22OS, Dyenamo). The prepared electrodes were sintered in a Nabertherm N 15/65HA oven at 75 °C for 30 min, at 135 °C for 15 min, at 325 °C for 5 min, at 375 °C for 5 min, at 450 °C for 15 min and at 500 °C for 15 min (Figure 11).[24]

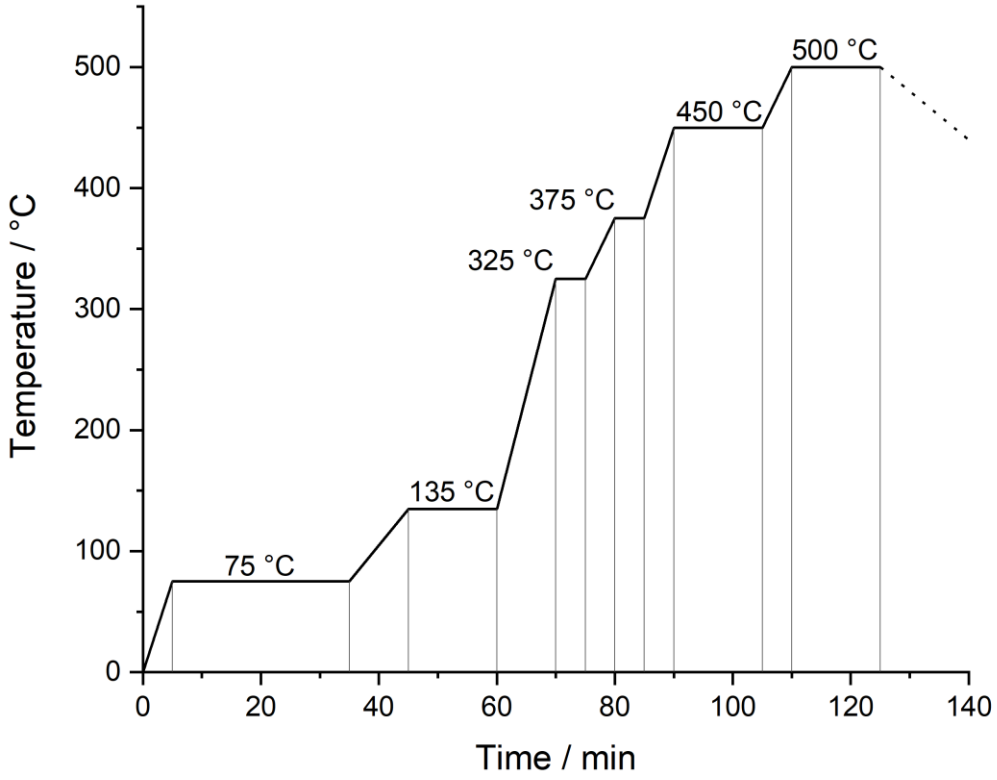

Figure 11: Temperature gradient used for the sintering process of the screen-printed TiO_2 electrodes.

The electrodes were cut with a CAMAG smartCUT glass cutter (Figure 12). The annealed TiO_2 electrodes were post-treated with a 40 mM aqueous $TiCl_4$ solution, rinsed with milliQ water and EtOH and sintered at 500 °C for 30 min before the dyeing process.

Figure 12: Photograph of the CAMAG smartCUT glass cutter and pincers. Photograph taken by Ewald Schönhofer.

2.2.3 Counter electrodes

The Pt counter electrodes were purchased from Solaronix (Solaronix Test Cell Platinum Electrodes), were washed with EtOH and heated on a hot plate at 450 °C for 30 min to remove volatile organic impurities.

2.2.4 Electrolyte

The electrolyte used for the preparation of the DSCs in this thesis consisted of 0.1 M LiI, 0.05 M I_2, 0.5 M 1-methylbenzimidazole and 0.6 M 1-butyl-3-methylimidazolium iodide in 3-methoxyproprionitrile. In Chapter 8 and Chapter 9 copper(I)/copper(II) based electrolytes in MeCN are introduced and the exact components described in the chapters.

2.2.5 Dyeing process

In order to functionalize the TiO_2 surface of the electrodes with the heteroleptic dyes $[Cu(L_{anchor})(L_{ancillary})]^+$, two different strategies were used: the ´surface-as-ligand, surface-as-complex´ strategy and the ´stepwise assembly´ strategy. Before dipping, the electrodes were rinsed with milliQ water and EtOH, dried in a stream of nitrogen and heated to 450 °C for 30 min on a hot plate. The homemade electrodes were post-treated with a 40 mM aqueous $TiCl_4$ solution (milliQ water) at 70 °C for 30 min, rinsed with milliQ water and EtOH, dried in a stream of nitrogen and heated to 450 °C for 30 min on a hot plate. For the preparation of the N719 reference electrodes, the TiO_2 electrodes were post-treated if they were homemade electrodes followed by washing and heating, or just rinsed and heated for the commercial electrodes in the same manner as mentioned before. After cooling the electrodes were immersed in a 0.3 mM EtOH solution of N719 (Solaronix) for 3 days. After soaking in the dye bath the electrodes were removed, washed with EtOH and dried.

2.2.5.1 ´Surface-as-ligand, surface-as-complex´ strategy

In Figure 13, the ´surface-as-ligand, surface-as-complex´ (´SALSAC´)[47] strategy is shown. After cooling, the electrodes were soaked in a 1.0 mM DMSO solution of the anchoring ligand for 24 h, washed with DMSO and EtOH and dried. The anchoring ligand functionalized electrodes were the immersed into 0.1 mM solutions of the homoleptic copper(I) complexes in an appropriate solvent, CH_2Cl_2, MeCN or acetone. After 3 days in the dye bath solution, the electrodes were taken out, washed with the same solvent used for the dye bath solution and dried in a stream of nitrogen yielding the heteroleptic copper(I) dyes adsorbed on the TiO_2 surfaces.

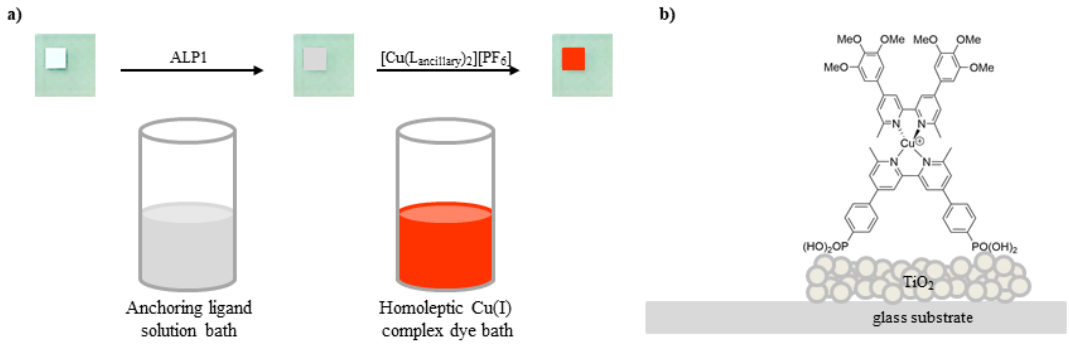

Figure 13: a) The ´surface-as-ligand, surface-as-complex´ (´SALSAC´) approach to functionalize an FTO/TiO_2 electrode with a heteroleptic $[Cu(L_{anchor})(L_{ancillary})]^+$ dye. b) A representative surface-anchored heteroleptic copper(I) dye.

2.2.5.2 ´Stepwise assembly´ strategy

In Figure 14, the ´stepwise assembly´ (´SW´)[65] strategy is shown. After cooling the electrodes were soaked in a 1.0 mM DMSO solution of the anchoring ligand for 24 h, washed with DMSO and EtOH and dried in a stream of nitrogen. The anchoring ligand functionalized electrodes were then immersed into a 2.0 mM MeCN solution of $[Cu(MeCN)_4][PF_6]$ for 24 h, washed with MeCN and dried. The electrodes were then soaked in a 1.0 mM DMSO solution of the ancillary ligand. After 3 days in the ancillary ligand solution the electrodes were taken out, washed with DMSO and EtOH and dried in a stream of nitrogen yielding the heteroleptic copper(I) dye adsorbed on the TiO_2 surface.

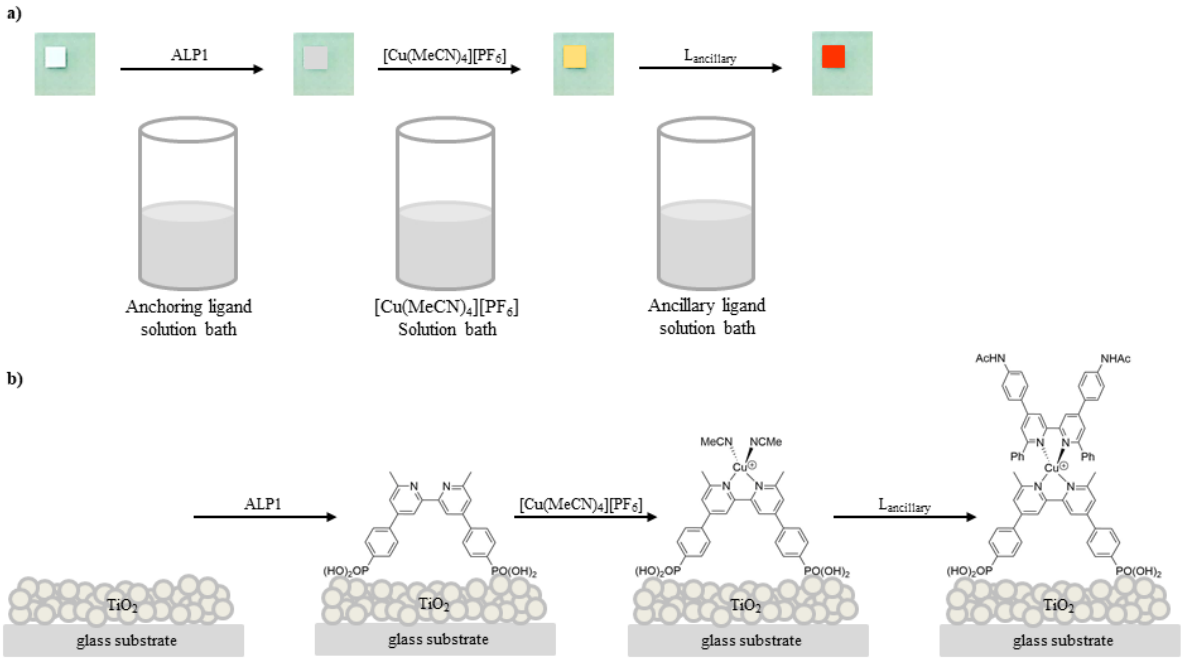

Figure 14: a) The ´stepwise assembly´ (´SW´) approach to functionalize an FTO/TiO_2 electrode with a heteroleptic $[Cu(L_{anchor})(L_{ancillary})]^+$ dye. b) ´Stepwise assembly´ on the TiO_2 surface with ALP1 anchored on the surface (second from left), proposed intermediate $[Cu(ALP1)(MeCN)_2]^+$ complex adsorbed on the surface (third from left) and a representative surface-anchored heteroleptic copper(I) dye for which the ´DW´ approach was used (right).

2.2.6 Cell assembly – device fabrication

The working and counter electrodes were combined with hot-melt sealing foils purchased from Solaronix (Solaronix Test Cell Gaskets, 60 μm) by heating while pressing them together with a soldering iron at 220 °C. To make sure that no degradation of the anchored dye can occur by heat, the head of the soldering iron was modified with a square hole with the size of the active area. After assembling of the two electrodes the cell was evacuated and flushed with nitrogen three times before introducing the electrolyte by vacuum back-filling via a pre-drilled hole in the counter electrode. The hole was sealed with a sealing foil and a covering glass. In a final step silver paint was added on both electrodes on the FTO glass to improve the contacts for the measurements.

2.3 Characterization of DSCs

2.3.1 Solid-state absorption measurements

For the solid-state absorption measurements transparent homemade or transparent commercial electrodes (Solaronix Test Cell Titania Electrodes Transparent) were functionalized with the heteroleptic copper(I) dyes or the N719 dye for the reference electrodes as described in Section 2.2.5. The electrodes were placed in a tailor-made holder in the spectrometer and the absorption spectra were recorded. A blank transparent TiO_2 electrode was measured in order to background correct the spectra by subtraction of the absorption spectra of the blank electrode. Furthermore the spectra were normalized for zero absorption at 800 nm.

2.3.2 Solar simulator measurements

For the solar simulator measurements the DSCs were fully masked. The mask was made from a black-coloured copper sheet with an aperture of average size of 0.0612 cm^2 (with a standard deviation of 1%) placed over the active area of the cell.[66,67] The area of the aperture in the mask was smaller than the surface area of the TiO_2, and additional black tape was used to complete the masking of the cell. The performance measurements were made by irradiating the DSC from behind. The tandem DSCs were measured by irradiating from the n-type working electrodes. Figure 15 shows the result of such a *J-V* measurement of a DSC, where J is the current density, and V is the potential. Figure 15 also shows all the important key parameters.

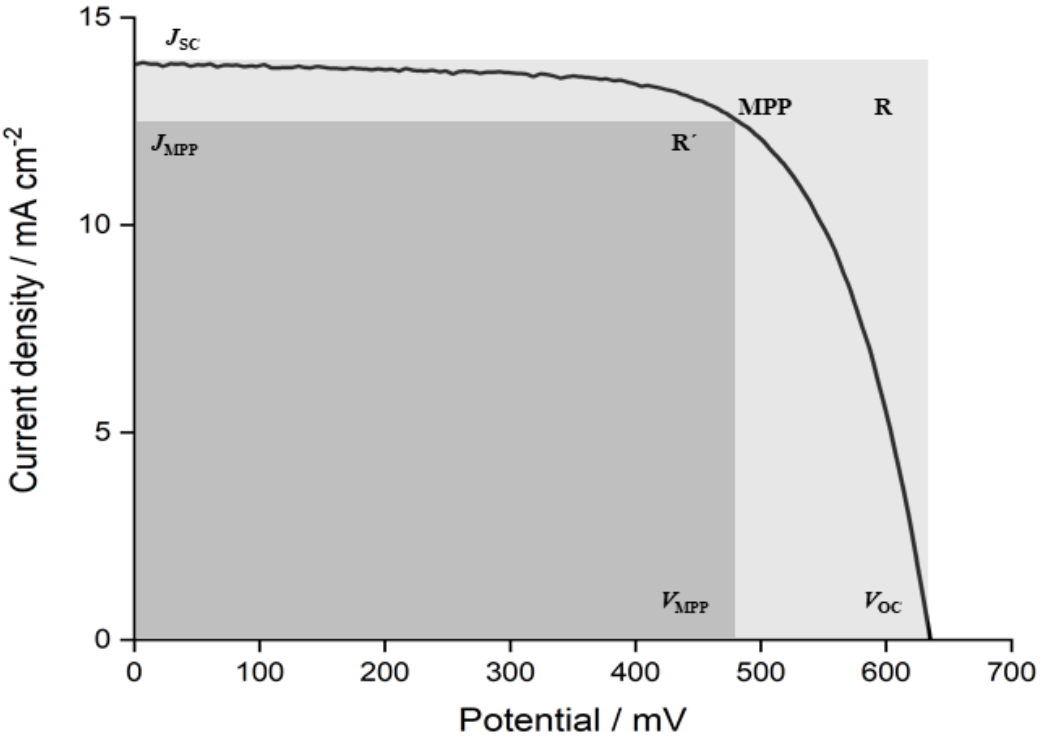

Figure 15: Result of a *J-V* measurement of DSC with N719 as dye with all the important key parameters.

In a solar simulator measurement, the current is recorded against voltage. The current is a one dimensional measured variable but the DSC consists of a two dimensional semiconductor material, therefore the current has to be divided by the measured active area of the cell. With this the measured current (I) is converted into current density (*J*) in units of mA/ cm^2. The short-circuit current density (J_{SC}) and the open-circuit voltage (V_{OC}) are two important measured variables. J_{SC} gives the highest possible current density the cell can reach at zero potential and V_{OC} gives the highest potential the cell can deliver at zero current. The rectangle R (Figure 15) defined by J_{SC} and V_{OC}, gives the theoretical maximum power P that the DSC could produce if no losses occur (Equation **(1)**).

$$P = V \times J \tag{1}$$

The theoretical power available from a DSC is important for the calculation of the fill factor (ff). The second rectangle R´ (Figure 15) is defined by J_{MPP} and V_{MPP}, and these two measured variables are the maximum current and the maximum potential that can be obtained depending on each other. The maximum power a DSC can deliver is the product of these two parameters. By division of R´ by R, the fill factor (ff) is calculated (Equation (**2**)). The fill factor is a measured variable which gives the quality of the DSC, as it depicts the difference between the ideal and the real system.

$$ff = \frac{V_{MPP} \times J_{MPP}}{V_{OC} \times J_{SC}} = \frac{R'}{R} \tag{2}$$

The most important parameter of a DSC is the photon to power conversion efficiency (η), often given as PCE. The efficiency of a DSC can be calculated by multiplication of the V_{OC}, the J_{SC} and the ff, divided by the power input (P_{in}) (Equation (**3**)).

$$\eta = \frac{V_{OC} \times J_{SC} \times ff}{P_{in}} \tag{3}$$

P_{in} is the value for the power of the incident light (sunlight), which is given to the system and set as I_S = 100 mW/ cm^2 = 1 sun at AM 1.5).

2.3.3 External Quantum Efficiency (EQE) measurement

The external quantum efficiency measurement (EQE) is also known as incident photon to current efficiency measurement (IPCE) and gives the overall charge injection collection measured under monochromatic light irradiation. The EQE describes the percentage of the number of photons converted to electrons by the DSC to the number of incident photons (Equation (**4**)). The incident photons are the photons of a specific energy or wavelength that hit the DSC.

$$EQE\ (\lambda) = \frac{electrons\ out\ (\lambda)}{Incident\ Photons\ (\lambda)} = \frac{J_{SC}\ (\lambda)}{q\Phi\ (\lambda)} = \frac{hc}{q} \times \frac{J_{SC}\ (\lambda)}{\lambda \times P_{in}\ (\lambda)}$$
$$= 1240 \times \frac{[W \times s \times nm]}{[A \times s]} \times \frac{J_{SC}\ (\lambda)[A \times cm^{-2}]}{\lambda[nm] \times P_{in}\ (\lambda)[W \times cm^{-2}]} \tag{4}$$

The value of the EQE at a specific wavelength depends on how much light is converted to electrons by the DSC. A maximum value of 100% for the EQE would be measured if all absorbed photons at a specific wavelength would be converted into electrons. It is also possible to calculate the short-circuit current (I_{SC}) of a DSC by integration of all EQE values measured over the whole spectrum multiplied by the incident light intensity (I_S) given at a specific wavelength (Equation (**5**)).[11]

$$I_{SC} = \int_0^\infty EQE\ (\lambda) \times I_S\ (\lambda) d\lambda \tag{5}$$

One disadvantage of the EQE is that optical properties of the DSC device itself, e.g. the light that is reflected or transmitted by the cell or light that is not absorbed, are not taken into account. A term including these device properties is the internal quantum efficiency (IQE), where the reflectance (*R*) and transmission (*T*) are subtracted and only the photons contributing to the charge generation are taken into account. In Equation (**6**) the calculation of the IQE is given, *R* is defined as the

hemispherical reflectance and T as the hemispherical transmission of the DSC at a specific wavelength.

$$IQE\ (\lambda) = \frac{EQE\ (\lambda)}{1 - R\ (\lambda) - T\ (\lambda)} \tag{6}$$

In this thesis the IQE was not used as a method for characterization of the DSC, only the EQE measurements were used to analyse the devices. In Figure 16, the EQE spectrum of an N719 DSC is shown. The measurements were performed over a range of wavelengths, from 350 to 750 nm. The EQE measurements were used to detect the light absorption and charge injection of the dyes. The DSCs were not masked for the EQE measurements.

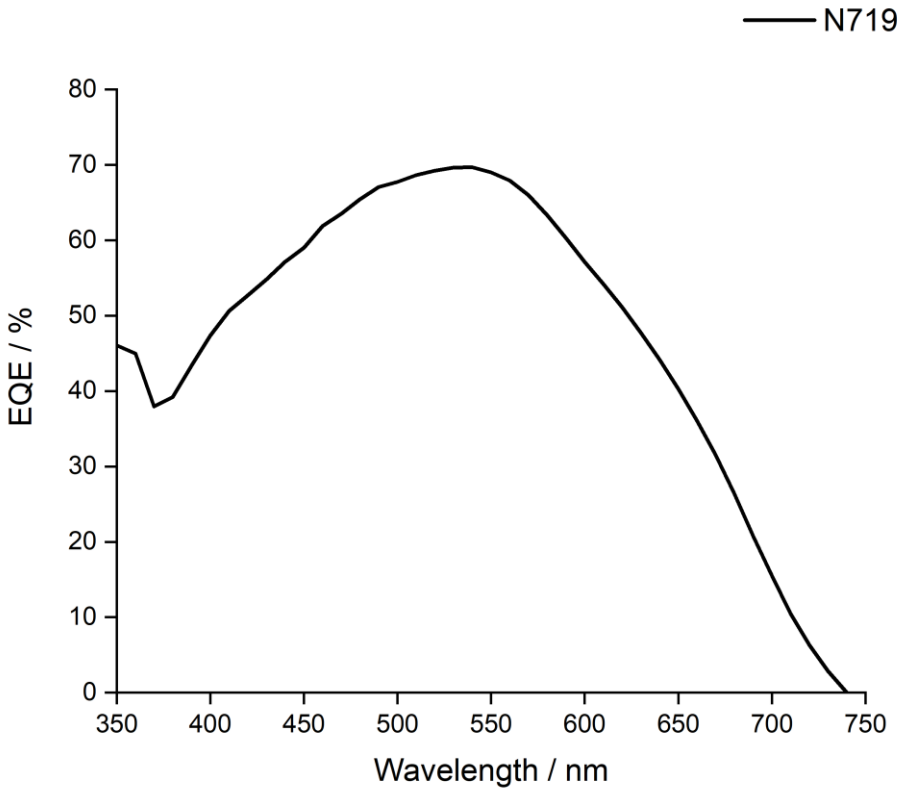

Figure 16: An EQE measurement of a DSC containing N719 as dye. Note the broad spectral response.

Chapter 3

Chapter 3 Anchoring Ligands

3.1 Motivation

As described in Chapter 2 (2.2.5.1 Figure 13) the assembling of the heteroleptic copper(I) dye absorbed on the TiO_2 surface is realized via a ´surface-as-ligand, surface-as-complex´ strategy.[47] The nature of these heteroleptic $[Cu(N^N)(N^N)´]^+$ dyes is preferential over homoleptic dyes as they feature the desired ´push-pull´ characteristics within their electronic properties facilitating the movement of the electron from the electrolyte, through the dye to the semiconductor.[52,68,69] It is well established that phosphonic acid anchoring groups are preferred over carboxylic acids in copper(I) dyes.[70,71] Furthermore it has been shown that phosphonic acid groups are preferred over the corresponding phosphonate ester groups in terms of anchoring to the surface and the resulting DCS performances.[72] In general the heteroleptic bis(diimine)copper(I) complexes used as dyes in n-type DSCs are difficult to isolate especially if the copper(I) centre is not protected towards ligand dissociation.[73,48,50,74] This can be explained by the nature of these heteroleptic complexes ($[Cu(L_{anchor})(L_{ancillary})]^+$) being labile in solution, undergoing ligand redistribution to give a statistical mixture of the heteroleptic and both homoleptic complexes (Equation (**7**)).[75]

$$2[Cu(L_{anchor})(L_{ancillary})]^+ \rightleftharpoons [Cu(L_{anchor})_2]^+ + [Cu(L_{ancillary})_2] \quad (7)$$

Fortunately, by using the ´surface-as-ligand, surface-as-complex´ approach it is not necessary to isolate the hetereoleptic copper(I) complex.[47,71,49,76,77] Nevertheless it is important to shield the tetrahedral copper(I) centre in $[Cu(N^N_{anchor})(N^N_{ancillary})´]^+$ against oxidation to square planar $[Cu(N^N_{anchor})(N^N_{ancillary})´]^{2+}$ (N^N = diimine).[78] The protection of the copper(I) centre towards oxidation is implemented by introducing methyl groups in the 6,6- positions of the anchoring ligand. This type of anchoring ligand ((6,6´-dimethyl-[2,2´-bipyridine]-4,4´-diyl)bis(4,1-phenylene))bis(phosphonic acid) (**1**) is proven to be very efficient in DSCs.[76,46] Changing the substituents in the 6,6´-positions on going from methyl to phenyl groups (L_{anchor} = **2**) could enhance the spectral response towards higher wavelengths.[75] The influence of the symmetry of the anchoring ligand was also taken into account and studied by comparison to an asymmetrical anchoring ligand (**3**). This chapter is focused on the synthesis of the different anchoring ligands **1**, **2** and **3** (Scheme 2). Furthermore examples for each anchoring ligand used in a DSC in combination with an ancillary ligand (Scheme 3) to build a heteroleptic copper(I) dye adsorbed on the electrodes surface is presented herein. The ancillary ligands used are 6-methyl-4-(3,4,5-trimethoxyphenyl)-2,2´-bipyridine (**7**) and 4,4´-bis(3,4,5-trimethoxyphenyl)-6,6´-dimethyl-2,2´-bipyridine (**11**) (Scheme 3). The detailed synthesis of those two ancillary ligands is described in the experimental part of Chapter 4 and Chapter 5 respectively. In Chapter 4 the application of both anchoring ligands **1** and **2** are studied in more detail, by combination with a whole set of similar ancillary ligands including $L_{ancillary}$ = **7** (Scheme 3).

Furthermore in Chapter 5 $L_{ancillary}$ = **11** and analogue ancillary ligands are investigated and their performances are verified in combination with anchoring ligand **1** (Scheme 2).

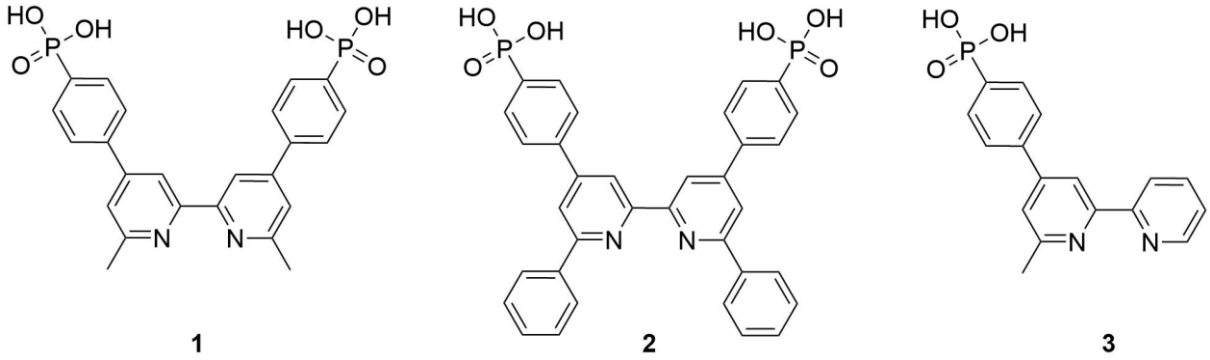

Scheme 2: Structure of anchoring ligands 1, 2 and 3.

3.2 Results

3.2.1 Solid state absorption spectra of copper(I) dyes with anchor **1**, **2** or **3** and different ancillary ligands

For the solid-state absorption spectra the heteroleptic copper(I) dyes were assembled step-wise on transparent, commercial TiO_2 electrodes to give $[Cu(\mathbf{1})(\mathbf{7})]^+$, $[Cu(\mathbf{1})(\mathbf{11})]^+$, $[Cu(\mathbf{2})(\mathbf{7})]^+$ and $[Cu(\mathbf{3})(\mathbf{11})]^+$ adsorbed on the electrode surfaces. The electrodes were washed with milliQ water, HPLC grade EtOH and dried in a stream of nitrogen, before heating at 450 °C for 30 min. After cooling, the electrodes were soaked in a 1.0 mM DMSO solutions of anchoring ligands **1**, **2** or **3** for 24 h, washed with DMSO and EtOH and dried. The anchoring ligand-functionalized electrodes were then immersed into solutions of the different homoleptic copper(I) complexes $[Cu(L_{ancillary})_2][PF_6]$ ($L_{ancillary}$ = **7 or 11**, 0.1 mM in CH_2Cl_2) (Scheme 3). After 3 days in the dye bath solution, the electrodes were taken out, washed with CH_2Cl_2 and dried in a stream of nitrogen. The solid-state absorption spectra were background-corrected by subtracting the absorption spectra of a blank electrode and normalized for zero absorption at 800 nm (Figure 17).

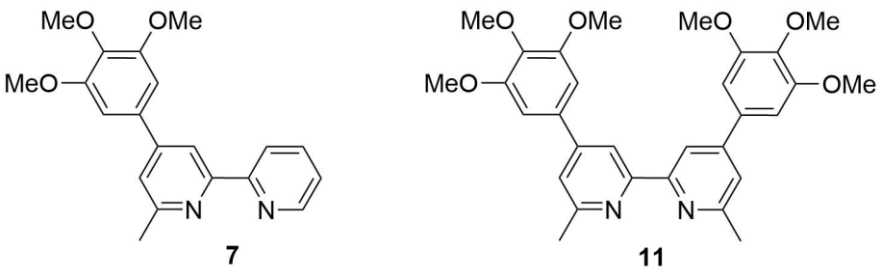

Scheme 3: Structure of the ancillary ligands used for testing the different anchoring ligands (1, 2 and 3).

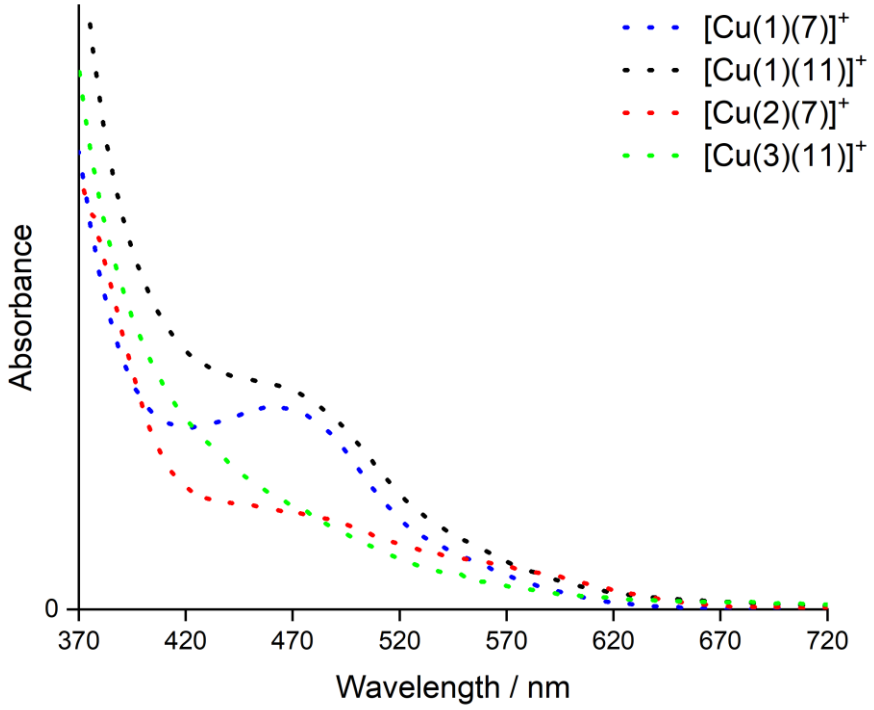

Figure 17: Solid-state absorption spectra of TiO_2 functionalized with dyes $[Cu(1)(7)]^+$, $[Cu(1)(11)]^+$, $[Cu(2)(7)]^+$ and $[Cu(3)(11)]^+$.

The solid state-absorption spectra in Figure 17 show that the MLCT bands of the electrodes with complexes using either anchoring ligand **1** or **2** appeared at λ_{max} ~ 460-470 nm. The dye containing anchoring ligand **3** in contrast does not give rise to a clear MLCT band declines (Figure 17 green curve). The comparison of the blue and red curves (Figure 17, dyes $[Cu(\mathbf{1})(\mathbf{7})]^+$ and $[Cu(\mathbf{2})(\mathbf{7})]^+$) shows that the change from methyl to phenyl groups in the 6,6´-positions of the anchoring ligand resulted in an overall lower absorption for anchoring ligand **2**. This decreased absorption can be explained by a lower dye-loading for anchoring ligand **2**. The phenomenon of the lower dye-loading is investigated in more detail in Chapter 4. However the change in the substituent of the anchoring ligand resulted in a slight increase in the absorption at longer wavelength (Figure 17 red curve 550 to 650 nm). Changing the corresponding ancillary from an asymmetrical ($L_{ancillary}$ = **7**, blue curve) to a symmetrical bipyridine ($L_{ancillary}$ = **11**, black curve) in combination with anchoring ligand **1** showed a slightly higher absorption for dye $[Cu(\mathbf{1})(\mathbf{11})]^+$ also exhibiting a shoulder for the MLCT absorption from ~ 425-470 nm.

3.2.2 DSC performances of dyes with anchor **1**, **2** and **3** with different ancillary ligands

In order to verify the binding ability and the resulting performance in the device, DSCs functionalized with copper(I) dyes with the three different anchoring ligands **ALP1** (**1**), **PhALP1** (**2**) and asymmetric **ALP1** (**3**) were prepared in combination with the two different ancillary ligands **7** and **11** shown in Scheme 3. The anchoring ligand **1** was tested in combination with both ancillary ligands shown in Scheme 3, but anchoring ligand **2** was only measured in combination with ancillary ligand **7** and anchoring ligand **3** combined with ancillary ligand **11**. The two ancillary ligands used in this test vary in terms of their symmetry. Ancillary ligand **7** is the asymmetrical analogue of ancillary ligand **11** (Scheme 3). Both ancillary ligands described in this chapter are studied in more details, including the synthetic route in later chapters of this thesis (Chapter 4 and Chapter 5).

The heteroleptic copper(I) dyes were assembled step-wise on commercial TiO_2 electrodes to give [Cu(**1**)(**7**)]$^+$, [Cu(**1**)(**11**)]$^+$, [Cu(**2**)(**7**)]$^+$ and [Cu(**3**)(**11**)]$^+$ adsorbed on the electrode surfaces. The commercial TiO_2 electrodes were washed with milliQ water and HPLC grade EtOH, dried in a stream of nitrogen and then heated at 450 °C for 30 min. After cooling, the electrodes were soaked in a 1.0 mM DMSO solution of anchoring ligands **1**, **2** or **3** for 24 h, washed with DMSO and EtOH and dried. The anchoring ligand-functionalized electrodes were then immersed into solutions of the different homoleptic copper(I) complexes [Cu($L_{ancillary}$)$_2$][PF_6] ($L_{ancillary}$ = **7** or **11**, 0.1 mM in CH_2Cl_2) (Scheme 3). After 3 days in the dye bath solution, the electrodes were taken out, washed with CH_2Cl_2 and dried in a stream of nitrogen. Each dye-soaked working electrode was assembled with a commercial Pt counter-electrode using a thermoplast hot-melt sealing foil. The electrolyte between the electrodes, an I^-/I_3^- electrolyte, was introduced by vacuum backfilling. Duplicate DSCs were prepared for each dye to verify the reproducibility of assembling the solar cells and the measurements respectively. In contrast to the solid-state absorption measurements described in the last section, commercial electrodes with a scattering layer were used for the *J-V* and EQE measurements shown in Figure 18 and Figure 19. The measurements were done in a fully masked mode by irradiating the cells from behind.[79,80] The average active area in the DSC measurements was 0.06012 cm^2 (with a standard deviation of 1%). The DSCs were measured on day 0, the day of assembling the cells. A DSC containing N719 as the sensitizer was prepared for each set and measured as reference. The relative efficiencies of the DSCs were calculated by setting the efficiency for N719 to 100%[81] for better comparison of the different dye combinations (Table 1).

3.2.2.1 Solar cell measurements

Anchoring ligand **1** generally performed the best in combination with the two ancillary ligands (**7** and **11**) used for this test yielding efficiencies between 1.75 and 1.96% with respect to 5.52 and 5.79% for an N719 reference cell. Changing the ancillary ligand from **7** to **11** showed a slight increase in the short circuit current density going from 4.33 to 4.73 mA/cm^2 (Figure 18 and Table 1). This increase is

in accordance with the higher absorption seen in the solid-state absorption spectra (Figure 17). In contrast anchoring ligand **2** only reached efficiencies of 0.29 and 0.39% with respect to 5.71% for an N719 reference cell. The fill factors and open circuit voltages for the DSCs containing anchoring ligand **1** and **2** were in a good range ff ~ 70% and V_{OC} ~ 474 – 571 mV. The difference in the performance of cells with either anchoring ligand **1** or **2** can be attributed to the lower short circuit current density of anchoring ligand **2** J_{SC} ~ 1.12 and 1.19 mA/cm^2 over anchoring ligand **1** yielding J_{SC} ~ 4.33 – 4.79 mA/cm^2 respectively (Figure 18 and Table 1). However anchoring ligand **3** yielded the poorest efficiencies of 0.02% for both DSCs measured with respect to 6.05% for an N719 reference cell. The low performances for dyes containing anchoring ligand **3** is associated with low short circuit current densities 0.34 and 0.42 mA/cm^2, low open circuit voltages 134 and 175 mV and low fill factors 34 and 38% (Figure 18 and Table 1). The duplicate DSCs in Table 1 confirmed the reproducibility of both the assembling and the measurements of the cells.

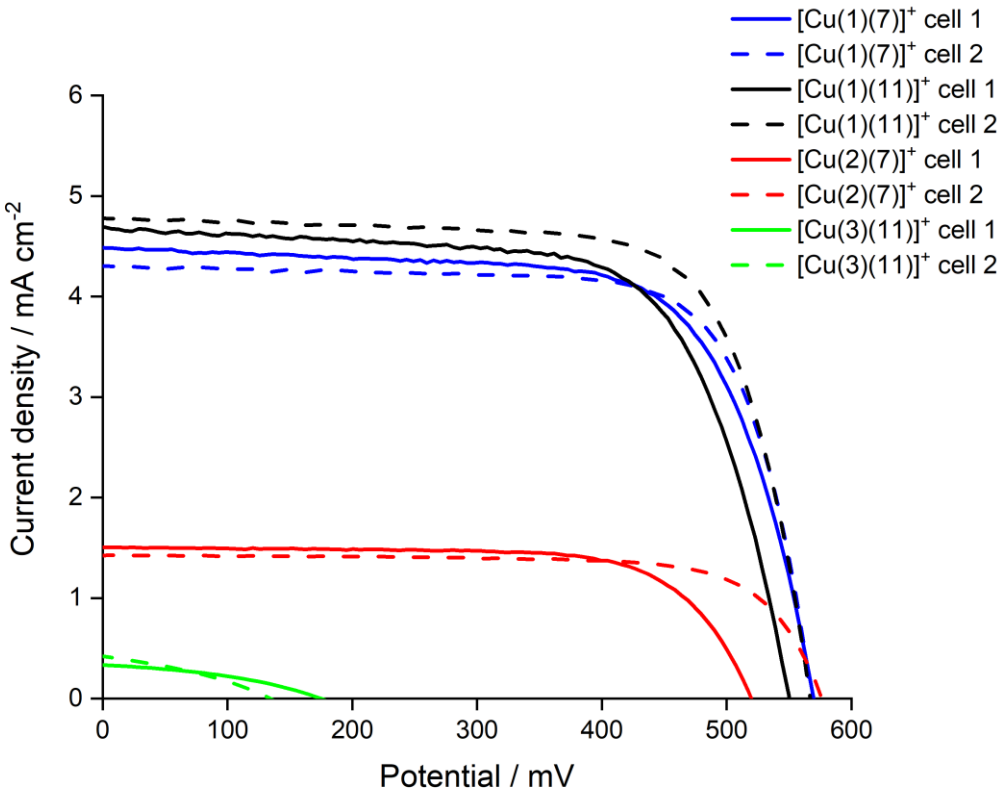

Figure 18: *J-V* curves for duplicate DSCs containing dyes [Cu(1)(7)]$^+$, [Cu(1)(11)]$^+$, [Cu(2)(7)]$^+$ and [Cu(3)(11)]$^+$ measured on day of cell assembling.

Table 1: Performance parameters of duplicate DSCs with dyes $[Cu(1)(7)]^+$, $[Cu(1)(11)]^+$, $[Cu(2)(7)]^+$ and $[Cu(3)(11)]^+$ compared to N719 as reference measured on the day of cell assembling.

Dye	J_{sc}/mA cm^{-2}	V_{OC}/mV	ff/%	η/%	Relative η/%
$[Cu(\mathbf{1})(\mathbf{7})]^+$	4.33	569	72	1.77	32.1
$[Cu(\mathbf{1})(\mathbf{7})]^+$	4.33	571	74	1.83	33.2
N719	13.61	623	65	5.52	100
$[Cu(\mathbf{1})(\mathbf{11})]^+$	4.68	550	68	1.75	30.2
$[Cu(\mathbf{1})(\mathbf{11})]^+$	4.79	567	72	1.96	33.9
N719	13.29	647	67	5.79	100
$[Cu(\mathbf{2})(\mathbf{7})]^+$	1.12	496	70	0.39	6.8
$[Cu(\mathbf{2})(\mathbf{7})]^+$	1.19	474	51	0.29	5.1
N719	13.38	640	67	5.71	100
$[Cu(\mathbf{3})(\mathbf{11})]^+$	0.34	175	38	0.02	0.33
$[Cu(\mathbf{3})(\mathbf{11})]^+$	0.42	134	34	0.02	0.33
N719	12.74	654	73	6.05	100

3.2.2.2 External Quantum Efficiency (EQE) measurements

Due to the very poor performances of DSCs assembled by using anchoring ligand **3**, no EQE specta of the cells containing $[Cu(\mathbf{3})(\mathbf{11})]^+$ were recorded. Figure 19 compares the EQE curves of $[Cu(\mathbf{1})(\mathbf{7})]^+$, $[Cu(\mathbf{1})(\mathbf{11})]^+$ and $[Cu(\mathbf{2})(\mathbf{7})]^+$. The curves show the lower photon-to-current conversion efficiencies of the dye containing ligand **2** as anchor over the DSCs with anchoring ligand **1**. These data are consistent with the results from the solar simulator measurements presented above. The DSCs with anchoring ligand **1** gave higher EQE_{max} values almost independent of the ancillary ligand used. The highest value for the EQE of DSCs with $[Cu(\mathbf{1})(\mathbf{7})]^+$ or $[Cu(\mathbf{1})(\mathbf{11})]^+$ were 42.2% and 45.3% respectively. The lower performing DSC with $[Cu(\mathbf{2})(\mathbf{7})]^+$ yielded a EQE_{max} value of 8.1% (Table 2). Although the EQE_{max} value for the DSC with anchoring ligand **2** was low, the shape of the curve confirmed the broadened spectral response from 550 to 650 nm already seen in the solid-state absorption spectra (Figure 17). The low overall performance of anchoring ligand **2** was consistent with the solid-state absorption spectra and the DSC performance measurement as well as the confirmation of these findings with the EQE spectra shown here is further investigated in Chapter 4 of this thesis. The change in the symmetry of the ancillary ligand from the asymmetric ($L_{ancillary}$ = **7**) to the symmetric ($L_{ancillary}$ = **11**) did not give a significant change in the photon to current conversion efficiencies of the cells (Figure 19 black and blue curves, Table 2). The DSC performance was slightly higher for $L_{ancillary}$ = **11**. The data were in accordance with a slightly higher J_{SC} values for $[Cu(\mathbf{1})(\mathbf{11})]^+$ (Figure 18 and Table 1) and could also be seen in the solid-state absorption spectrum (Figure 17 black curve) giving a higher absorption with a shoulder for this dye.

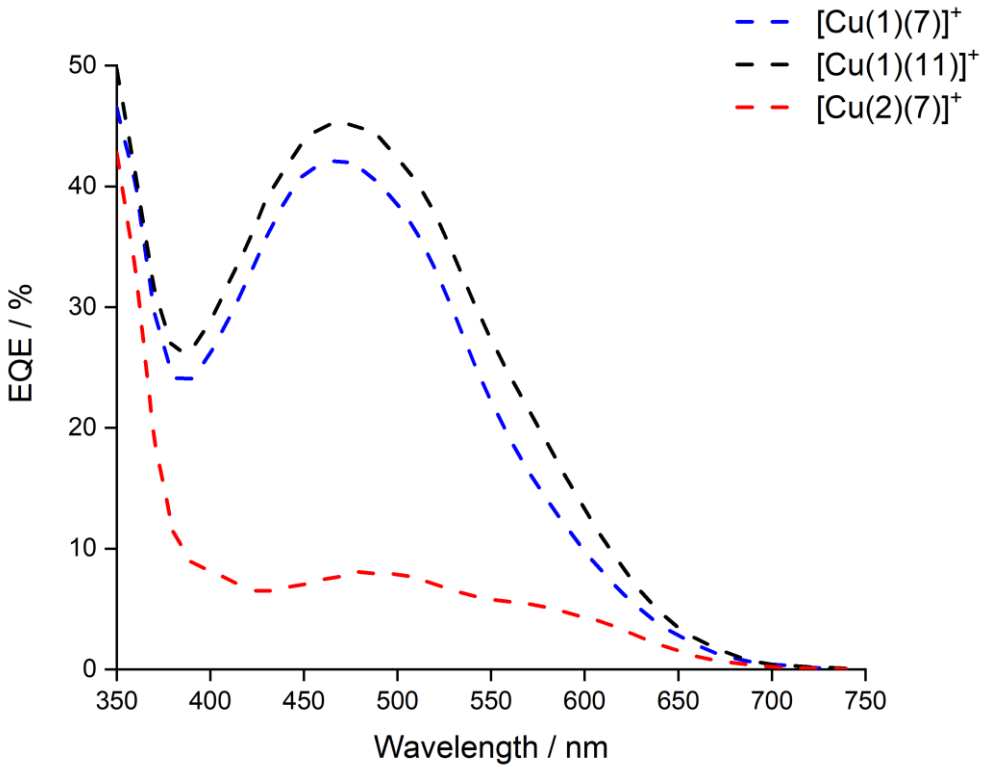

Figure 19: EQE spectra for DSCs containing the dyes $[Cu(1)(7)]^+$, $[Cu(1)(11)]^+$ and $[Cu(2)(7)]^+$ measured on the day of cell assembling.

Table 2: EQE maxima for DSCs containing dyes $[Cu(1)(7)]^+$, $[Cu(1)(11)]^+$ and $[Cu(2)(7)]^+$.

Dye	λ_{max} / nm	EQE_{max} / %
$[Cu(\mathbf{1})(\mathbf{7})]^+$	470	42.2
$[Cu(\mathbf{1})(\mathbf{11})]^+$	470	45.3
$[Cu(\mathbf{2})(\mathbf{7})]^+$	480	8.1

3.3 Conclusion

In this chapter three different anchoring ligands **1**, **2** and **3** were presented and there performances in DSCs investigated in combination with two ancillary ligands **7** and **11** were assessed. All the anchoring ligands had a phosphonic acid anchoring unit attached to a 2,2´-bipyridine via a phenyl spacer. Anchoring ligand **1** and **2 (ALP1** and **PhALP1**) differed in the substituents in the 6,6´-position of the bpy unit being either methyl (**1**, **ALP1**) or phenyl (**2**, **PhALP1**) groups. In contrast to these two anchoring ligands, **3** (**asym. ALP1**) was the asymmetrical analogue of **ALP1**. Similar to this $L_{ancillary}$ **7** is the asymmetrical complement of $L_{ancillary}$ **11**, other than that both ancillary ligands are 3,4,5-methoxy substituted at the phenyl ring para to the bpy unit. DSCs containing dyes $[Cu(\mathbf{1})(\mathbf{7})]^+$, $[Cu(\mathbf{1})(\mathbf{11})]^+$,

[Cu(**2**)(**7**)]$^+$ and [Cu(**3**)(**11**)]$^+$ were assembled and characterized. The photoconversion efficiencies showed an overall higher performance for DSCs with **ALP1** as the anchoring ligand, almost independent of the ancillary ligand used with relative η between 30.2 and 33.9% (relative to 100% set for N719). DSCs with the **PhALP1** anchoring ligand in contrast yielded lower relative η of 5.1 and 6.8% (relative to 100% set for N719). The lower cell performance is associated with lower short circuit current density values (Table 1). The **asym. ALP1** anchoring ligand showed the lowest power conversion efficiencies (relative η = 0.33%) which is coherent with both, low J_{SC} and V_{OC} values (J_{SC} ~ 0.34 mA/cm^2 and V_{OC} ~ 134 mV, Table 1) and poor fill factors ff ~ 34%. The photon to current conversion efficiency values confirmed the better performance of DSCs with anchoring ligand **1** (EQE_{max} > 42%) over anchoring ligand **2** (EQE_{max} = 8.1 %) (Table 2). Nevertheless the DSCs with the **PhALP1** anchoring ligand showed a broadened spectral response from 550 to 650 nm in both the solid-state absorption (Figure 17) and the EQE spectra (Figure 19 and Table 2). This phenomena of the broadened spectral response of the **PhALP1** anchoring ligand can be explained due to the phenyl substituents in the 6,6´-position of the bipyridine causing flattening of the copper(I) coordination sphere leading to changes in the profile of the MLCT band.[82] Still the overall performance of DSCs with this anchoring ligand **2** was lower. The influence on the low performance of the bulkier anchoring ligand **2** is further investigated in Section 4.3.3 of the next chapter. The better anchoring ability and photoconversion efficiency of DSCs with the **ALP1** anchoring ligand was confirmed and is used in the following chapters to investigate the influences of different ancillary ligands.[71,76,75,83]

The asymmetrical anchoring ligand (**3**) was not investigated further. Nevertheless future work should concentrate on investigating ancillary ligands that might perform better with the **asym. ALP1** anchoring ligand as its smaller size could possibly yield a higher overall dye concentration absorbed on the TiO_2 surface.

3.4 Experimental - synthesis of the anchoring ligands

One of the key steps in the synthesis of the anchoring ligand is the deprotection of the corresponding tetraethyl ester to the phosphonic acid. In the following synthesis of the three anchoring ligands **1**, **2** and **3** two different routes to deprotect the tetraethyl ester are shown (Scheme 4 and Scheme 5).

3.4.1 Synthesis of ((6,6´-dimethyl-[2,2´-bipyridine]-4,4´-diyl)bis(4,1-phenylene))bis(phosphonic acid) (**1**) (**ALP1**)

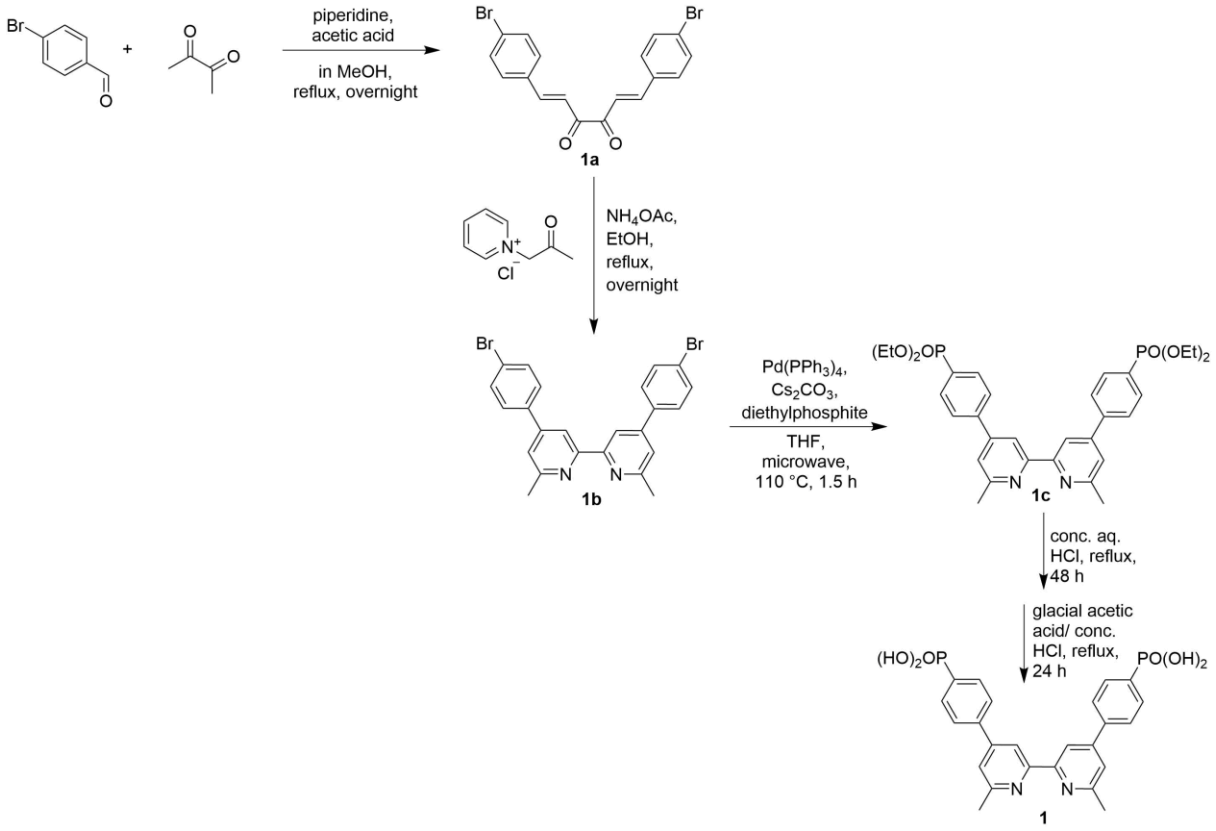

Scheme 4: Synthesis of the ALP1 anchoring ligand (1).

Compound **1a** and **1b** were prepared according to the literature using the Kröhnke strategy[84]. For the further synthesis compound **1b** was used from an in house stock.[46] Compound **1b** (1.0 g, 2.02 mmol), [$Pd(PPh_3)_4$] (410 mg, 0.355 mmol) and Cs_2CO_3 (1.43 g, 4.39 mmol) were combined in anhydrous THF in a 10-20 mL microwave vial equipped with a stir bar under argon. Diethylphosphite (1.11 g, 1.03 mL, 8.06 mmol) was added with a syringe before the vial was sealed and the reaction mixture was heated under microwave irradiation to 110 °C for 90 min. The reaction mixture was filtered, washed with THF (20 mL) and the yellow solution was concentrated under reduced pressure. The residue was dissolved in CH_2Cl_2 (20 mL) and stirred with decolourising charcoal for 30 min, then filtered over Celite and washed with CH_2Cl_2. The solvent was removed and an oily brown-yellowish residue was obtained, which was dissolved in acetone (5 mL) and filtered through a short silica plug eluting with acetone (25 mL). A pale yellow solution was obtained and concentrated under reduced pressure. A 1:1 mixture of pentane/hexane was added until the solution became turbid, followed by

heating until a clear solution was obtained. After cooling to room temperature a precipitate was formed and collected by filtration yielding compound **1c** as off-white powder (833 mg, 67.6%). Compound **1c** was dissolved in aqueous 6 M HCl (70 mL) and heated to reflux for 48 h. The solvent was removed under reduced pressure, leaving a pale yellow residue. This was dissolved in glacial acetic acid (35 mL), 5 drops of concentrated aqueous HCl were added and the mixture was heated at 120 °C for 6 h. After cooling to room temperature water (~ 20 mL) was added and a precipitate was formed. Anchoring ligand **1** was collected by filtration as off-white solid (143 mg, 0.288 mmol, 70.1%). The spectroscopic data matched those reported in the literature[75].

3.4.2 Synthesis of ((6,6´-diphenyl-[2,2´-bipyridine]-4,4´-diyl)bis(4,1-phenylene))bis(phosphonic acid) (**2**) (**PhALP1**)

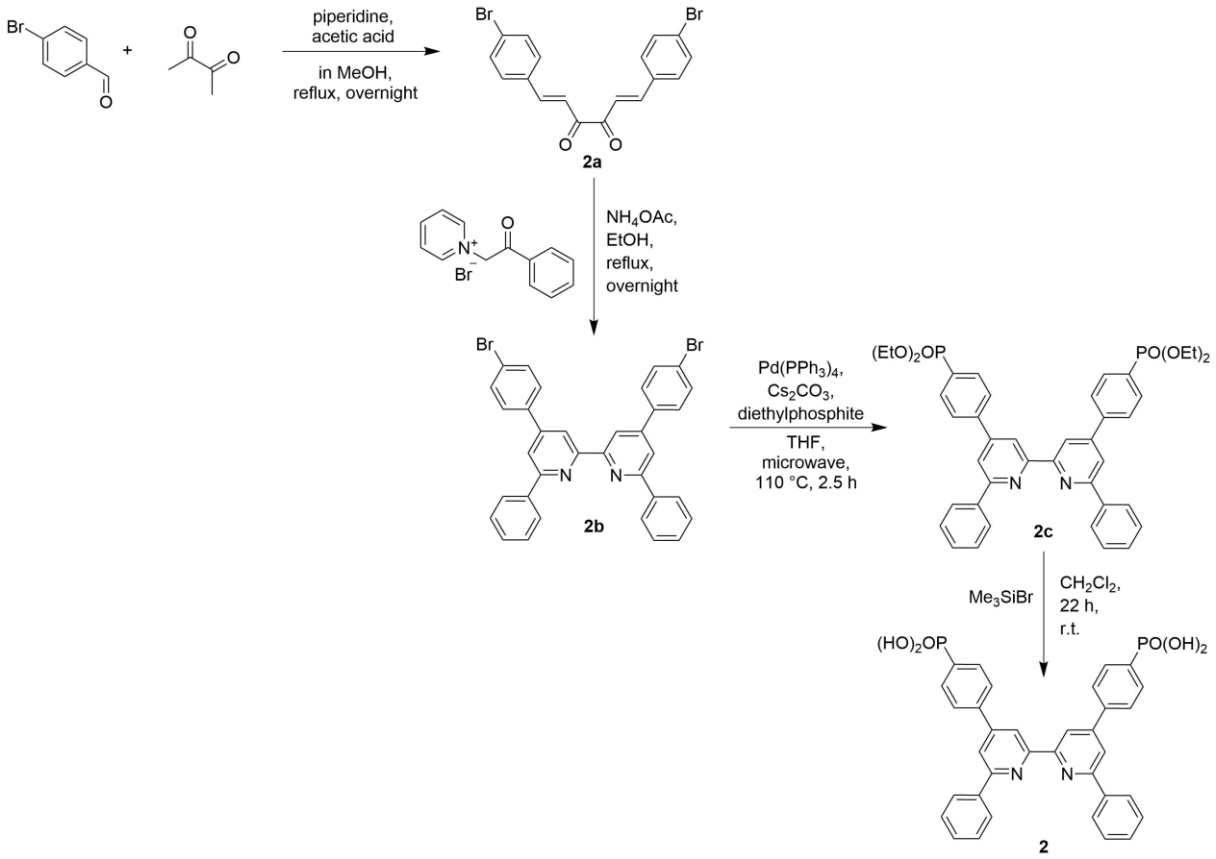

Scheme 5: Synthesis of the PhALP1 anchoring ligand (2).

Bromobenzaldehyde (5.0 g, 27 mmol), acetic acid (0.13 mL, 2.28 mmol) and piperidine (0.23 ml, 2.28 mmol) were dissolved in 30 mL MeOH. 2,3-Butandione (1.18 mL, 13.5 mmol) in MeOH (14 mL) were added dropwise at room temperature. The reaction mixture was heated to reflux overnight. A precipitate was formed, filtered off and washed with cold MeOH (10 mL). After drying in air compound **2a** was isolated as brown powder (710 mg, 13.5 mmol, 12.5%) and used for the following reaction step without further purification. Compound **2a** (702 mg, 1.67 mmol), 1-(2-oxopphenyl)pyridinium bromide (1858 mg, 6.68 mmol) and NH_4OAc (1017 mg, 13.2 mmol) were

dissolved in 50 mL EtOH and heated to reflux overnight. After cooling to room temperature, a precipitate was formed, filtered off and washed with cold EtOH yielding a beige solid (427 mg). The crude was purified by recrystallisation from MeOH / EtOH (5:1, 60 mL) and dried in air. Compound **2b** was isolated as beige solid (376 mg, 1.67 mmol, 36.4%). Compound **2b** (198 mg, 0.32 mmol), $[Pd(PPh_3)_4]$ (141 mg, 0.122 mmol) and Cs_2CO_3 (323 mg, 0.992 mmol) were combined in anhydrous THF in a 10-20 mL microwave vial equipped with a stir bar under argon. Diethylphosphite (115 mg, 0.106 mL, 0.832 mmol) was added with a syringe before the vial was sealed and the reaction mixture was heated under microwave irradiation to 110 °C for 150 min. The reaction mixture was filtered, washed with THF (20 mL) and the brownish solution was concentrated under reduced pressure. The residue was dissolved in CH_2Cl_2 (20 mL) and stirred with decolourising charcoal for 10 min, then filtered over Celite and washed with CH_2Cl_2 (20 mL). The resulting yellow solution was concentrated to dryness and acetone (25 mL) was added, and a white precipitate was formed. The precipitate was filtered off and washed with Et_2O (20 mL) and dried in air yielding compound **2c** as white solid (52 mg, 0.32 mmol, 22.2%). Compound **2c** (25 mg, 0.034 mmol) and Me_3SiBr (104 mg, 0.682 mmol) were dissolved in dry CH_2Cl_2 (4 mL) and stirred for 22 h at room temperature. The reaction mixture was quenched with water (~ 20 mL) and an off-white precipitate formed which was collected by filtration and washed with water (~ 10 mL). The organic phase was extracted with water (2 x 15 mL). The combined aqueous phases were concentrated under reduced pressure and toluene (50 mL) was added and the solvent removed. The residue was dried under high vacuum yielding **2** as an off-white solid (12.4 mg, 0.0199 mmol, 58.6%). The spectroscopic data matched to those reported in the literature[75].

3.4.3 Synthesis of 6-methyl-[2,2´bipyridine]-4,1-phenyl-4-phosphonic acid (**3**) (**asym. ALP1**)

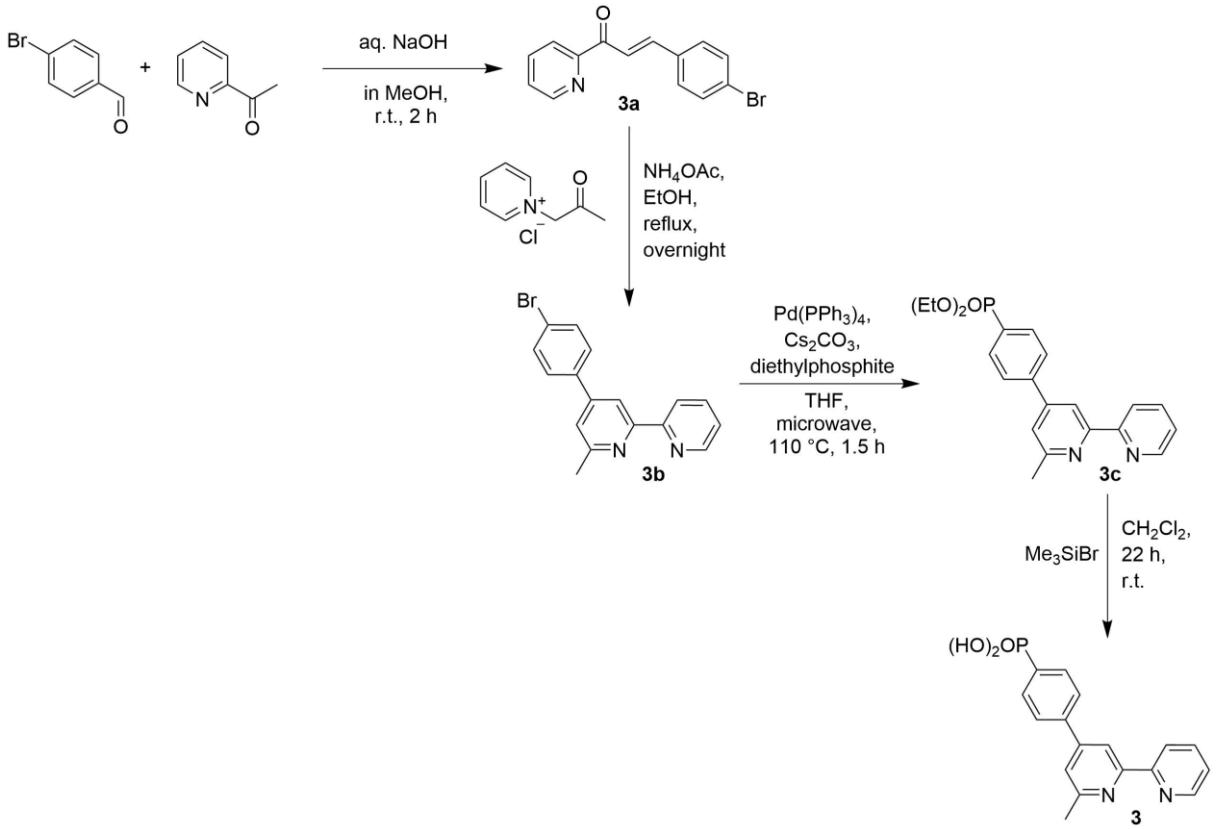

Scheme 6: Synthesis of the asymmetrical anchoring ligand (asym. ALP1) (3).

2-Acetylpyridine (1.31 g, 10.8 mmol) and bromobenzaldehyde (2.00 g, 10.8 mmol) were dissolved in MeOH (100 mL). Then solid NaOH (0.44 g, 0.22 mmol) in 22 mL water was added. The reaction mixture was stirred for 2 h at room temperature. A white precipitate formed, was collected by filtration and washed with water (~ 20 mL) and MeOH (3 x ~ 15 mL). Compound **3a** was isolated as off-white solid (1.29 g, 4.482 mmol, 41.5%) and used without further purification for the next synthetic step.[85,86] Compound **3a** (5.39 g, 18.7 mmol), 1-(2-oxopropy)pyridinium chloride (3.21 g, 18.7 mmol) and NH_4OAc (43.2 g, 561 mmol) were suspended in EtOH (300 mL). The suspension was heated to reflux overnight. The solution was cooled to room temperature and a precipitate formed. The precipitate was filtered off and washed with cold MeOH to yield compound **3b** as off-white solid (1.29 g, 3.97 mmol, 21.2%).[83] Compound **3b** (537 mg, 1.65 mmol), [$Pd(PPh_3)_4$] (334 mg, 0.289 mmol) and Cs_2CO_3 (1165 mg, 3.58 mmol) were combined in anhydrous THF in a 10-20 mL microwave vial equipped with a stir bar under argon. Diethylphosphite (907 mg, 0.84 mL, 6.57 mmol) was added with a syringe before the vial was sealed and the reaction mixture was heated under microwave irradiation to 110 °C for 90 min. The reaction mixture was filtered, washed with THF (35 mL) and the brownish solution was concentrated under reduced pressure. The residue was dissolved in CH_2Cl_2 (25 mL) and stirred with decolourising charcoal for 10 min, then filtered over Celite and washed with CH_2Cl_2 (30 mL). The resulting yellow solution was concentrated to dryness and acetone (25 mL) was added, and a white

precipitate was formed. The precipitate was filtered off and washed with Et_2O (20 mL) and dried in air yielding compound **3c** as white solid (297 mg, 0.78 mmol, 47.1%). Compound **3c** (739 mg, 1.93 mmol) and Me_3SiBr (14.7 g, 12.7 mL, 96.5 mmol) were dissolved in dry CH_2Cl_2 (70 mL) and stirred overnight at room temperature. The reaction mixture was quenched with water (~ 100 mL). The organic phase was extracted with water (3 x ~ 50 mL). The combined aqueous phases were concentrated under reduced pressure and toluene (50 mL) was added and the solvent removed. The residue was dried under high vacuum yielding **3** as an off-white solid (346 mg, 1.06 mmol, 54.9%).

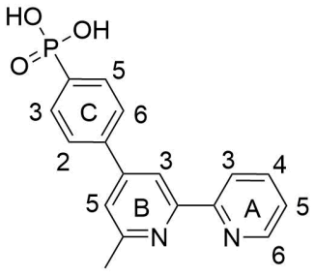

Scheme 7: Structure of the asymmetric anchoring ligand (3) with atom labelling for NMR assignments.

^{1}H NMR (500 MHz, DMSO-d_6) δ/ppm 8.79 (d, J = 4.2 Hz, 1H, H^{A6}), 8.60(s, 1H, H^{B3}), 8.57 (d, J = 7.9 Hz, 1H, H^{A3}), 8.14 (t, J = 7.5 Hz, 1H, H^{A4}), 8.02 (dd, J = 8.2,3.0 Hz, 2H, H^{C2+C6}), 7.89 (s, 1H, H^{B5}), 7.85 (m, 2H, H^{C3+C5}), 7.63 (m, 1H, H^{A5}), 2.71 (s, 3H, H^{Me}).

^{13}C NMR (126 MHz, DMSO-d_6) δ/ppm 158.2 (C^{B6}), 152.9 (C^{B2}), 152.6 (C^{A2}), 149.3 (C^{B4}), 148.4 (C^{A6}), 139.1 (C^{A4}), 139.9 (C^{C1}), 138.6 (C^{A4}), 136.3 (C^{C4}), 131.4 ($C^{C3/C5}$), 131.3 ($C^{C3/C5}$), 126.69 ($C^{C2/C6}$), 126.85 ($C^{C2/C6}$), 125.2 (C^{A5}), 122.3 (C^{B5}), 121.9 (C^{A3}), 116.4 (C^{B3}), 23.4 (C^{Me}).

ESI-MS *m/z* 226.31 $[M + H]^+$ (calc. 227.09).

Chapter 4

Chapter 4 Asymmetric ancillary ligands in bis(diimine)copper(I) dyes

4.1 Motivation

As discussed in Chapter 3, the performance of copper(I) based dye sensitized solar cells is strongly dependent on the anchoring ligand unit. [71,76] It was shown that the 6,6´-diphenyl substituent in the **PhALP1** anchoring ligand broadens the spectral response of the copper(I) dye towards the red end of the visible spectrum and features a similar steric shielding effect to the copper(I) centre as the dimethyl substituents on the **ALP1** anchoring ligand.[46] The combination of this diphenyl substituted anchoring ligand led to a bleaching effect of the dye-sensitized working electrode in the presence of the I^-/I_3^- electrolyte or lithium iodide.[75] As a consequence of this bleaching effect the DSCs resulted in poor cell performances. To overcome the bleaching problem asymmetrical ancillary ligands were investigated to minimize the repulsion between the lager substituents around the copper(I)bis(diimine) coordination centre if both - the anchoring and the ancillary ligand are 6,6´disubstituted.[83] Part of the ligand synthesis in this chapter was done in cooperation with Dr. Sven Y. Brauchli.

4.2 Synthetic approach

The Kröhnke synthesis[84] was used to prepare the asymmetrical ancillary ligands (**4-7**). The synthesis of the ((6,6´-diphenyl-[2,2´-bipyridine]-4,4´-diyl)bis(4,1-phenylene))bis(phosphonic acid) was presented earlier.[75] The deprotection step of the corresponding ester was optimized using Me_3SiBr (instead of the previously used concentrated acid treatment for 3 days). Scheme 8 displays the synthetic route of the ancillary ligands, Scheme 9 shows the modified anchoring ligand synthesis.

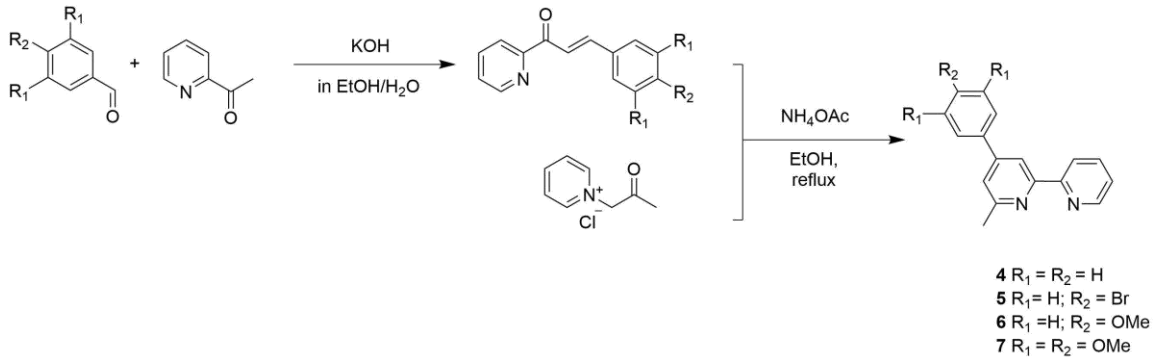

Scheme 8: Synthesis of the asymmetrical ancillary ligands from a literature procedure.

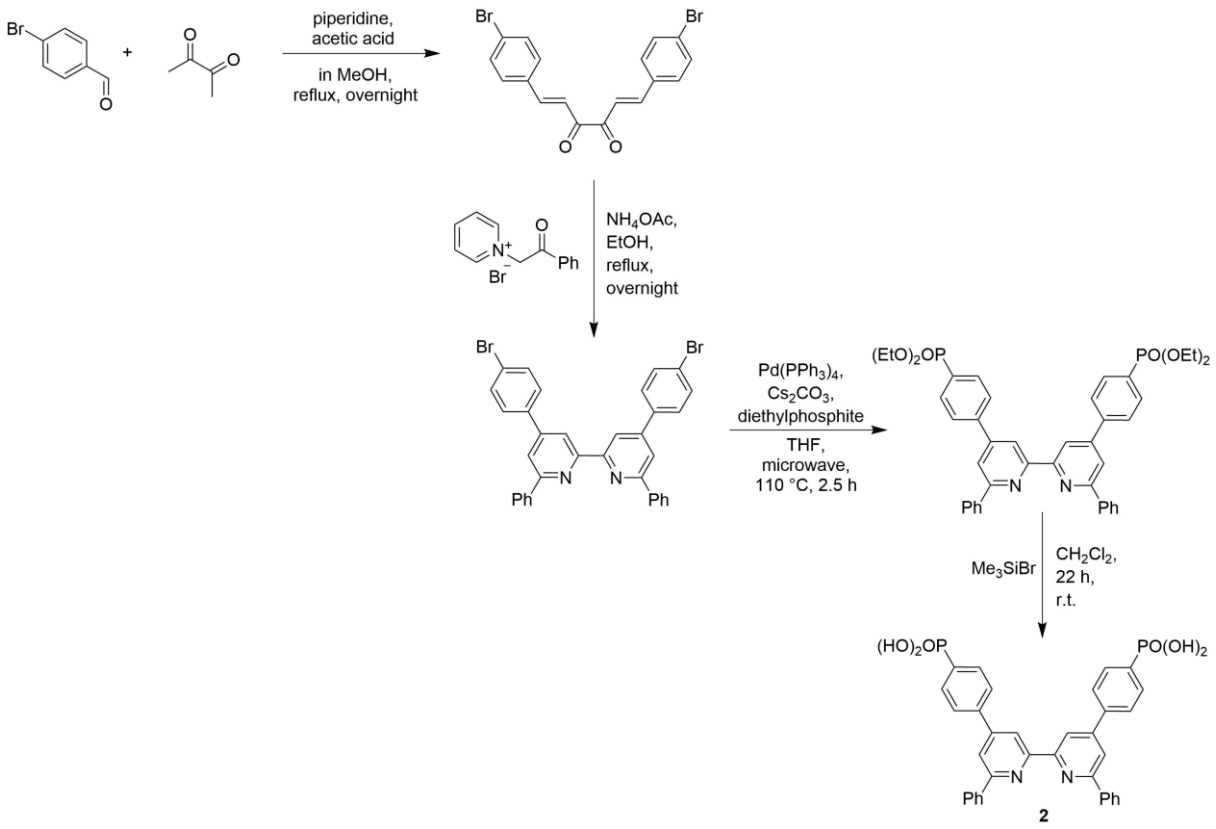

Scheme 9: Modified anchoring ligand synthesis using Me_3SiBr.

The corresponding homoleptic copper(I) complexes (Scheme 10) were prepared using a standard method combining $[Cu(MeCN)_4][PF_6]$[87] with two equivalents of the ligand **4-7** and were isolated as dark red-orange solids in 79.2-90.0% yield. In the electrospray mass spectrum the highest mass peak of each complex corresponded to the $[M - PF_6]^+$ ion and showed a characteristic isotope pattern corresponding to the simulated patter. The ^1H and ^{13}C NMR spectra of the complexes were recorded in CD_2Cl_2 and assigned using 2D methods.

In Figure 20 the solution absorption spectra of the complexes are shown. The corresponding absorption maxima are given in Table 3 and were established by recording the spectra at different concentrations. The solution absorption spectra are prevailed by the high-energy $\pi^*\leftarrow\pi$ transitions and broad MLCT bands with $\lambda_{max} \approx 470$ nm (Table 3). Comparing the extinction coefficient value for the MLCT band of $[Cu(\mathbf{7})_2][PF_6]$ (9300 $dm^3\ mol^{-1}\ cm^{-1}$) to that of a complex of a similar ligand[88] known from the literature verified the consistency of the data.

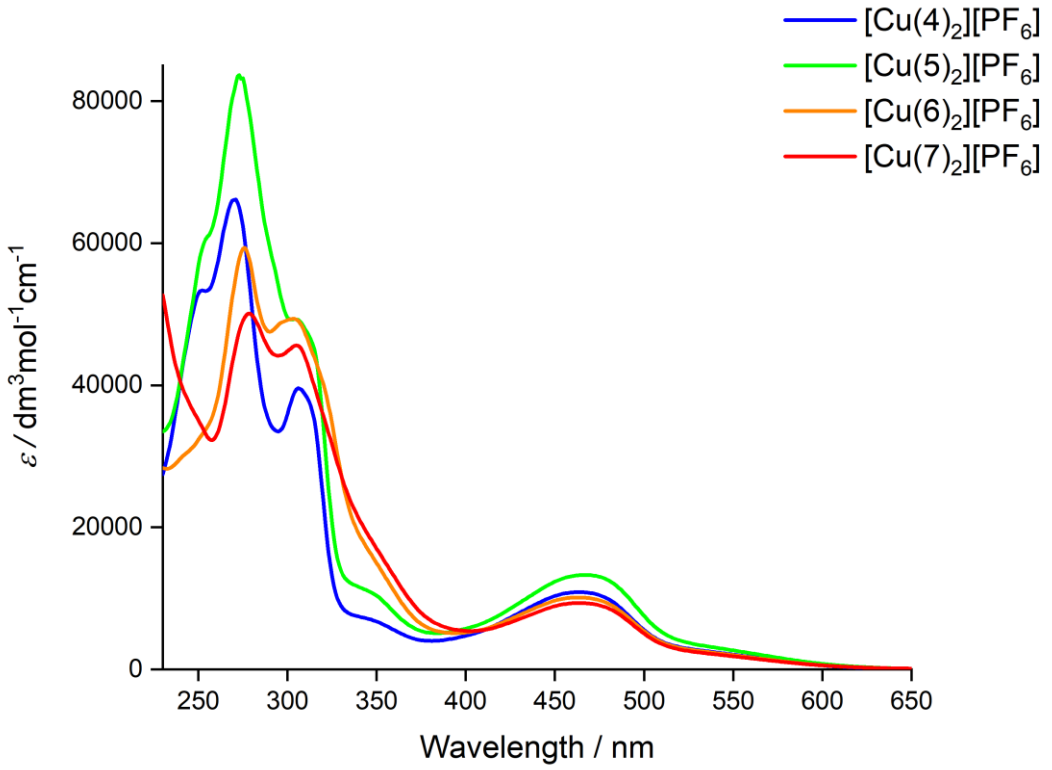

Figure 20: Solution (CH_2Cl_2) absorption spectra for complexes $[Cu(L_{ancillary})_2][PF_6]$ with $L_{ancillary}$ = 4-7 (5×10^{-5} mol dm^{-3}).

Table 3: Absorption maxima for $[Cu(L_{ancillary})_2][PF_6]$ with $L_{ancillary}$ = 4-7 (CH_2Cl_2, 5×10^{-5} mol dm^{-3}; sh = shoulder; ε values are rounded to the nearest 100 dm^{-3} mol^{-1} cm^{-1}).

	λ_{max}/nm (ε_{max}/dm^3 mol^{-1} cm^{-1})	
Complex	π*←π	MLCT
$[Cu(\mathbf{4})_2][PF_6]$	248 (53 700), 237 (65 000), 311 (38300), 354 (6300)	470 (10 800)
$[Cu(\mathbf{5})_2][PF_6]$	257 sh (61 700), 267 (82 200), 308 sh (48 400), 353 (9800)	467 (13 300)
$[Cu(\mathbf{6})_2][PF_6]$	278 (58 300), 306 (49 000), 354 sh (15 400)	468 (10 100)
$[Cu(\mathbf{7})_2][PF_6]$	282 (49 200), 309 (44 600), 353 sh (15 800)	470 (9300)

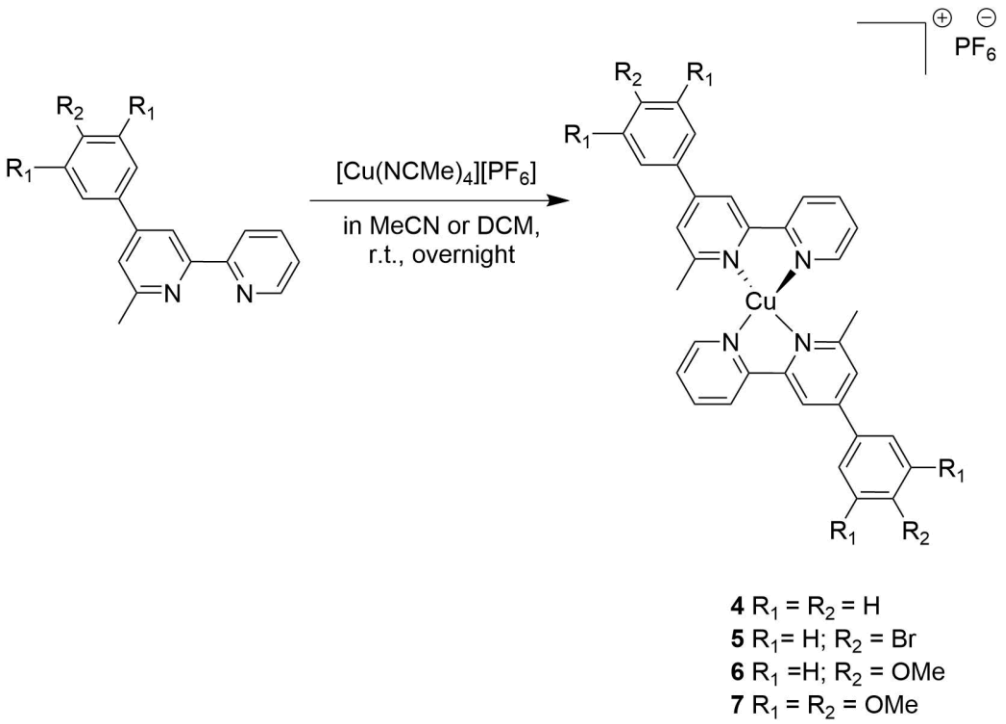

Scheme 10: General synthetic route for the homoleptic copper(I) complexes.

The detailed synthetic routes and the analytical data to the ligands **4**-**7** and the homoleptic Cu(I) complexes are given in the experimental section of this chapter.

The ´surface-as-ligand, surface-as-complex´[47] strategy (Section 2.2.5.1 Figure 13) was used to assemble heteroleptic $[Cu(L_{anchor})(L_{ancillary})]^+$ dyes adsorbed on the TiO_2 surface using anchoring ligand **2** and ancillary ligands ($L_{ancillary}$ = **4**-**7**). The performances of the DSCs containing these dyes were then compared with those of DSCs containing the $[Cu(L_{anchor})(L_{ancillary})]^+$ dyes composed of the asymmetrical ancillary ligands (**4**-**7**) and anchoring ligand ALP1[46] (**1**) (Scheme 11).

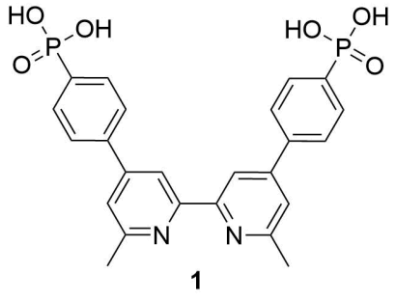

Scheme 11: Structure of the ALP1 anchoring ligand (1).

4.3 Results

4.3.1 Solid state absorption spectra

The heteroleptic copper(I) dyes were assembled step-wise on transparent TiO_2 electrodes to give $[Cu(\mathbf{1})(\mathbf{4})]^+$, $[Cu(\mathbf{1})(\mathbf{5})]^+$, $[Cu(\mathbf{1})(\mathbf{6})]^+$, $[Cu(\mathbf{1})(\mathbf{7})]^+$, $[Cu(\mathbf{2})(\mathbf{4})]^+$, $[Cu(\mathbf{2})(\mathbf{5})]^+$, $[Cu(\mathbf{2})(\mathbf{6})]^+$ and $[Cu(\mathbf{2})(\mathbf{7})]^+$ adsorbed on the electrode surfaces. The commercial TiO_2 electrodes were washed with milliQ water and HPLC grade EtOH, dried in a stream of nitrogen and then heated at 450 °C for 30 min. After cooling, the electrodes were soaked in a 1.0 mM DMSO solutions of anchoring ligands **1** or **2** for 24 h, washed with DMSO and EtOH and dried. The anchoring ligand-functionalized electrodes were then immersed into solutions of the different homoleptic copper(I) complexes $[Cu(L_{ancillary})_2][PF_6]$ ($L_{ancillary}$ = **4**, **5**, **6** or **7**, 0.1 mM in CH_2Cl_2). After 3 days in the dye bath solution, the electrodes were taken out, washed with CH_2Cl_2 and dried in a stream of nitrogen. In Figure 21 the background corrected and normalized solid-state absorption spectra of the functionalized electrodes are shown.

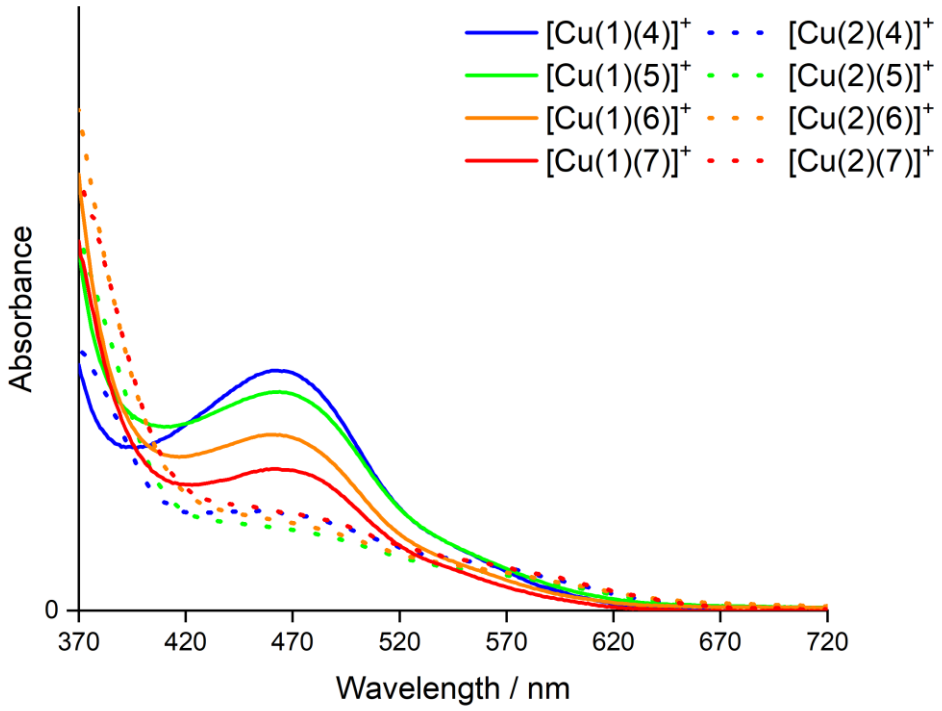

Figure 21: Solid-state absorption spectra of transparent TiO_2 functionalized with $[Cu(1)(L_{ancillary})]^+$ and $[Cu(2)(L_{ancillary})]^+$ ($L_{ancillary}$ = 4-7).

The MLCT absorption maxima of the dyes with anchoring ligand **1** appeared at λ_{max} 466-468 nm. By changing the anchoring ligand from **1** to **2** inserting a phenyl group in the 6,6´-position of the anchoring ligand resulted in a decrease of the absorption maxima. Nevertheless the change in the 6,6´-substituents on going from methyl to phenyl groups resulted in an increase in the absorption at

longer wavelengths (Figure 22). A lower dye-loading was in accordance with the decreased absorption for anchoring ligand **2**. The decreased absorption indicated that less dye was formed on the surface during the exchange process between the anchored ligand and the homoleptic copper(I) complex. This might refer to a problem of steric hindrance between the phenyl groups of the bulky anchoring ligand **2** and the ancillary ligand.

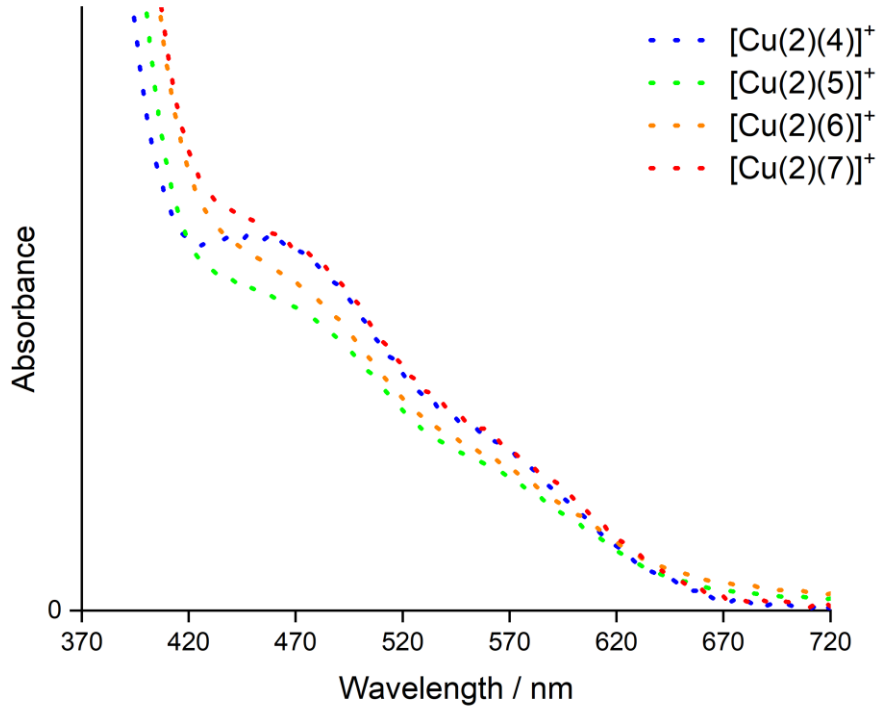

Figure 22: Expansion of the solid-state absorption spectra of TiO_2 functionalized with $[Cu(2)(L_{ancillary})]^+$ ($L_{ancillary}$ = 4-7).

Figure 23 illustrates a comparison of the solid-state absorption spectra of electrodes functionalized with $[Cu(\mathbf{1})(\mathbf{4})]^+$, $[Cu(\mathbf{2})(\mathbf{4})]^+$ or N719. The spectra in Figure 23, the lower intensity MLCT bands exhibited by copper(I) dyes over the well-performing N719 dye, confirming an overall lower spectral response and basically missing light-harvesting at lower energies.

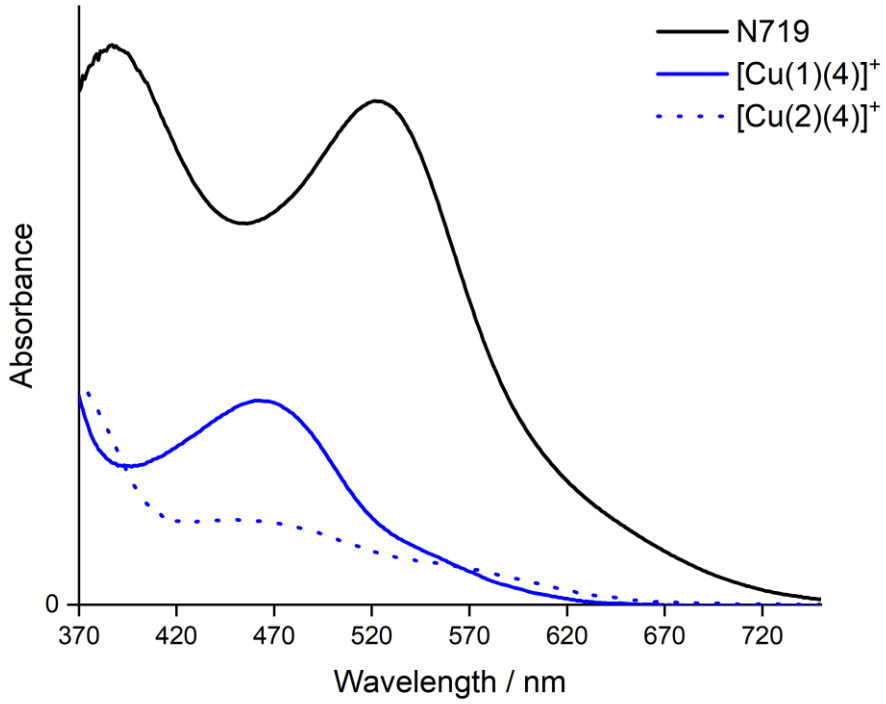

Figure 23: Solid-state absorption spectra of TiO_2 functionalized with $[Cu(1)(4)]^+$, $[Cu(2)(4)]^+$ or N719.

4.3.2 DSC performances

Working electrodes for the DSCs were made using the ´surface-as-ligand, surface-as-complex´ strategy to obtain the heteroleptic copper(I) dyes absorbed on the electrode surface in the same manner as mentioned in the last section for the solid-state absorption measurements. Each dye-soaked working electrode was assembled with a commercial Pt counter-electrode using a thermoplast hot-melt sealing foil. The electrolyte between the electrodes was introduced by vacuum backfilling as mentioned before. Duplicate DSCs were prepared for each dye to verify the reproducibility of assembling the solar cells and the measurements respectively.

4.3.2.1 Solar cell measurements

The solar simulator measurements of the DSCs were performed in a fully-masked mode[79,80] to avoid false influence from scattered light (average active area 0.06012 cm^2 with a standard deviation of 1%). All DSCs containing anchoring ligand **1** and **2** and ancillary ligands **4**-**7** were measured on the day of assembling (day 0), day 1 and day 7. A DSC containing N719 was prepared and measured as a reference cell. For better comparison of the different dye combinations, the relative efficiencies of the DSCs with respect to N719 set at 100%[81] were calculated (Table 4).

The cells containing anchoring ligand **1** in general performed the best, yielding efficiencies of between 1.43 and 2.12%, whereas the DSCs containing anchoring ligand **2** only reached efficiencies of 0.07-0.63%. The fill factors and the open circuit voltages of all the cells were in a good range ff ~ 70% and V_{OC} ~444 – 598 mV. The lack of good performance is associated with a low short circuit current density which could be measured around 0.55 – 1.6 mA/cm^2 for DSCs containing anchoring ligand **2**. Anchoring ligand **1** on the other hand yielded higher J_{SC} ~ 3.77- 5.00 mA/cm^2 (Table 4). The *J-V* curves in Figure 24 and Figure 25 clearly show the better performance of DSCs containing anchoring ligand **1** over anchoring ligand **2**. On varying the ancillary ligand the best performance could be measured with [Cu(**1**)(**6**)]$^+$ and [Cu(**2**)(**6**)]$^+$ followed by [Cu(**1**)(**4**)]$^+$ and [Cu(**2**)(**4**)]$^+$, yielding the highest efficiency of 2.12% for [Cu(**1**)(**6**)]$^+$ and 1.99% for [Cu(**1**)(**4**)]$^+$. The combination of these best ancillary ligands **4** and **6** in combination with the anchoring ligand **2** gave efficiencies of 0.58 and 0.63%, respectively. Furthermore the duplicate DSCs in Table 4 confirmed the reproducibility of both the construction and the measurement of the cells. Measurements over time showed a slight decrease on day 1 which stabilized until day 7 for [Cu(**1**)(L$_{ancillary}$)]$^+$ (L$_{ancillary}$ = **4-7**) (Table 5). In contrast, the DSCs fabricated with ancillary ligand **2** showed an overall decrease in cell performance over a period of 7 days (Table 6).

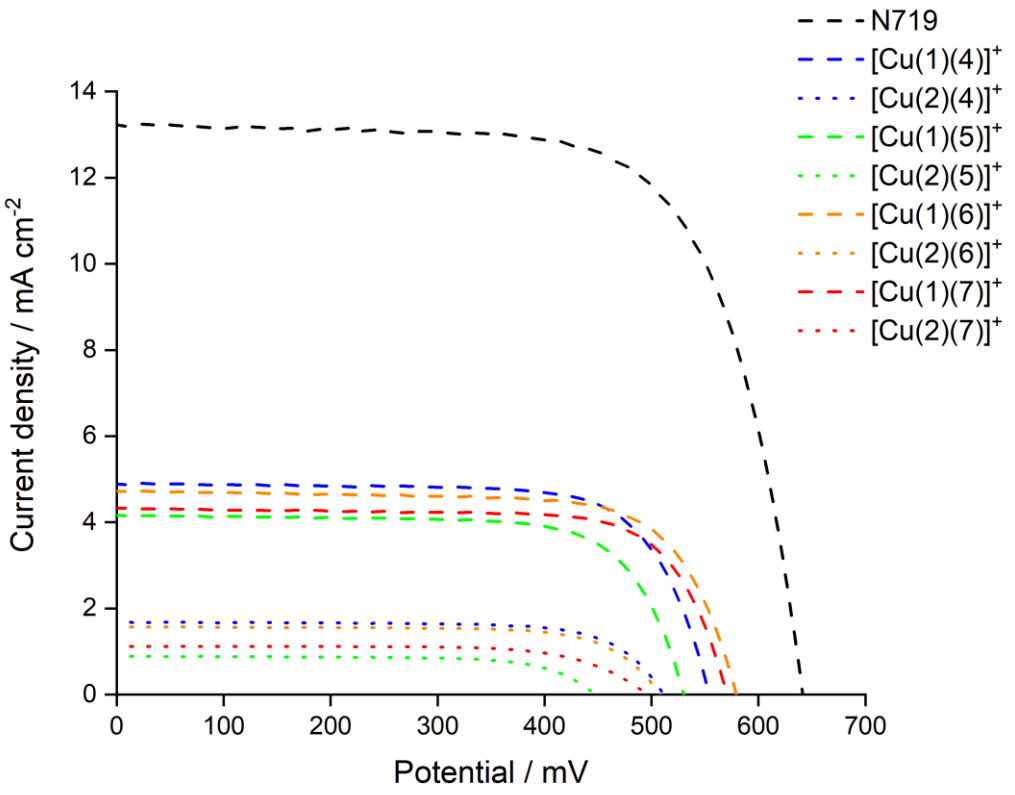

Figure 24: *J-V* curves for DSCs with dye [Cu(1)(L$_{ancillary}$)]$^+$, [Cu(2)(L$_{ancillary}$)]$^+$ (L$_{ancillary}$ = 4-7) and N719 measured on day of cell assembling.

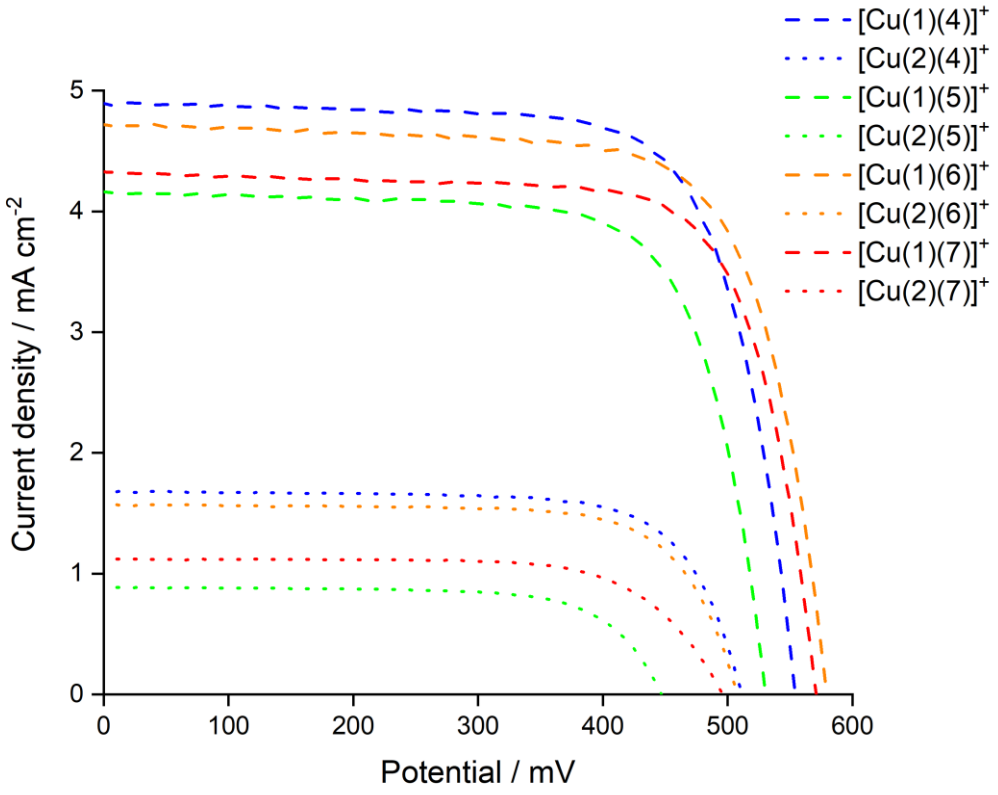

Figure 25: *J-V* curves for DSCs containing dyes $[Cu(1)(L_{ancillary})]^+$ and $[Cu(2)(L_{ancillary})]^+$ ($L_{ancillary}$ = 4-7) measured on the day of cell assembling (expansion of Figure 24).

Table 4: Performance parameters of duplicate DSCs with $[Cu(1)(L_{ancillary})]^+$ and $[Cu(2)(L_{ancillary})]^+$ ($L_{ancillary}$ = 4-7) compared to N719 as reference measured on the day of cell assembling.

Dye	J_{sc}/mA cm^{-2}	V_{OC}/mV	ff/%	η/%	Relative η/%
$[Cu(\mathbf{1})(\mathbf{4})]^+$	4.99	555	69	1.92	34.8
$[Cu(\mathbf{1})(\mathbf{4})]^+$	4.91	554	73	1.99	36.1
$[Cu(\mathbf{1})(\mathbf{5})]^+$	4.29	522	71	1.58	28.6
$[Cu(\mathbf{1})(\mathbf{5})]^+$	4.21	525	70	1.54	27.9
$[Cu(\mathbf{1})(\mathbf{6})]^+$	4.96	583	73	2.12	38.4
$[Cu(\mathbf{1})(\mathbf{6})]^+$	4.73	579	72	1.98	35.9
$[Cu(\mathbf{1})(\mathbf{7})]^+$	4.33	569	72	1.77	32.1
$[Cu(\mathbf{1})(\mathbf{7})]^+$	4.33	571	74	1.83	33.2
N719	13.61	623	65	5.52	100
$[Cu(\mathbf{2})(\mathbf{4})]^+$	1.68	511	73	0.63	11.0
$[Cu(\mathbf{2})(\mathbf{4})]^+$	1.48	502	73	0.54	9.5
$[Cu(\mathbf{2})(\mathbf{5})]^+$	0.89	447	71	0.28	4.9
$[Cu(\mathbf{2})(\mathbf{5})]^+$	0.90	444	71	0.28	4.9
$[Cu(\mathbf{2})(\mathbf{6})]^+$	1.57	508	73	0.58	10.2
$[Cu(\mathbf{2})(\mathbf{6})]^+$	1.45	507	73	0.54	9.5
$[Cu(\mathbf{2})(\mathbf{7})]^+$	1.12	496	70	0.39	6.8
$[Cu(\mathbf{2})(\mathbf{7})]^+$	1.19	474	51	0.29	5.1
N719	13.38	640	67	5.71	100

Table 5: Performance parameters of duplicate DSCs containing $[Cu(1)(L_{ancillary})]^+$ ($L_{ancillary}$ = 4-7) compared to N719 measured on day 1 and day 7 after cell assembling.

Dye	J_{sc}/mA cm^{-2}	V_{OC}/mV	ff/%	η/%	Relative η/%
1 day after DSC fabrication					
$[Cu(\mathbf{1})(\mathbf{4})]^+$	4.47	572	69	1.77	31.3
$[Cu(\mathbf{1})(\mathbf{4})]^+$	4.31	561	74	1.78	31.4
$[Cu(\mathbf{1})(\mathbf{5})]^+$	4.12	539	71	1.58	27.9
$[Cu(\mathbf{1})(\mathbf{5})]^+$	3.89	537	71	1.48	26.1
$[Cu(\mathbf{1})(\mathbf{6})]^+$	4.80	585	75	2.09	36.9
$[Cu(\mathbf{1})(\mathbf{6})]^+$	5.00	581	73	2.11	37.3
$[Cu(\mathbf{1})(\mathbf{7})]^+$	3.99	594	71	1.69	29.9
$[Cu(\mathbf{1})(\mathbf{7})]^+$	4.00	598	74	1.77	31.3
N719	13.17	676	64	5.66	100
7 days after DSC fabrication					
$[Cu(\mathbf{1})(\mathbf{4})]^+$	4.29	582	63	1.57	26.9
$[Cu(\mathbf{1})(\mathbf{4})]^+$	4.22	575	73	1.77	30.3
$[Cu(\mathbf{1})(\mathbf{5})]^+$	3.88	566	72	1.58	27.1
$[Cu(\mathbf{1})(\mathbf{5})]^+$	4.13	551	63	1.43	24.5
$[Cu(\mathbf{1})(\mathbf{6})]^+$	4.65	589	74	2.03	34.8
$[Cu(\mathbf{1})(\mathbf{6})]^+$	4.93	575	73	2.07	35.4
$[Cu(\mathbf{1})(\mathbf{7})]^+$	3.77	587	73	1.61	27.6
$[Cu(\mathbf{1})(\mathbf{7})]^+$	4.07	589	71	1.70	29.1
N719	13.01	705	64	5.84	100

Table 6: Performance parameters of duplicate DSCs containing $[Cu(2)(L_{anillary})]^+$ ($L_{ancillary}$ = 4-7) compared to N719 measured on day 1 and day 7 after cell assembling.

Dye	J_{sc}/mA cm^{-2}	V_{OC}/mV	ff/%	η/%	Relative η/%
1 day after DSC fabrication					
$[Cu(\mathbf{2})(\mathbf{4})]^+$	1.12	505	70	0.40	6.7
$[Cu(\mathbf{2})(\mathbf{4})]^+$	0.77	485	73	0.27	4.6
$[Cu(\mathbf{2})(\mathbf{5})]^+$	0.94	466	59	0.26	4.4
$[Cu(\mathbf{2})(\mathbf{5})]^+$	0.69	449	68	0.21	3.5
$[Cu(\mathbf{2})(\mathbf{6})]^+$	1.01	504	72	0.37	6.2
$[Cu(\mathbf{2})(\mathbf{6})]^+$	0.85	494	73	0.31	5.2
$[Cu(\mathbf{2})(\mathbf{7})]^+$	0.64	490	71	0.22	3.7
$[Cu(\mathbf{2})(\mathbf{7})]^+$	0.55	465	66	0.17	2.9
N719	13.32	652	68	5.93	100
7 days after DSC fabrication					
$[Cu(\mathbf{2})(\mathbf{4})]^+$	0.86	503	62	0.27	4.4
$[Cu(\mathbf{2})(\mathbf{4})]^+$	0.79	498	66	0.26	4.2
$[Cu(\mathbf{2})(\mathbf{5})]^+$	0.58	489	26	0.07	1.1
$[Cu(\mathbf{2})(\mathbf{5})]^+$	0.75	466	56	0.20	3.3
$[Cu(\mathbf{2})(\mathbf{6})]^+$	1.10	513	70	0.40	6.5
$[Cu(\mathbf{2})(\mathbf{6})]^+$	0.72	484	73	0.26	4.2
$[Cu(\mathbf{2})(\mathbf{7})]^+$	0.55	495	69	0.19	3.1
$[Cu(\mathbf{2})(\mathbf{7})]^+$	0.43	458	68	0.13	2.1
N719	13.10	672	70	6.13	100

To confirm the reproducibility of assembling and measuring the DSCs, sets of four DSCs with each of dyes $[Cu(\mathbf{1})(\mathbf{4})]^+$, $[Cu(\mathbf{1})(\mathbf{5})]^+$, $[Cu(\mathbf{1})(\mathbf{5})]^+$and $[Cu(\mathbf{1})(\mathbf{7})]^+$ were built (Figure 26, Figure 27, Figure 28 and Figure 29). The graphs of four DSCs per dye clearly verified the consistency of building and quantifying the devices.

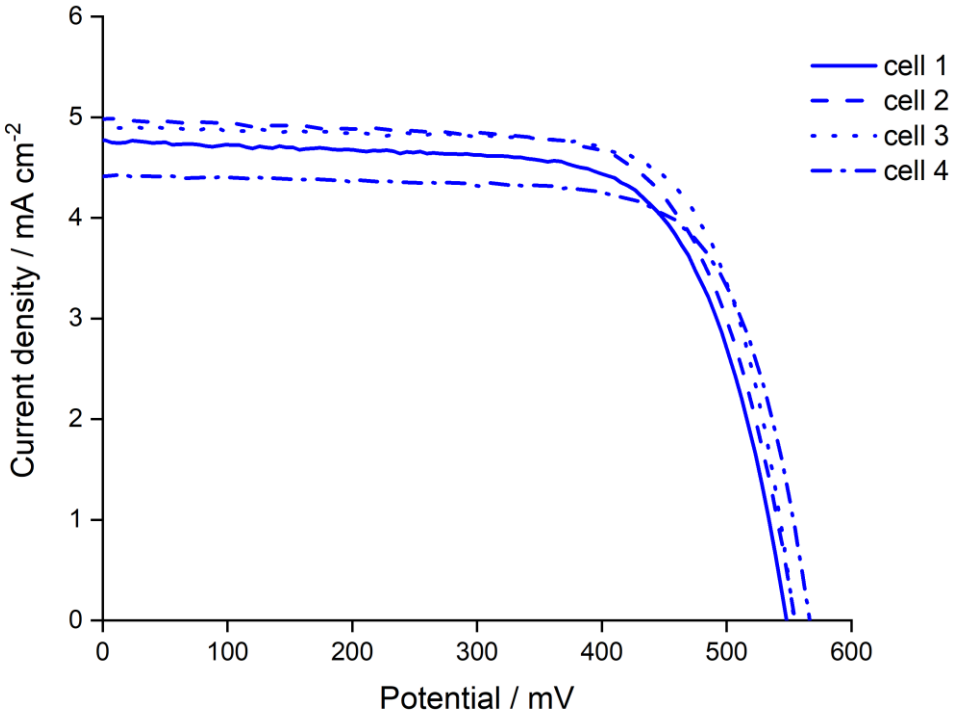

Figure 26: *J-V* curves for sets of four DSCs containing dye $[Cu(1)(4)]^+$ measured on the day of cell assembling to confirm reproducibility.

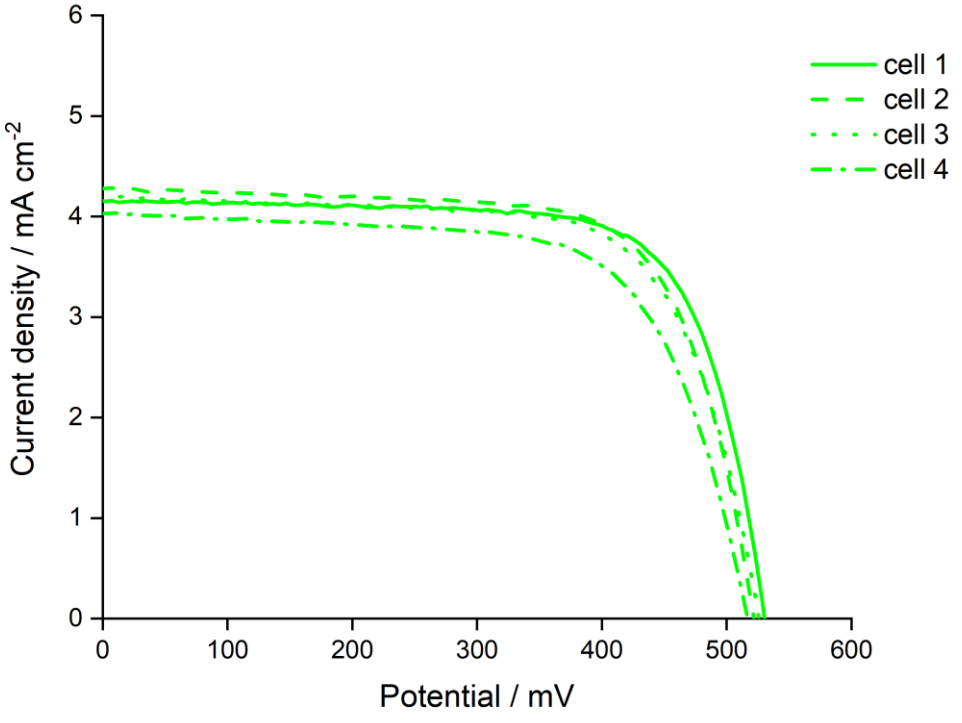

Figure 27: *J-V* curves for sets of four DSCs containing dye $[Cu(1)(5)]^+$ measured on the day of cell assembling to confirm reproducibility.

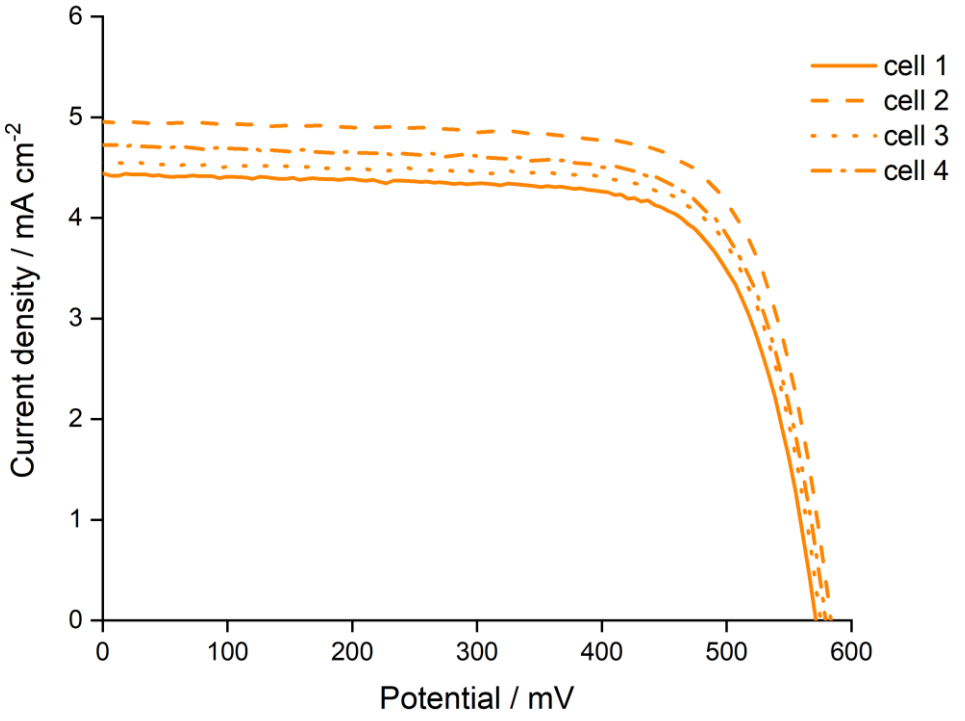

Figure 28: *J-V* curves for sets of four DSCs containing dye $[Cu(1)(6)]^+$ measured on the day of cell assembling to confirm reproducibility.

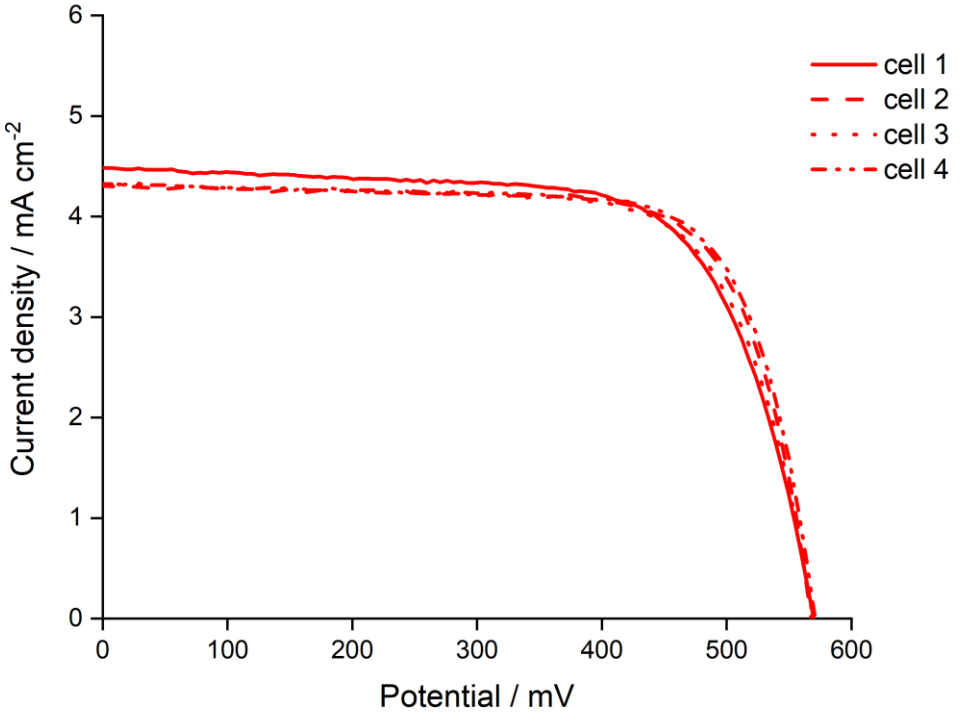

Figure 29: *J-V* curves for sets of four DSCs containing dye $[Cu(1)(7)]^+$ measured on the day of cell assembling to confirm reproducibility.

4.3.2.2 External Quantum Efficiency (EQE) measurements

Figure 30 compares the EQE curves of [Cu(**1**)($L_{ancillary}$)]$^+$ and [Cu(**2**)($L_{ancillary}$)]$^+$ ($L_{ancillary}$ = **4**-**7**) to that of N719. It is obvious that the photon to current conversion efficiencies of the copper(I) based dyes are lower than that of N719, and lose the lower energy contribution made by N719.

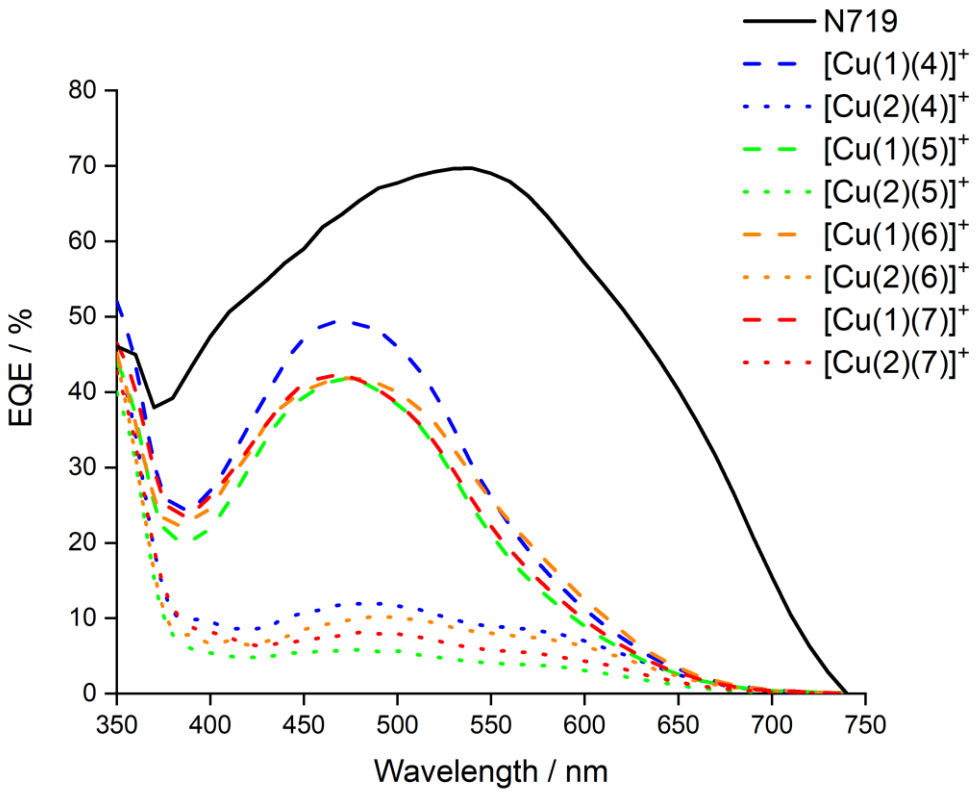

Figure 30: EQE spectra of DSCs containing [Cu(1)($L_{ancillary}$)]$^+$ and [Cu(2)($L_{ancillary}$)]$^+$ ($L_{ancillary}$ = 4-7) and N719.

The zoom in of the EQE spectra shown in Figure 31 were consistent with the data from the solar simulator measurements discussed above. The DSCs containing anchoring ligand **1** clearly gave a higher EQE_{max} value independent of the ancillary ligand. The highest value for the EQE of DSCs with [Cu(**1**)($L_{ancillary}$)]$^+$ ($L_{ancillary}$ = **4**-**7**) were in the range of 41.8 to 49.4% (Table 7). The lower performing DSCs for the combination of anchoring ligand **2** with ancillary ligands **4**-**7** yielded EQE_{max} values of < 12% (Table 7). Nevertheless the shape of the EQE curves with anchoring ligand **2** verified the broadened spectral response from 550 to 650 nm already seen in the solid- state absorption spectra (Figure 21 and Figure 22).

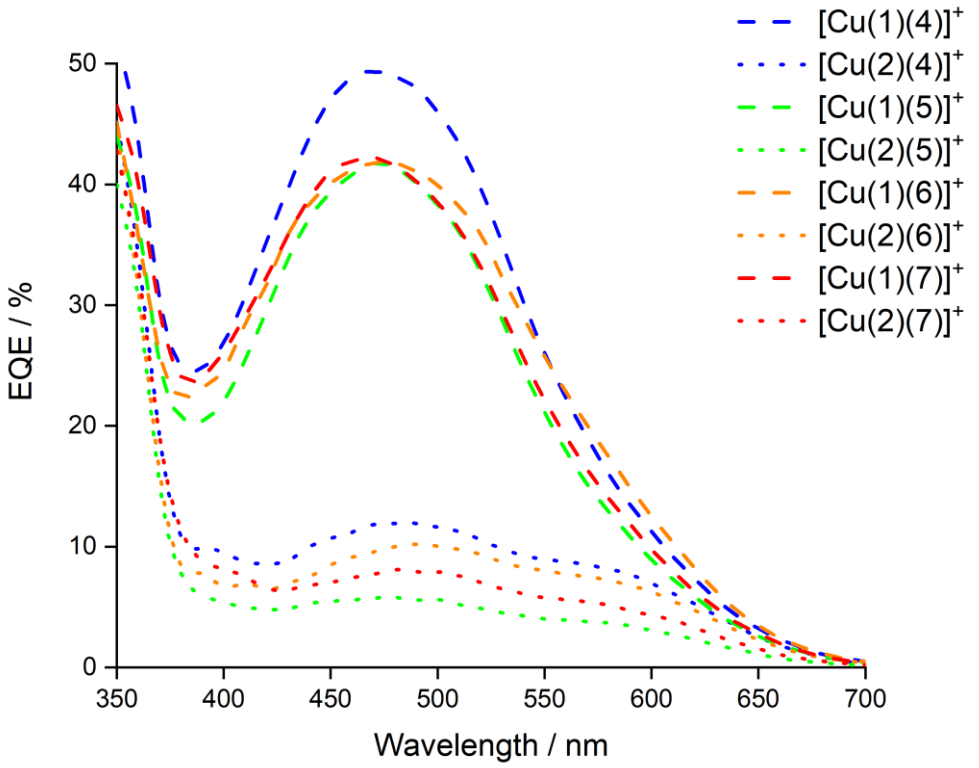

Figure 31: EQE spectra for DSCs containing dyes $[Cu(1)(L_{ancillary})]^+$ and $[Cu(2)(L_{ancillary})]^+$ ($L_{ancillary}$ = 4-7).

Table 7: EQE maxima for DSCs containing dyes $[Cu(1)(L_{ancillary})]^+$ and $[Cu(2)(L_{ancillary})]^+$ ($L_{ancillary}$ = 4-7).

Dye	λ_{max} / nm	EQE_{max} / %
$[Cu(\mathbf{1})(\mathbf{4})]^+$	470	49.4
$[Cu(\mathbf{2})(\mathbf{4})]^+$	490	11.9
$[Cu(\mathbf{1})(\mathbf{5})]^+$	470	41.8
$[Cu(\mathbf{2})(\mathbf{5})]^+$	480	5.8
$[Cu(\mathbf{1})(\mathbf{6})]^+$	470	41.8
$[Cu(\mathbf{2})(\mathbf{6})]^+$	490	10.2
$[Cu(\mathbf{1})(\mathbf{7})]^+$	470	42.2
$[Cu(\mathbf{2})(\mathbf{7})]^+$	480	8.1

The low overall cell performance for anchoring ligand **2** discussed in the previous section as well as was shown in the solid state-absorption spectra and the confirmation of the low photon to current conversion efficiencies presented herein will be further explored in the next section.

4.3.3 Dye bleaching and regeneration

The general decay of the cell performance for DSCs containing $[Cu(\mathbf{2})(L_{ancillary})]^+$ ($L_{ancillary}$ = **4**-**7**) shown in Table 6 and the low EQE_{max} values (Table 7) discussed in the previous section along with the lower solid-state absorption spectra (Figure 21) indicated a low dye loading on the TiO_2 surface. Even by eye it could be clearly seen that the working electrodes with anchoring ligand **2** appeared in a lighter red- orange colour compared to those having the combination of anchoring ligand **1** with ancillary ligands **4**-**7** adsorbed on the surface (Figure 32). In Figure 32 an electrode functionalized with N719, the ruthenium-based dye used as reference, is also shown for comparison.

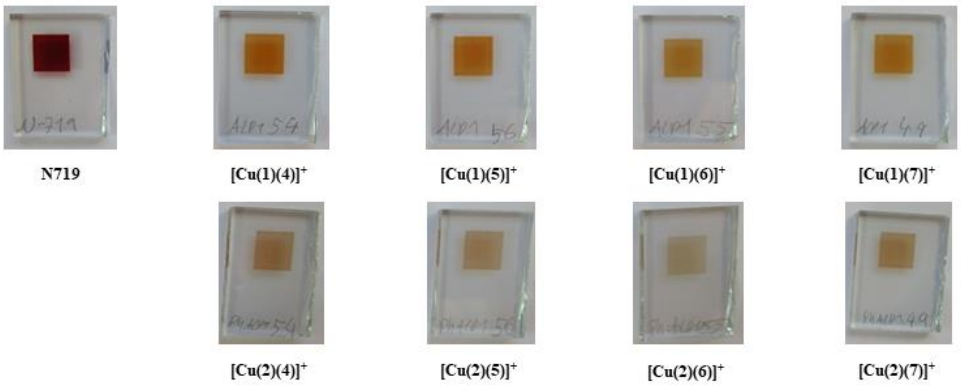

Figure 32: Photographs of the electrodes after the dyeing process.

The orange colour of the electrodes bleached even more after backfilling with the electrolyte. This finding indicated that the heteroleptic dye adsorbed on the TiO_2 surface is not stable in the presence of the components of the electrolyte. For further investigation of this phenomena solid-state absorption spectra of transparent TiO_2 electrodes modified with dye $[Cu(\mathbf{2})(\mathbf{5})]^+$ were measured. The functionalized electrodes were then immersed either into a solution of LiI in 3-methoxypropionitrile or in a solution of the standard I^-/I_3^- electrolyte used in the DSCs for 15 min. After this dipping process the orange colour of the electrodes bleached (Figure 33 left and middle). The recorded solid-state absorption spectra confirmed the result seen by eye, as the MLCT band arising from the adsorbed dye decreased in intensity (Figure 34and Figure 35). These data were consistent with the suggested explanation that the copper(I) centre is attacked by the I^- ion causing the bleaching of the dye[75]. The bleached electrodes were then either dipped again into the homoleptic $[Cu(\mathbf{5})_2]^+$ dye solution or in a solution of $[Cu(NCMe)_4)][PF_6]$ in MeCN followed by soaking in a CH_2Cl_2 solution of ligand **5**. The electrodes were washed with CH_2Cl_2 and dried after the dyeing process. The recovery of the orange colour of the electrodes (Figure 33 right) together with the regain in the intensity of the MLCT bands in the solid-state absorption spectra (Figure 34 and Figure 35 blue curves) confirmed the successful regeneration of the dye on the surface. Furthermore the investigation of this bleaching and regeneration phenomena of the dye was evidence of a proper binding of the anchoring ligand on the TiO_2 surface.

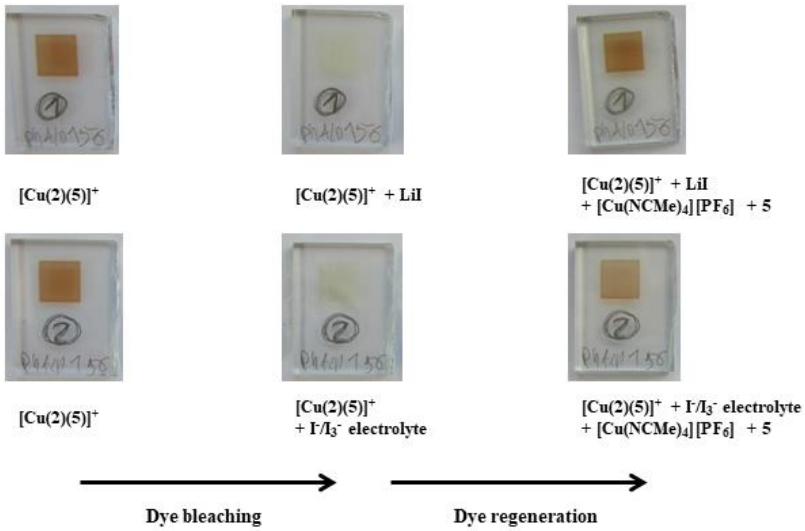

Figure 33: Photographs of the electrodes used for the dye bleaching and regeneration tests.

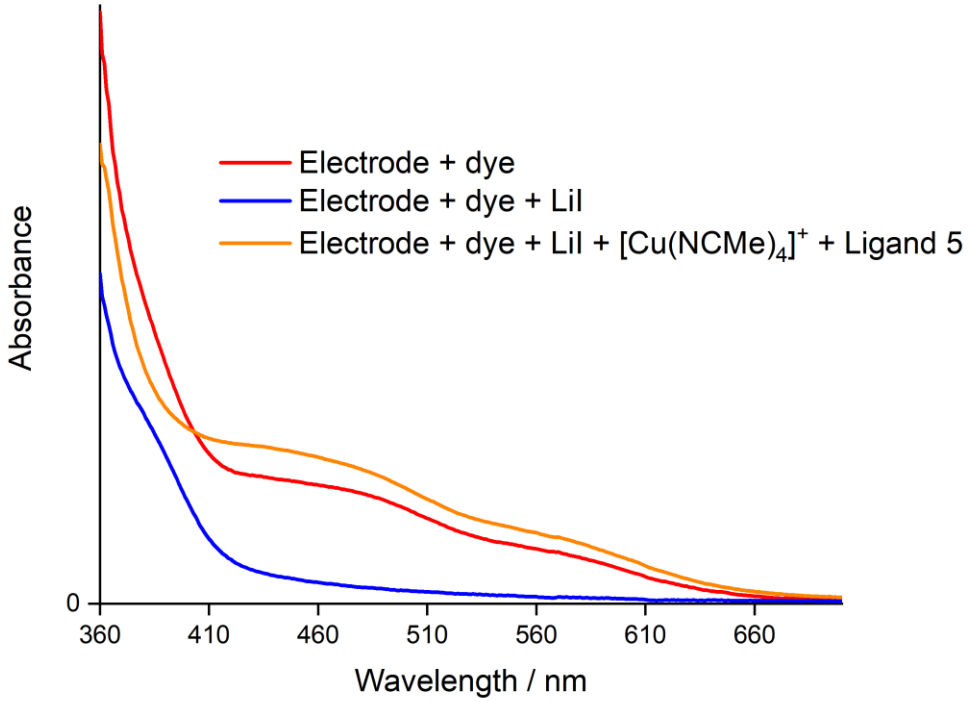

Figure 34: Solid-state absorption spectra of transparent electrodes functionalized with $[Cu(2)(5)]^+$ (red), treated with an LiI solution (blue), then $[Cu(NCMe)_4][PF_6]$ followed by ligand 5 (orange).

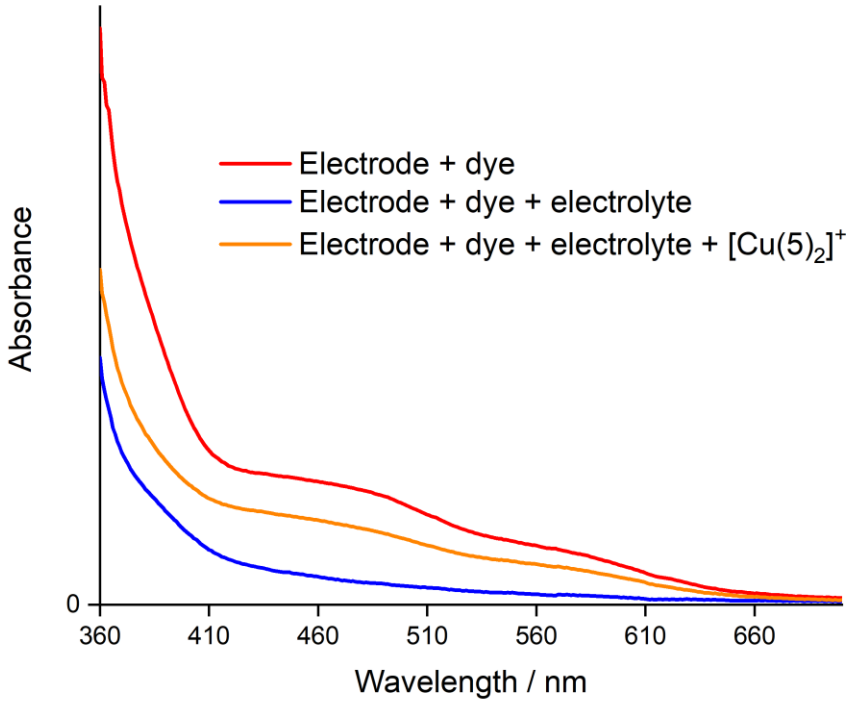

Figure 35: Solid-state absorption spectra of transparent electrodes functionalized with $[Cu(2)(5)]^+$ (red), treated with an I^-/I_3^- electrolyte (blue), followed by $[Cu(5)_2][PF_6]$ (orange).

4.4 Conclusion

Four new ancillary ligands and the corresponding homoleptic Cu(I) complexes were synthesized. The ´surface-as-ligand, surface-as-complex´ strategy was used to functionalize the TiO_2 electrodes with the heteroleptic copper(I) dyes using two different anchoring ligands (ligands **1** and **2**). The two ligands used in this set had a phosphonic acid anchoring unit attached to the 2,2´-bipyridine via a phenyl spacer; the differences between these two ligands were the substituents in the 6,6´-positions of the bpy unit, having either methyl- (ligand **1**) or phenyl- groups (ligand **2**) attached. DSCs containing these ligands were assembled and characterized. The photoconversion efficiencies and the EQE spectra showed an overall higher performance for DSCs in which the dye contained anchoring ligand **1** (EQE_{max} > 41%) compared to anchoring ligand **2** (Table 7). The general higher cell performances of dyes with the four ancillary ligands (**4**-**7**) combined with anchoring ligand **1** showed the following trend **4** ~ **6** > **7** > **5** on day 0. The best performing cell yielded an efficiency of 2.12%. After a period of 7 days the trend changed into the following order **6** > **4** ~ **7** > **5**. This trend could be explained in terms of the electron-donating effects of the methoxy group in the phenyl 4- position enabling the favoured ´push-pull´ characteristics of the dye. Ancillary ligand **7** in contrast showed a slightly lower performance of 1.83% which could indicate that the –I effects of the 3, 5- substituents compete with the + M effect of the methoxy substituent in 4-position. The cell performance (η < 1%) and the lower

EQE_{max} (< 12%) (Table 7) $[Cu(\mathbf{2})(L_{ancillary})]^+$ could also be brought into relation with a lower dye loading observed in the solid-state absorption spectra. Although the bigger substituent in anchoring ligand **2** led to a broadened spectral response towards higher wavelength, the overall solid-state absorption spectra (Figure 21 and Figure 22) indicated lower dye loading probably as a result of steric hindrance between the anchoring and ancillary ligand around the copper(I) centre of the heteroleptic dyes adsorbed on the TiO_2 surface. Despite the fact that the steric repulsion around the copper(I) centre of the dye resulted dye bleaching in the presents of the I^- ion the dye could be successfully regenerated on the surface. The conclusion to be taken out of this effect was a stable binding of the anchoring ligand onto the TiO_2 surface of the working electrode.

Further work in this field should concentrate on substituents in the 6, 6´-positions of the anchoring ligand featuring an enhanced absorbance at lower energies, e.g. a benzyl group being more flexible towards pushing the aromatic ring away from the copper(I) centre. Also other substituents with a conjugated system bonded via a longer chain to the 6,6´-position of the anchoring ligand could possibly yield a gain at longer wavelengths along with preventing the steric crowding around the metal centre.

4.5 Experimental

The detailed synthesis for the anchoring ligands **1** and **2** used in this chapter to functionalize the electrodes surface with the heteroleptic dyes via a ligand exchange reaction on the surface are given in the experimental section of Chapter 3.

4.5.1 6-Methyl-4-phenyl-2,2´-bipyridine (**4**)

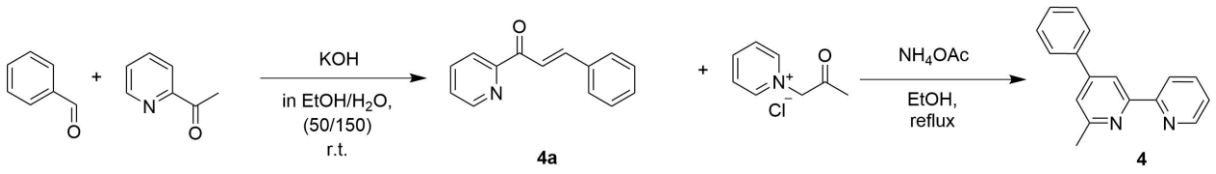

Scheme 12: Synthesis of ancillary ligand 4.

Benzaldehyde (2.17 g, 20.0 mmol) and solid KOH (2.24 g, 40.0 mmol) in 50 mL water were dissolved in EtOH 50 mL. The solution was cooled and 2-Acetylepyridine (2.47 g, 20.0 mmol) in 8 mL EtOH was added dropwise over a period of 20 min. The solution was stirred for 30 min at under 10 °C and more water was added from time to time. The formed precipitate was filtered off and washed with water and diethyl ether. Upon washing with ether the solvent dissolved. The collected ether phase was dried over $MgSO_4$ and filtered. The solvent was removed and the green oil was purified via column chromatography (silica, CH_2Cl_2) yielding compound **4a** (2.65 g, 12.65 mmol, 63.3%).[89] Compound **4a** (1.89 g, 9.03 mmol) and 1-(2-oxopropy)pyridinium chloride (1.55 g, 9.03 mmol) were dissolved in EtOH (40 mL). A solution of NH_4OAc (20.9 g, 271 mmol) in EtOH (40 mL) was added and the reaction mixture was heated to reflux overnight. The solvent was removed under reduced pressure, the

residue was dissolved in CH_2Cl_2, extracted with CH_2Cl_2/water (3 x 100 mL) and dried over $MgSO_4$ After filtration from $MgSO_4$ the solvent was removed *in vacuo* and a brown oil was obtained. The solid was purified by column chromatography (alumina, CH_2Cl_2) and 6-methyl-4-phenyl-2,2´-bipyridine (**4**) was obtained as off-white solid (1.77 g, 7.18 mmol, 79.6%).[83]

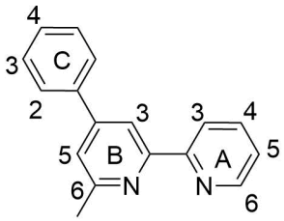

Scheme 13: Structure of ligand 4 with atom labelling for NMR assignments.

^{1}H NMR (500 MHz, CD_3CN) δ/ppm 8.67(ddd, *J* = 4.8, 1.8, 0.9 Hz, 1H, H^{A6}), 8.49 (m, 1H, H^{B3}), 8.45 (ddd, *J* = 8.0, 1.1, 1.1 Hz, 1H, H^{A3}), 7.89 (m, 1H, H^{A4}), 7.79 (m, 2H, H^{C2}), 7.54 (m, 3H, H^{C3+B5}), 7.48, (m, 1H, H^{C4}), 7.39 (m, 1H, H^{A5}), 2.64 (s, 3H, H^{Me}).

^{13}C NMR (126 MHz, CD_3CN) δ/ppm 159.7 (C^{B6}), 157.0 ($C^{A2/B2}$), 156.9 ($C^{A2/B2}$), 150.2 (C^{A6}), 150.15 (C^{B4}), 139.9 (C^{C1}), 138.0 (C^{A4}), 130.1 (C^{C3}), 130.0 (C^{C4}), 127.9 (C^{C2}), 124.9 (C^{A5}), 122.1 (C^{B5}), 121.4 (C^{A3}), 116.4 (C^{B3}), 24.7 (C^{Me}).

4.5.2 6-Methyl-4-(4-bromophenyl)-2,2´-bipyridine (**5**)

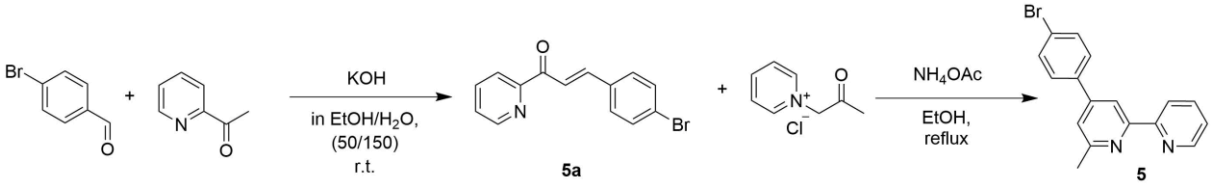

Scheme 14: Synthesis of ancillary ligand 5.

2-Acetylpyridine (2.42 g, 20.0 mmol) and bromobenzaldehyde (3.70 g, 20.0 mmol) were dissolved in EtOH (100 mL). Then solid KOH (2.24 g, 40 mmol) in 25 mL water was added. Upon addition of the base, two phases formed and more EtOH was added until the phase separation disappeared. As soon as the product started to precipitate, the reaction mixture was stirred for further 30 min at 10 °C. The precipitate was filtered off and washed with water. The solid was purified using column chromatography (silica, hexane : ethyl acetate (4:1)) yielding compound **5a** as off-white solid (2.55 g, 8.84 mmol, 44.2%).[85,86] Compound **5a** (2.00 g, 6.94 mmol), 1-(2-oxopropy)pyridinium chloride (1.19 g, 6.94 mmol) and NH_4OAc (16.1 g, 208 mmol) were suspended in EtOH (120 mL). The suspension was heated to reflux overnight. The solution was cooled to room temperature and a precipitate formed. The precipitate was filtered off and washed with cold MeOH to yield 6-methyl-4-(4-bromophenyl)-2,2´-bipyridine (**5**) as off-white solid (608 mg, 1.87 mmol, 26.8%).[83]

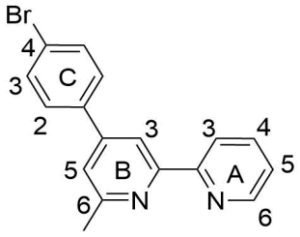

Scheme 15: Structure of ligand 5 with atom labelling for NMR assignments.

^{1}H NMR (500 MHz, CD_3CN) δ/ppm 8.67 (ddd, *J* = 4.8, 1.8, 0.9 Hz, 1H, H^{A6}), 8.45 (m, 2H, H^{B3+A3}), 7.90 (td, *J* = 7.8, 1.8 Hz, 1H,H^{A4}), 7.70 (m, 4H, H^{C2+C3}), 7.52 (dd, *J* = 1.7, 0.5 Hz, 1H, H^{B5}), 7.39 (ddd, *J* = 7.5, 4.8, 1.2 Hz, 1H, H^{A5}), 2.64 (s, 3H, H^{Me}).

^{13}C NMR (126 MHz, CD_3CN) δ/ppm 159.9 (C^{B6}), 157.0 (C^{B2}), 156.8 (C^{A2}), 150.2 (C^{A6}), 149.0 (C^{B4}), 138.5 (C^{C1}), 138.0 (C^{A4}), 133.2 (C^{C3}), 129.9 (C^{C2}), 125.0 (C^{A5}), 123.8 (C^{C4}), 121.9 (C^{B5}), 121.7 (C^{A3}), 116.3 (C^{B3}), 24.7 (C^{Me}).

ESI-MS *m/z* 325.0 $[M + H]^+$ (calc. 325.0).

Found C 62.90, H 4.02, N 8.57; $C_{17}H_{13}BrN_2$ requires C 62.79, H 4.03, N 8.61%.

4.5.3 6-Methyl-4-(4-methoxyphenyl)-2,2´-bipyridine (**6**)

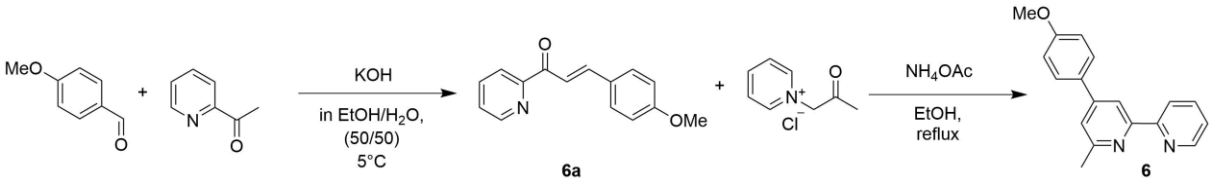

Scheme 16: Synthesis of ancillary ligand 6.

4-Anisaldehyde (2.43 mL, 20.0 mmol) was dissolved in EtOH (50 mL). The solution was cooled to around 2 °C and solid KOH (2.24 g, 40 mmol) in 50 mL water were added. Acetylpyridine (2.42 g, 20 mmol) was diluted in EtOH (8 mL) and added dropwise over 10 min to the reaction mixture. Water (30 mL) was added until a turbid suspension was formed. The reaction was stirred for additional 10 min at 5 °C and a precipitate formed. Compound **6a** was collected by filtration (3.09 g, 12.9 mmol, 64.7%).[85] Compound **6a** (2.50 g, 10.4 mmol) and 1-(2-oxopropy)pyridinium chloride (1.79 g, 10.4 mmol) were dissolved in EtOH (50 mL). A solution of NH_4OAc (24.2 g, 313 mmol) in EtOH (50 mL) was added. The reaction mixture was heated to reflux overnight and allowed to cool to room temperature. The product precipitated, collected by filtration and washed with cold MeOH. 6-Methyl-4-(4-methoxyphenyl)-2,2´-bipyridine (**6**) was isolated as off-white solid (928 mg, 3.35 mmol, 32.3%).[83]

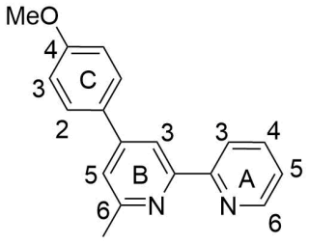

Scheme 17: Structure of ligand 6 with atom labelling for NMR assignments.

^{1}H NMR (500 MHz, CD_3CN) δ/ppm 8.67 (ddd, *J* = 4.7, 1.8, 0.9 Hz, 1H, H^{A6}), 8.44 (m, 2H, H^{B3+A3}), 7.89 (td, *J* = 7.7, 1.8 Hz, 1H,H^{A4}), 7.75 (m, 2H, H^{C2}), 7.50 (d, *J* = 1.5 Hz, 1H, H^{B5}), 7.38 (ddd, *J* = 7.5, 4.8, 1.2 Hz, 1H, H^{A5}), 7.07 (m, 2H, H^{C3}), 3.85 (s, 3H, H^{OMe}), 2.62 (s, 3H, H^{Me}).

^{13}C NMR (126 MHz, CD_3CN) δ/ppm 161.6 (C^{C4}), 159.6 (C^{B6}), 157.1 (C^{A2}), 156.8 (C^{B2}), 150.2 (C^{A6}), 149.7 (C^{B4}), 138.0 (C^{A4}), 131.4 (C^{C1}), 129.2 (C^{C2}), 124.8 (C^{A5}), 121.7 (C^{A3}), 121.4 (C^{B5}), 115.9 (C^{B3}), 115.5 (C^{C3}), 56.1 (C^{OMe}), 24.7 (C^{Me}).

ESI-MS *m/z* 277.1 $[M + H]^+$ (calc. 277.1).

Found C 78.11, H 5.86, N 10.02; $C_{18}H_{16}N_2O$ requires C 78.24, H 5.84, N 10.14%.

4.5.4 6-Methyl-4-(3,4,5-trimethoxyphenyl)-2,2´-bipyridine (**7**)

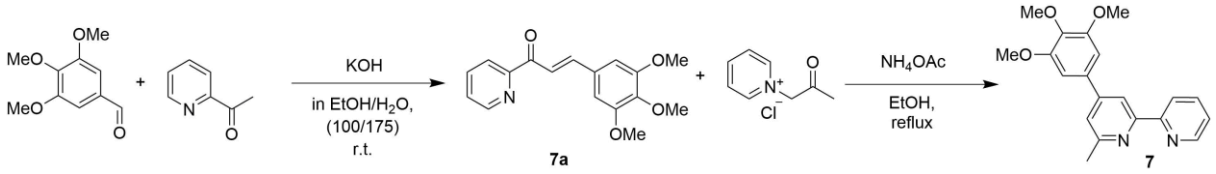

Scheme 18: Synthesis of ancillary ligand 7.

2-Acetylpyridine (1.98 g, 16.3 mmol) and 3,4,5-trimethoxybenzaldehyde (3.20 g, 16.3 mmol) were dissolved in EtOH (100 mL) and solid KOH (1.83 g, 32.6 mmol) in water (75 mL) was added. More water (~ 100 mL) was added until a precipitate started to form. The suspension was kept stirring for additional 10 min. Compound **7a** was collected by filtration, washed with water and diethyl ether and dried in vacuo (2.72 g, 9.09 mmol, 55.7%).[85] 1-(2-Oxopropy)pyridinium chloride (1.43 g, 8.35 mmol), compound **7a** (2.50 g, 8.35 mmol) and NH_4OAc (19.7 g, 251 mmol) were suspended in EtOH (120 mL) and heated to reflux. Upon heating, the reaction mixture turned from a yellow suspension to an orange, then dark red solution. The reaction was refluxed for 2 days, then cooled to room temperature and stirred for additional 36 h. The solvent was removed *in vacuo* and the crude product was purified by column chromatography (alumina, CH_2Cl_2). 6-methyl-4-(3,4,5-trimethoxyphenyl)-2,2´-bipyridine (**7**) was isolated as red-orange oil which crystallized after standing for 24 h (2.32 g, 6.89 mmol, 82.5%). [83]

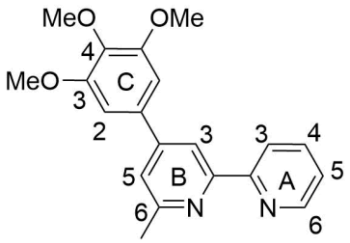

Scheme 19: Structure of ligand 7 with atom labelling for NMR assignments.

^{1}H NMR (500 MHz, CD_3CN) δ/ppm 8.67 (ddd, *J* = 4.7, 1.8, 0.9 Hz, 1H, H^{A6}), 8.44 (m, 2H, H^{B3+A3}), 7.88 (td, *J* = 7.7, 1.8 Hz, 1H,H^{A4}), 7.53 (d, *J* = 1.4 Hz, 1H, H^{B5}), 7.38 (ddd, *J* = 7.5, 4.8, 1.2 Hz, 1H, H^{A5}), 7.01 (s, 1H, H^{C2}), 3.90 (s, 6H, H^{OMe-C3}), 3.78 (s, 3H, H^{OMe-C4}), 2.63 (s, 3H, H^{Me}).

^{13}C NMR (126 MHz, CD_3CN) δ/ppm 159.5 (C^{B6}), 157.1 (C^{A2}), 156.9 (C^{B2}), 154.8 (C^{C3}), 150.2 (C^{B4}), 150.15 (C^{A6}), 139.9 (C^{C4}), 138.0 (C^{A4}), 135.1 (C^{C1}), 124.9 (C^{A5}), 122.2 (C^{B5}), 121.8 (C^{A3}), 116.4 (C^{B3}), 105.4 (C^{C2}), 60.9 (C^{OMe-C4}), 56.9 (C^{OMe-C3}), 24.7 (C^{Me}).

ESI-MS *m/z* 337.1 $[M + H]^+$ (calc. 337.2).

Found C 71.28, H 6.02, N 8.26; $C_{20}H_{20}N_2O_3$ requires C 71.41, H 5.99, N 8.33%.

4.5.5 $[Cu(\mathbf{4})_2][PF_6]$

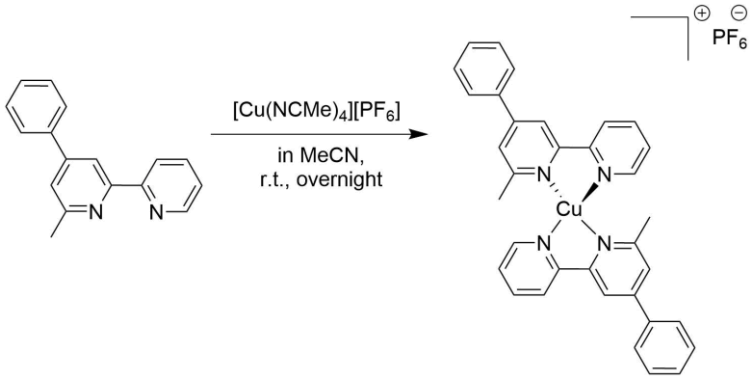

Scheme 20: Synthesis of $[Cu(4)_2][PF_6]$.

Ligand **4** (500 mg, 2.03 mmol) and tetrakis(acetonitrile)copper(I) hexafluoridophosphate (378 mg, 1.02 mmol,) were dissolved in MeCN (25 mL) and stirred overnight at room temperature. The solution was concentrated under vacuum and Et_2O (25 mL) was added. As no precipitate was formed, the solution was filtered and the solvent removed from the filtrate under reduced pressure. $[Cu(\mathbf{4})_2]PF_6]$ was isolated as dark red-orange solid (1.19 g, 1.7 mmol, 83.7%).[83]

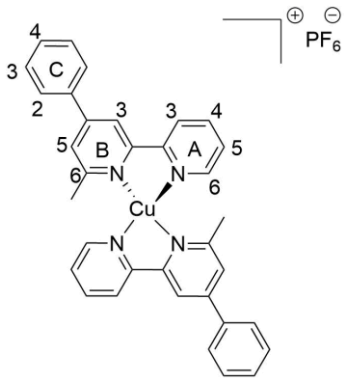

Scheme 21: Structure of $[Cu(4)_2][PF_6]$ with atom labelling for NMR assignments.

^{1}H NMR (500 MHz, CD_2Cl_2) δ/ppm 8.55 (dd, *J* = 5.0, 1.6 Hz, 2H, H^{A6}), 8.45 (d, *J* = 8.1 Hz, 2H, H^{A3}), 8.38 (d, *J* = 1.8 Hz, 2H, H^{B3}), 8.13 (td, *J* = 7.6, 1.6 Hz, 2H, H^{A4}), 7.84 (m, 4H, H^{C2}), 7.71 (d, *J* = 1.9 Hz, 2H, H^{B5}), 7.59 (m, 8H, $H^{A5+C3+C4}$), 2.37 (s, 6H, H^{Me}).

^{13}C NMR (126 MHz, CD_2Cl_2) δ/ppm 158.2 (C^{B6}), 153.0 ($C^{A2/B2}$), 152.4 ($C^{A2/B2}$), 151.1 (C^{B4}), 149.2 (C^{A6}), 138.6 (C^{A4}), 137.6 (C^{C1}), 130.5 (C^{C4}), 129.9 (C^{C3}), 127.7 (C^{C2}), 126.8 (C^{A5}), 124.3 (C^{B5}), 122.6 (C^{A3}), 117.7 (C^{B3}), 25.7 (C^{Me}).

ESI-MS *m/z* 555.2 $[M - PF_6]^+$ (calc. 555.2).

Found C 58.39, H 4.37, N 8.35; $C_{34}H_{28}CuF_6N_4P$ requires C 58.24, H 4.03, N 7.99%.

4.5.6 $[Cu(\mathbf{5})_2][PF_6]$

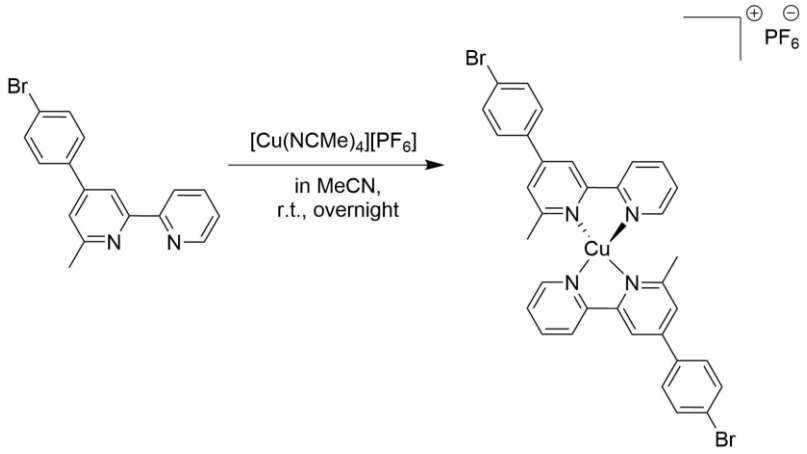

Scheme 22: Synthesis of $[Cu(5)_2][PF_6]$.

Ligand **5** (350 mg, 1.08 mmol) and tetrakis(acetonitrile)copper(I) hexafluoridophosphate (201 mg, 0.54 mmol) were dissolved in MeCN (25 mL) and stirred overnight at room temperature. The solution was filtered and the solvent was removed *in vacuo*. $[Cu(\mathbf{5})_2][PF_6]$ was isolated as dark red-orange solid (835 mg, 0.972 mmol, 90.0%).[83]

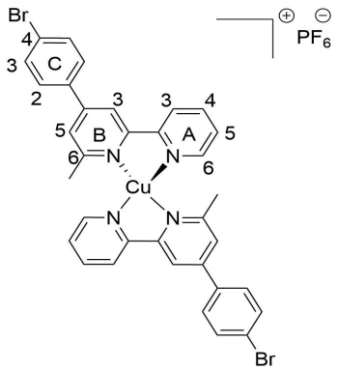

Scheme 23: Structure of [Cu(5)$_2$][PF$_6$] with atom labelling for NMR assignments.

^{1}H NMR (500 MHz, CD_2Cl_2) δ/ppm 8.54 (d, *J* = 4.6 Hz, 2H, H^{A6}), 8.46 (d, *J* = 8.1 Hz, 2H, H^{A3}), 8.35 (s, 2H, H^{B3}), 8.14 (t, *J* = 7.3 Hz, 2H, H^{A4}), 7.71 (m, 8H, H^{C2+C3}), 7.76 (s, 2H, H^{B5}), 7.59 (m, 2H, H^{A5}), 2.35 (s, 6H, H^{Me}).

^{13}C NMR (126 MHz, CD_2Cl_2) δ/ppm 157.9 (C^{B6}), 152.3 (C^{A2}), 152.0 (C^{B2}), 149.3 (C^{B4}), 148.8 (C^{A6}), 138.1 (C^{A4}), 136.0 (C^{C1}), 132.6 (C^{C3}), 128.8 (C^{C2}), 126.4 (C^{A5}), 124.4 (C^{C4}), 123.6 (C^{B5}), 122.1 (C^{A3}), 116.9 (C^{B3}), 25.2 (C^{Me}).

ESI-MS *m/z* 713.0 $[M - PF_6]^+$ (calc. 713.0).

Found C 47.59, H 3.37, N 6.78; $C_{34}H_{26}Br_2CuF_6N_4P$ requires C 47.54, H 3.05, N 6.52%.

4.5.7 [Cu(**6**)$_2$][PF$_6$]

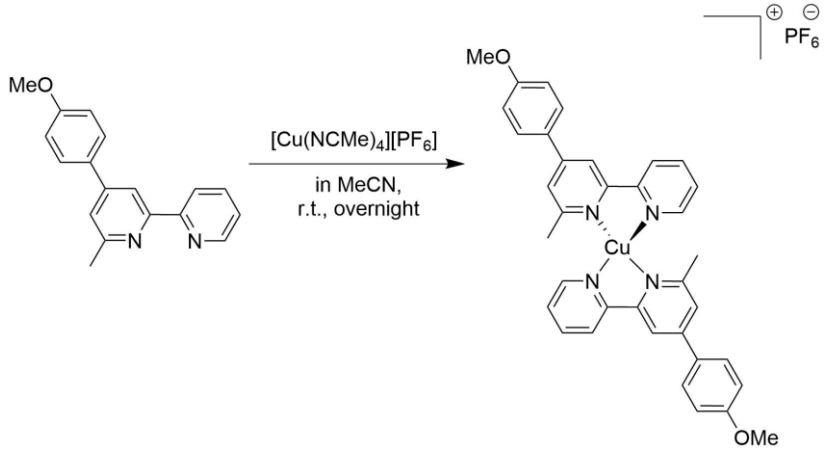

Scheme 24: Synthesis of [Cu(6)$_2$][PF$_6$].

Ligand **6** (500 mg, 1.81 mmol) and tetrakis(acetonitrile)copper(I) hexafluoridpohosphate (337 mg, 0.905 mmol,) were dissolved in MeCN (25 mL) and stirred overnight at room temperature. The solution was concentration under vacuum, filtered and the solvent of the filtrate was removed under reduced pressure. [Cu(**6**)$_2$][PF$_6$] was isolated as dark red-orange solid (1.16 g, 1.52 mmol, 84.2%).[83]

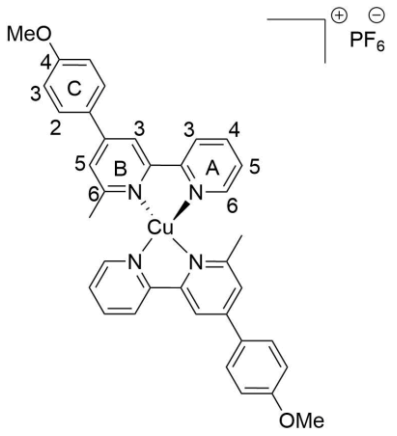

Scheme 25: Structure of [Cu(6)$_2$][PF$_6$] with atom labelling for NMR assignments.

^{1}H NMR (500 MHz, CD_2Cl_2) δ/ppm 8.53 (d, *J* = 4.9 Hz, 2H, H^{A6}), 8.44 (d, *J* = 8.1 Hz, 2H, H^{A3}), 8.34 (s, 2H, H^{B3}), 8.12 (m, 2H, H^{A4}), 7.80 (d, *J* = 8.4 Hz, 4H, H^{C2}), 7.66 (s, 2H, H^{B5}), 7.57 (m, 2H, H^{A5}), 7.11 (d, *J* = 8.4 Hz, 4H, H^{C3}), 3.90 (s, 6H, H^{OMe}), 2.33 (s, 6H, H^{Me}).

^{13}C NMR (126 MHz, CD_2Cl_2) δ/ppm 161.9 (C^{C4}), 158.0 (C^{B6}), 153.2 (C^{A2}), 152.3 (C^{B2}), 150.5 (C^{B4}), 149.2 (C^{A6}), 138.5 (C^{A4}), 129.6 (C^{C1}), 129.0 (C^{C2}), 126.7 (C^{A5}), 123.6 (C^{B5}), 122.5 (C^{A3}), 117.0 (C^{B3}), 115.4 (C^{C3}), 56.1 (C^{OMe}), 25.8 (C^{Me}).

ESI-MS *m/z* 615.2 $[M - PF_6]^+$ (calc. 615.2).

Found C 55.43, H 4.37, N 7.60; $C_{36}H_{32}CuF_6N_4O_2P$ requires C 55.49, H 4.40, N 7.19%.

4.5.8 [Cu(**7**)$_2$][PF$_6$]

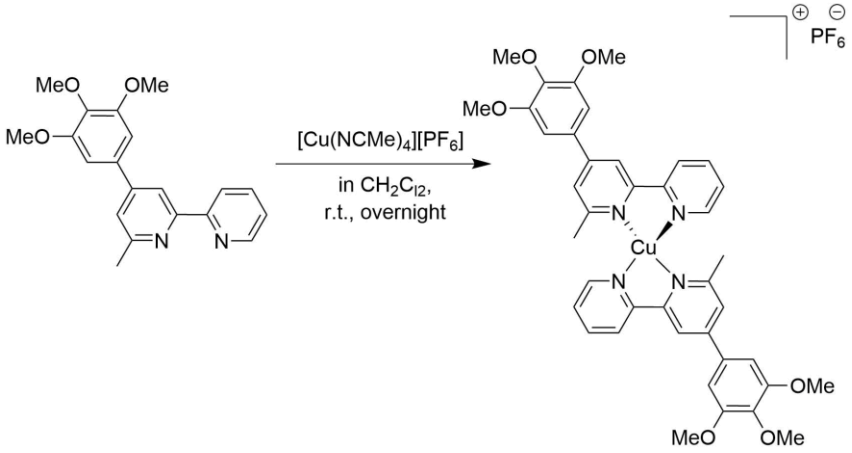

Scheme 26: Synthesis of [Cu(7)$_2$][PF$_6$].

A solution of tetrakis(acetonitrile)copper(I) hexafluoridophosphate (716 mg, 1.92 mmol) in CH_2Cl_2 (5-10 mL) was added dropwise to a solution of ligand **7** (1.29 g, 3.84 mmol, 1 eq.) in CH_2Cl_2 (20 mL) and stirred overnight at room temperature. The solution was concentration under vacuum and Et_2O (25 mL) was added. The product did not precipitate and therefore all solvent was removed under vacuum and the residue redissolved in MeCN (~ 25 mL). Et_2O (20 mL) was added, the mixture was

filtered and the solvent was removed to yield [Cu(**7**)$_2$][PF_6] as dark red-orange solid (2.41 g, 2.73 mmol, 71.2%).[83]

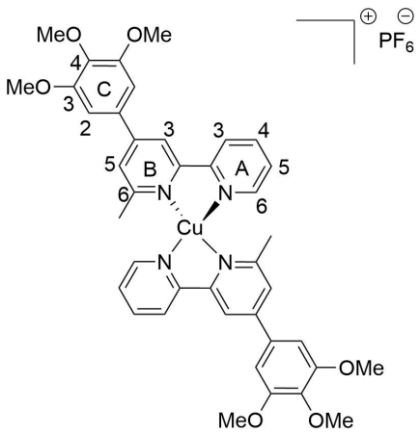

Scheme 27: Structure of [Cu(7)$_2$][PF_6] with atom labelling for NMR assignments.

^{1}H NMR (500 MHz, CD_2Cl_2) δ/ppm 8.54 (d, *J* = 4.4 Hz, 2H, H^{A6}), 8.47 (d, *J* = 8.0 Hz, 2H, H^{A3}), 8.32 (s, 2H, H^{B3}), 8.14 (m, 2H, H^{A4}), 7.66 (s, 2H, H^{B5}), 7.58 (m, 2H, H^{A5}), 6.98 (s, 4H, H^{C2}), 3.98 (s, 12H, $H^{OMe\text{-}C3}$), 3.88 (s, 6H, $H^{OMe\text{-}C4}$), 2.36 (s, 6H, H^{Me}).

^{13}C NMR (126 MHz, CD_2Cl_2) δ/ppm 158.2 (C^{B6}), 154.7 (C^{C3}), 153.0 (C^{A2}), 152.4 (C^{B2}), 151.2 (C^{B4}), 149.3 (C^{A6}), 140.5 (C^{C4}), 138.6 (C^{A4}), 133.2 (C^{C1}), 126.9 (C^{A5}), 124.4 (C^{B5}), 122.7 (C^{A3}), 117.6 (C^{B3}), 105.1 (C^{C2}), 61.1 ($C^{OMe\text{-}C4}$), 57.0 ($C^{OMe\text{-}C3}$), 25.74 (C^{Me}).

ESI-MS *m/z* 735.2 $[M - PF_6]^+$ (calc. 735.2).

Chapter 5

Chapter 5 Symmetric ancillary ligands in bis(diimine)copper(I) dyes

5.1 Motivation

As discussed in Chapter 4, methoxy substituents, especially 4-methoxy-phenyl substituents at the 4-position of the bpy ancillary ligand, have an electron-donating effect enhancing the desired ´push-pull´ characteristic of the dye.[83] Nevertheless, the overall cell performances with these asymmetrical ancillary ligands (**4-7**) in combination with the better performing anchoring ligand **ALP1** did not exceed 36% of the performance of an N719 reference cell set at 100%. Nevertheless, the methoxy-substituted ancillary ligands seemed to be promising candidates for application as dyes in DSCs. Based on the results presented in Chapter 4, a set of symmetrical ancillary ligands substituted with different numbers of methoxy groups on the phenyl-substituents of the 4,4´-diphenyl-2,2´-bipyridines were investigated in order to further study the effects of electron-donating groups in bis(diimine)copper(I) dyes for dye-sensitized solar cells. Some of the ligand precursors used in this chapter were synthesized by Dr. Sven Y. Brauchli.

5.2 Synthetic approach

The preparation of the symmetrical methoxy-substituted ancillary ligands (**8-11**) used the Kröhnke[84] strategy. The synthesis of the ((6,6´-dimethyl-[2,2´-bipyridine]-4,4´-diyl)bis(4,1-phenylene))bis(phosphonic acid) (**ALP1**)[75] used as anchoring ligand in this chapter was presented in the experimental section of Chapter 3. Scheme 28 displays the general synthetic route for the ancillary ligands.

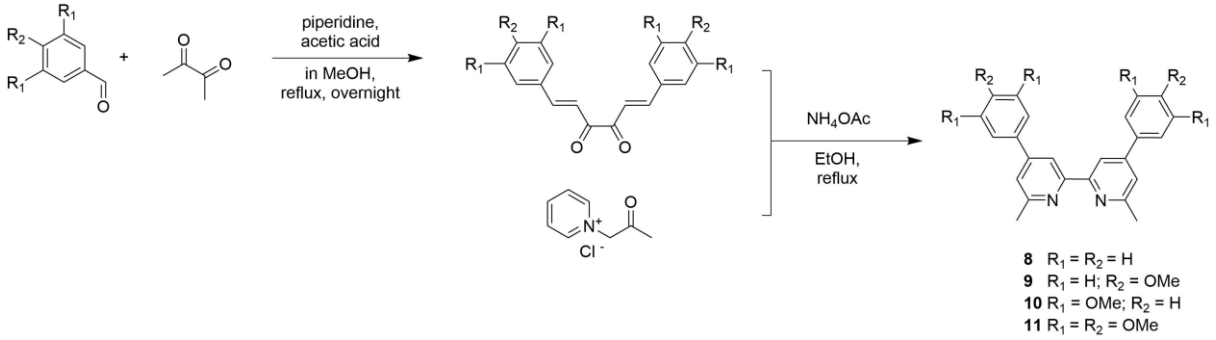

Scheme 28: Synthesis of the symmetrical ancillary ligands (8-11) from literature precursors.

The corresponding homoleptic copper(I) complexes (Scheme 29) were prepared using a standard method by combination of $[Cu(MeCN)_4][PF_6]$[87] with two equivalents of the ligand **8-11** and were isolated as dark red to dark red-ochre solids in 69.5-84.5% yield. In the electrospray mass spectrum the highest mass peak of each complex corresponded to the $[M - PF_6]^+$ ion and showed a characteristic

isotope pattern corresponding to the simulated pattern. The ^{1}H and ^{13}C NMR spectra of the complexes were recorded in $CDCl_3$ or CD_3CN and assigned using 2D methods.

In Figure 36 the solution absorption spectra of the complexes are shown. The corresponding absorption maxima are given in Table 8 and were established by recording the spectra at different concentrations. The solution absorption spectra are dominated by high-energy π*←π transitions [Cu(**8**)$_2$][PF_6]; and π*←π and π*←*n* transitions for [Cu(**9**)$_2$][PF_6], [Cu(**10**)$_2$][PF_6] and [Cu(**11**)$_2$][PF_6]. Furthermore broad MLCT bands with λ_{max} = 482-486 nm arise for all the complexes (Table 8). Comparing the extinction coefficient value for the MLCT band of [Cu(**9**)$_2$][PF_6] (11 400 $dm^3\ mol^{-1}\ cm^{-1}$) to a literature value[90] of the same complex measured in a different solvent verified the consistency of the data.[91]

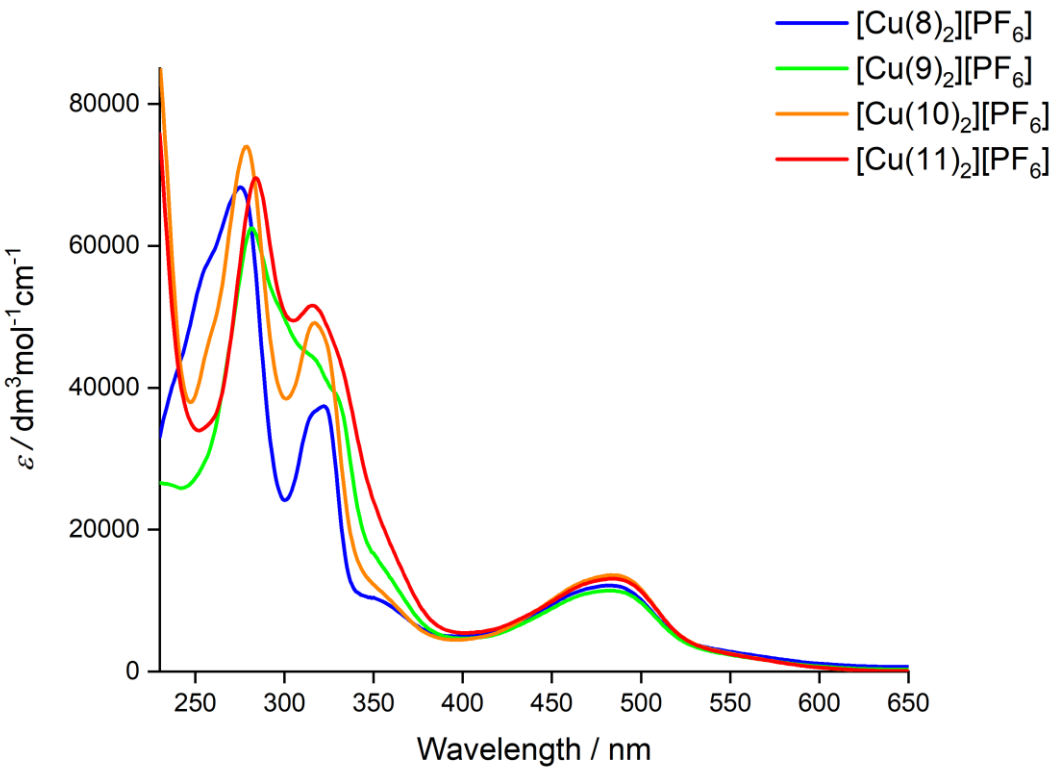

Figure 36: Solution (CH_2Cl_2) absorption spectra of complexes [Cu($L_{ancillary}$)$_2$][PF_6] with $L_{ancillary}$ = 8-11 (1×10^{-5} mol dm^{-3}).

Table 8: Absorption maxima for $[Cu(L_{ancillary})_2][PF_6]$ with $L_{ancillary}$ = 8-11 (CH_2Cl_2, 1 × 10^{-5} mol dm^{-3}; sh = shoulder; ε values are rounded to the nearest 100 dm^{-3} mol^{-1} cm^{-1}).

	λ_{max}/nm (ε_{max}/dm^3 mol^{-1} cm^{-1})	
Complex	π*←π and π*←*n*	MLCT
$[Cu(\mathbf{8})_2][PF_6]$	255 sh (56 600), 275 (68 300), 322 (37 400), 356 sh (10 900)	483 (11 400)
$[Cu(\mathbf{9})_2][PF_6]$	282 (62 500), 316 sh (44 300), 329 sh (39 000), 357 sh (14 100)	484 (11 400)
$[Cu(\mathbf{10})_2][PF_6]$	278 (73 900), 318 (49 000), 354 sh (11 400)	486 (13 600)
$[Cu(\mathbf{11})_2][PF_6]$	285 (69 400), 316 (51 600)	482 (13 100)

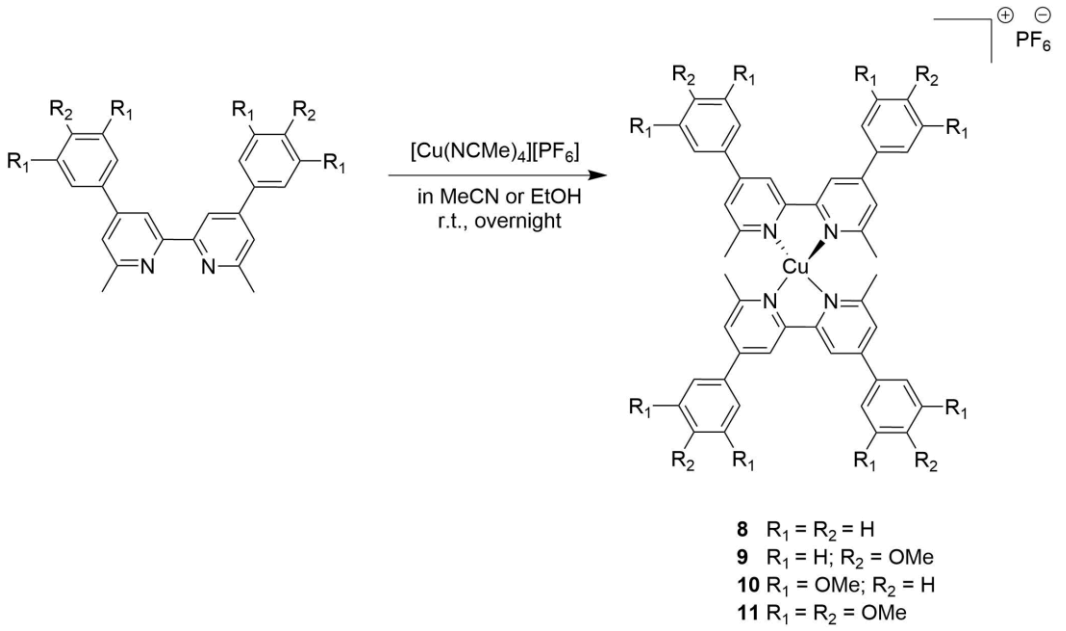

Scheme 29: General synthetic route for the homoleptic copper(I) complexes.

The detailed synthetic routes to and the analytical data for the ancillary ligands **8**-**11** shown in Scheme 28 are given in the experimental section of this chapter. The synthesis of the homoleptic Cu(I) complexes (Scheme 29) and the corresponding analytical data are presented in the experimental section of this chapter.[91]

In order to functionalize the TiO_2 surface of the electrodes with the heteroleptic dyes $[Cu(L_{anchor})(L_{ancillary})]^+$ the ´surface-as-ligand, surface-as-complex´[47] (SALSAC) (Figure 37) strategy was used. The **ALP1**[46] (**1**) anchoring ligand (Scheme 2) was used in combination with the ancillary ligands **8**-**11** to assemble the heteroleptic dyes adsorbed on the TiO_2 surface. DSCs containing these dyes were compared to a N719 reference cell.[91]

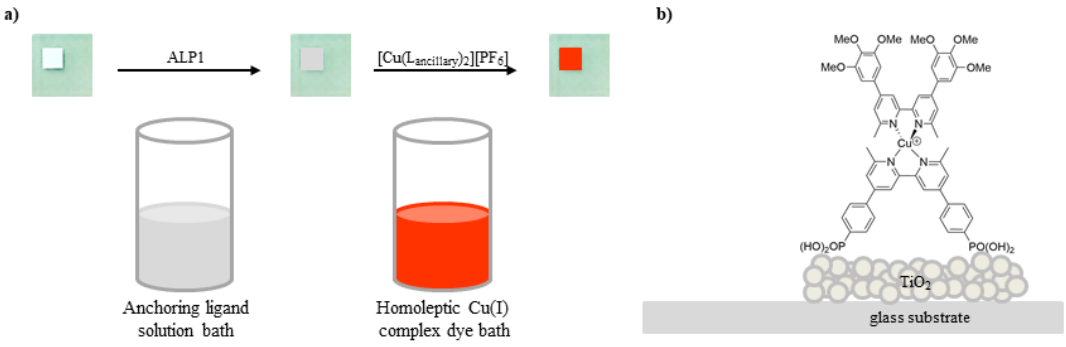

Figure 37: a) The ´surface-as-ligand, surface-as-complex´ approach to functionalize an FTO/TiO_2 electrode with a heteroleptic $[Cu(L_{anchor})(L_{ancillary})]^+$ dye. b) Surface-anchored $[Cu(1)(11)]^+$.

5.3 Results

5.3.1 Solid state absorption spectra

For the solid-state absorption measurements the copper(I) dyes were assembled with the ´surface-as-ligand, surface-as-complex´[47] strategy on transparent TiO_2 electrodes to give $[Cu(\mathbf{1})(\mathbf{8})]^+$, $[Cu(\mathbf{1})(\mathbf{9})]^+$,$[Cu(\mathbf{1})(\mathbf{10})]^+$ and $[Cu(\mathbf{1})(\mathbf{11})]^+$ adsorbed on the electrode surfaces. The commercial TiO_2 electrodes were washed with milliQ water and HPLC grade EtOH, dried in a stream of nitrogen and then heated at 450 °C for 30 min. After cooling, the electrodes were soaked in a 1.0 mM DMSO solution of anchoring ligand **1** for 24 h, washed with DMSO and EtOH and dried. The anchoring ligand-functionalized electrodes were then immersed into solutions of the different homoleptic copper(I) complexes $[Cu(L_{ancillary})_2][PF_6]$ ($L_{ancillary}$ = **8**, **9**, **10** or **11**, 0.1 mM in CH_2Cl_2). After 3 days in the dye bath solution, the electrodes were taken out, washed with CH_2Cl_2 and dried in a stream of nitrogen. Figure 38 shows the background corrected and normalized solid-state absorption spectra of the functionalized electrodes.[91]

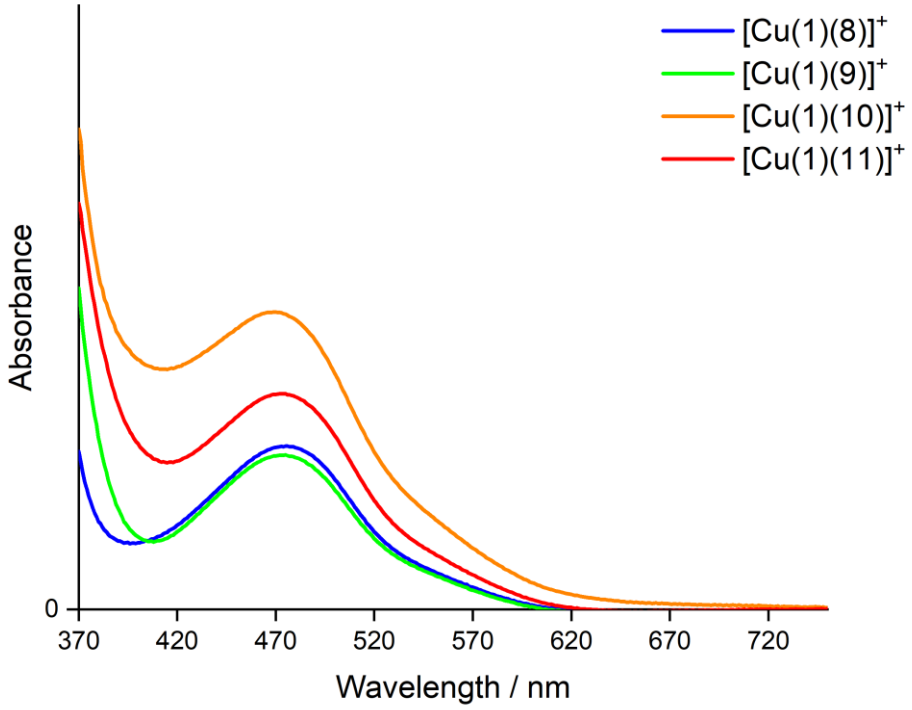

Figure 38: Solid-state absorption spectra of transparent TiO_2 functionalized with $[Cu(1)(L_{ancillary})]^+$ ($L_{ancillary}$ = 8-11).

The MLCT absorption maxima of the transparent TiO_2 electrodes functionalized with dyes $[Cu(\mathbf{1})(L_{ancillary})]^+$ ($L_{ancillary}$ = **8-11**) appeared at λ_{max} 469-475 nm (Figure 38). The unsubstituted ancillary ligand **8** and the mono-methoxy substituted ancillary ligand **9** showed the lowest absorption (Figure 38 blue and green curves). Inserting two methoxy groups in the 3,5-positions of the phenyl spacer yielded the highest absorption in the solid-state spectra (Figure 38 orange curve). Introducing a third methoxy group in the 4-position of the phenyl spacer resulted in a decrease of the absorption (Figure 38 red curve).[91]

Figure 39 illustrates a comparison of the solid-state absorption spectra of electrodes functionalized with $[Cu(\mathbf{1})(\mathbf{8})]^+$, $[Cu(\mathbf{1})(\mathbf{9})]^+$, $[Cu(\mathbf{1})(\mathbf{10})]^+$, $[Cu(\mathbf{1})(\mathbf{11})]^+$ or N719. The lower intensity MLCT band exhibited by copper(I) dyes over the well-performing N719 dye (Figure 39), confirms an overall lower spectral response.

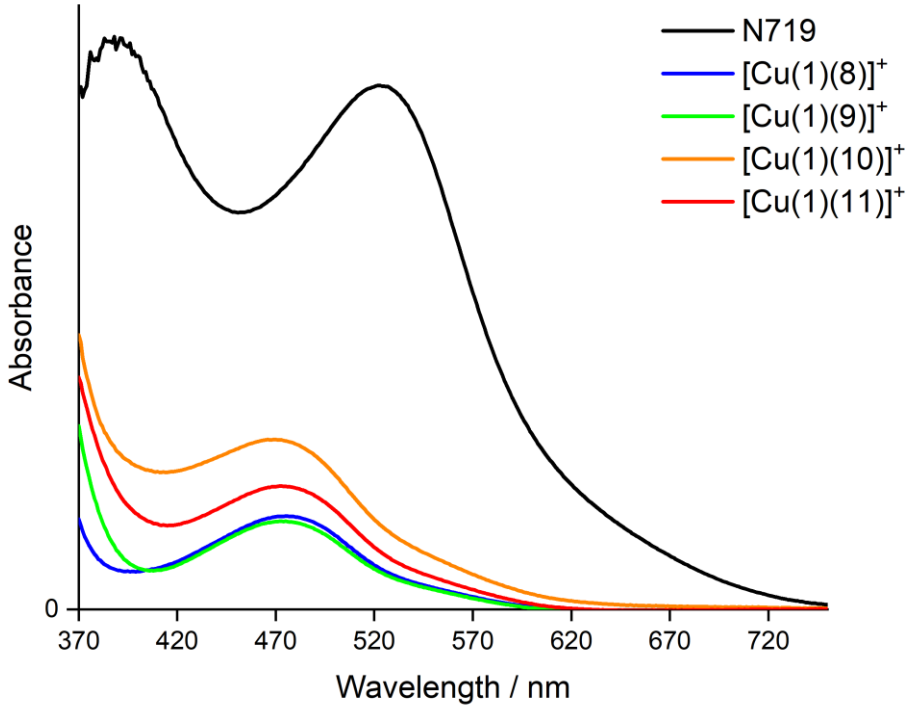

Figure 39: Solid-state absorption spectra of transparent TiO_2 functionalized with $[Cu(1)(L_{ancillary})]^+$ ($L_{ancillary}$ = 8-11) compared to N719.

5.3.2 DSC performances

The heteroleptic copper(I) dyes were adsorbed on the electrode surfaces using the ´surface-as-ligand, surface-as-complex´[47] strategy as mentioned in the last section for the solid-state absorption spectra to prepare the working electrodes for the DSCs. Each dye-soaked working electrode was assembled with a commercial Pt counter-electrode using a thermoplast hot-melt sealing foil. The electrolyte between the electrodes was introduced by vacuum back-filling before the DSCs were sealed. Duplicate DSCs were prepared for each dye to confirm the reproducibility of the performance parameters.

5.3.2.1 Solar cell measurements

To avoid false influences from scattered light, the solar simulator measurements of the DSCs were performed in a fully-masked mode with an average active area size of 0.06012 cm^2 (with a standard deviation of 1%).[79,80] All DSCs with dyes $[Cu(\mathbf{1})(L_{ancillary})]^+$ with $L_{ancillary}$ = **8-11** were measured on the day of assembling (day 0), day 1, day 3 and day 7. As the solar cells were assembled and measured in three different sets, a DSCs containing N719 as reference cell was prepared for each of the sets. For better comparison of the different dye combinations, the relative efficiencies of the DSCs with respect to N719 set at 100%[72] were calculated (Table 9, Table 10, Table 11 and Table 12). The N719 reference cell 1 was measured together with the DSCs containing dyes $[Cu(\mathbf{1})(\mathbf{8})]^+$ and $[Cu(\mathbf{1})(\mathbf{11})]^+$, N719 cell 2 together with $[Cu(\mathbf{1})(\mathbf{9})]^+$ and reference cell 3 with the DSCs containing $[Cu(\mathbf{1})(\mathbf{10})]^+$. The

highest short circuit current densities (J_{SC}) were achieved with ancillary ligands **9** and **11**, yielding values of 4.87 and 4.79 mA/cm^2 respectively (Figure 40, Figure 41 and Table 9). The DSCs with ancillary ligand **11** also yielded the highest open circuit voltages (V_{OC}) of 550 and 567 mV. Changing the ancillary ligand from **8** to **9** and **11** and going from a simple phenyl substituted bpy ligand to 4-methoxyphenyl and 3,5-dimethoxy- or 3,4,5-trimethoxyphenyl substituted ancillary ligands resulted in an increased in J_{SC} for both, **9** and **11** but a decreased V_{OC} for **9** (Figure 40 and Table 9). The electron releasing 4-methoxy substituents in ancillary ligand **9** enhance the desired ´push-pull´ system of the dye resulting in an increased J_{SC} (Table 9). The DSCs with dye [Cu(**1**)(**10**)]$^+$ yielded the lowest values for J_{SC} 3.68 and 3.90 mA/cm^2 and V_{OC} 516 and 528 mV. The lower values for this dye can be explained by the –I-effect of the methoxy substituents in 3,5-positions pulling the electrons away from the metal centre. The fill factors (ff) for all the cells were good and in the range of 68- 73%. On varying the ancillary ligand the best performance could be measured with [Cu(**1**)(**11**)]$^+$, followed by [Cu(**1**)(**9**)]$^+$ and [Cu(**1**)(**8**)]$^+$, yielding efficiencies of 1.96% for [Cu(**1**)(**11**)]$^+$, 1.82% for [Cu(**1**)(**9**)]$^+$ and 1.66% for [Cu(**1**)(**8**)]$^+$ (Table 9). The lowest power conversion efficiencies were measured for DSCs with [Cu(**1**)(**10**)]$^+$ yielding 1.43% and 1.46% (Table 9). The *J-V* curves for the DSCs with [Cu(**1**)($L_{ancillary}$)]$^+$ ($L_{ancillary}$ = **8**-**11**) are shown in Figure 40 and Figure 41.The duplicate DSCs in Table 9 confirmed the reproducibility of both the construction and the measurement of the cells. Measurements over time showed a slight decrease on day 1 which stabilized until day 7 (Table 10, Table 11 and Table 12). Unfortunately one DSC with [Cu(**1**)(**10**)]$^+$ died yielding a higher decrease in both the open circuit voltage and the short circuit current density resulting in a low performance of only 1.29% (Table 10). Figure 42 to Figure 47 show the development of the *J-V* curves over time for the cells.[91]

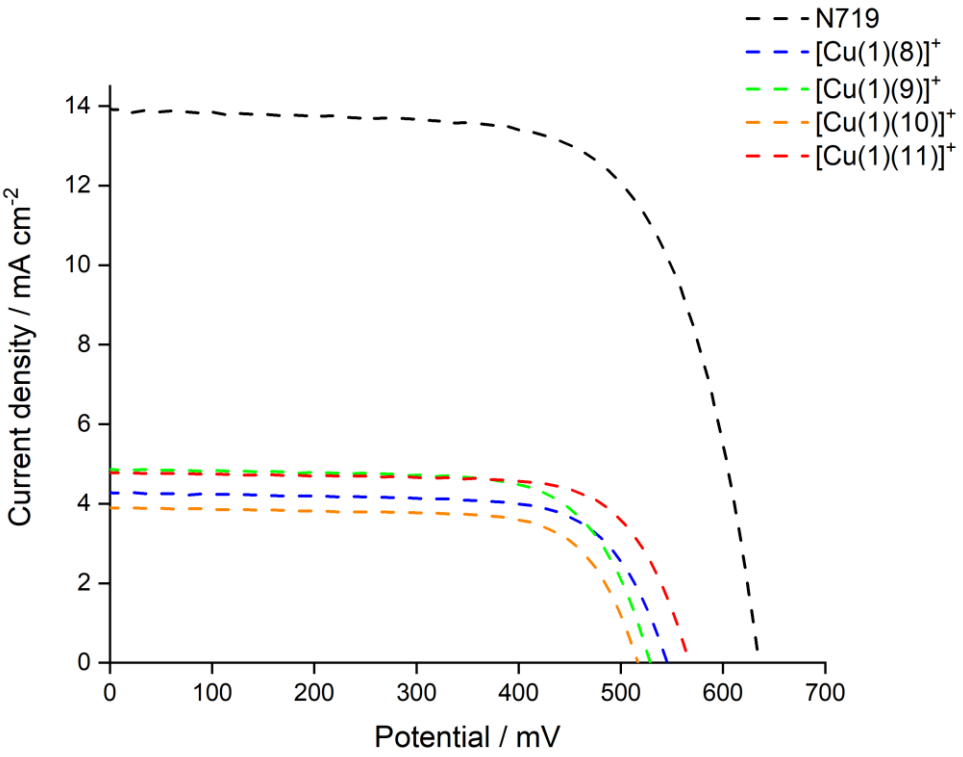

Figure 40: *J-V* curves for DSCs with dyes $[Cu(1)(L_{ancillary})]^+$ ($L_{ancillary}$ = 8-11) and N719 measured on the day of cell assembly.

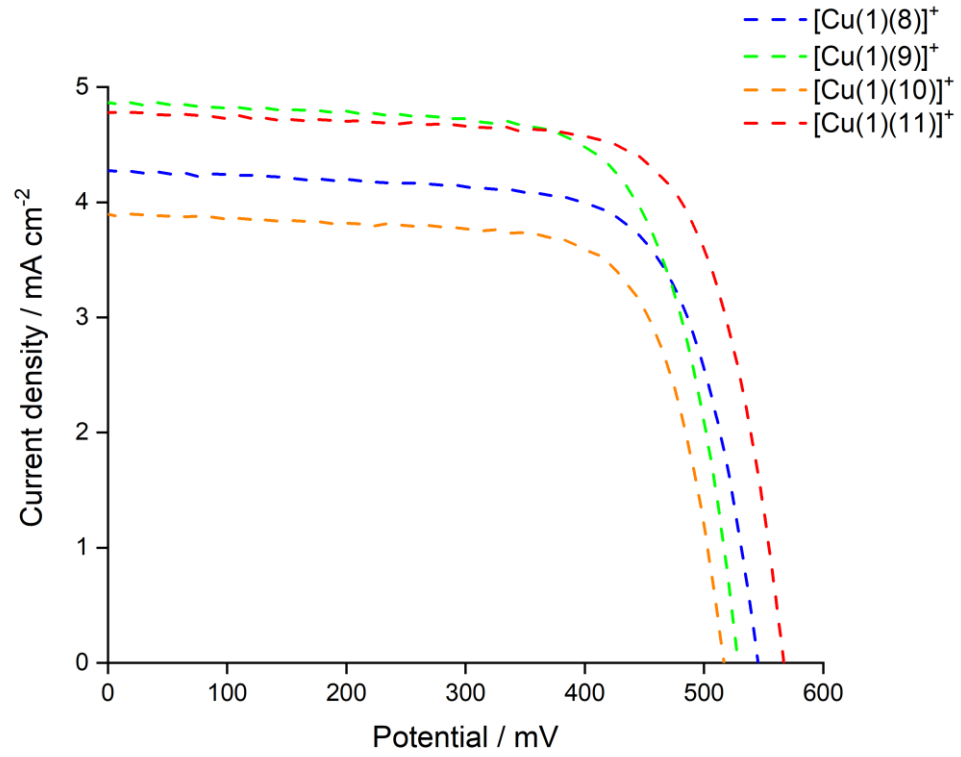

Figure 41: *J-V* curves for DSCs containing dyes $[Cu(1)(L_{ancillary})]^+$ ($L_{ancillary}$ = 8-11) measured on the day of cell assembly (expansion of Figure 40).

Table 9: Performance parameters of duplicate DSCs with $[Cu(1)(L_{ancillary})]^+$ ($L_{ancillary}$ = 8-11) compared to three N719 cells as references measured on the day of cell assembly.

Dye	J_{sc}/mA cm^{-2}	V_{OC}/mV	ff/%	η/%	Relative η/%
$[Cu(\mathbf{1})(\mathbf{8})]^+$	4.27	545	71	1.66	28.7
$[Cu(\mathbf{1})(\mathbf{8})]^+$	4.20	536	70	1.58	27.3
N719 cell 1	13.29	647	67	5.79	100
$[Cu(\mathbf{1})(\mathbf{9})]^+$	4.87	528	71	1.82	30.1
$[Cu(\mathbf{1})(\mathbf{9})]^+$	4.74	524	72	1.80	29.8
N719 cell 2	13.91	635	68	6.04	100
$[Cu(\mathbf{1})(\mathbf{10})]^+$	3.68	528	73	1.43	25.4
$[Cu(\mathbf{1})(\mathbf{10})]^+$	3.90	516	72	1.46	26.0
N719 cell 3	13.42	631	66	5.62	100
$[Cu(\mathbf{1})(\mathbf{11})]^+$	4.79	567	72	1.96	33.9
$[Cu(\mathbf{1})(\mathbf{11})]^+$	4.68	550	68	1.75	30.2
N719 cell 1	13.29	647	67	5.79	100

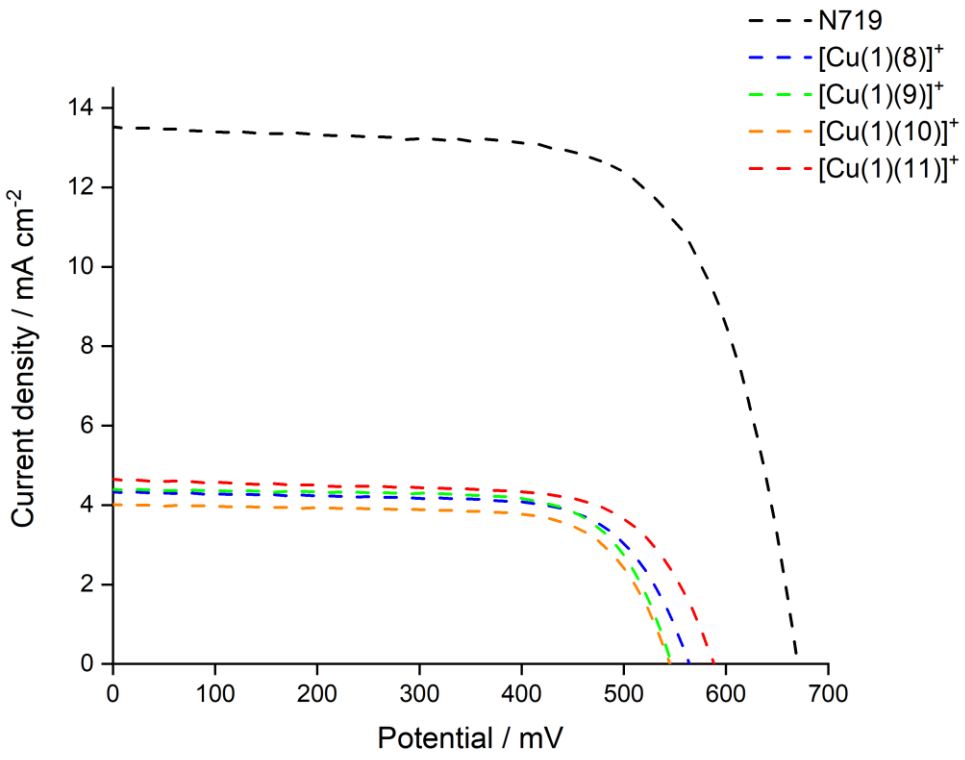

Figure 42: *J-V* curves for DSCs with dyes $[Cu(1)(L_{ancillary})]^+$ ($L_{ancillary}$ = 8-11) and N719 measured on day 1 after cell assembly.

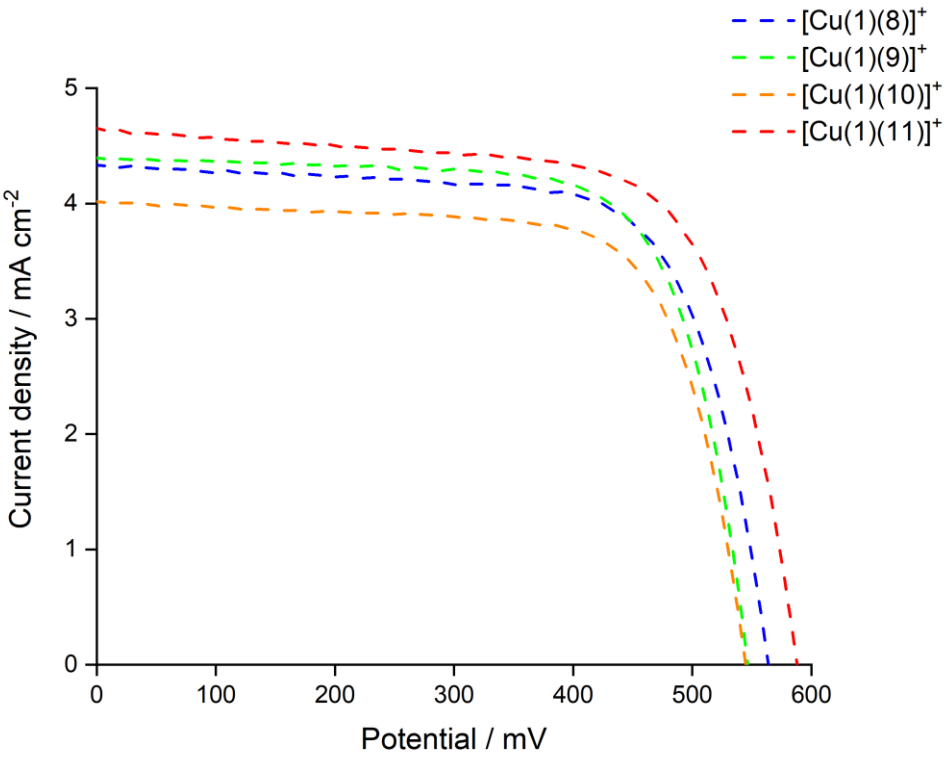

Figure 43: *J-V* curves for DSCs containing dyes $[Cu(1)(L_{ancillary})]^+$ ($L_{ancillary}$ = 8-11) measured on day 1 after cell assembly (expansion of Figure 42).

Table 10: Performance parameters for duplicate DSCs with $[Cu(1)(L_{ancillary})]^+$ ($L_{ancillary}$ = 8-11) compared to three N719 cells as references measured on day 1 after cell assembly.

Dye	J_{sc}/mA cm^{-2}	V_{OC}/mV	ff/%	η/%	Relative η/%
$[Cu(\mathbf{1})(\mathbf{8})]^+$	4.30	552	70	1.67	28.3
$[Cu(\mathbf{1})(\mathbf{8})]^+$	4.33	564	71	1.72	29.2
N719 cell 1	13.04	667	68	5.90	100
$[Cu(\mathbf{1})(\mathbf{9})]^+$	4.40	546	72	1.73	27.8
$[Cu(\mathbf{1})(\mathbf{9})]^+$	4.89	556	70	1.90	30.5
N719 cell 2	13.56	670	69	6.23	100
$[Cu(\mathbf{1})(\mathbf{10})]^+$	3.26	536	74	1.29	22.6
$[Cu(\mathbf{1})(\mathbf{10})]^+$	4.02	545	72	1.57	27.5
N719 cell 3	13.30	637	67	5.70	100
$[Cu(\mathbf{1})(\mathbf{11})]^+$	4.80	557	68	1.81	30.7
$[Cu(\mathbf{1})(\mathbf{11})]^+$	4.66	588	69	1.89	32.0
N719 cell 1	13.04	667	68	5.90	100

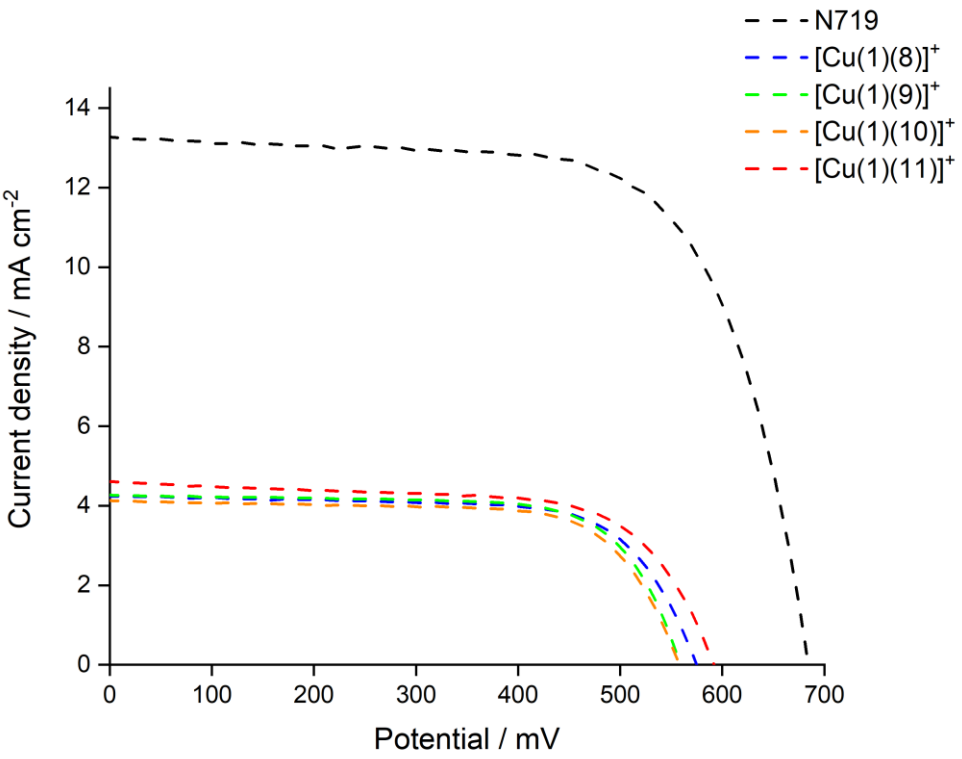

Figure 44: *J-V* curves for DSCs containing dyes $[Cu(1)(L_{anillary})]^+$ ($L_{ancillary}$ = 8-11) and N719 measured on day 3 after cell assembly.

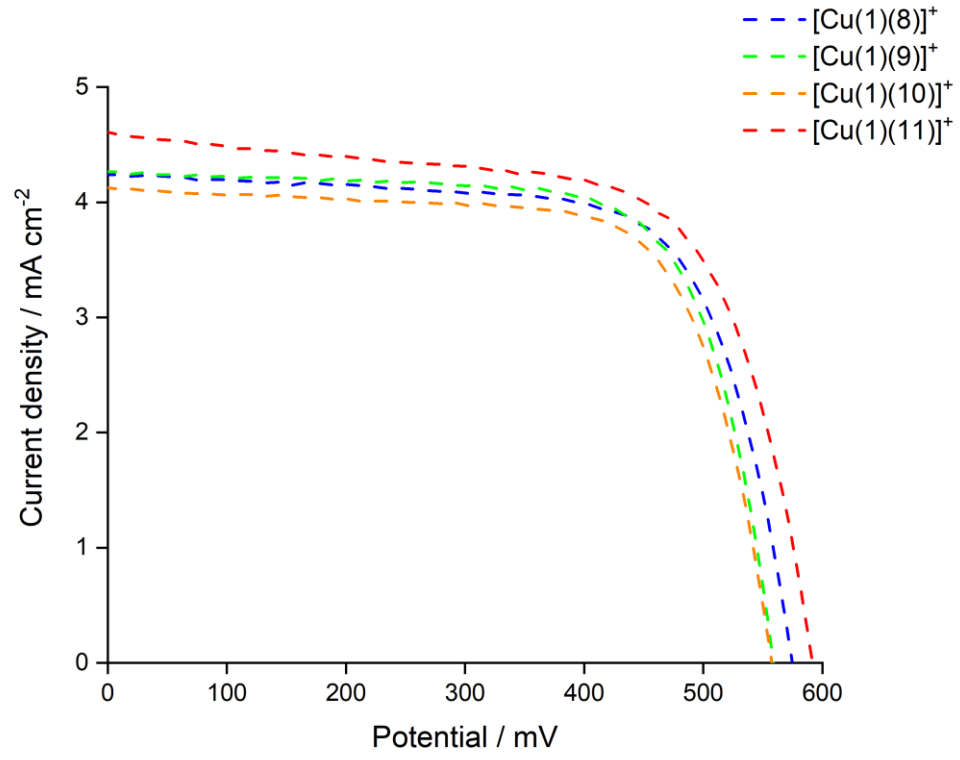

Figure 45: *J-V* curves for DSCs containing dyes $[Cu(1)(L_{ancillary})]^+$ ($L_{ancillary}$ = 8-11) measured on day 3 after cell assembly (expansion of Figure 44).

Table 11: Performance parameters of duplicate DSCs with $[Cu(1)(L_{ancillary})]^+$ ($L_{ancillary}$ = 8-11) compared to three N719 cells as references measured on day 3 after cell assembly.

Dye	J_{sc}/mA cm^{-2}	V_{OC}/mV	ff/%	η/%	Relative η/%
$[Cu(\mathbf{1})(\mathbf{8})]^+$	4.23	562	70	1.67	28.8
$[Cu(\mathbf{1})(\mathbf{8})]^+$	4.23	574	70	1.71	29.5
N719 cell 1	12.76	669	68	5.80	100
$[Cu(\mathbf{1})(\mathbf{9})]^+$	4.26	559	71	1.70	27.4
$[Cu(\mathbf{1})(\mathbf{9})]^+$	4.95	568	67	1.89	30.4
N719 cell 2	13.33	684	68	6.21	100
$[Cu(\mathbf{1})(\mathbf{10})]^+$	3.20	539	74	1.27	21.9
$[Cu(\mathbf{1})(\mathbf{10})]^+$	4.12	557	71	1.63	28.1
N719 cell 3	13.26	654	67	5.80	100
$[Cu(\mathbf{1})(\mathbf{11})]^+$	4.77	561	68	1.81	31.2
$[Cu(\mathbf{1})(\mathbf{11})]^+$	4.61	591	67	1.81	31.2
N719 cell 1	12.76	669	68	5.80	100

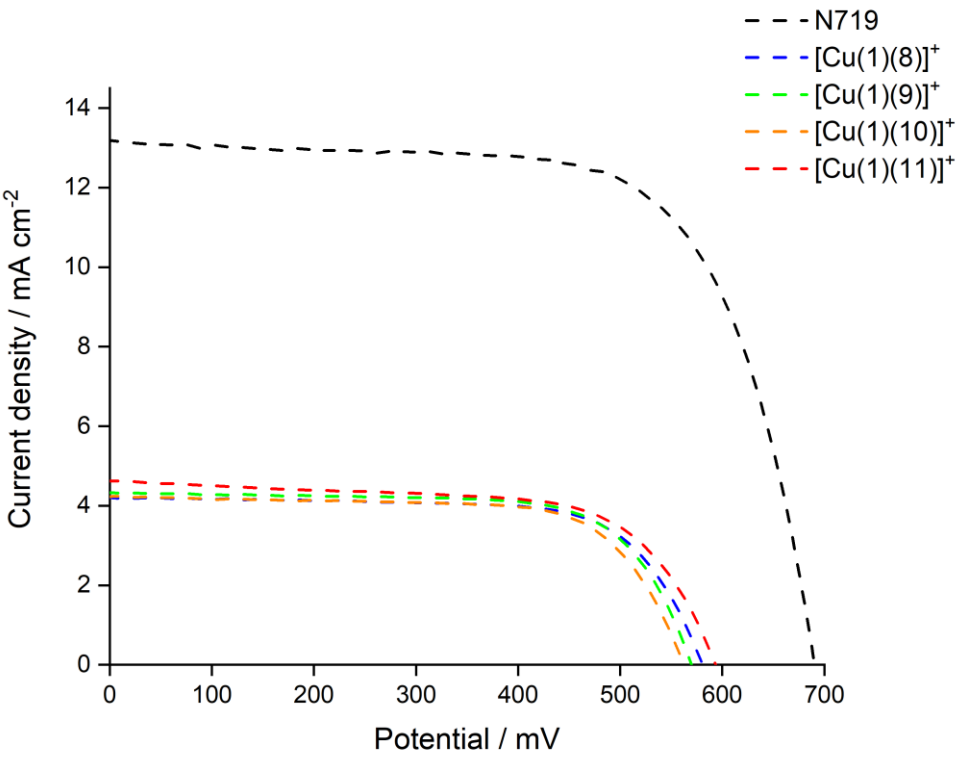

Figure 46: *J-V* curves for DSCs with dyes $[Cu(1)(L_{ancillary})]^+$ ($L_{ancillary}$ = 8-11) and N-719 measured on day 7 after cell assembly.

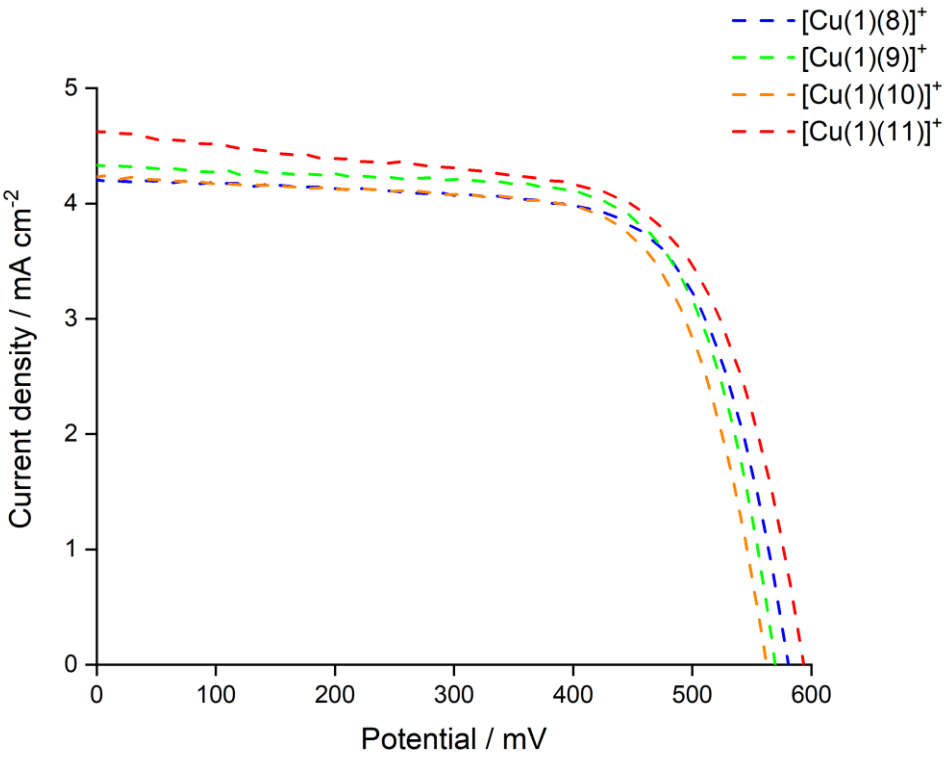

Figure 47: *J-V* curves for DSCs containing dyes $[Cu(1)(L_{ancillary})]^+$ ($L_{ancillary}$ = 8-11) measured on day 7 after cell assembly (expansion of Figure 46).

Table 12: Performance parameters of duplicate DSCS with $[Cu(1)(L_{ancillary})]^+$ ($L_{ancillary}$ = 8-11) compared to three N719 cells as references measured on day 7 after cell assembly.

Dye	J_{sc}/mA cm^{-2}	V_{OC}/mV	ff/%	η/%	Relative η/%
[Cu(**1**)(**8**)]$^+$	4.19	573	70	1.68	29.0
[Cu(**1**)(**8**)]$^+$	4.22	580	70	1.72	29.7
N719 cell 1	12.70	670	68	5.80	100
[Cu(**1**)(**9**)]$^+$	4.33	569	71	1.74	28.0
[Cu(**1**)(**9**)]$^+$	5.02	565	65	1.86	30.0
N719 cell 2	13.23	690	68	6.21	100
[Cu(**1**)(**10**)]$^+$	3.23	541	74	1.29	21.8
[Cu(**1**)(**10**)]$^+$	4.30	562	70	1.70	28.8
N719 cell 3	13.05	673	67	5.91	100
[Cu(**1**)(**11**)]$^+$	4.75	580	67	1.86	32.1
[Cu(**1**)(**11**)]$^+$	4.64	593	65	1.80	31.0
N719 cell 1	12.70	670	68	5.80	100

5.3.2.2 External Quantum Efficiency (EQE) measurements

Figure 48 compares the EQE curves of $[Cu(\mathbf{1})(L_{ancillary})]^+$ ($L_{ancillary}$ = **8-11**) to that of N719. The curves clearly show the lower photon to current conversion efficiencies of the copper(I) based dyes over that of N719. Furthermore the curves show the lack of photoconversion efficiency of the copper(I) based dyes at longer wavelengths in contrast to N719 (Figure 48 black curve).

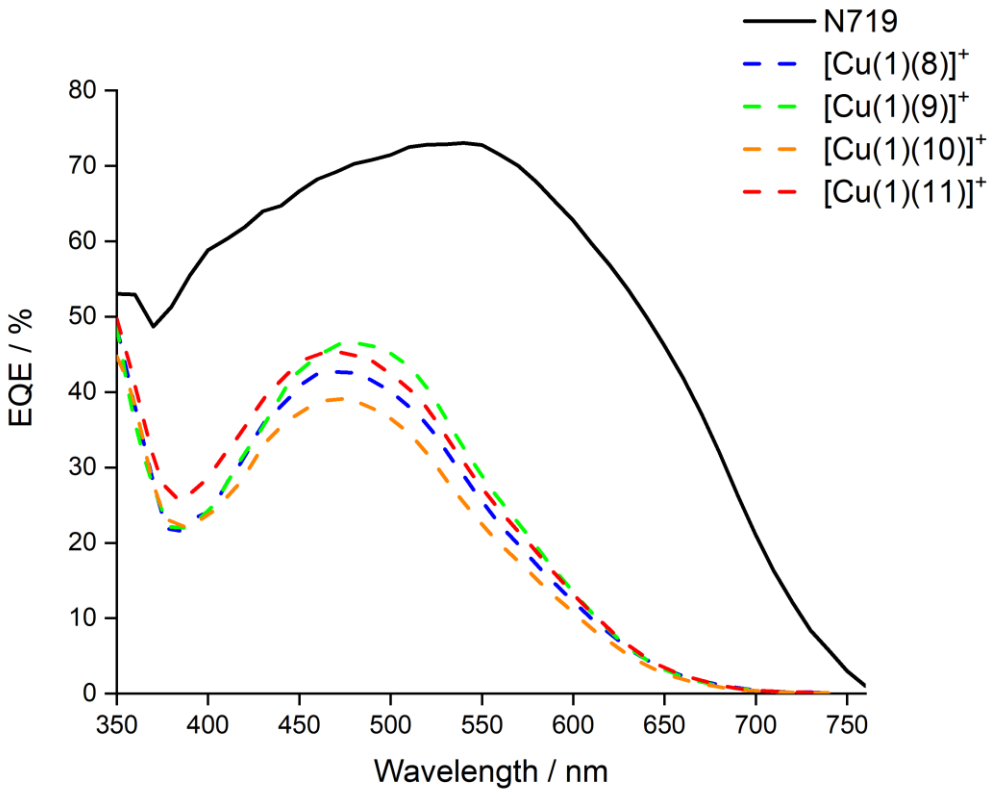

Figure 48: EQE spectra of DSCs containing dyes $[Cu(1)(L_{ancillary})]^+$ ($L_{ancillary}$ = 8-11) and N719.

The EQE spectra shown in Figure 49 reflect the trends of the J_{SC} data from the solar simulator measurements discussed in the last section. The highest values for the EQE were achieved with dye $[Cu(\mathbf{1})(\mathbf{9})]^+$ yielding EQE_{max} values of 45.3 and 46.5% at λ_{max} = 480 nm, followed by $[Cu(\mathbf{1})(\mathbf{11})]^+$ with values of 44.9 and 45.3% at λ_{max} = 470 nm (Figure 49 and Table 13). The data were consistent with the absorption maxima found for the solid-state absorption spectra shown in Figure 38. A broader spectral response towards higher wavelengths was found for $[Cu(\mathbf{1})(\mathbf{11})]^+$ in both, the solid-state absorption spectra (Figure 38) and the EQE spectra (Figure 49 and Table 13) which compensates for the slightly lower EQE_{max} value of the DSCs with this dye compared to the DSCs with $[Cu(\mathbf{1})(\mathbf{9})]^+$. The EQE_{max} values for DSCs with $[Cu(\mathbf{1})(\mathbf{8})]^+$ were measured to be 41.9 and 42.7% (Table 13). The DSCs with $[Cu(\mathbf{1})(\mathbf{10})]^+$ yielded the lowest EQE_{max} values of 38.0 and 39.1% (Table 13). The low values measured for the photon to current conversion efficiencies of DSCs with $[Cu(\mathbf{1})(\mathbf{10})]^+$ were consistent with the lower photoconversion efficiencies of the solar simulator measurements.[91]

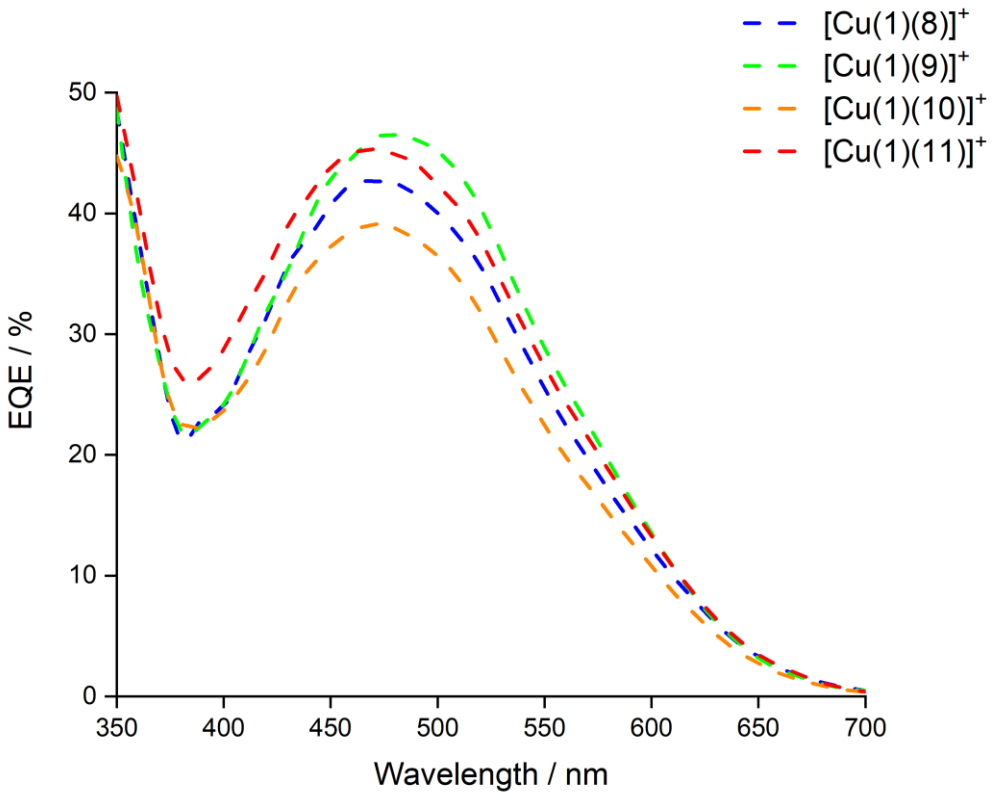

Figure 49: EQE spectra for DSCs containing dyes $[Cu(1)(L_{ancillary})]^+$ ($L_{ancillary}$ = 8-11).

Table 13: EQE maxima for duplicate DSCs containing dyes $[Cu(1)(L_{ancillary})]^+$ ($L_{ancillary}$ = 8-11).

Dye	λ_{max} / nm	EQE_{max} / %
$[Cu(\mathbf{1})(\mathbf{8})]^+$	470	42.7
$[Cu(\mathbf{1})(\mathbf{8})]^+$	470	41.9
$[Cu(\mathbf{1})(\mathbf{9})]^+$	480	46.5
$[Cu(\mathbf{1})(\mathbf{9})]^+$	480	45.3
$[Cu(\mathbf{1})(\mathbf{10})]^+$	470	39.1
$[Cu(\mathbf{1})(\mathbf{10})]^+$	470	38.0
$[Cu(\mathbf{1})(\mathbf{11})]^+$	470	45.3
$[Cu(\mathbf{1})(\mathbf{11})]^+$	470	44.9

5.4 Conclusion

In this chapter four ancillary ligands and the corresponding homoleptic Cu(I) complexes were synthesized and characterized. The ´surface-as-ligand, surface-as-complex´ (Figure 37) strategy was used to functionalize the TiO_2 electrodes with the heteroleptic copper(I) dyes using the **ALP1** anchoring ligand (**1**) and the ancillary ligands **8**-**11**. The ancillary ligands presented in this chapter had

a 6,6´-dimethyl-2,2´-bipyridine unit substituted in the 4,4´-positions with phenyl- (**8**), 4-methoxyphenyl- (**9**), 3,5-dimethoxyphenyl- (**10**) or 3,4,5-trimethoxyphenyl- substituents (**11**). DSCs containing dyes $[Cu(\mathbf{1})(L_{ancillary})]^+$ ($L_{ancillary}$ = **8**-**11**) were assembled and characterized. In order to prove the reproducibility of cell assembling and the measurements duplicate DSCs were built for each dye. The best performance was obtained for $[Cu(\mathbf{1})(\mathbf{11})]^+$ with a relative efficiency of 33.9% with respect to N719 set at 100%. The DSCs containing dyes $[Cu(\mathbf{1})(\mathbf{9})]^+$ and $[Cu(\mathbf{1})(\mathbf{8})]^+$ yielded relative efficiencies of 29.8% and 28.7%, respectively, compared to N719 set at 100%. The lowest relative cell performance was measured for $[Cu(\mathbf{1})(\mathbf{10})]^+$ with 26.0% relative to N719 set at 100%. These cells showed the lowest values for the short-circuit current density and the open-circuit voltages. While the values of the short-circuit current density for the cells with $[Cu(\mathbf{1})(\mathbf{9})]^+$ and $[Cu(\mathbf{1})(\mathbf{11})]^+$ are similar, the DSCs with $[Cu(\mathbf{1})(\mathbf{9})]^+$ showed a decline in the open-circuit voltage resulting in a lower overall cell performance. Similar trends were found for the EQE and solid-state absorption measurements for all dyes. Although the EQE_{max} values for DSCs with $[Cu(\mathbf{1})(\mathbf{11})]^+$ were slightly lower than the ones for $[Cu(\mathbf{1})(\mathbf{9})]^+$, cells containing $[Cu(\mathbf{1})(\mathbf{11})]^+$ were predominant in their spectral response at higher energies. The electron releasing methoxy groups for ancillary ligand **9** seemed to be beneficial in terms of the desired ´push-pull´ system for n-type dyes. In contrast the –I effect of the methoxy groups in *meta*-position for ancillary ligand **10** resulted lower cell performances. Interestingly the +M effect of the methoxy group in *para*-position seemed to outperform the negative influence of the –I effect of the 3,5-methoxy substituents if both effects are combined, resulting in the highest photoconversion efficiency for DSCs with ancillary ligand **11**.[91,92,93,94]

To conclude this chapter it can be clearly seen that electron releasing groups in the phenyl framework of the ancillary ligand enhance the photon to power conversion efficiency of DSCs. Further work in this field should concentrate on studying more electron donating groups as substituents for the ancillary ligands. Furthermore, more thorough investigations on the influences of the *para*- or *meta*- and both *para*- and *meta*-substituents should be done.

5.5 Experimental

The detailed synthesis for anchoring ligand **1** used in this chapter for the functionalization of the electrode surfaces with the heteroleptic dyes using the ´surface-as-ligand, surface-as-complex´ (Figure 37) strategy is shown in the experimental part of Chapter 3.

5.5.1 4,4´-Diphenyl-6,6´-dimethyl-2,2´-bipyridine (**8**)

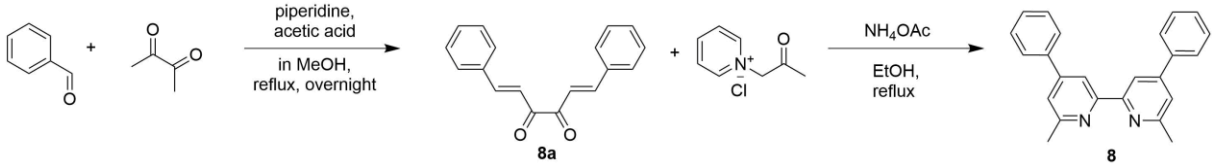

Scheme 30: Synthesis of ancillary ligand 8.

Benzaldehyde (5.01 g, 47.20 mmol), piperidine (0.39 mL, 3.99 mmol) and acetic acid (0.23 mL, 3.99 mmol) were dissolved in 40 mL MeOH. 2,3-Butandione (2.06 mL, 23.6 mmol) was dissolved in 10 mL MeOH, added dropwise to the benzaldehyde solution and heated to reflux overnight. The reaction mixture was cooled to room temperature followed by cooling in the freezer overnight resulting in the precipitation of the product. The product was filtered off and washed with cold MeOH, yielding **8a** as an ochre solid (0.23 g, 0.88 mmol, 3.73%).[95] Compound **8a** (0.23 g, 0.88 mmol), 1-(2-oxopropyl)pyridinium chloride (0.58 g, 3.39 mmol) and NH_4OAc (0.52 g, 6.70 mmol) were dissolved in 25 mL EtOH and heated to reflux overnight. The solution was cooled to room temperature, a precipitate formed. The precipitate was filtered off and washed cold MeOH. The crude product was recrystallized from MeOH and washed with diethyl ether yielding ligand **8** as an ochre solid (90.0 mg, 0.27 mmol, 31.6%).[84,91,95]

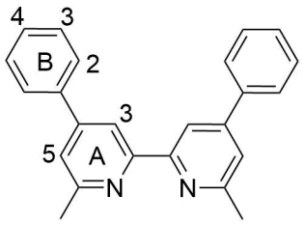

Scheme 31: Structure of ligand 8 with atom labelling for NMR assignments.

^{1}H NMR (500 MHz, $CDCl_3$) δ/ppm 9.09 (d, *J* = 1.5 Hz, 2H, H^{A3}), 8.18 (m, 4H, H^{B2}), 7.89 (d, *J* = 1.3 Hz, 2H, H^{A5}), 7.60 (m, 6H, H^{B3+B4}), 3.21 (s, 6H, H^{Me}).

^{13}C NMR (126 MHz, $CDCl_3$) δ/ppm 157.4 (C^{A6}), 156.6 (C^{A4}), 143.6 (C^{A2}), 134.7 (C^{B1}), 132.3 (C^{B4}), 130.0 (C^{B3}), 128.7 (C^{B2}), 125.8 (C^{A5}), 125.0 (C^{A3}), 21.1 (C^{Me}).

5.5.2 4,4´-Di(4-methoxyphenyl)-6,6´-dimethyl-2,2´-bipyridine (**9**)

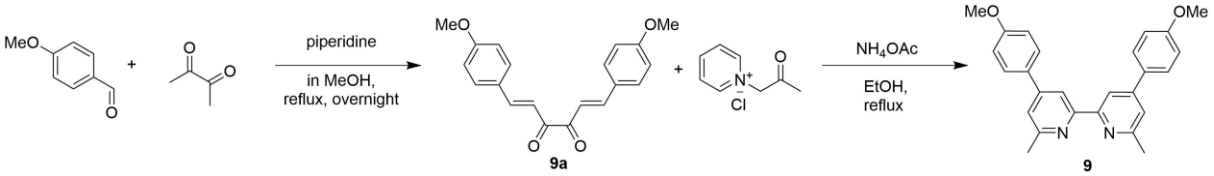

Scheme 32: Synthesis of ancillary ligand 9.

p-Anisaldehyde (4.08 g, 30.0 mmol), 2,3-butandione (1.31 mL, 15 mmol) and piperidine (0.99 mL, 10.0 mmol) were dissolved in 80 mL EtOH and heated to reflux for 2 h. The mixture was cooled to room temperature followed by cooling in the fridge for 24 h. A precipitate was formed, separated by filtration and washed with cold MeOH. Compound **9a** was isolated as orange-yellow solid (378 mg, 1.20 mmol, 8.0%).[90,95] Compund **9a** (387 mg, 1.20 mmol), 1-(2-oxopropyl)pyridinium chloride (412 mg, 2.40 mmol) and NH_4OAc (2.31 g, 30 mmol) were dissolved in 80 mL EtOH and heated to reflux for 4 h. A precipitate was formed, collected by filtration and washed with cold MeOH. The crude product was recrystallized from EtOH / pentane yielding ligand **9** as colourless needles (175 mg, 0.44 mmol, 36.8%).[84,90,91,95]

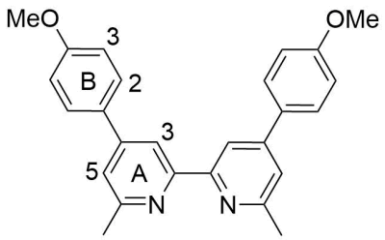

Scheme 33: Structure of ligand 9 with atom labelling for NMR assignments.

^{1}H NMR (500 MHz, $CDCl_3$) δ/ppm 8.43 (d, *J* = 1.6 Hz, 2H, H^{A3}), 7.72 (m, 4H, H^{B2}), 7.37 (d, *J* = 1.7 Hz, 2H, H^{A5}), 7.02 (m, 4H, H^{B3}), 3.88 (s, 6H, H^{OMe}), 2.70 (s, 6H, H^{Me}).

^{13}C NMR (126 MHz, $CDCl_3$) δ/ppm 160.5 (C^{B4}), 158.4 (C^{A6}), 156.8 (C^{A2}), 149.1 (C^{A4}), 131.3 (C^{B1}), 128.5 (C^{B2}), 120.6 (C^{A5}), 116.3 (C^{A3}), 114.5 (C^{B3}), 55.5 (C^{OMe}), 25.0 (C^{Me}).

5.5.3 4,4´-Di(3,5-dimethoxyphenyl)-6,6´-dimethyl-2,2´-bipyridine (**10**)

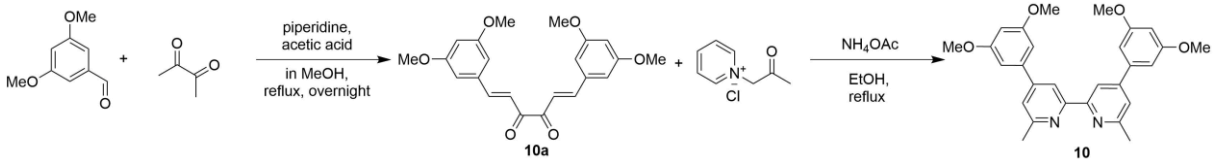

Scheme 34: Synthesis of ancillary ligand 10.

3,5-Dimethoxybenzaldehyde (4.99 g, 29.4 mmol), acetic acid (0.14 mL, 2.48 mmol) and piperidine (0.25 mL, 2.48 mmol) were dissolved in 65 mL MeOH. 2,3-Butandione (1.28 mL, 14.7 mmol) was dissolved in 15 mL MeOH and added dropwise at room temperature. The reaction was heated to reflux overnight. A precipitate was formed and the mixture was allowed to cool to room temperature. Compound **10a** was collected by filtration as yellow solid (902 mg, 2.35 mmol, 16%) and washed with cold MeOH.[96] Compound **10a** (902 mg, 2.35 mmol), 1-(2-oxopropyl)pyridinium chloride (156 mg, 9.08 mmol) and NH_4OAc (1.38 g, 18 mmol) were dissolved in EtOH and heated to reflux overnight. The solution was cooled to room temperature, a precipitate was formed. Ligand **10** was isolated by filtration as an off-white solid (285 mg, 0.62 mmol, 13.2%).[84,91,96]

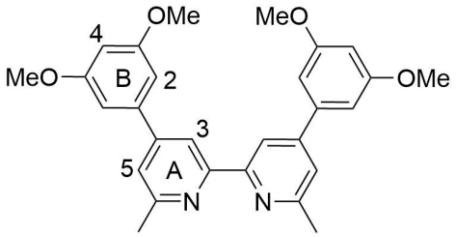

Scheme 35: Structure of ligand 10 with atom labelling for NMR assignments.

^{1}H NMR (500 MHz, $CDCl_3$) δ/ppm 9.05 (s, 2H, H^{A3}), 7.69 (s, 2H, H^{A5}), 7.17 (d, *J* = 1.9 Hz, 4H, H^{B2}), 6.62 (t, *J* = 2.0 Hz, 2H, H^{B4}), 3.94 (s, 12H, H^{OMe}), 3.05 (s, 6H, H^{Me}).

^{13}C NMR (126 MHz, $CDCl_3$) δ/ppm 161.8 (C^{B3}), 157.5 (C^{A6}), 154.8 (C^{A4}), 147.5 (C^{A2}), 137.8 (C^{B1}), 124.8 (C^{A5}), 122.7 (C^{A3}), 106.3 (C^{B2}), 103.4 (C^{B4}), 56.2 (C^{OMe}), 22.1 (C^{Me}).

5.5.4 4,4´-Di(3,4,5-trimethoxyphenyl)-6,6´-dimethyl-2,2´-bipyridine (**11**)

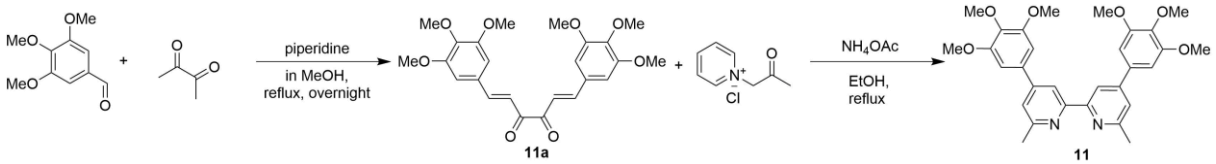

Scheme 36: Synthesis of ancillary ligand 11.

A suspension of 3,4,5-trimethoxybenzaldehyde (18.0 g, 89.9 mmol) and piperidine (0.897 mL, 8.99 mmol) in 150 mL MeOH was heated to 50 °C and stirred until dissolved. A solution of 2,3-butandione (3.97 mL, 45.0 mmol) in 30 mL MeOH was added dropwise. The reaction mixture was heated to reflux for 4 h and slowly cooled to room temperature over 1 h. The formed precipitate was filtered off and washed with diethyl ether. Compound **11a** was isolated as an orange solid (3.65 g, 11.3 mmol, 13.0%). Compound **11a** (858 mg, 1.94 mmol), 1-(2-oxopropyl)pyridinium chloride (666 mg, 3.88 mmol) and NH_4OAc (4.49 g, 58.2 mmol) were dissolved in 100 mL EtOH and heated to reflux overnight. The solution was cooled to room temperature, a precipitate was formed. The precipitate was filtered off and dried with diethyl ether. Ligand **11** was isolated as orange solid (230 mg, 0.445 mmol, 23.1%).[84,91]

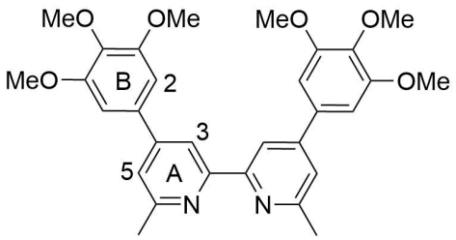

Scheme 37: Structure of ligand 11 with atom labelling for NMR assignments.

^{1}H NMR (500 MHz, $CDCl_3$) δ/ppm 8.40 (d, *J* = 1.7 Hz, 2H, H^{A3}), 7.35 (d, *J* = 1.6 Hz, 2H, H^{A5}), 6.93 (s, 4H, H^{B2}), 3.97 (s, 12H, H^{OMe3}), 3.92 (s, 6H, H^{OMe4}), 2.72 (s, 6H, H^{Me}).

^{13}C NMR (126 MHz, $CDCl_3$) δ/ppm 158.6 (C^{A6}), 156.7 (C^{A2}), 153.8 (C^{B3}), 150.0 (C^{A4}), 139.0 (C^{B4}), 134.9 (C^{B1}), 121.4 (C^{A5}), 116.9 (C^{A3}), 104.8 (C^{B2}), 61.2 (C^{OMe3}), 56.8 (C^{OMe4}), 24.9 (C^{Me}).

5.5.5 [Cu(**8**)$_2$][PF_6]

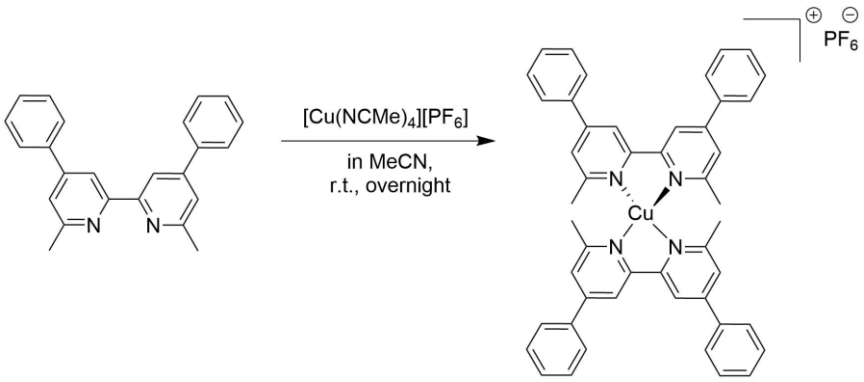

Scheme 38: Synthesis of [Cu(8)$_2$][PF_6].

Ligand **8** (90.2 mg, 0.268 mmol) and $[Cu(NCMe)_4][PF_6]$ (49.9 mg, 0.134 mmol) were dissolved in 25 mL MeCN and stirred overnight at room temperature. The solution was filtered, the solvent was

removed under reduced pressure and the resulting dark red solid was washed several times with diethyl ether to yield [Cu(**8**)$_2$][PF$_6$] as dark red solid (95 mg, 0.108 mmol, 80.4%).[91]

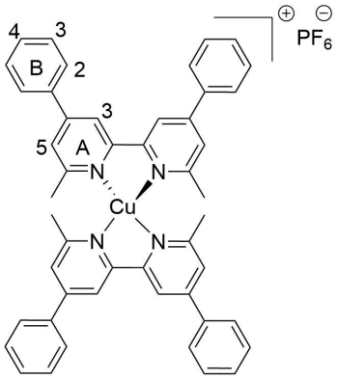

Scheme 39: Structure of [Cu(8)$_2$][PF$_6$] with atom labelling for NMR assignments.

^{1}H NMR (500 MHz, CD_3CN) δ/ppm 8.68 (s, 4H, H^{A3}), 7.96 (d, *J* = 7.1 Hz, 8H, H^{B2}), 7.85 (s, 4H, H^{A5}), 7.60 (dt, *J* = 11.9, 6.9 Hz, 12H, H^{B3+B4}), 2.42 (s, 12H, H^{Me}).

^{13}C NMR (126 MHz, CD_3CN) δ/ppm 158.8 (C^{A6}), 153.3 (C^{A2}), 151.2 (C^{A4}), 138.1 (C^{B1}), 130.9 (C^{B4}), 130.3 (C^{B3}), 128.4 (C^{B2}), 124.6 (C^{A5}), 118.8 (C^{A3}), 25.5 (C^{Me}).

ESI-MS *m/z* 735.24 [M-PF$_6$]$^+$ (calc. 735.25).

5.5.6 [Cu(**9**)$_2$][PF$_6$]

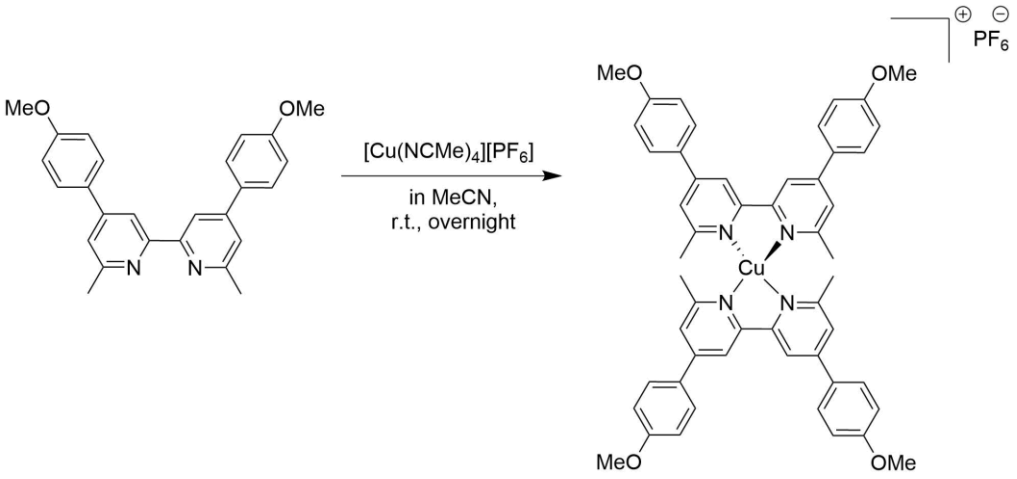

Scheme 40: Synthesis of [Cu(9)$_2$][PF$_6$].

Ligand **9** (150 mg, 0.378 mmol) and [Cu(NCMe)$_4$][PF$_6$] (70.4 mg, 0.189 mmol) were dissolved in 20 mL MeCN and stirred overnight at room temperature. The reaction was concentrated under reduced pressure and diethyl ether was added to precipitate the complex. As no precipitation took place the solution was filtered and concentrated to dryness under reduced pressure. The resulting solid was

washed several times with diethyl ether yielding [Cu(**9**)$_2$][PF$_6$] as dark red-ochre solid (160 mg, 0.16 mmol, 84.5%).[91]

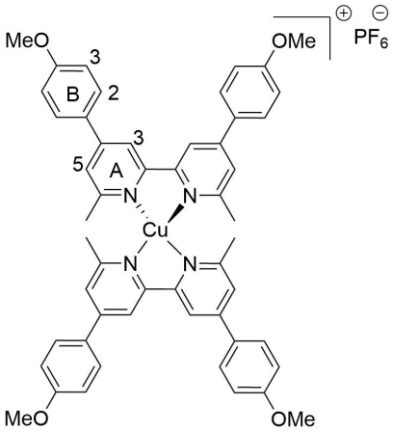

Scheme 41: Structure of [Cu(9)$_2$][PF$_6$] with atom labelling for NMR assignments.

^{1}H NMR (500 MHz, $CDCl_3$) δ/ppm 8.35 (s, 4H, H^{A3}), 7.79 (d, *J* = 8.3 Hz, 8H, H^{B2}), 7.63 (s, 4H, H^{A5}), 7.11 (d, *J* = 8.1 Hz, 8H, H^{B3}), 3.91 (s, 12H, H^{OMe}), 2.35 (s, 12H, H^{Me}).

^{13}C NMR (126 MHz, $CDCl_3$) δ/ppm 161.3 (C^{B4}), 157.4 (C^{A6}), 152.3 (C^{A2}), 150.2 (C^{A4}), 129.2 (C^{B1}), 128.5 (C^{B2}), 123.0 (C^{A5}), 116.6 (C^{A3}), 114.9 (C^{B3}), 55.5 (C^{OMe}), 25.3 (C^{Me}).

ESI-MS *m/z* 855.31 $[M\text{-}PF_6]^+$ (calc. 855.30).

5.5.7 [Cu(**10**)$_2$][PF$_6$]

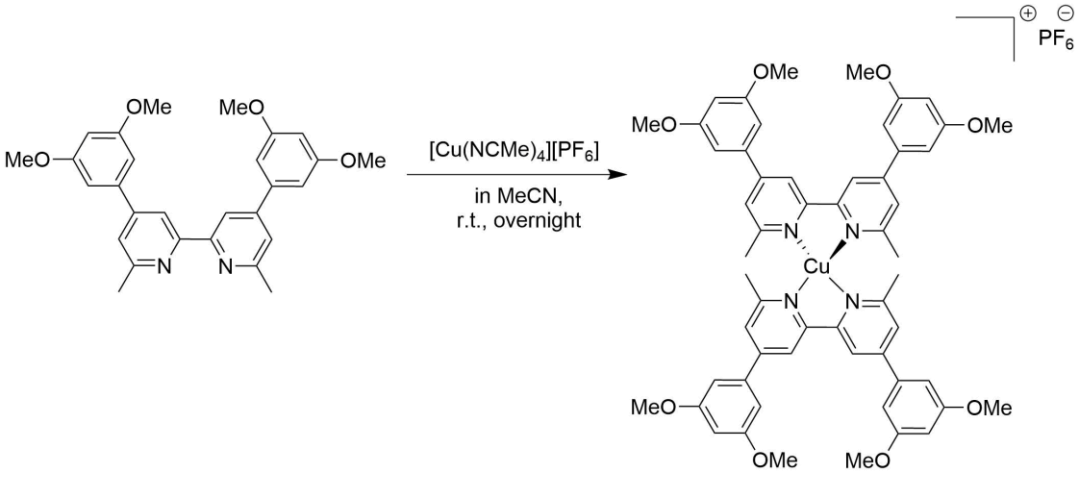

Scheme 42: Synthesis of [Cu(10)$_2$][PF$_6$].

Ligand **10** (150 mg, 0.329 mmol) and [Cu(NCMe)$_4$][PF$_6$] (61.3 mg, 0.165 mmol) were dissolved in 25 mL MeCN and stirred overnight at room temperature. The solution was filtered and the solvent was removed under reduced pressure. The resulting solid was washed several times with diethyl ether yielding [Cu(**10**)$_2$][PF$_6$] as dark red solid (135 mg, 0.121 mmol, 73.2%).[91]

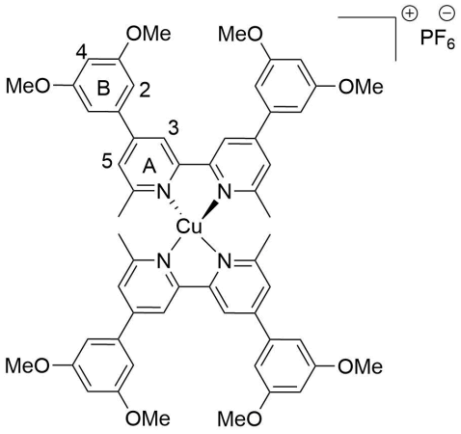

Scheme 43: Structure of [Cu(10)$_2$][PF$_6$] with atom labelling for NMR assignments.

^{1}H NMR (500 MHz, CD_3CN) δ/ppm 8.68 (s, 4H, H^{A3}), 7.83 (s, 4H, H^{A5}), 7.08 (d, *J* = 2.0 Hz, 8H, H^{B2}), 6.67 (s, 4H, H^{B4}), 3.89 (s, 24H, H^{OMe}), 2.34 (s, 12H, H^{Me}).

^{13}C NMR (126 MHz, CD_3CN) δ/ppm 162.6 (C^{B3}), 158.6 (C^{A6}), 153.3 (C^{A2}), 151.0 (C^{A4}), 140.2 (C^{B1}), 124.9 (C^{A5}), 119.0 (C^{A3}), 106.7 (C^{B2}), 102.2 (C^{B4}), 56.4 (C^{OMe}), 25.4 (C^{Me}).

ESI-MS *m/z* 975.31 $[M\text{-}PF_6]^+$ (calc. 975.34).

5.5.8 [Cu(**11**)$_2$][PF$_6$]

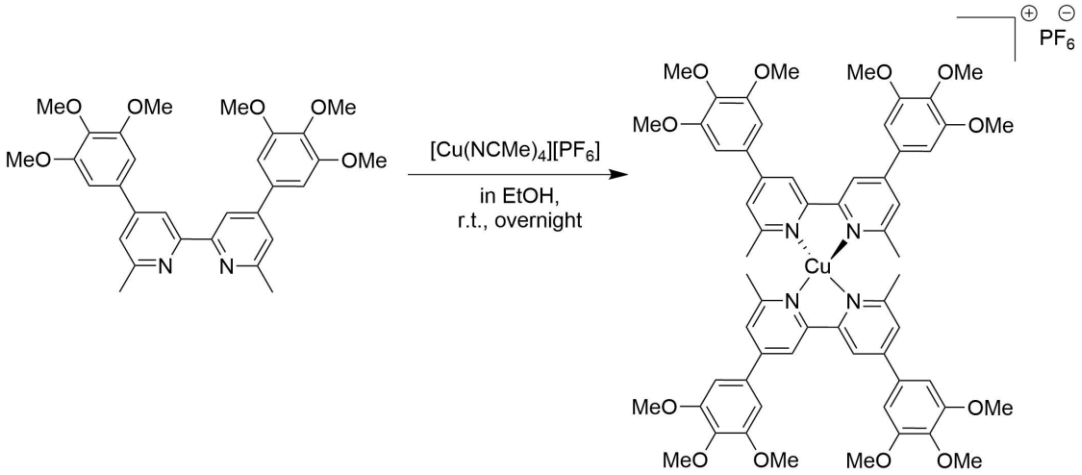

Scheme 44: Synthesis of [Cu(11)$_2$][PF$_6$].

Ligand **11** (226 mg, 0.437 mmol) and [Cu(NCMe)$_4$][PF$_6$] (81.5 mg, 0.219 mmol) are dissolved in 25 mL EtOH and stirred for 4 h at room temperature. Water was added and the organic solvent removed under reduced pressure. The residue was filtered over celite, washed with water and diethyl ether and redissolved in MeCN. The solvent was removed under reduced pressure yielding [Cu(**11**)$_2$][PF$_6$] as dark red solid (189 mg, 0.152 mmol, 69.5%).[91]

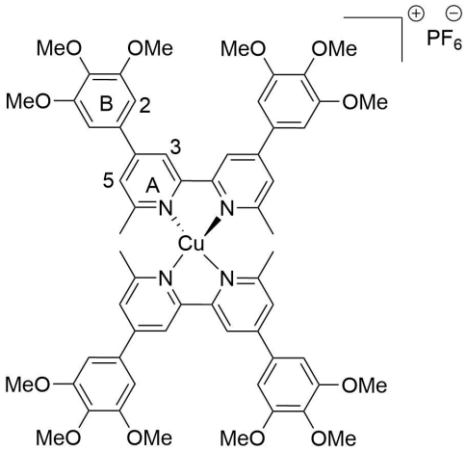

Scheme 45: Structure of $[Cu(11)_2][PF_6]$ with atom labelling for NMR assignments.

^{1}H NMR (500 MHz, $CDCl_3$) δ/ppm 8:29 (s, 4H, H^{A3}), 7.63 (s, 4H, H^{A5}), 6.97 (s, 8H, H^{B2}), 3.99 (s, 24H, H^{OMe3}), 3.93 (s, 12H, H^{OMe4}), 2.39 (s, 12H, H^{Me}).

^{13}C NMR (126 MHz, $CDCl_3$) δ/ppm 156.4 (C^{A6}), 152.0 (C^{A2}), 151.1 (C^{A4}), 154.2 (C^{B3}), 139.9 (C^{B4}), 133.4 (C^{B1}), 124.3 (C^{A5}), 117.7 (C^{A3}), 105.0 (C^{B2}), 61.2 (C^{OMe4}), 56.7 (C^{OMe3}), 25.5 (C^{Me}).

ESI-MS *m/z* 1095.30 $[M\text{-}PF_6]^+$ (calc. 1095.38).

Chapter 6

Chapter 6 Amide and amino ancillary ligands in bis(diimine)copper(I) dyes – Schiff-base chemistry

6.1 Motivation

As discussed in Chapter 5, the substituents in the 4,4´-positions of the phenyl spacer at the 4,4´-position of the bpy ancillary ligands have a strong influence on the overall cell performances.[91] The idea of enhanced cell performances based on the influence of substituents in the 4,4´-position of the phenyl spacer is investigated further in this chapter. The *para*-position was found to have the highest influence on enhancing the desired ´push-pull´ characteristics of the dye.[91] In order to further increase the π-system and with this the desired ´push-pull´ characteristics of the dye, the idea was to synthesize an ancillary ligand with an amino group in the 4,4´-position of the phenyl spacer which can undergo a Schiff-base reaction to easily tune the ancillary ligand.

6.2 Synthetic approach

The preparation of the ancillary ligands (**12**-**14**) used the Kröhnke[84] strategy. The synthesis of 4,4´-di(4-aminophenyl)-6,6´-dimethyl-2,2´-bipyridine (**13**), the ancillary ligand to undergo a Schiff-base reaction, was done by a deprotection reaction of **12** using 6 M HCl. Scheme 46 displays the general synthetic route for the ancillary ligands. The general synthetic route to the Schiff-base ancillary ligands is shown in Scheme 47.[97] The synthesis of the ((6,6´-dimethyl-[2,2´-bipyridine]-4,4´-diyl)bis(4,1-phenylene))bis(phosphonic acid) (**ALP1**)[75] used as anchoring ligand in this chapter was presented in the experimental section of Chapter 3.

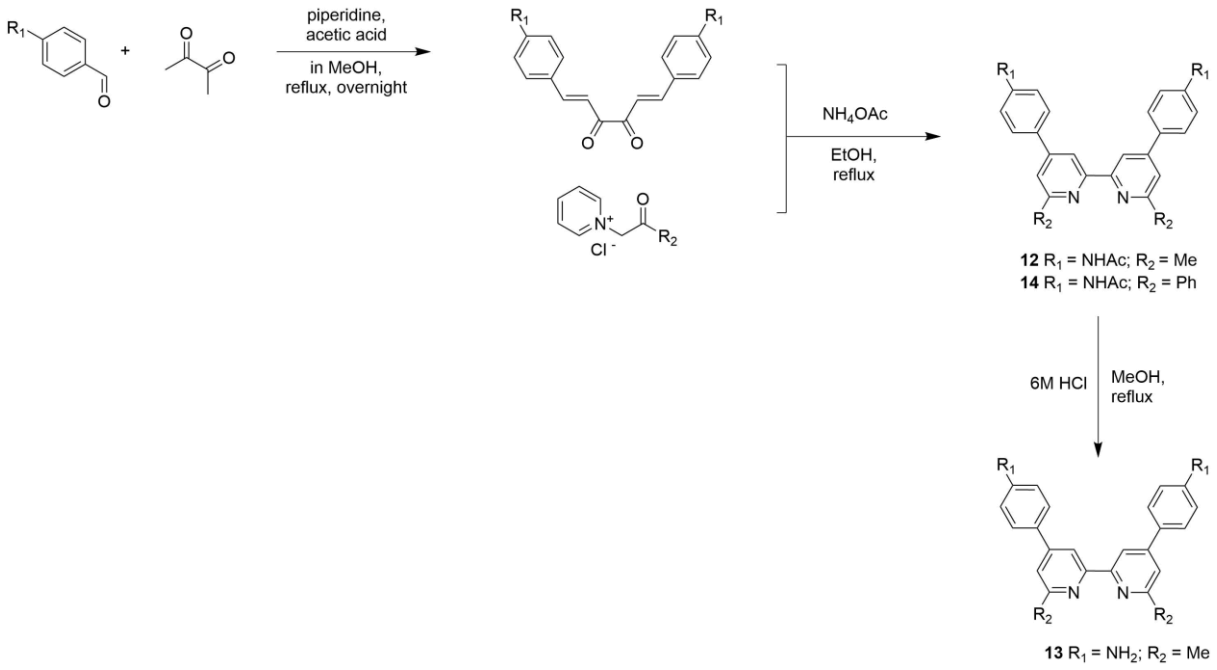

Scheme 46: Synthesis of the ancillary ligands (12-14).

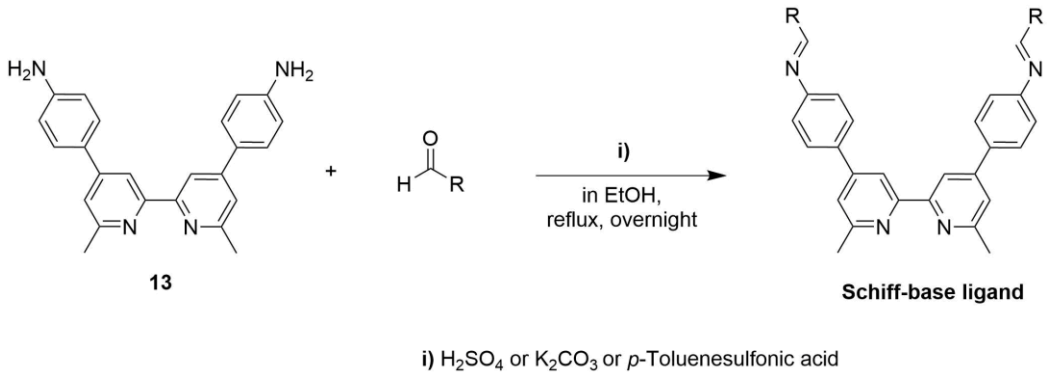

Scheme 47: General synthetic route of the Schiff-base ligands.

Unfortunately the reaction of 4,4´-di(4-aminophenyl)-6,6´-dimethyl-2,2´-bipyridine (**13**) with an aldehyde to the corresponding Schiff-base ligand was unsuccessful. Therefore only ancillary ligands **12-14** were investigated further.

The corresponding homoleptic copper(I) complexes (Scheme 48) were prepared using a standard method by combining $[Cu(MeCN)_4][PF_6]$[87] with two equivalents of the ligands **12-14** and were isolated as dark red solids for $[Cu(\mathbf{12})_2][PF_6]$ and $[Cu(\mathbf{13})_2][PF_6]$ with 64.2% and 74.7% yield, respectively, and as a black-grey solid for $[Cu(\mathbf{14})_2][PF_6]$. In the MALDI-TOF mass spectrum, the highest mass peak for $[Cu(\mathbf{12})_2][PF_6]$ corresponded to the $[M - PF_6]^{5+}$($[Cu(\mathbf{12})_2 + 4H]^{5+}$) ion and showed a characteristic isotope pattern matching the simulated pattern. For $[Cu(\mathbf{13})_2][PF_6]$ the highest mass peak in the electrospray mass spectrum corresponded to the $[M - PF_6]^+$ ion and showed a characteristic isotope pattern matching the simulated pattern. Unfortunately for $[Cu(\mathbf{14})_2][PF_6]$, the

mass spectrum did not exhibit a peak envelope corresponding to the parent mass. The ^{1}H and ^{13}C NMR spectra of the complexes were recorded in CD_3CN, CD_2Cl_2 or $(CD_3)_2CO$ and assigned using 2D methods.

In Figure 50 the solution absorption spectra of the complexes are shown. Unfortunately it was not possible to measure a solution absorption spectra of [Cu(**14**)$_2$][PF_6] as the complex dissociated in solution (Figure 51 b)). From the ^{1}H NMR spectrum in Figure 51 it can be seen that ancillary ligand **14** (Figure 51 a)) was pure but the corresponding homoleptic copper(I) complex could not be characterized by NMR spectroscopy as several species were formed in solution (Figure 51 b)). Furthermore the solubility was very poor making spectral assignment by 2D techniques and identification of the different species difficult. It may be proposed that the solution contains a mixture of homoleptic [Cu(**14**)$_2$][PF_6], heteroleptic [Cu(**14**)(MeCN)$_2$][PF_6] (acetonitrile ligands come from the [Cu(MeCN)$_4$][PF_6] used for the complexation reaction) and [Cu(**14**)(Me_2CO)$_2$][PF_6] from the acetone used as solvent to prepare the solution.[75] Nonetheless, this mixture was used for DSC dye assembly as discussed later. The absorption maxima for [Cu(**12**)$_2$][PF_6] and [Cu(**13**)$_2$][PF_6] are given in Table 14 and were established by recording the spectra at different concentrations. The solution absorption spectra are dominated by high-energy $\pi^*\leftarrow\pi$ and $\pi^*\leftarrow n$ transitions. The broad MLCT bands for the copper(I) complexes [Cu(**12**)$_2$][PF_6] and [Cu(**13**)$_2$][PF_6] arise at λ_{max} = 485 and 483 nm, respectively (Table 14). The $\pi^*\leftarrow\pi$ and $\pi^*\leftarrow n$ transitions of [Cu(**12**)$_2$][PF_6] resulted in higher extinction coefficient values (90 521 dm^3 mol^{-1} cm^{-1}) (Table 14) compared to the ones of [Cu(**13**)$_2$][PF_6] (75 495 dm^3 mol^{-1} cm^{-1}) (Table 14) which could be in accordance with a stronger lone pair character of ancillary ligand **12**.

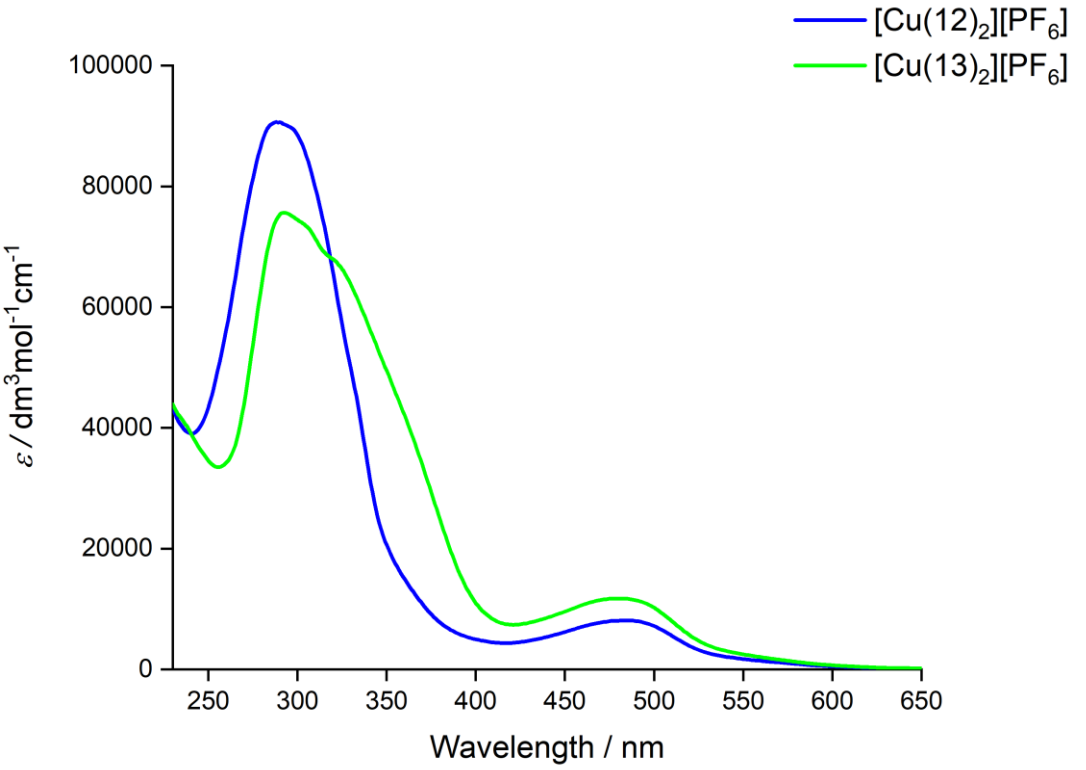

Figure 50: Solution (MeCN) absorption spectra of complexes $[Cu(12)_2][PF_6]$ and $[Cu(13)_2][PF_6]$ (1×10^{-5} mol dm^{-3}).

Table 14: Absorption maxima for $[Cu(12)_2][PF_6]$ and $[Cu(13)_2][PF_6]$ (MeCN, 1×10^{-5} mol dm^{-3}; sh = shoulder; ε values are rounded to the nearest 100 dm^{-3} mol^{-1} cm^{-1}).

	λ_{max}/nm (ε_{max}/dm^3 mol^{-1} cm^{-1})	
Complex	π*←π and π*←*n*	MLCT
$[Cu(\mathbf{12})_2][PF_6]$	288 (90 521), 299 sh (88 710), 334 sh (42 954)	485 (8178)
$[Cu(\mathbf{13})_2][PF_6]$	293 (75 495), 306 sh (73 260), 322 sh (67 544), 367 sh (36 644)	483 (11 828)

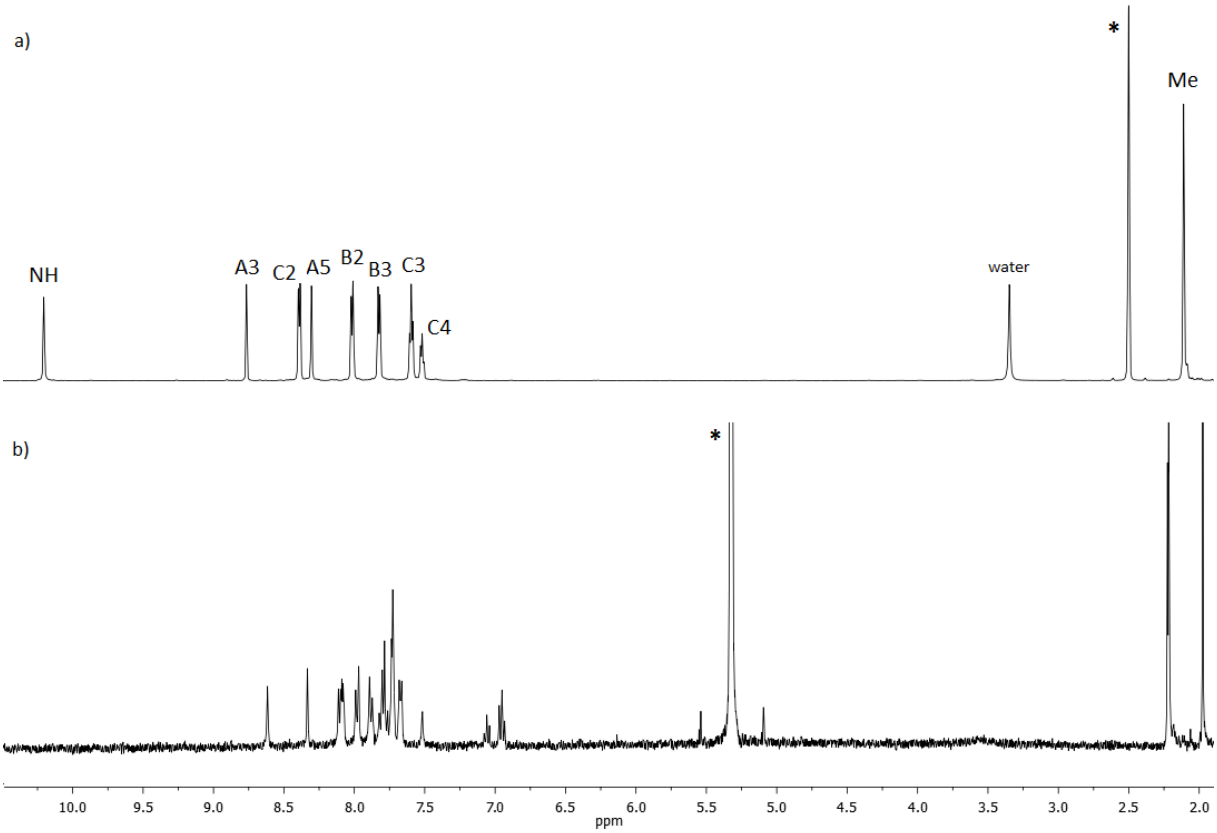

Figure 51: a) 600 MHz NMR spectrum of ancillary ligand 14 in $(CD_3)_2CO$ and b) 400 MHz NMR spectrum of $[Cu(14)_2][PF_6]$ in CD_2Cl_2 showing more than one species (* = residual solvent).

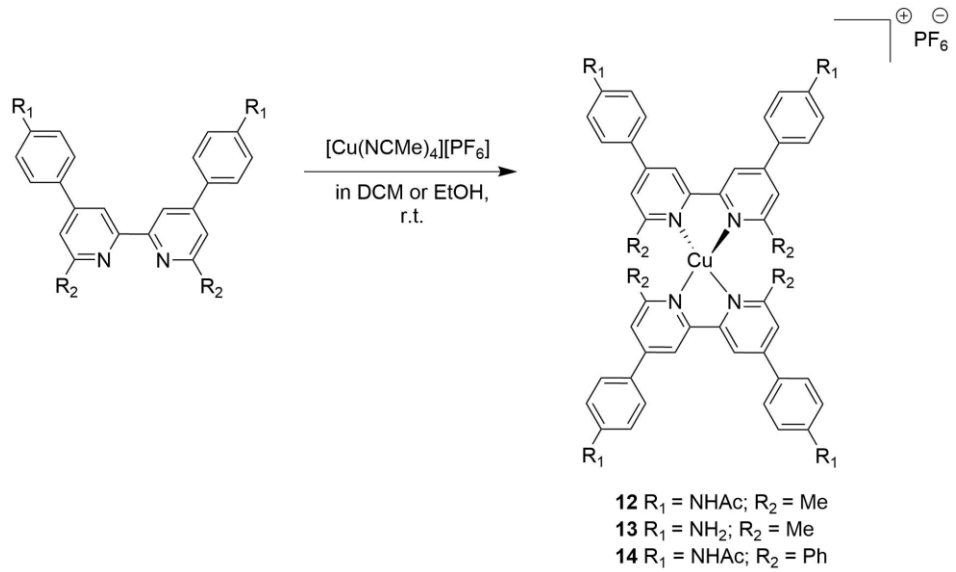

Scheme 48: General synthetic route for the homoleptic Cu(I) complexes.

The detailed synthetic route to the ancillary ligands **12-14** shown in Scheme 46 and the corresponding copper(I) complexes (Scheme 48), as well as the analytical data are given in the experimental section of this chapter.

In order to functionalize the TiO_2 surface of the electrodes with the heteroleptic dyes $[Cu(L_{anchor})(L_{ancillary})]^+$ the ´surface-as-ligand, surface-as-complex´[47] (SALSAC) strategy (Figure 37) was used. **ALP1**[46] (**1**) (Scheme 2) was used in combination with the ancillary ligands **12-14** to assemble the heteroleptic dyes adsorbed on the TiO_2 surface. As the solution absorption spectra measurements indicated that complex $[Cu(\mathbf{14})_2)][PF_6]$ dissociated in solution, a second dipping strategy was used to obtain the heteroleptic dye $[Cu(\mathbf{1})(\mathbf{14})]^+$ adsorbed on the TiO_2 surface. For this dipping strategy a solution of the ancillary ligand **14** was used. Furthermore this adapted dipping strategy was used to investigate if there is a difference in the amount of the absorbed dye depending on the purity of the homoleptic dye. This modified ´surface-as-ligand; surface-as-complex´ strategy is explained in detail in the next section (6.3.1) and is named ´stepwise assembly´ (SW). DSCs containing the dyes $[Cu(\mathbf{1})(L_{ancillary})]^+$ ($L_{ancillary}$ = **12-14**) were compared to a N719 reference cell.

6.3 Results

6.3.1 Solid state absorption spectra

For the solid-state absorption measurements, the copper(I) dyes were assembled with the ´surface-as-ligand; surface-as-complex´[47] strategy on transparent TiO_2 electrodes to give $[Cu(\mathbf{1})(\mathbf{12})]^+$, $[Cu(\mathbf{1})(\mathbf{13})]^+$ and $[Cu(\mathbf{1})(\mathbf{14})]^+$ adsorbed on the electrode surfaces. The commercial TiO_2 electrodes were washed with milliQ water and HPLC grade EtOH, dried in a stream of nitrogen and heated at 450 °C for 30 min. After cooling, the electrodes were soaked in a 1.0 mM DMSO solution of anchoring ligand **1** for 24 h, washed with DMSO and EtOH and dried. The anchoring-ligand functionalized electrodes were then immersed into 0.1 mM MeCN solutions of the homoleptic copper(I) complexes $[Cu(\mathbf{12})_2][PF_6]$ or $[Cu(\mathbf{13})_2][PF_6]$, respectively or a 0.1 mM acetone solution of $[Cu(\mathbf{14})][PF_6]$ for 3 days. As mentioned above, the solution of the homoleptic copper(I) complex with ancillary ligand **14** appear to exist as mixture.[75] After soaking in the dye bath solutions, the electrodes were taken out, washed with MeCN and dried in a stream of nitrogen. The second dipping strategy used for ancillary ligand **14** to assemble the heteroleptic copper(I) dye $[Cu(\mathbf{1})(\mathbf{14})]^+$ adsorbed on the electrodes surface, was the `stepwise assembly´[65]. For this procedure the cleaning and anchoring ligand functionalization of the TiO_2 electrode was the same as described above. The anchoring ligand functionalized electrode was then immersed in a 2.0 mM MeCN solution of $[Cu(MeCN)_4][PF_6]$ for 24 h, washed with MeCN, dried and immersed into a 1.0 mM DMSO solution of ancillary ligand **14**. After 3 days in the ligand solution, the electrode was taken out, washed with DMSO and EtOH and dried in a stream of nitrogen to yield $[Cu(\mathbf{1})(\mathbf{14})]^+$ adsorbed on the electrodes surface (Figure 52).

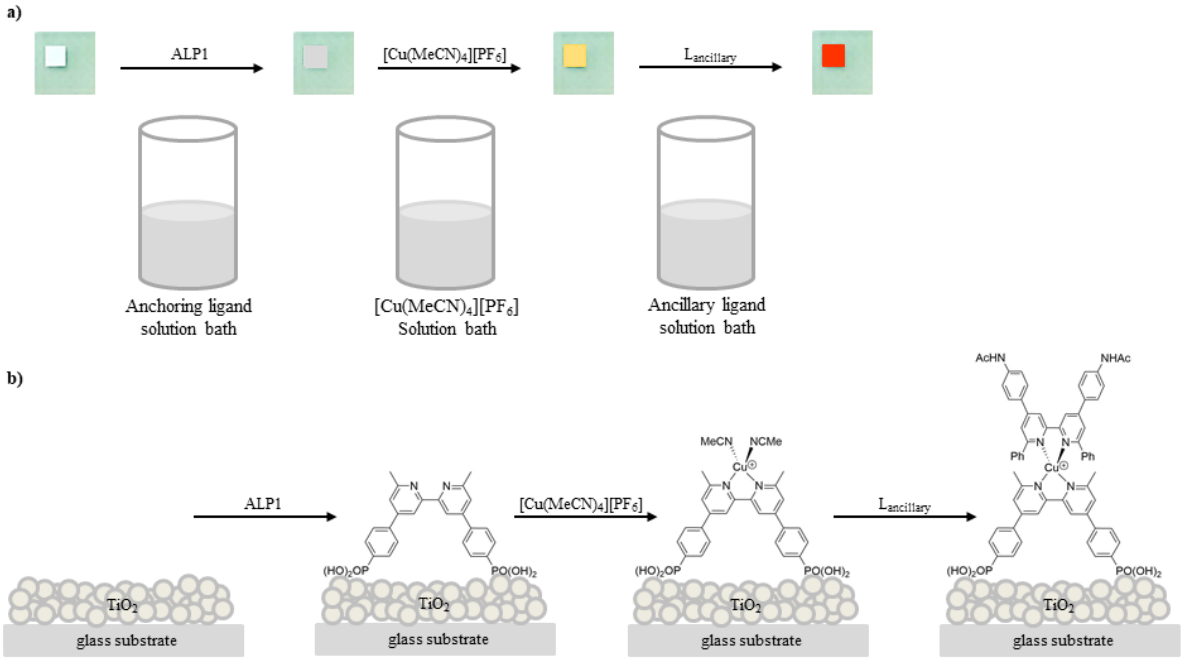

Figure 52: a) The ´stepwise assembly´ approach to functionalize an FTO/TiO_2 electrode with a heteroleptic $[Cu(L_{anchor})(L_{ancillary})]^+$ dye. b) ´Stepwise assembly´ on the TiO_2 surface with ALP1 anchored on the surface (second from left), proposed intermediate $[Cu(ALP1)(MeCN)_2]^+$ complex adsorbed on the surface (third from left) and surface-anchored $[Cu(1)(14)]^+$ (right).

Figure 53 shows the background corrected and normalized solid-state absorption spectra of the electrodes functionalized with the heteroleptic copper(I) complexes.

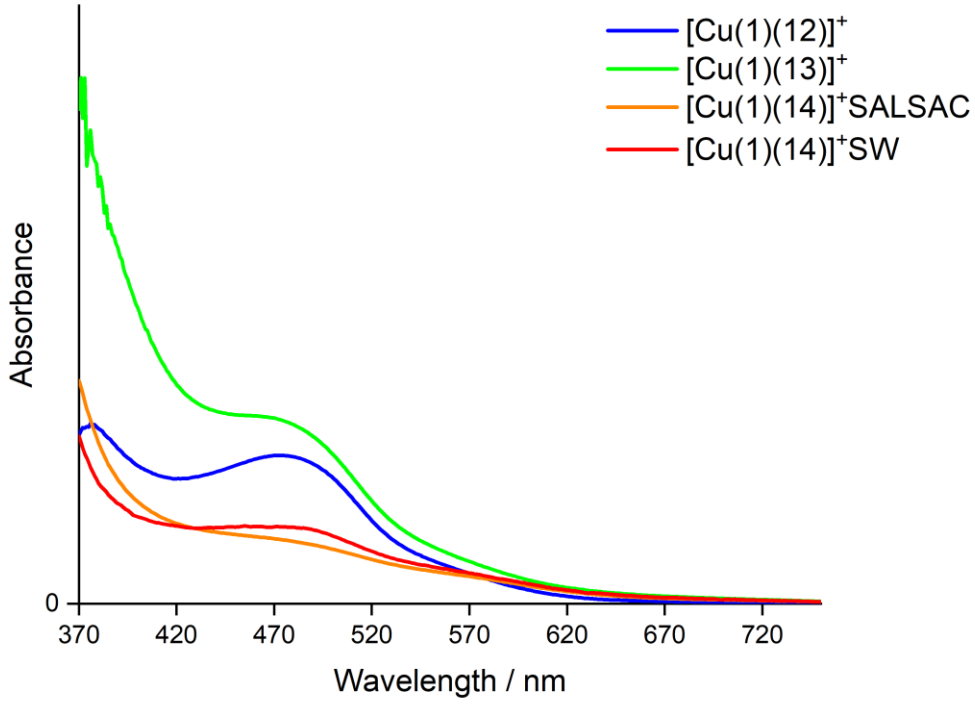

Figure 53: Solid-state absorption spectra of transparent TiO_2 functionalized with $[Cu(1)(L_{ancillar})]^+$ ($L_{ancillar}$y = 12-14) (SW = ´stepwise´ strategy).

The MLCT absorption maxima of the transparent TiO_2 electrodes functionalized with $[Cu(\mathbf{1})(L_{ancillary})]^+$ ($L_{ancillary}$ = **12-14**) appeared at λ_{max} = 470-488 nm (Figure 53). The complex with ancillary ligand **12** substituted with acetamido groups in the 4-positions of the phenyl spacer showed a second absorption maxima at λ_{max} 377 nm (Figure 53 blue curve), which presumably arises from $\pi^*\leftarrow n$ transitions involving the lone pair of the acetyl substituents in ancillary ligand **12**. The highest absorption in the solid-state absorption spectra was measured for ancillary ligand **13** (Figure 53 green curve), this is in accordance with the solution absorption spectra of the homoleptic copper(I) complexes with ancillary ligands **12** and **13** (Figure 50), where $[Cu(\mathbf{13})_2][PF_6]$ also yielded the highest absorption. Furthermore the electrode functionalized with dye $[Cu(\mathbf{1})(\mathbf{13})]^+$ adsorbed on the TiO_2 surface yielded a higher absorption at lower wavelengths (370-425 nm) (Figure 53 green curve) compared to dyes $[Cu(\mathbf{1})(\mathbf{12})]^+$ and $[Cu(\mathbf{1})(\mathbf{14})]^+$. Comparing the solid-state absorption spectra of the different dipping procedures for dye $[Cu(\mathbf{1})(\mathbf{14})]^+$ (Figure 53 orange and red curve) it can be seen that the ´stepwise` approach yielded a slightly higher absorption in the MLCT than the SALSAC strategy. This finding can be explained due to the possible mixture of heteroleptic copper(I) complexes adsorbed on the surface in the SALSAC approach, as the dipping solution is presumed to contain a mixture of $[Cu(\mathbf{14})_2][PF_6]$, $[Cu(\mathbf{14})(MeCN)_2][PF_6]$ from $[Cu(MeCN)_4][PF_6]$ and $[Cu(\mathbf{14})(Me_2CO)][PF_6]$.[75] Nevertheless the MLCT band in the solid-state absorption spectra for $[Cu(\mathbf{1})(\mathbf{14})]^+$ SALSAC (Figure 53 orange curve) confirmed that the desired heteroleptic copper(I) complex was formed on the surface. Although the ^1H NMR spectrum of $[Cu(\mathbf{14})_2][PF_6]$ exhibited that the complex dissociated in solution (Figure 51 b)) the similarity in the solid-state absorption spectra of $[Cu(\mathbf{1})(\mathbf{14})]^+$ SALSAC and $[Cu(\mathbf{1})(\mathbf{14})]^+$ SW (Figure 53 orange and red curves) verified the existence of the heteroleptic copper(I) complex adsorbed on the TiO_2 surfaces. Furthermore the electrodes containing $[Cu(\mathbf{1})(\mathbf{14})]^+$ showed the lowest absorption of the three dyes. This is in accordance with previous findings (Chapter 4) that the bulky substituent in the 6,6´-positions of the bpy unit of ancillary ligand **14** might lead to the problem of steric hindrance between the anchoring and ancillary ligand.[75,83]

Figure 54 shows the comparison of the solid-state absorption spectra of electrodes functionalized with $[Cu(\mathbf{1})(\mathbf{12})]^+$, $[Cu(\mathbf{1})(\mathbf{13})]^+$, $[Cu(\mathbf{1})(\mathbf{14})]^+$ or N719. The lower intensity of the MLCT bands for the copper(I) dyes compared to the N719 dye (Figure 54) verifies an overall lower spectral response. Nevertheless the electrode functionalized with dye $[Cu(\mathbf{1})(\mathbf{13})]^+$ yielded a promising result for the solid-state absorption spectra as it showed comparable high absorption values in the range from 370-425 nm to N719 (Figure 54 black and green curves).

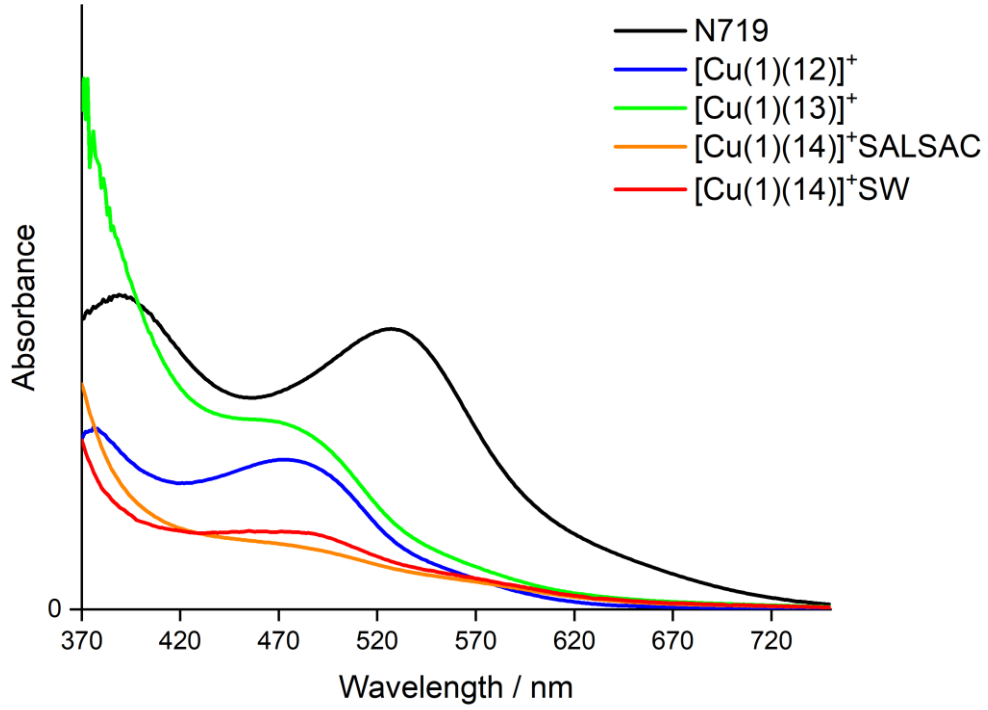

Figure 54: Solid-state absorption spectra of transparent TiO_2 functionalized with $[Cu(1)(L_{ancillary})]^+$ ($L_{ancillary}$ = 12-14) compared to N719.

6.3.2 DSC performances

The heteroleptic copper(I) dyes were adsorbed on the electrode surfaces using the SALSAC[47] or `stepwise`[65] strategy as mentioned in the last section for the solid-state absorption measurements to prepare the dye-functionalized working electrodes for the DSCs. The TiO_2 electrodes used for building the solar cells had an additional scattering layer. Each functionalized electrode was assembled with a commercial Pt counter-electrode using a thermoplast hot-melt sealing foil. The electrolyte between the electrodes was introduced by vacuum back-filling before the DSCs were sealed. Duplicate DSCs were prepared for each dye to confirm reproducibility of the performance parameters.

6.3.2.1 Solar cell measurements

The solar simulator measurements of the DSCs were performed in a fully-masked mode with an average area size of 0.06012 cm^2 (with a standard deviation of 1%) in order to prevent false influence from scattered light.[79,80] All DSCs with dyes $[Cu(\mathbf{1})(L_{ancillary})]^+$ with $L_{ancillary}$ = **12-14** were measured on the day of assembling (day 0), day 1 and day 4. A DSC containing dye N719 was prepared and measured as reference. The relative efficiencies of the DSCs with respect to N719 set to 100%[72] were calculated in order to have a better comparison of the different dye combinations (Table 15, Table 16 and Table 17). The highest short circuit current densities (J_{SC}) were achieved for ancillary ligand **14** using the ´SALSAC´ strategy yielding 5.04 and 5.14 mA/cm^2 for duplicate cells, followed by ancillary

ligand **12** and **13** with 4.41 and 4.32 mA/cm^2 respectively (Figure 55, Figure 56 and Table 15). The DSCs containing ancillary ligand **14** using the ´stepwise´ approach yielded the lowest value for J_{SC} with 4.23 mA/cm^2 (Figure 55, Figure 56 and Table 15). In terms of the open circuit voltages (V_{OC}) DSCs containing ancillary ligands **13** and **14** (´SALSAC´) yielded the highest values with 595 and 592 mV. Changing the dipping strategy for ancillary ligand **14** to the ´stepwise´ approach resulted in a decrease for both, the J_{SC} and V_{OC} (Figure 56 and Table 15) for these DSCs. The lowest values for the open circuit voltage was achieved for DSCs containing ancillary ligand **12**, substituted with acetamido groups in the 4,4´-positions of the phenyl spacer. Changing from the acetamido to the amine substituents in the 4,4´-positions of the phenyl spacer, on going from ancillary ligand **12** to **13** resulted in an increase in J_{SC} and V_{OC} and the overall DSC performances. The higher values for DSCs with dye [Cu(**1**)(**13**)]$^+$ can be explained due to the +M effect of the amine[98] groups in the 4,4´- positions pushing the electrons towards the metal centre, enhancing the desired ´push-pull´ characteristics of the dye. In contrast the acetamido groups have an inductive effect pulling the electrons away from the metal centre in dye [Cu(**1**)(**12**)]$^+$. The highest values in both the J_{SC} and the V_{OC} for ancillary ligand **14** can be rationalized by an increase in the π- system ongoing from methyl- to phenyl-substituents in the 6,6´-positions of the bpy unit. Enhancing the π- system on going from ancillary ligand **12** to **14** seemed to compensate for –I effect of the substituents in the 4,4´- positions. Although the dye solution containing [Cu(**14**)$_2$][PF_6] did not consist of pure homoleptic copper(I) complex, the overall conversion efficiency of the DSCs functionalized with this mixture yielded the highest efficiency of 2.24% (Table 15). Changing the dipping procedure of [Cu(**1**)(**14**)]$^+$ resulted in an decrease of the cell performance, yielding an efficiency of 1.78% (Table 15). On varying the ancillary ligand, going from amide to amine[98] substituents for ligand **12** and **13** a better performance could be measured with [Cu(**1**)(**13**)]$^+$ yielding an efficiency of 1.81% (Table 15). The lowest power conversion efficiency was measured with dye [Cu(**1**)(**12**)]$^+$ yielding 1.77% (Table 15). The fill factors (ff) for all the cells were in a good range of 69- 73%. The *J-V* curves for the DSCs with [Cu(**1**)($L_{ancillary}$)]$^+$ ($L_{ancillary}$ = **12-14**) are shown in Figure 55 and Figure 56. The duplicate DSCs in Table 15 confirmed the reproducibility of both the construction and the measurement of the cells. Measurements over time showed a slight decrease on day 1 which stabilized until day 4 (Table 15 and Table 17). Unfortunately two DSCs did not work well over time because of the formation of crystals within the electrolyte. Figure 55 to Figure 60 show the development of the *J-V* curves over time for the cells.

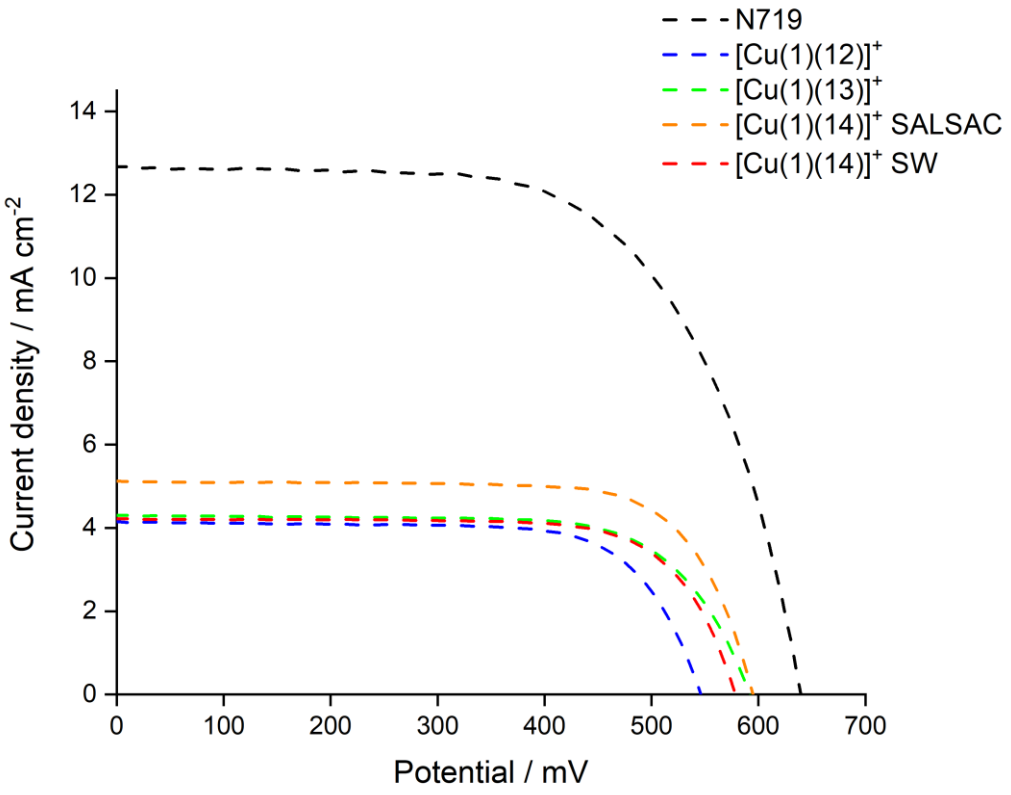

Figure 55: *J-V* curves for DSCs with dyes $[Cu(1)(L_{ancillary})]^+$ ($L_{ancillary}$ = 12-14) and N719 measured on the day of cell assembly.

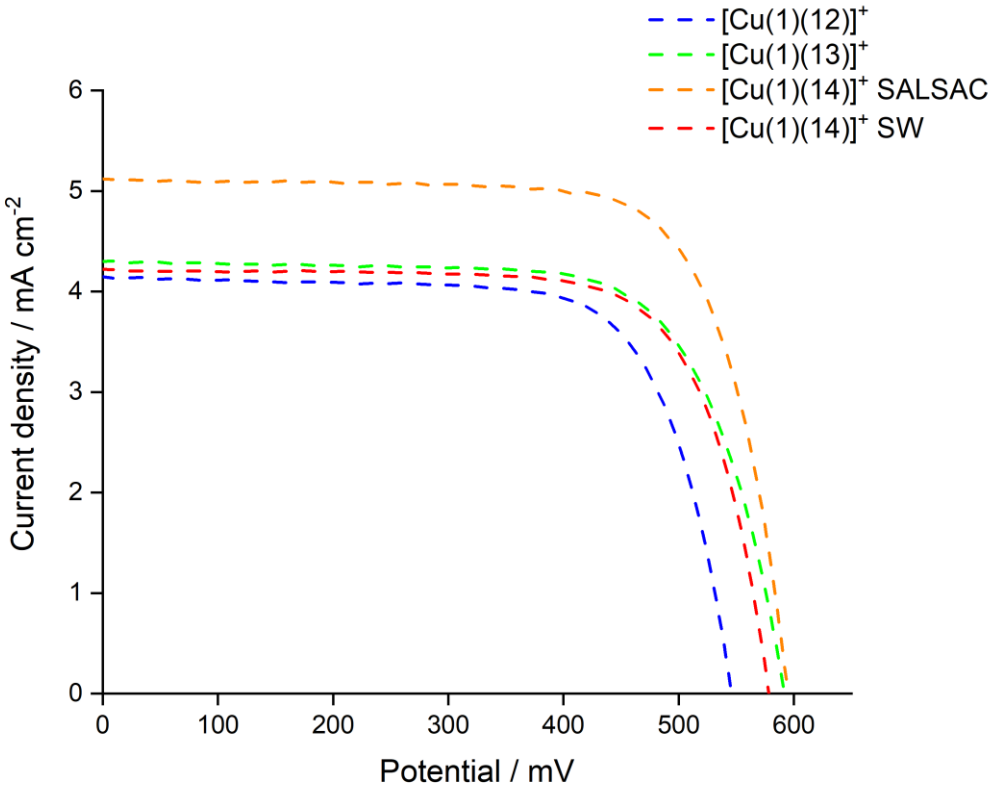

Figure 56: *J-V* curves for DSCs containing dyes $[Cu(1)(L_{ancillary})]^+$ ($L_{ancillary}$ = 12-14) measured on the day of cell assembly (expansion of Figure 55).

Table 15: Performance parameters of duplicate DSCs with $[Cu(1)(L_{ancillary})]^+$ ($L_{ancillary}$ = 12-14) compared to N719 as reference measured on the day of cell assembly.

Dye	J_{sc}/mA cm^{-2}	V_{OC}/mV	ff/%	η/%	Relative η/%
$[Cu(\mathbf{1})(\mathbf{12})]^+$ **SALSAC**	4.16	546	72	1.63	31.8
$[Cu(\mathbf{1})(\mathbf{12})]^+$ **SALSAC**	4.41	565	71	1.77	34.5
$[Cu(\mathbf{1})(\mathbf{13})]^+$ **SALSAC**	4.32	592	71	1.81	35.3
$[Cu(\mathbf{1})(\mathbf{13})]^+$ **SALSAC**	3.89	588	69	1.58	30.8
$[Cu(\mathbf{1})(\mathbf{14})]^+$ **SALSAC**	5.04	588	72	2.13	41.5
$[Cu(\mathbf{1})(\mathbf{14})]^+$ **SALSAC**	5.14	595	73	2.24	43.7
$[Cu(\mathbf{1})(\mathbf{14})]^+$ **SW**	4.23	578	73	1.78	34.7
$[Cu(\mathbf{1})(\mathbf{14})]^+$ **SW**	4.17	581	71	1.73	33.7
N719	12.72	639	63	5.13	100

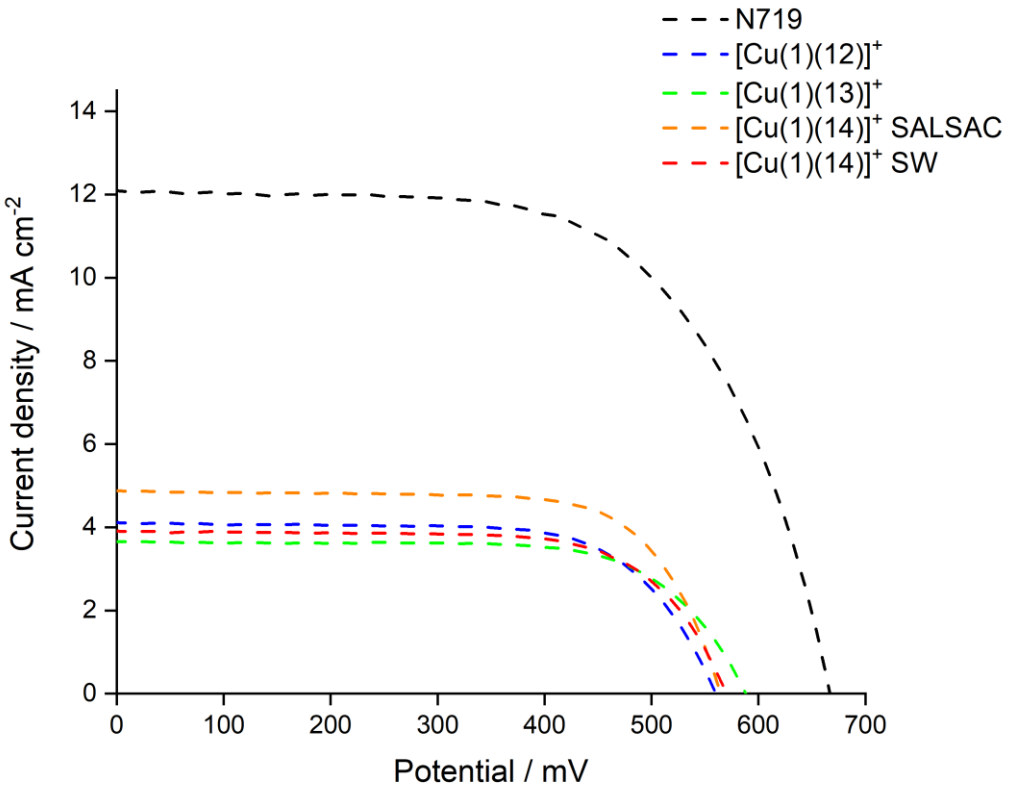

Figure 57: *J-V* curves for DSCs with dyes $[Cu(1)(L_{ancillary})]^+$ ($L_{ancillary}$ = 12-14) and N719 measured on day 1 after cell assembly.

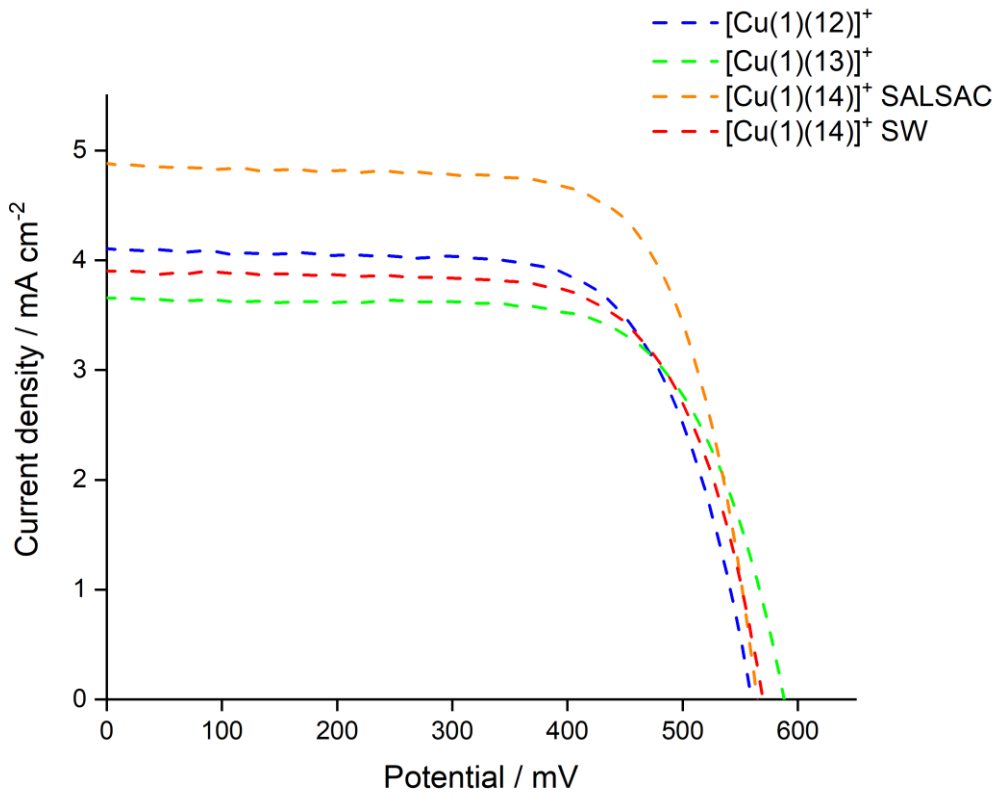

Figure 58: *J-V* curves for DSCs containing dyes [Cu(1)($L_{ancillary}$)]$^+$ ($L_{ancillary}$ = 12-14) measured on day 1 after cell assembly (expansion of Figure 57).

Table 16: Performance parameters of duplicate DSCs with [Cu(1)($L_{ancillary}$)]$^+$ ($L_{ancillary}$ = 12-14) compared to N719 as reference measured on day 1 after cell assembly.

Dye	J_{sc}/mA cm^{-2}	V_{OC}/mV	ff/%	η/%	Relative η/%
[Cu(**1**)(**12**)]$^+$ **SALSAC**	3.95	550	68	1.48	29.4
[Cu(**1**)(**12**)]$^+$ **SALSAC**	4.12	560	69	1.59	31.6
[Cu(**1**)(**13**)]$^+$ **SALSAC**	3.76	588	69	1.50	29.8
[Cu(**1**)(**13**)]$^+$ **SALSAC**	3.42	581	67	1.33	26.4
[Cu(**1**)(**14**)]$^+$ **SALSAC**	4.83	560	70	1.90	37.8
[Cu(**1**)(**14**)]$^+$ **SALSAC**	4.89	565	71	1.97	39.2
[Cu(**1**)(**14**)]$^+$ **SW**	3.78	570	72	1.55	30.8
[Cu(**1**)(**14**)]$^+$ **SW**	3.92	569	69	1.55	30.8
N719	12.49	667	60	5.03	100

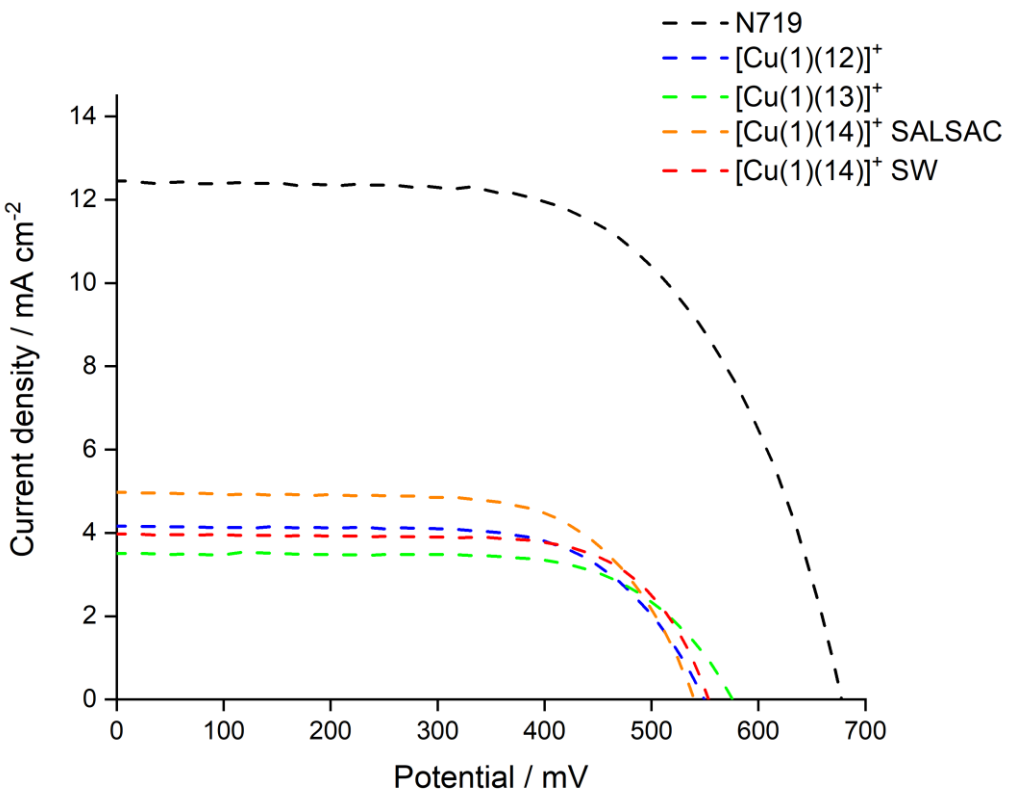

Figure 59: *J-V* curves for DSCs with dyes $[Cu(1)(L_{ancillary})]^+$ ($L_{ancillary}$ = 12-14) and N719 measured on day 4 after cell assembly.

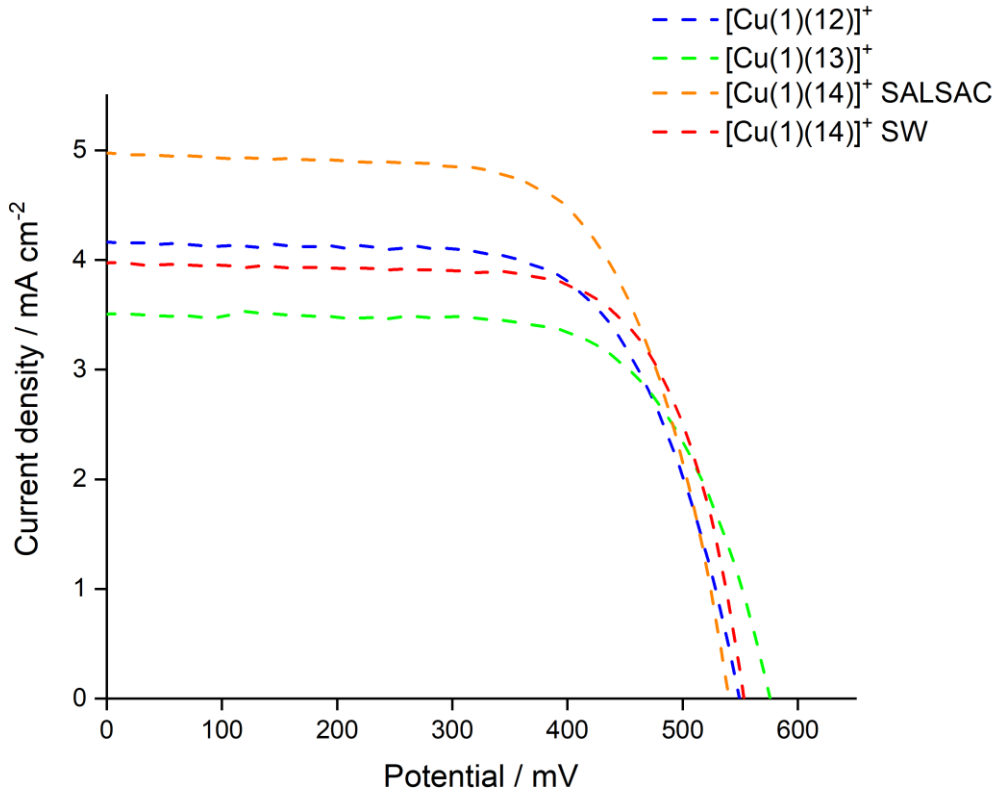

Figure 60: *J-V* curves for DSCs with dyes $[Cu(1)(L_{ancillary})]^+$ ($L_{ancillary}$ = 12-14) measured on day 4 after cell assembly (expansion of Figure 59).

Table 17: Performance parameters for duplicate DSCs with dyes $[Cu(1)(L_{ancillary})]^+$ ($L_{ancillary}$ = 12-14) compared to N719 as reference cell measured on day 4 after cell assembly.

Dye	J_{sc}/mA cm^{-2}	V_{OC}/mV	ff/%	η/%	Relative η/%
[Cu(**1**)(**12**)]$^+$ **SALSAC**	4.06	546	62	1.37	26.3
[Cu(**1**)(**12**)]$^+$ **SALSAC**	4.18	549	66	1.53	29.3
[Cu(**1**)(**13**)]$^+$ **SALSAC**	3.52	576	68	1.73	33.1
[Cu(**1**)(**13**)]$^+$ **SALSAC**	3.29	573	64	1.21	23.2
[Cu(**1**)(**14**)]$^+$ **SALSAC**	4.88	538	67	1.77	33.9
[Cu(**1**)(**14**)]$^+$ **SALSAC**	4.99	540	67	1.79	34.3
[Cu(**1**)(**14**)]$^+$ **SW**	3.99	553	70	1.55	29.7
[Cu(**1**)(**14**)]$^+$ **SW**	4.20	556	64	1.49	28.5
N719	13.03	677	59	5.22	100

6.3.2.2 External Quantum Efficiency (EQE) measurements

Figure 61 compares the EQE curves of $[Cu(\mathbf{1})(L_{ancillary})]^+$ ($L_{ancillary}$ = **12-14**) to that of N719. The curves clearly show the lower photon to current conversion efficiencies of copper(I) based dyes over that of N719. Moreover the curves show the lack of photoconversion efficiency at longer wavelengths for copper(I) based dyes over that of N719 (Figure 61 black curve).

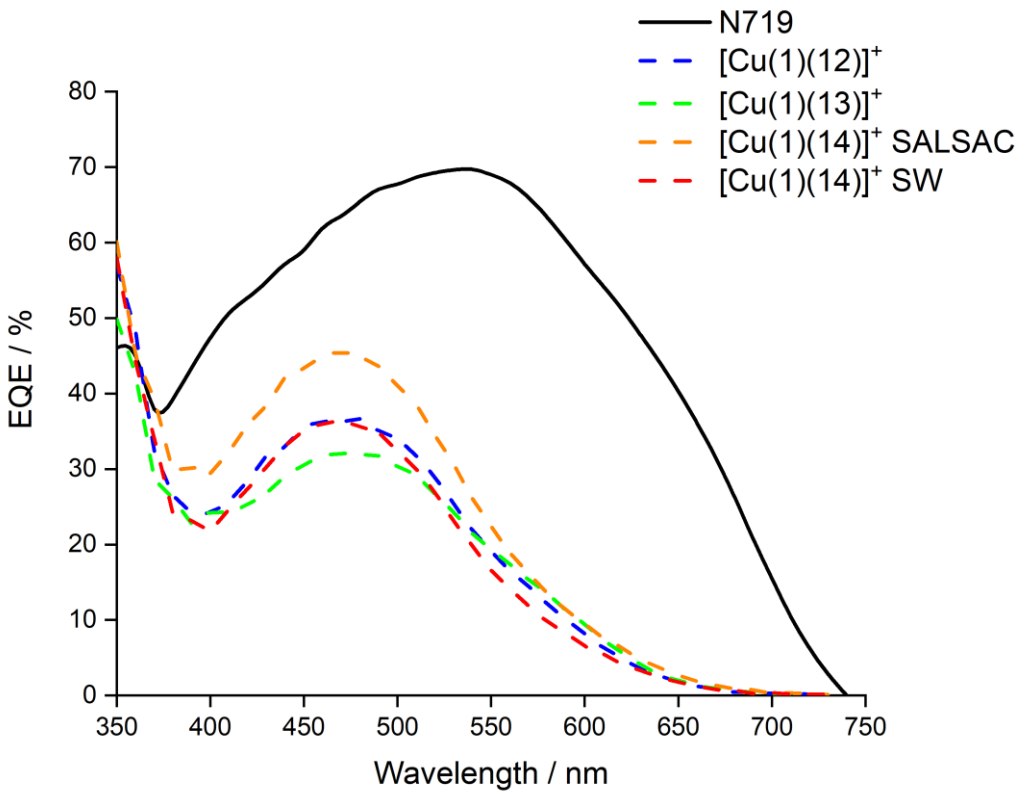

Figure 61: EQE spectra of DSCs containing dyes $[Cu(1)(L_{ancillary})]^+$ ($L_{ancillary}$ = 12-14) and N719.

The EQE spectra shown in Figure 62 reflect the trends of the J_{SC} data from the solar simulator measurements discussed in the last section. Although the EQE curves are lower for DSCs with dye [Cu(**1**)(**13**)]$^+$ a broadened spectral response towards higher wavelengths was found for this dye in both the solid-state absorption spectra (Figure 54) and the EQE spectra (Figure 62) which compensates for the slightly lower EQE_{max} value of DSCs with this dye compared to [Cu(**1**)(**12**)]$^+$ and [Cu(**1**)(**14**)]$^+$. The highest values for the EQE were achieved with dye [Cu(**1**)(**14**)]$^+$ using the ´SALSAC´ strategy, yielding values of 45.0 and 45.6% at λ_{max} 460 and 470 nm respectively (Figure 62 and Table 18) and were consistent with the highest photoconversion efficiencies of the solar simulator measurements. The change in the dipping procedure resulted in a decrease in photoconversion efficiencies for DSCs with [Cu(**1**)(**14**)]$^+$ for the ´stepwise´ approach yielding lower EQE_{max} values of 32.3 and 36.4% (Table 18) which is in accordance with the data from the solar simulator measurements. The EQE_{max} values for DSCs with [Cu(**1**)(**12**)]$^+$ were measured to be at 33.0 and 36.7% (Table 18). The DSCs with [Cu(**1**)(**13**)]$^+$ yielded the lowest EQE_{max} values of 31.1 and 32.2% (Table 18).

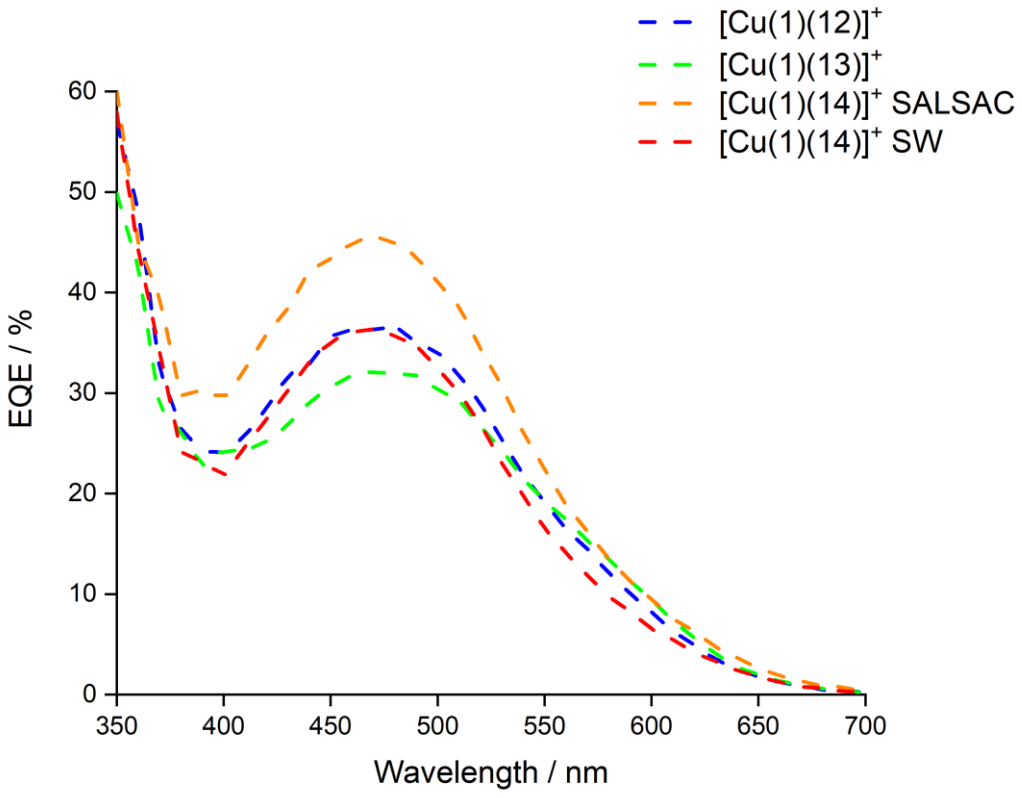

Figure 62: EQE spectra of DSCs containing dyes [Cu(1)($L_{ancillary}$)]$^+$ ($L_{ancillary}$ = 12-14).

Table 18: EQE maxima for duplicate DSCs containing dyes $[Cu(1)(L_{ancillary})]^+$ ($L_{ancillary}$ = 12-14).

Dye	λ_{max} / nm	EQE_{max} / %
$[Cu(\mathbf{1})(\mathbf{12})]^+$ **SALSAC**	450	33.0
$[Cu(\mathbf{1})(\mathbf{12})]^+$ **SALSAC**	450	36.7
$[Cu(\mathbf{1})(\mathbf{13})]^+$ **SALSAC**	470	32.2
$[Cu(\mathbf{1})(\mathbf{13})]^+$ **SALSAC**	470	31.1
$[Cu(\mathbf{1})(\mathbf{14})]^+$ **SALSAC**	460	45.0
$[Cu(\mathbf{1})(\mathbf{14})]^+$ **SALSAC**	470	45.6
$[Cu(\mathbf{1})(\mathbf{14})]^+$ **SW**	460	32.3
$[Cu(\mathbf{1})(\mathbf{14})]^+$ **SW**	470	36.4

6.4 Conclusion

In this chapter three ancillary ligands and the homoleptic copper(I) complexes $[Cu(\mathbf{12})_2][PF_6]$ and $[Cu(\mathbf{13})_2][PF_6]$ were synthesized and characterized. The ´surface-as-ligand, surface-as-complex strategy was used to functionalize the TiO_2 electrodes with the heteroleptic copper(I) dyes using the **ALP1** anchoring ligand (**1**) and the ancillary ligands **12-14**. Furthermore a second dipping strategy, the ´stepwise´ approach was used to functionalize the TiO_2 electrodes with dye $[Cu(\mathbf{1})(\mathbf{14})]^+$ adsorbed on the surface. The ancillary ligands **12** and **13** presented in this chapter had a 6,6´-dimethyl-2,2´-bipyridine unit substituted in the 4,4´-positions with 4-acetamidophenyl- (**12**) or 4-aminophenyl- (**13**) substituents. Ancillary ligand **14** contained a 6,6´-diphenyl-2,2´-bipyridine unit substituted with 4-acetamidophenyl in the 4,4´-positions. DSCs containing dyes $[Cu(\mathbf{1})(L_{ancillary})]^+$ ($L_{ancillary}$ = **12-14**) were assembled and characterized. In order to prove the reproducibility of cell assembling and the measurements duplicate DSCs were built for each dye. The best performance was obtained for $[Cu(\mathbf{1})(\mathbf{14})]^+$, using the ´surface-as-ligand, surface-as-complex´ strategy with a relative efficiency of 43.7% with respect to N719 set at 100%. The DSCs containing dyes $[Cu(\mathbf{1})(\mathbf{12})]^+$ and $[Cu(\mathbf{1})(\mathbf{13})]^+$ yielded relative efficiencies of 34.5 and 35.3%, respectively, compared to N719 set at 100%. The change in the dipping strategy for dye $[Cu(\mathbf{1})(\mathbf{14})]^+$ using the ´stepwise´ approach yielded a relative efficiency of 34.7% with respect to N719 set at 100%; which was lower than for the `SALSAC´ strategy. While the short-circuit current densities for the cells with $[Cu(\mathbf{1})(\mathbf{12})]^+$, $[Cu(\mathbf{1})(\mathbf{13})]^+$ and $[Cu(\mathbf{1})(\mathbf{14})]^+$ (´stepwise´ approach) are in a similar range J_{SC} ~ 3.89-4.41 mA/cm^2; DSCs containing $[Cu(\mathbf{1})(\mathbf{14})]^+$ using the ´SALSAC´ strategy exceeded the values for J_{SC}, yielding 5.04 and 5.14 mA/cm^2, respectively. While the open-circuit voltages for $[Cu(\mathbf{1})(\mathbf{13})]^+$ and $[Cu(\mathbf{1})(\mathbf{14})]^+$ (`SALSAC´ strategy) are similar yielding values for V_{OC} of 588-595 mV, the DSCs with dye for $[Cu(\mathbf{1})(\mathbf{12})]^+$ resulted in the lowest values for V_{OC} of 546 and 565 mV. The lower values for DSCs with for $[Cu(\mathbf{1})(\mathbf{12})]^+$ are in accordance with previous findings that the –I effect of the acetamido substituents

in the 4,4´-positions have a negative influence on the overall cell performances. Although dye [Cu(**1**)(**14**)]$^+$ should also suffer from the negative influence of the –I effect of the substituents in the 4,4´-positions it seemed that introducing a bigger π-system, the phenylgroups in the 6,6´-positions of the bpy unit overcomes this influence. The electron releasing[91] amine groups for ancillary ligand **13** seemed to be beneficial in terms of the desired ´push-pull´ system for n-type dyes, nevertheless DSCs containing [Cu(**1**)(**13**)]$^+$ are still exceeded by DSCs with dye [Cu(**1**)(**14**)]$^+$. Similar trends are found in the EQE spectra for the dyes. Although the EQE_{max} values for DSCs with [Cu(**1**)(**13**)]$^+$ than those of [Cu(**1**)(**12**)]$^+$, cells containing [Cu(**1**)(**13**)]$^+$ were predominant in their spectral response at higher energies.

To conclude this chapter, it can be seen that electron releasing groups in the ancillary ligand can enhance the photon to power conversion efficiency of DSCs which confirms the findings in the previous chapter. Nevertheless an increased π-system seems to compensate for the negative influence of the –I effect of the electron withdrawing substituents in 4,4´-positions of the phenyl spacer. Further investigations should be done combining an increased π-system with electron donating groups as substituents for ancillary ligands. Furthermore it could be interesting to see if the combination of the findings of Chapter 5, the influences of the *para*- and *meta*-substituents[91] and the results presented here could further increase the photoconversion efficiency of copper(I) based DSCs.

6.5 Experimental

The synthesis of the **ALP1** anchoring ligand (**1**) used in this chapter to functionalize the electrode surfaces with the heteroleptic dyes using the ´surface-as-ligand, surface-as-complex´ or ´stepwise assembly´ strategy is shown in the experimental section of Chapter 3.

6.5.1 4,4´-Di(4-acetamidophenyl)-6,6´-dimethyl-2,2´-bipyridine (**12**)

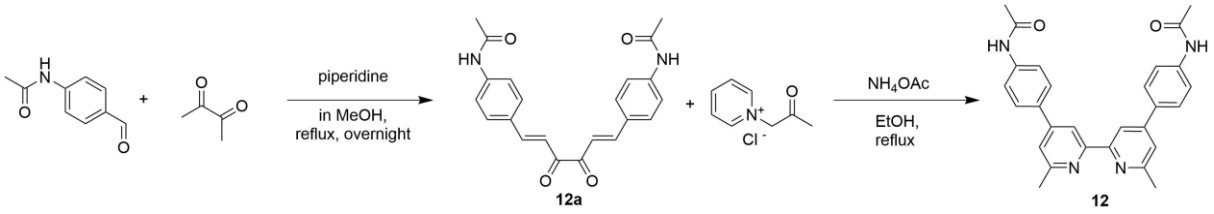

Scheme 49: Synthesis of ancillary ligand 12.

4-Acetamidobenzaldehyde (4.01 g, 24.6 mmol) and piperidine (0.205 mL, 1.08 mmol) were dissolved in 60 mL MeOH. 2,3-Butandione (1.08 mL, 12.3 mmol) were dissolved in 15 mL MeOH and dropwise. The reaction mixture was heated to reflux for 24 h and allowed to cool to room temperature. A precipitate was formed, filtered off and washed with cold MeOH and diethyl ether, and recrystallized from MeOH. Compound **12a** was isolated as dark orange solid (1.15 g, 3.06 mmol, 24.9%). Compound **12a** (1.15 g, 3.06 mmol), 1-(2-oxoppropyl)pyridinium) chloride (2.02 g,

11.8 mmol) and NH_4OAc (1.81 g, 23.5 mmol) were dissolved in 100 mL EtOH and heated to reflux overnight. The solution was cooled to room temperature, a precipitate was formed. The precipitate was filtered off and washed with cold EtOH. The product was recrystallized from MeOH and washed with diethyl ether. Ligand **12** was isolated as beige-yellow solid (619 mg, 1.374 mmol, 46.7%).[84]

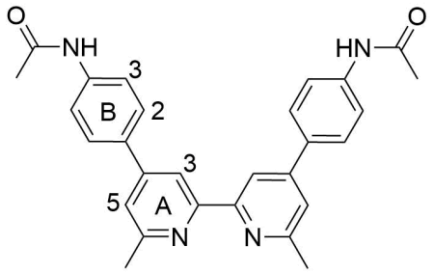

Scheme 50: Structure of ligand 12 with atom labelling for NMR assignments.

^{1}H NMR (600 MHz, DMSO-d_6) δ/ppm 10.17 (s, 2H, H^{NH}), 8.46 (s, 2H, H^{A3}), 7.82 (d, J = 7.8 Hz, 4H, H^{B2}), 7.77 (d, J = 8.0 Hz, 4H, H^{B3}), 7.63 (s, 2H, H^{A5}), 2.64 (s, 6H, H^{Me}), 2.09 (s, 6H, H^{MeAc}).

^{13}C NMR (151 MHz, DMSO-d_6) δ/ppm 168.6 ($C^{C=O}$), 158.3 (C^{A6}), 155.5 (C^{A2}), 148.0 (C^{A4}), 140.4 (C^{B4}), 131.8 (C^{B1}), 127.3 (C^{B2}), 120.4 (C^{A5}), 119.4 (C^{B3}), 114.6 (C^{A3}), 24.4 (C^{Me}), 24.1 (C^{MeAc}).

MALDI-TOF-MS *m/z* 453.7 $[M + 3H]^{3+}$ (calc. 453.23).

6.5.2 4,4´-Di(4-aminophenyl)-6,6´-dimethyl-2,2´-bipyridine (**13**)

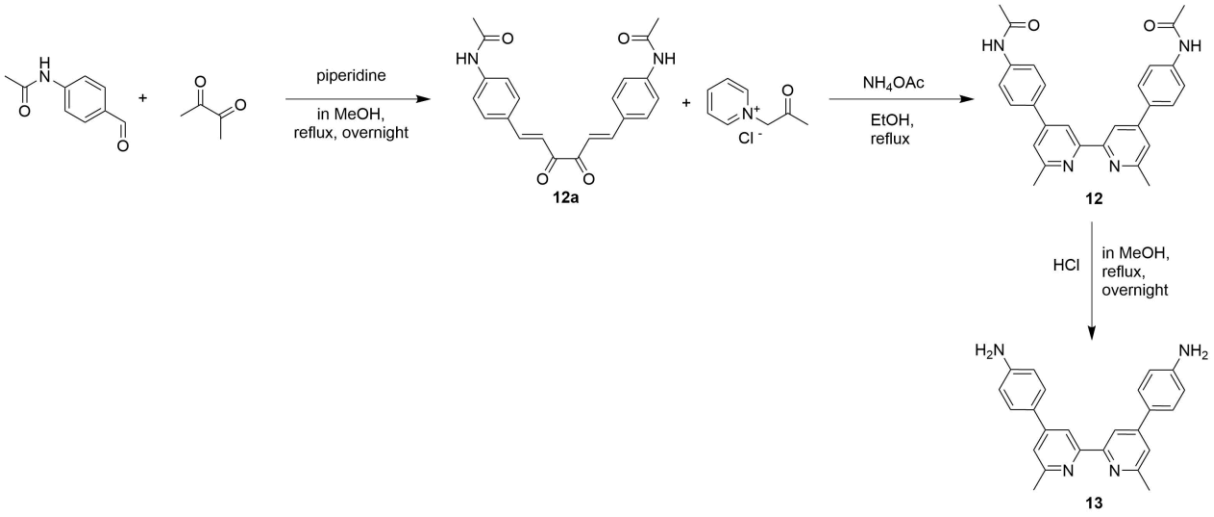

Scheme 51: Synthesis of ancillary ligand 13.

The synthesis for compound **12a** and the ligand **12** was the same as described before. Ligand **12** (259 mg, 0.575 mmol) was dissolved in 30 mL MeOH. 6 M HCl (0.24 mL, 1.44 mmol) was added and the reaction mixture was heated to reflux overnight. After cooling to room temperature the pH was set to basic with aq. NaOH and the resulting mixture was extracted three times with CH_2Cl_2 (~25 mL), dried over $MgSO_4$ and evaporated to dryness. Ligand **13** was isolated as dark orange to reddish brown solid (178 mg, 0.486 mmol, 84.6%).

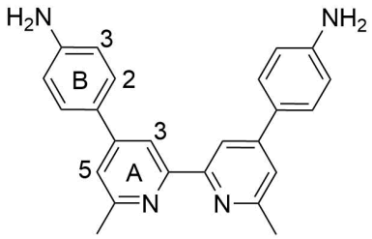

Scheme 52: Structure of ligand 13 with atom labelling for NMR assignments.

^{1}H NMR (600 MHz, DMSO-d_6) δ/ppm 8.37 (s, 2H, H^{A3}), 7.57 (d, J = 7.3 Hz, 4H, H^{B2}), 7.50 (s, 2H, H^{A5}), 6.70 (d, J = 7.3 Hz, 4H, H^{B3}), 5.53 (s, 4H, H^{NH2}), 2.59 (s, 6H, H^{Me}).

^{13}C NMR (151 MHz, DMSO-d_6) δ/ppm 157.8 (C^{A6}), 155.4 (C^{A2}), 150.2 (C^{B4}), 148.5 (C^{A4}), 127.5 (C^{B2}), 123.9 (C^{B1}), 119.0 (C^{A5}), 114.1 (C^{B3}), 113.5 (C^{A3}), 24.4 (C^{Me}).

ESI-MS *m/z* 367.11 $[M + H]^+$ (calc. 366.18).

6.5.3 4,4´-Di(4-acetamidophenyl)-6,6´-diphenyl-2,2´-bipyridine (**14**)

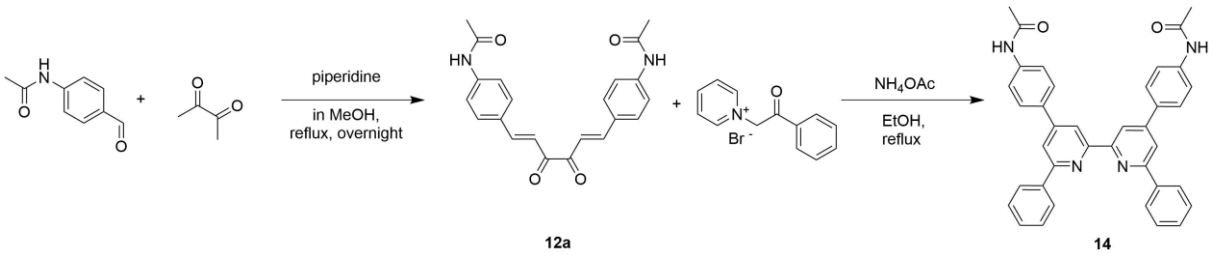

Scheme 53: Synthesis of ancillary ligand 14.

The synthesis for compound **12a** was the same as described before. Compound **12a** (2.07 g, 5.5 mmol), 1-(2-oxopphenyl)pyridinium bromide (5.9 g, 21.2 mmol) and NH_4OAc (3.22 g, 41.8 mmol) were dissolved in 100 mL EtOH and heated to reflux overnight. The solution was cooled to room temperature, a precipitate was formed. The precipitate was filtered off and washed with cold EtOH and diethylether. Ligand **14** was isolated as green-ochre solid (107 mg, 1.86 mg, 35.2%).[84]

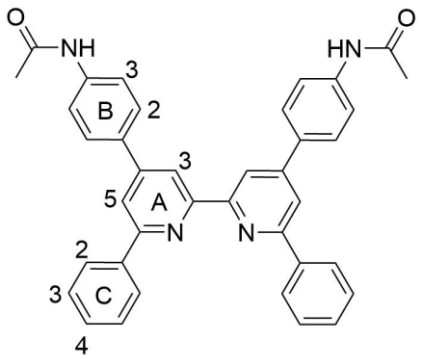

Scheme 54: Structure of ligand 14 with atom labelling for NMR assignments.

^{1}H NMR (600 MHz, DMSO-d_6) δ/ppm 10.20 (s, 2H, H^{NH}), 8.77 (s, 2H, H^{A3}), 8.39 (d, J = 7.2 Hz, 4H, H^{C2}), 8.30 (s, 2H, H^{A5}), 8.02 (d, J = 7.8 Hz, 4H, H^{B2}), 7.82 (d, J = 7.8 Hz, 4H, H^{B3}), 7.60 (t, J = 7.1 Hz, 4H, H^{C3}), 7.52 (t, J = 7.0 Hz, 2H, H^{C4}), 2.11 (s, 6H, H^{Me}).

^{13}C NMR (151 MHz, DMSO-d_6) δ/ppm 168.6 ($C^{C=O}$), 156.6 (C^{A6}), 156.0 (C^{A2}), 149.1 (C^{A4}), 140.6 (C^{B4}), 138.7 (C^{C1}), 131.9 (C^{B1}), 129.3 (C^{C4}), 128.9 (C^{C3}), 127.7 (C^{B2}), 127.1 (C^{C2}), 119.4 (C^{B3}), 117.8 (C^{A5}), 116.4 (C^{A3}), 24.2 (C^{Me}).

6.5.4 [Cu(**12**)$_2$][PF$_6$]

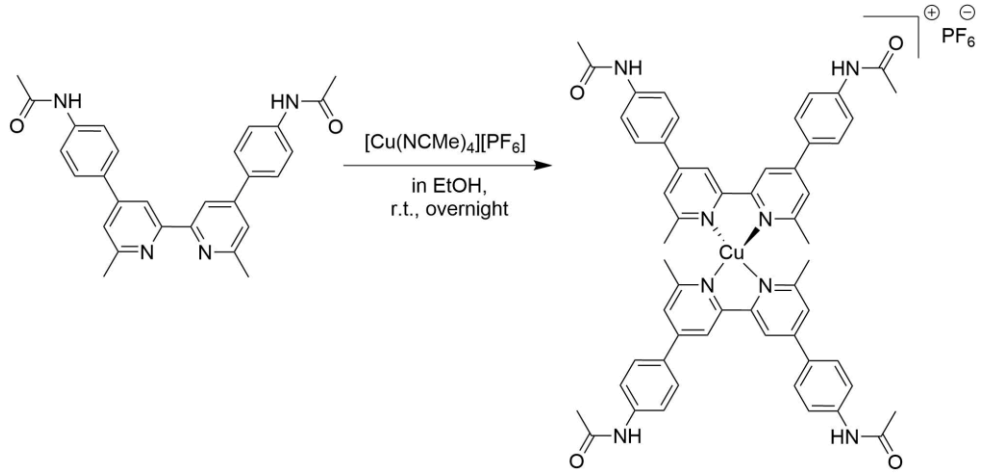

Scheme 55: Synthesis of [Cu(12)$_2$][PF$_6$].

Ligand **12** (45.5 mg, 0.101 mmol) was suspended in 30 mL EtOH and a solution of [Cu(NCMe)$_4$][PF$_6$] (18.8 mg, 0.0505 mmol) in 10 mL EtOH was added. The reaction mixture was stirred overnight at room temperature and 50 mL water was added. The organic solvent was evaporated and the aq. Solution was filtered over celite, washed with water an diethyl ether and redissolved with MeCN to yield [Cu(**12**)$_2$][PF$_6$] as dark red solid (36 mg, 0.032 mmol, 64.2%).

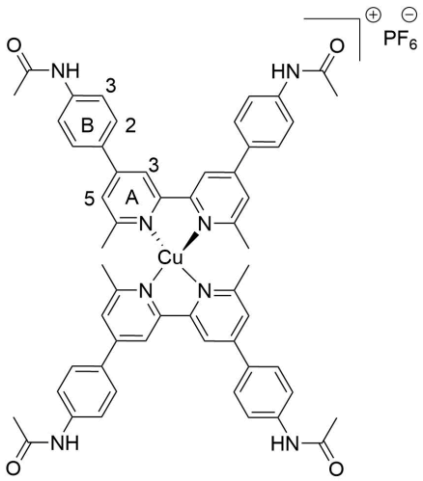

Scheme 56: Structure of [Cu(12)$_2$][PF$_6$] with atom labelling for NMR assignments.

^{1}H NMR (500 MHz, CD_3CN) δ/ppm 8.64 (s, 4H, H^{A3}), 8.54 (s, 4H, H^{NH}), 7.92 (d, *J* = 8.6 Hz, 8H, H^{B2}), 7.79 (s, 4H, H^{A5}), 7.77 (d, *J* = 8.5 Hz, 8H, H^{B3}), 2.14 (s, 12H, H^{Me}), 2.11 (s, 12H, H^{MeAc}).

^{13}C NMR (126 MHz, CD_3CN) δ/ppm 169.6 ($C^{C=O}$), 158.6 (C^{A6}), 153.3 (C^{A2}), 150.5 (C^{A4}), 141.8 (C^{B4}), 132.6 (C^{B1}), 129.0 (C^{B2}), 123.8 (C^{A5}), 120.6 (C^{B3}), 118.1 (C^{A3}), 24.4 ($C^{Me+MeAc}$).

MALDI-TOF-MS *m/z* 967.8 $[M - PF_6 + 4\ H]^{5+}$ (calc. 967.37).

6.5.5 $[Cu(\mathbf{13})_2][PF_6]$

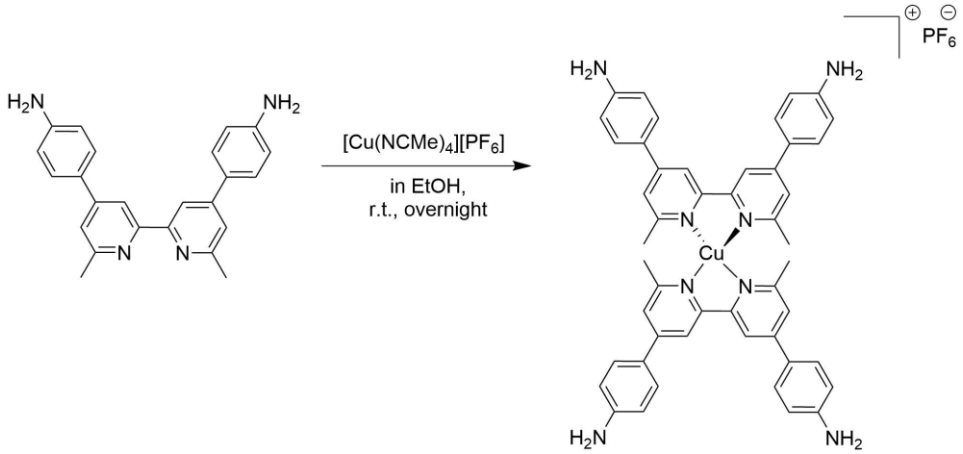

Scheme 57: Synthesis of $[Cu(13)_2][PF_6]$.

Ligand **13** (178 mg, 0.486 mmol) was suspended in 40 mL EtOH and a solution of $[Cu(NCMe)_4][PF_6]$ (90.6 mg, 0.243 mmol) in 10 mL EtOH was added. The reaction mixture was stirred overnight at room temperature and 50 mL water was added. The organic solvent was evaporated and the aq. solution was filtered over celite, washed with water an diethyl ether and redissolved with MeCN to yield $[Cu(\mathbf{13})_2][PF_6]$ as dark red solid (171 mg, 0.182 mmol, 74.7%).

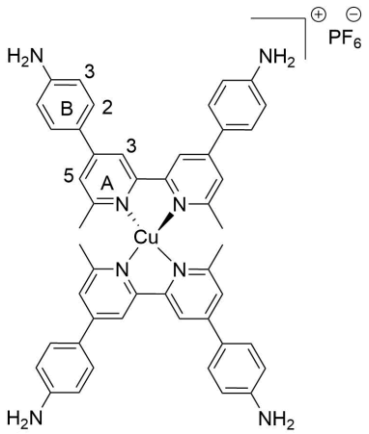

Scheme 58: Structure of $[Cu(13)_2][PF_6]$ with atom labelling for NMR assignments.

^{1}H NMR (600 MHz, CD_2Cl_2) δ/ppm 8.34 (s, 4H, H^{A3}), 7.67 (d, *J* = 7.5 Hz, 8H, H^{B2}), 7.59 (s, 4H, H^{A5}), 6.85 (d, *J* = 7.7 Hz, 8H, H^{B3}), 4.11 (s, 8H, H^{NH2}), 2.31 (s, 12H, H^{Me}).

^{13}C NMR (151 MHz, CD_2Cl_2) δ/ppm 157.7 (C^{A6}), 152.9 (C^{A2}), 150.5 (C^{A4}), 149.5 (C^{B4}), 128.7 (C^{B2}), 126.6 (C^{B1}), 122.5 (C^{A5}), 116.3 (C^{A3}), 115.7 (C^{B3}), 25.6 (C^{Me}).

ESI-MS *m/z* 795.6 $[M\text{-}PF_6]^+$ (calc. 795.3).

6.5.6 $[Cu(\mathbf{14})_2][PF_6]$

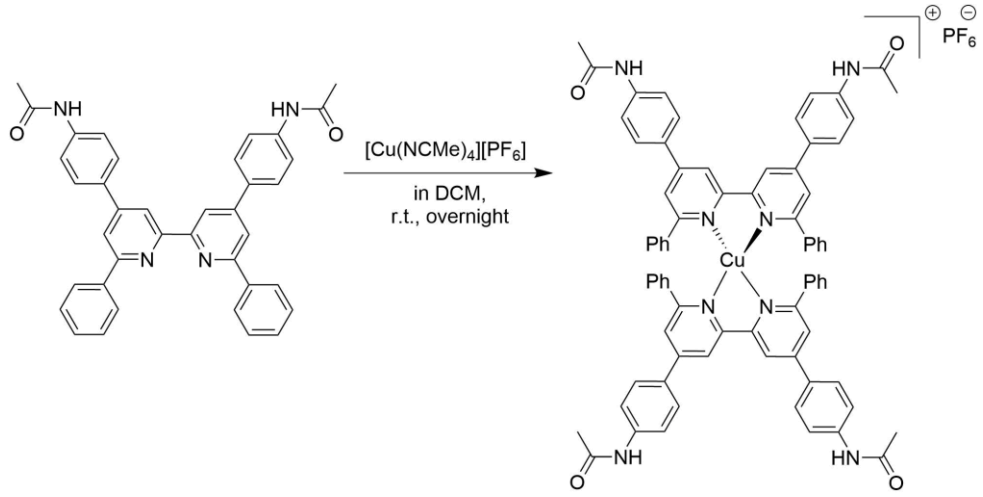

Scheme 59: Synthesis of $[Cu(14)_2][PF_6]$.

Ligand **14** (500 mg, 0.87 mmol) was suspended in 15 mL CH_2Cl_2 and a solution of $[Cu(NCMe)_4][PF_6]$ (162 mg, 0.435 mmol) in 10 mL CH_2Cl_2 was added. The reaction mixture was stirred overnight at room temperature, filtered and the solvent was removed under reduced pressure to yield $[Cu(\mathbf{14})_2][PF_6]$ as black-grey solid (478 mg, 0.352 mmol, 80.9%). From the NMR measurement it could be seen that the homoleptic copper(I) complex dissociated in solution as mentioned before. Therefore the NMR assignment of the complex $[Cu(\mathbf{14})_2)][PF_6]$ was not possible.

Chapter 7

Chapter 7 4-Methoxycarbonylphenyl and 4-ethylphenyl functionalized-ancillary ligands in bis(diimine)copper(I) dyes

7.1 Motivation

As shown in earlier chapters the highest influence on the performance of the DSC is the type of ancillary ligand used in combination with the stable anchoring ligand **ALP1**.[46] As discussed in Chapter 5 and Chapter 6, the substituents in the 4,4´-positions of the phenyl spacer at the 4,4´-positions of the bpy unit have a high influence on the cell performance.[91] In this chapter two new ancillary ligands are investigated bearing methoxycarbonyl or ethyl- substituents in the 4,4´-position of the phenyl spacer.

7.2 Synthetic approach

The Kröhnke[84] strategy was used for the preparation of these two ancillary ligands (**15** and **16**). In Scheme 60 the general synthetic route for the ancillary ligands is shown. The detailed synthetic route and the analytical data of the **ALP1**[75] anchoring ligand used in this chapter were presented in the experimental section of Chapter 3.

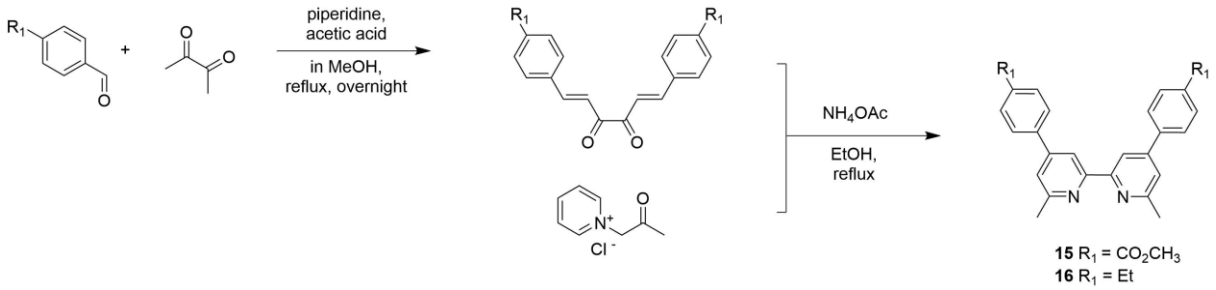

Scheme 60: General synthetic route of ancillary ligand 15 and 16.

The corresponding homoleptic copper(I) complexes (Scheme 61) were prepared using a standard method by combination of $[Cu(MeCN)_4][PF_6]$[87] with two equivalents of the ligands **15** or **16** and were isolated as dark red solids in 74.5% yield for $[Cu(\mathbf{15})_2][PF_6]$ and 78.6% yield for $[Cu(\mathbf{16})_2][PF_6]$. In the electrospray mass spectrum the highest mass peak of each complex corresponded to the $[M - PF_6]^+$ ion and showed a characteristic isotope pattern corresponding to the simulated pattern. The ^1H and ^{13}C NMR spectra of the complexes were recorded in $CDCl_3$ and assigned using 2D methods.

In Figure 63 the solution absorption spectra of the complexes are shown. The corresponding absorption maxima are given in Table 19 and were established by recording the spectra at different concentrations. The solution absorption spectra are dominated by high-energy $\pi^*\leftarrow\pi$ and $\pi^*\leftarrow n$ transitions for $[Cu(\mathbf{15})_2][PF_6]$; and $\pi^*\leftarrow\pi$ transitions for $[Cu(\mathbf{16})_2][PF_6]$. Furthermore broad MLCT bands with λ_{max} = 494 nm for $[Cu(\mathbf{15})_2][PF_6]$ and λ_{max} = 486 nm for $[Cu(\mathbf{16})_2][PF_6]$ (Table 19).

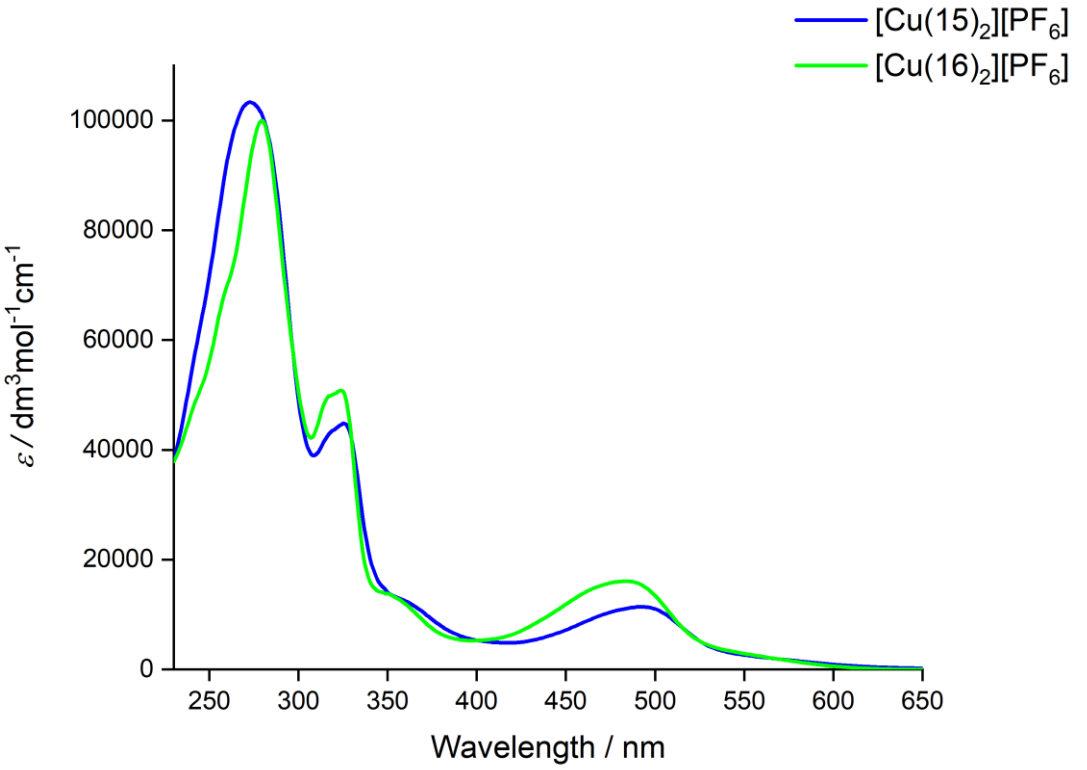

Figure 63: Solution (CH_2Cl_2) absorption spectra of complexes $[Cu(15)_2][PF_6]$ and $[Cu(16)_2][PF_6]$ (1×10^{-5} mol dm^{-3}).

Table 19: Absorption maxima for $[Cu(15)_2][PF_6]$ and $[Cu(16)_2][PF_6]$ (CH_2Cl_2, 1×10^{-5} mol dm^{-3}; sh = shoulder; ε values are rounded to the nearest 100 dm^{-3} mol^{-1} cm^{-1}).

	λ_{max}/nm (ε_{max}/dm^3 mol^{-1} cm^{-1})	
Complex	π*←π and π*←*n*	MLCT
$[Cu(\mathbf{15})_2][PF_6]$	244 sh (61 786), 273 (103 401), 317 sh (42 767), 326 (44 542), 366 sh (11 890)	494 (11 454)
$[Cu(\mathbf{16})_2][PF_6]$	257 sh (65 583), 279 (100 040), 315 sh (49 242), 324 (50 829), 360 sh (12 108)	486 (16 155)

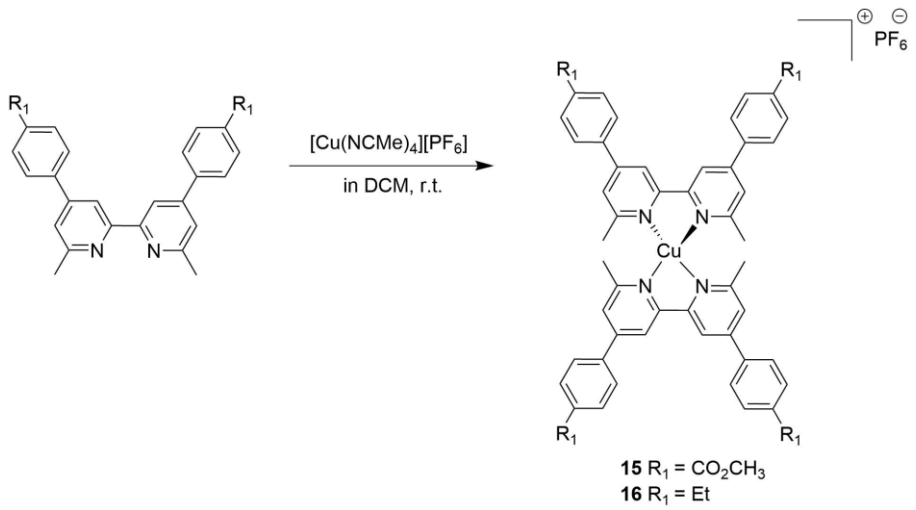

Scheme 61: General synthetic route for the homoleptic Cu(I) complexes.

The detailed synthetic routes to the ligands **15** and **16** (Scheme 60), as well as the homoleptic copper (I) complex synthesis (Scheme 61) and the analytical data are given in the experimental section of this chapter.

In order to functionalize the TiO_2 surface of the electrodes with the heteroleptic dyes $[Cu(L_{anchor})(L_{ancillary})]^+$ the ´surface-as-ligand, surface-as-complex´[47] strategy (Figure 37) was used. **ALP1**[46] (**1**) (Scheme 2) was used in combination with the ancillary ligands **15** and **16** to assemble the heteroleptic dyes adsorbed on the TiO_2 surface. DSCs containing the dyes $[Cu(\mathbf{1})(\mathbf{15})]^+$ and $[Cu(\mathbf{1})(\mathbf{16})]^+$ were compared to a N719 reference cell.

7.3 Results

7.3.1 Solid state absorption spectra

For the solid-state absorption measurements the copper(I) dyes were assembled with the ´surface-as-ligand; surface-as-complex´[47] strategy on transparent TiO_2 electrodes to give $[Cu(\mathbf{1})(\mathbf{15})]^+$ and $[Cu(\mathbf{1})(\mathbf{16})]^+$ adsorbed on the electrodes surface. The commercial TiO_2 electrodes were washed with milliQ water and HPLC grade EtOH, dried in a stream of nitrogen and heated at 450 °C for 30 min. After cooling, the electrodes were soaked in a 1.0 mM DMSO solution of anchoring ligand **1** for 24 h, washed with DMSO and EtOH and dried. The anchoring-ligand functionalized electrodes were then immersed into 0.1 mM CH_2Cl_2 solutions of the homoleptic copper(I) complexes $[Cu(\mathbf{15})_2][PF_6]$ or $[Cu(\mathbf{16})_2][PF_6]$ for 3 days. After soaking in the dye bath solutions, the electrodes were taken out, washed with CH_2Cl_2 and dried in a stream of nitrogen. Figure 64 shows the background corrected and normalized solid-state absorption spectra of the functionalized electrodes.

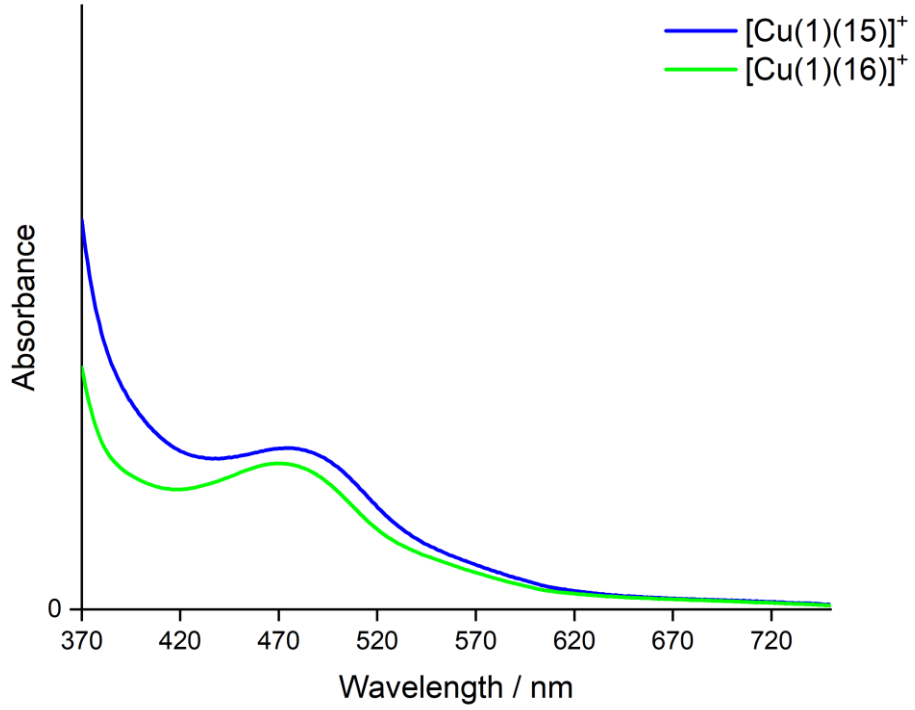

Figure 64: Solid-state absorption spectra of transparent TiO_2 functionalized with $[Cu(1)(15)]^+$ and $[Cu(1)(16)]^+$.

The MLCT absorption maxima of the transparent TiO_2 electrodes functionalized with dyes $[Cu(\mathbf{1})(\mathbf{15})]^+$ and $[Cu(\mathbf{1})(\mathbf{16})]^+$ appeared at λ_{max} 474 and 471 nm, respectively (Figure 64). The ancillary ligand **15** substituted with methoxycarbonyl groups in the 4,4´-positions of the phenyl spacer resulted in a higher absorption compared to ancillary ligand **16**. Furthermore the electrode functionalized with $[Cu(\mathbf{1})(\mathbf{15})]^+$ shows a higher absorption at smaller wavelengths as well as a slightly broaden spectral response towards the red end of the visible spectrum (Figure 64 blue curve).

Figure 65 illustrates the comparison of the solid-state absorption spectra of electrodes functionalized with $[Cu(\mathbf{1})(\mathbf{15})]^+$, $[Cu(\mathbf{1})(\mathbf{16})]^+$ or N719. The lower MLCT bands exhibited by copper(I) dyes over the well performing N719 dye (Figure 65) confirms an overall lower spectral response.

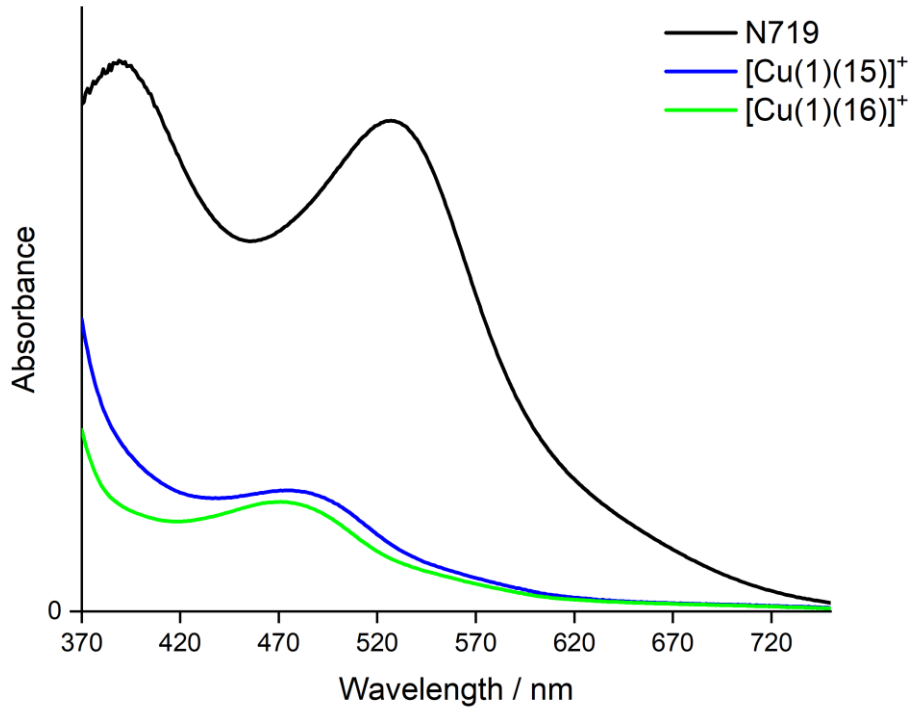

Figure 65: Solid-state absorption spectra of transparent TiO_2 functionalized with $[Cu(1)(15)]^+$ and $[Cu(1)(16)]^+$ compared to N719.

7.3.2 DSC performances

The heteroleptic copper(I) dyes were adsorbed on the electrode surface using the ´surface-as-ligand, surface-as-complex´[47] strategy (SALSAC) in a similar manner as mentioned before for the preparation of the solid-state absorption spectra. In contrast to the electrodes for the solid-state absorption spectra, the TiO_2 electrodes for preparing the working electrodes for the DSCs had an additional TiO_2 scattering layer. Each dye-soaked working electrode was assembled with a commercial Pt counter electrode using a thermoplast hot-melt sealing foil, by pressing the electrodes together while heating. The electrolyte between the electrodes was introduced by vacuum back-filling prior to the sealing of the DSCs. Duplicate DSCs were prepared for both dyes to confirm reproducibility of the performance parameters.

7.3.2.1 Solar cell measurements

The solar simulator measurements of the DSCs were performed in a fully-masked mode with an average area size of 0.06012 cm^2 (with a standard deviation of 1%) in order to prevent false influence from scattered light.[79,80] All DSCs with dyes $[Cu(\mathbf{1})(L_{ancillary})]^+$ with $L_{ancillary}$ = **15** and **16** were measured on the day of assembling (day 0), day 1 and day 4 after cell assembling. A DSC containing dye N719 was prepared and measured as reference. The relative efficiencies of the DSCs with respect

to N719 set to 100%[72] were calculated in order to have a better comparison of the different dye combinations (Table 20, Table 21 and Table 22). The highest short-circuit current density (J_{SC}) was achieved with ancillary ligand **15**, yielding values of 4.89 and 5.15 mA/cm^2 respectively (Figure 66, Figure 67 and Table 20). The DSCs with dye [Cu(**1**)(**16**)]$^+$ yielded values of 4.28 and 4.63 mA/cm^2 in the J_{SC} (Figure 66, Figure 67 and Table 20). In terms of the open-circuit voltages (V_{OC}) the DSCs with ancillary ligand **15** also yielded the highest values of 576 and 580 mV (Figure 66, Figure 67 and Table 20). The values in the open-circuit voltages for the cells containing ancillary ligand **16** were measured to be 552 and 557 mV (Figure 66, Figure 67 and Table 20). The fill factors (ff) of all the cells were good and in the range of 69-73% (Table 20). Although the methoxycarbonyl substituents in the 4,4´-positions of the phenyl spacer in ancillary ligand **15** have a –M effect these cells yielded higher values in both the short-circuit current density and the open-circuit voltage compared to the ethyl substituent in ancillary ligand **16** which features a +I effect. On varying the ancillary ligand the best performance could be measured with [Cu(**1**)(**15**)]$^+$ yielding efficiencies of 2.05 and 2.06% (Table 20). The DSCs with dye [Cu(**1**)(**16**)]$^+$ yielded slightly lower efficiencies of 1.73 and 1.82% (Table 20). The J-V curves for the DSCs with [Cu(**1**)(**15**)]$^+$ and [Cu(**1**)(**16**)]$^+$ are shown in Figure 66 and Figure 67. The duplicate DSCs in Table 20 confirmed the reproducibility of both the construction and the measurement of the cells. The measurements over time showed a slight decrease for all the cells on day 1 and day 4 (Table 20, Table 21 and Table 22), nevertheless the cells were stable over this period of time. Figure 66 to Figure 71 show the development of the *J-V* curves over time for the cells.

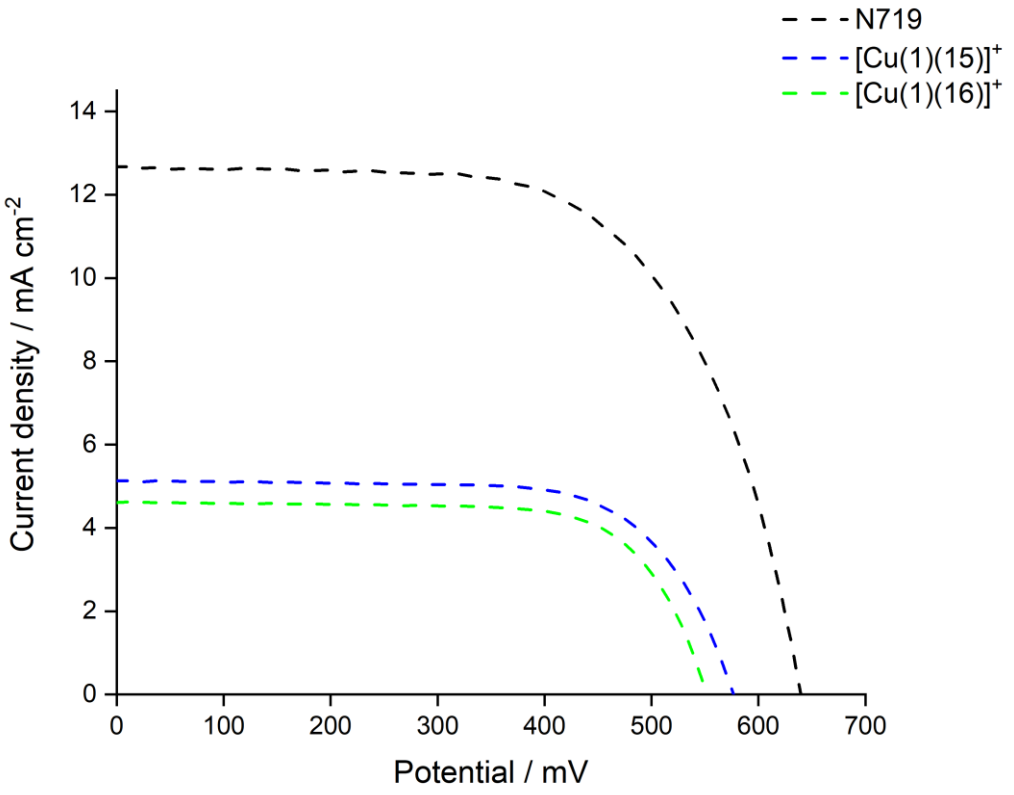

Figure 66: *J-V* curves for DSCs with dyes $[Cu(1)(15)]^+$, $[Cu(1)(16)]^+$ and N719 measured on the day of cell assembly.

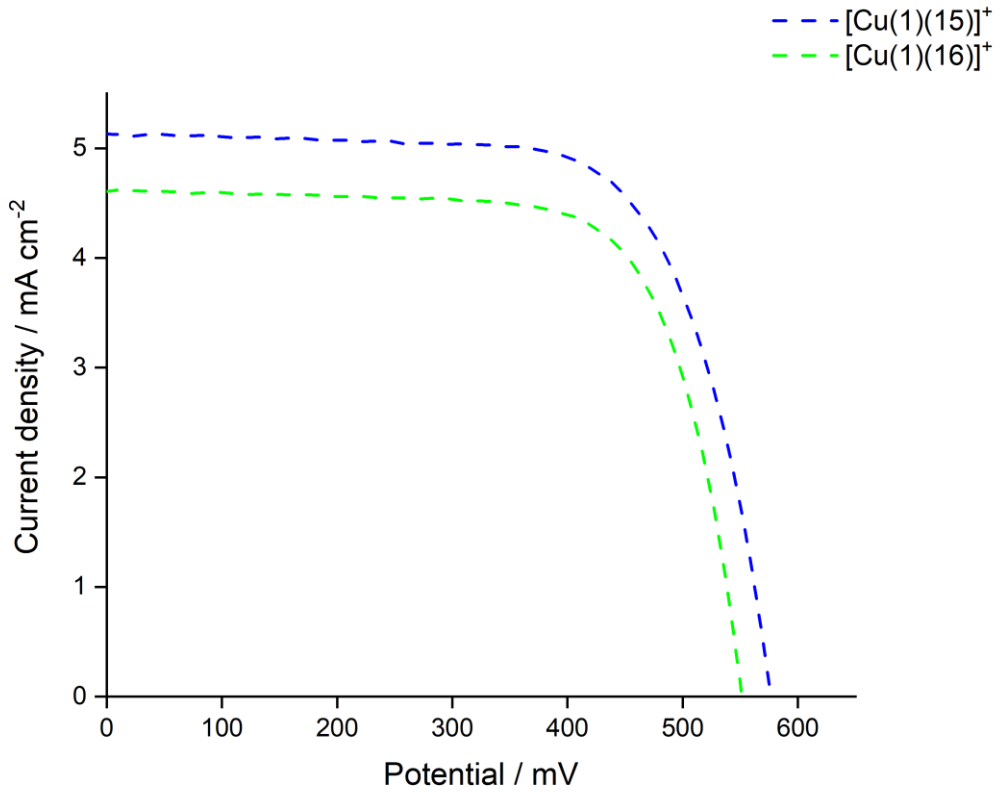

Figure 67: *J-V* curves for DSCs containing dyes $[Cu(1)(15)]^+$ and $[Cu(1)(15)]^+$ measured on the day of cell assembly (expansion of Figure 66).

Table 20: Performance parameters of duplicate DSCs with [Cu(1)(15)]$^+$ and [Cu(1)(16)]$^+$ compared to N719 as reference cell measured on the day of cell assembly.

Dye	J_{sc}/mA cm^{-2}	V_{OC}/mV	ff/%	η/%	Relative η/%
[Cu(**1**)(**15**)]$^+$	5.15	576	69	2.06	40.2
[Cu(**1**)(**15**)]$^+$	4.89	580	72	2.05	40.0
[Cu(**1**)(**16**)]$^+$	4.63	552	71	1.82	35.5
[Cu(**1**)(**16**)]$^+$	4.28	557	73	1.73	33.7
N719	12.72	639	63	5.13	100

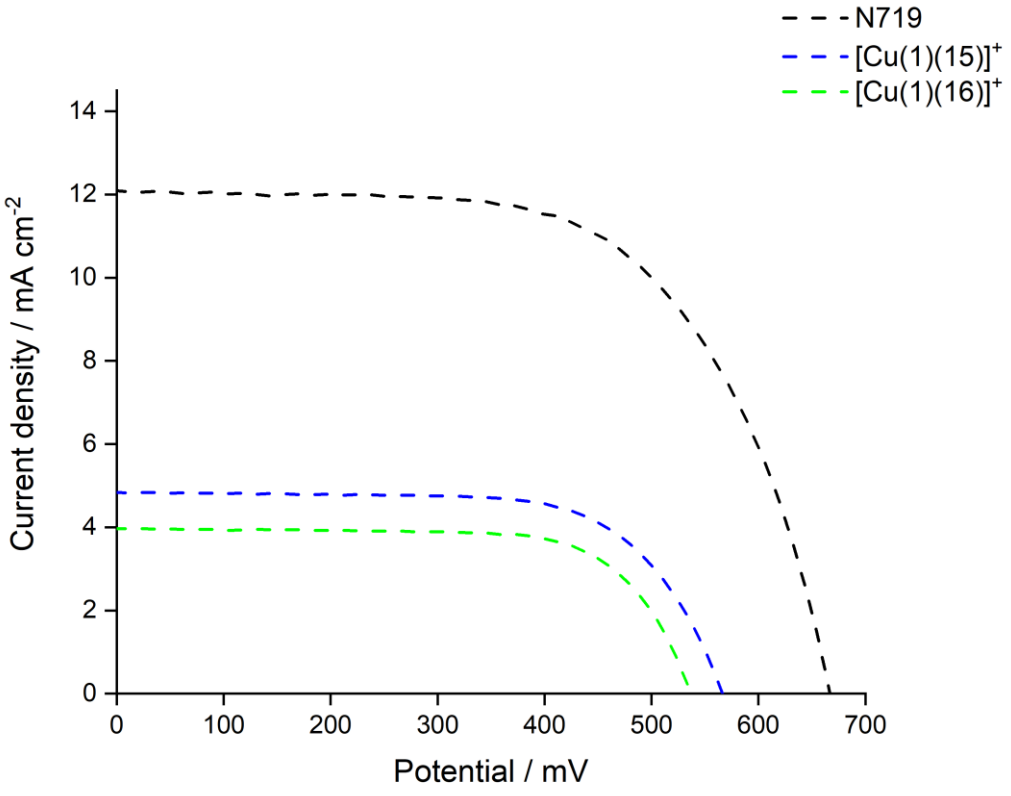

Figure 68: *J-V* curves for DSCs containing dyes [Cu(1)(15)]$^+$, [Cu(1)(16)]$^+$ and N719 measured on day 1 after cell assembly.

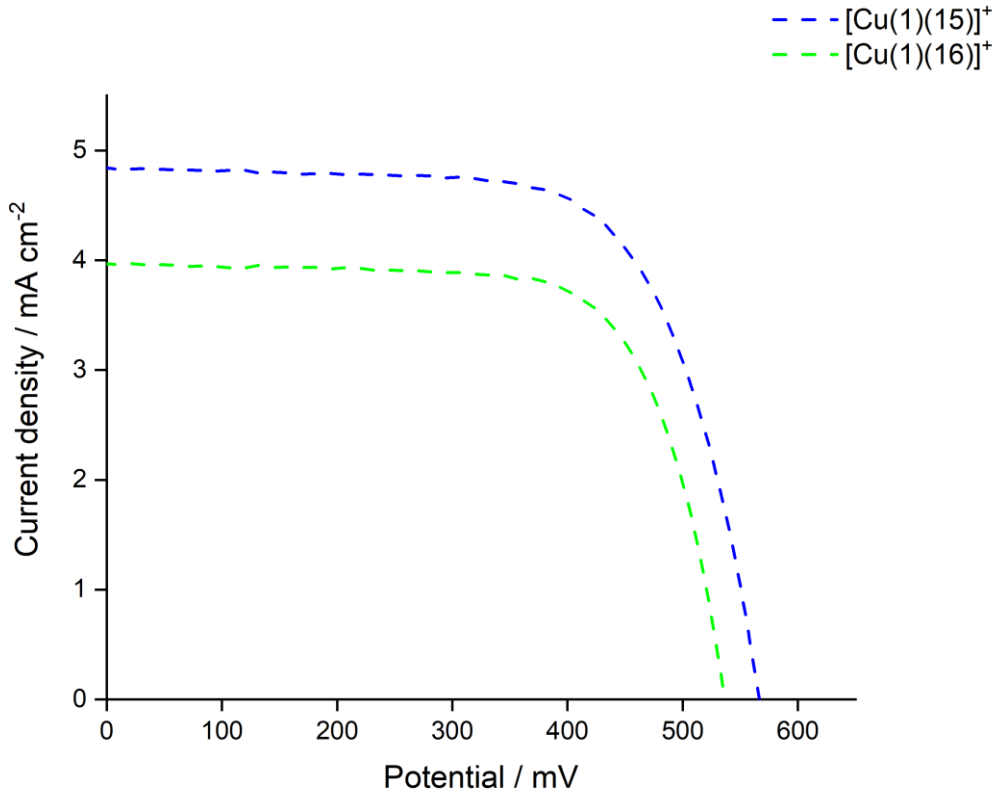

Figure 69: *J-V* curves for DSCs containing dyes [Cu(1)(15)]$^+$ and [Cu(1)(16)]$^+$ measured on day 1 after cell assembly (expansion of Figure 68).

Table 21: Performance parameters of duplicate DSCs with [Cu(1)(15)]$^+$ and [Cu(1)(16)]$^+$ compared to N719 as reference cell measured on day 1 after cell assembly.

Dye	J_{sc}/mA cm^{-2}	V_{OC}/mV	ff/%	η/%	Relative η/%
[Cu(**1**)(**15**)]$^+$	4.86	566	68	1.87	37.2
[Cu(**1**)(**15**)]$^+$	4.66	570	72	1.91	38.0
[Cu(**1**)(**16**)]$^+$	3.98	536	71	1.51	30.0
[Cu(**1**)(**16**)]$^+$	3.82	543	71	1.48	29.4
N719	12.49	667	60	5.03	100

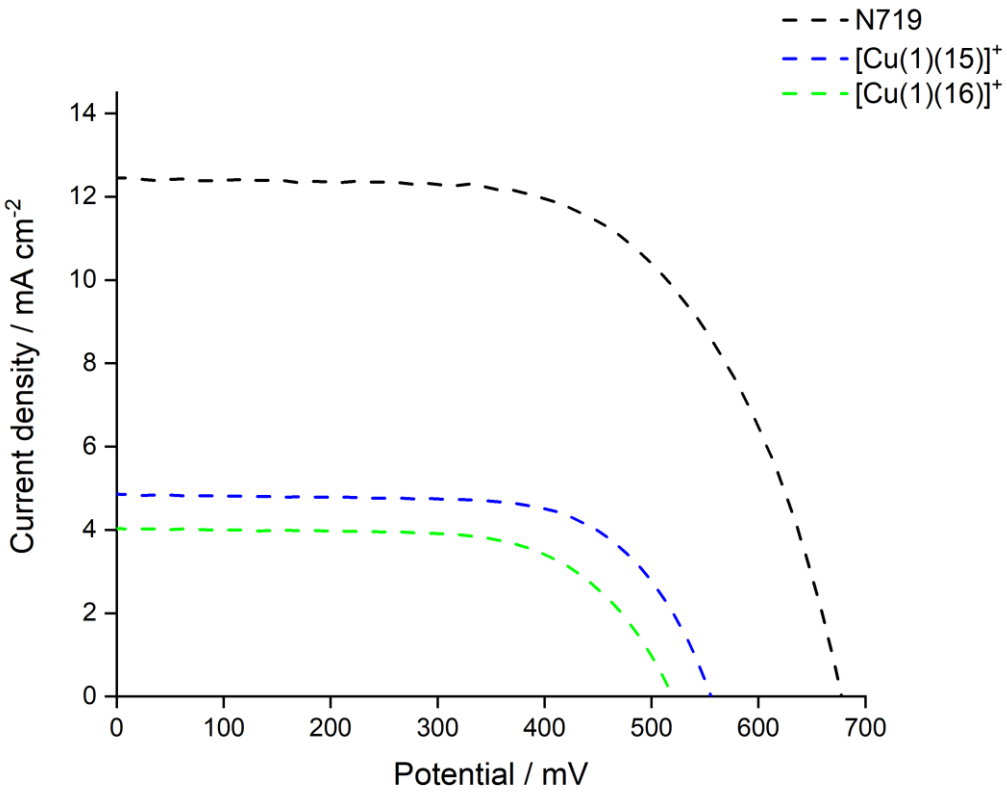

Figure 70: *J-V* curves for DSCs with dyes $[Cu(1)(15)]^+$, $[Cu(1)(16)]^+$ and N719 measured on day 4 after cell assembly.

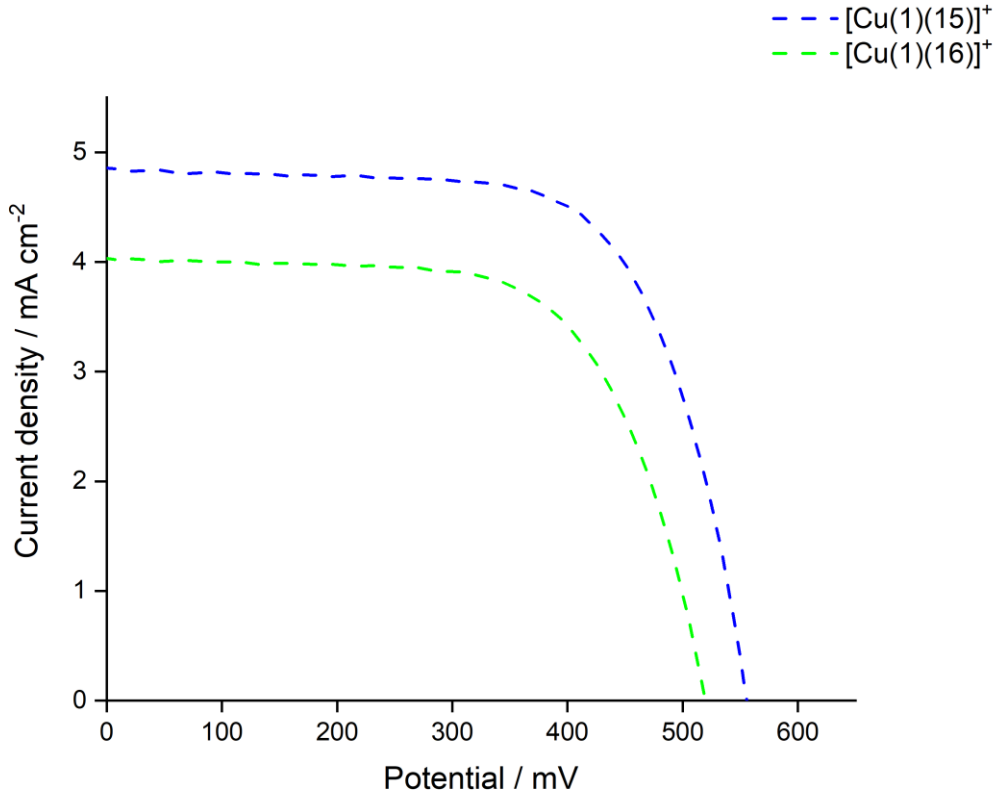

Figure 71: *J-V* curves for DSCs with dyes $[Cu(1)(15)]^+$, $[Cu(1)(16)]^+$ measured on day 4 after cell assembly (Figure 70).

Table 22: Performance parameters of duplicate DSCs with [Cu(1)(15)]$^+$ and [Cu(1)(16)]$^+$ compared to N719 as reference cell measured on day 4 after cell assembly

Dye	J_{sc}/mA cm^{-2}	V_{OC}/mV	ff/%	η/%	Relative η/%
[Cu(**1**)(**15**)]$^+$	4.86	556	68	1.83	35.1
[Cu(**1**)(**15**)]$^+$	4.58	555	71	1.80	34.5
[Cu(**1**)(**16**)]$^+$	4.04	519	65	1.37	26.3
[Cu(**1**)(**16**)]$^+$	3.70	528	67	1.32	25.3
N719	13.03	677	59	5.22	100

7.3.2.2 External Quantum Efficiency (EQE) measurements

In Figure 72 the EQE curves of DSCs with [Cu(**1**)(**15**)]$^+$ and [Cu(**1**)(**16**)]$^+$ are compared to N719. The curves clearly represent the lack of photoconversion efficiency of the copper(I) based dyes at longer wavelengths in contrast to the well performing N719 dye (Figure 72 black curve). Moreover the curves show the lower photon to current conversion efficiencies of the dyes [Cu(**1**)(**15**)]$^+$ and [Cu(**1**)(**15**)]$^+$ over that of N719.

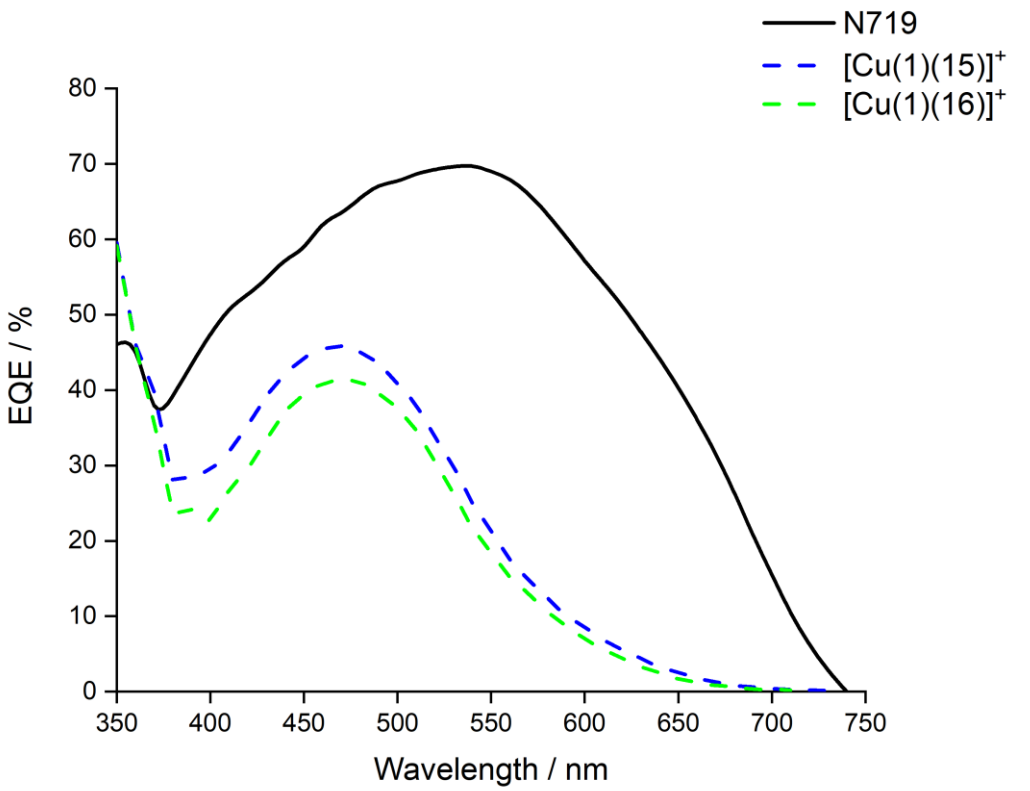

Figure 72: EQE spectra of DSCs containing dyes [Cu(1)(15)]$^+$, [Cu(1)(16)]$^+$ and N719.

The EQE spectra shown in Figure 73 reflect the trends of J_{SC} data from the solar simulator measurements discussed in the last section. The higher values for the EQE were achieved with DSCs

containing dye [Cu(**1**)(**15**)]$^+$ yielding EQE_{max} values of 45.0 and 45.8% at λ_{max} 470 nm (Figure 73 and Table 23). The data were consistent with the absorption maxima found for the solid-state absorption spectra shown in Figure 64. A slightly broader spectral response was found for [Cu(**1**)(**15**)]$^+$ in both, the solid-state absorption spectra (Figure 64) and the EQE spectra (Figure 73 and Table 23), compared to DSCs with dye [Cu(**1**)(**16**)]$^+$. The EQE_{max} values for DSCs with dye [Cu(**1**)(**16**)]$^+$ were measured to be 38.2 and 41.4% at λ_{max} 450 and 470 nm, respectively (Table 23).

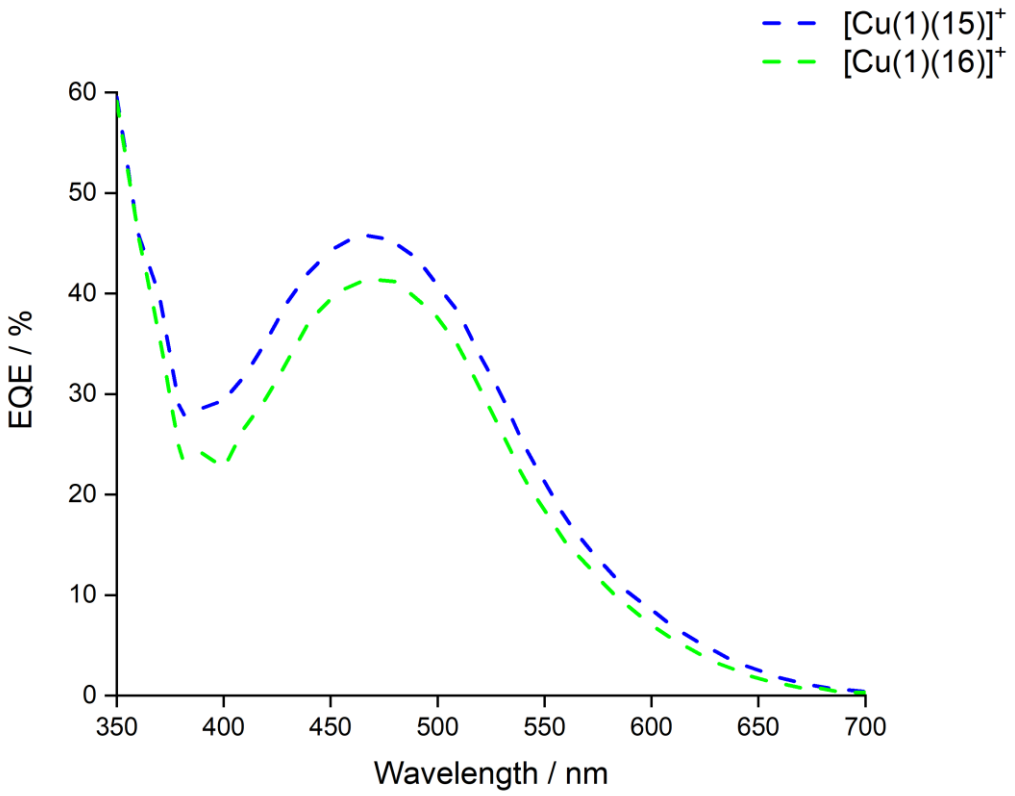

Figure 73: EQE spectra of DSCs containing dyes [Cu(1)(15)]$^+$ and [Cu(1)(16)]$^+$.

Table 23: EQE maxima for duplicate DSCs containing dyes [Cu(1)(15)]$^+$ and [Cu(1)(16)]$^+$.

Dye	λ_{max} / nm	EQE_{max} / %
[Cu(**1**)(**15**)]$^+$	470	45.8
[Cu(**1**)(**15**)]$^+$	470	45.0
[Cu(**1**)(**16**)]$^+$	470	41.4
[Cu(**1**)(**16**)]$^+$	450	38.2

7.4 Conclusion

In this chapter two ancillary ligands and the corresponding homoleptic copper(I) complexes $[Cu(\mathbf{15})_2][PF_6]$ and $[Cu(\mathbf{16})_2][PF_6]$ were synthesized and characterized. The ´surface-as-ligand, surface-as-complex´ strategy was used to functionalize the TiO_2 electrodes with the heteroleptic copper(I) dyes using the **ALP1** anchoring ligand (**1**) and the two ancillary ligand **15** and **16**. The ancillary ligands **15** and **16** presented in this chapter had a 6,6´-dimethyl-2,2´-bipyridine unit substituted in the 4,4´-positions with 4-methoxycarbonylphenyl- (**15**) or 4-ethylphenyl (**16**) substituents. DSCs containing dyes $[Cu(\mathbf{1})(\mathbf{15})]^+$ and [Cu(**1**)(**16**)]+ were assembled and characterized. In order to prove the reproducibility of the cell assembling and the measurements duplicate DSCs were built for each dye. The best performance was obtained for $[Cu(\mathbf{1})(\mathbf{15})]^+$ with a relative efficiency of 40.2% with respect to N719 set at 100%. The DSC with dye $[Cu(\mathbf{1})(\mathbf{16})]^+$ yielded a relative efficiency of 35.5% with respect to N719 set at 100%. While the difference in the short-circuit current densities for the two dyes presented here is not that big, the main difference was found in the open-circuit voltages being 557 and 580 mV for $[Cu(\mathbf{1})(\mathbf{15})]^+$ and $[Cu(\mathbf{1})(\mathbf{16})]^+$, respectively. Similar trends were found for the EQE and solid-state absorption measurements for these two dyes. The electrodes functionalized with dye $[Cu(\mathbf{1})(\mathbf{15})]^+$ yielded higher values in both, the solid-state absorption and EQE measurements. Furthermore a slightly broadened spectral response was found for ancillary ligand 15 in the solid-state absorption spectra. The ethyl substituents in the 4,4´-positions of the phenyl-spacer of ancillary ligand **16** feature a weak +I effect which should enhance the performance of the DSCs in terms of the desired ´push-pull´ system for n-type dyes and could help preventing recombination of the excited dye with the electrolyte. Although the methyl acetate substituents in ancillary ligand **15** have a –M effect which should be detrimental in terms of electron movement towards the semiconductor, it seems that a stronger lone pair character has a positive influence on the performance of the dye.

In conclusion it can be stated that electron rich groups in phenyl framework of the ancillary ligand can have a positive effect on the photon to power conversion efficiency of the DSCs. As seen in earlier chapters that the positions of these substituents in the phenyl framework of the ancillary ligand can have an additional impact on the dye performance, further investigations could be done in this field.

7.5 Experimental

The synthesis for the A**LP1** anchoring ligand (**1**) used in this chapter for the functionalization of the TiO_2 electrodes with the heteroleptic copper(I) dyes using the ´surface-as-ligand, surface-as-complex´ strategy is described in details in the experimental section of Chapter 3.

7.5.1 4,4´-Di(4-methoxycarbonylphenyl)-6,6´-dimethyl-2,2´-bipyridine (**15**)

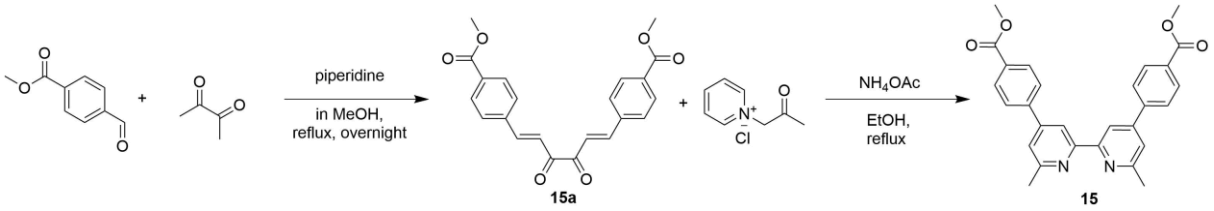

Scheme 62: Synthesis of ancillary ligand15.

Methyl-4-formylbenzoate (4.92 g, 30.0 mmol) and piperidine (0.25 mL, 2.53 mmol) were dissolved in 35 mL MeOH. A solution of 2,3-butandione (1.31 mL, 15.0 mmol) in 15 mL MeOH was added dropwise. The reaction mixture was heated to reflux overnight. A precipitate was formed and filtered off after the reaction mixture was allowed to cool to room temperature. The precipitate was washed with cold MeOH yielding compound **15a** as light yellow solid (1.59 g, 4.19 mmol, 28%). Compound **15a** (1.5 g, 3.96 mmol), 1-(2-oxopropyl)pyridinium chloride (2.72 g, 15.9 mmol) and NH_4OAc (2.42 g, 31.4 mmol) were dissolved in 150 mL EtOH and heated to reflux overnight. The reaction mixture was allowed to cool to room temperature and a precipitate was formed. The precipitate was collected by filtration, washed with cold EtOH, recrystallized from MeOH and dried with diethyl ether. Ligand **15** was isolated as off-white solid (794 mg, 1.75 mmol, 66.4%).[84,99]

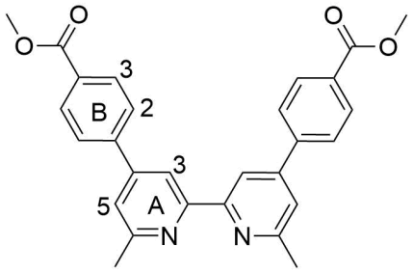

Scheme 63: Structure of ligand 15 with atom labelling for NMR assignments. NMR assignments.

^{1}H NMR (600 MHz, $CDCl_3$) δ/ppm 8.52 (s, 2H, H^{A3}), 8.17 (d, *J* = 7.3 Hz, 4H, H^{B3}), 7.83 (d, *J* = 7.6 Hz, 4H, H^{B2}), 7.43 (s, 2H, H^{A5}), 3.97 (s, 6H, H^{OMe}), 2.73 (s, 6H, H^{Me}).

^{13}C NMR (151 MHz, $CDCl_3$) δ/ppm 166.9 ($C^{C=O}$), 158.9 (C^{A6}), 156.6 (C^{A2}), 148.6 (C^{A4}), 143.3 (C^{B1}), 130.5 (C^{B4}), 130.4 (C^{B3}), 127.4 (C^{B2}), 121.5 (C^{A5}), 116.9 (C^{A3}), 52.4 (C^{OMe}), 24.9 (C^{Me}).

7.5.2 4,4´-Di(4-ethylphenyl)-6,6´-dimethyl-2,2´-bipyridine (**16**)

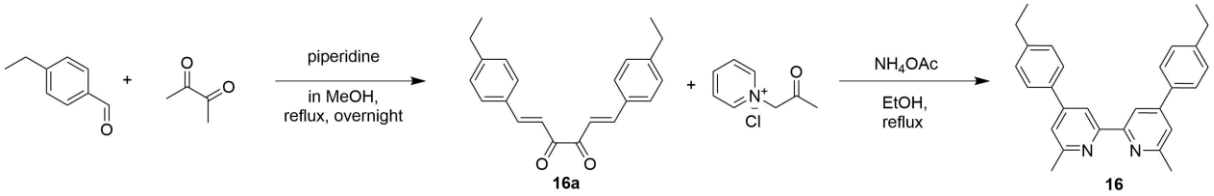

Scheme 64: Synthesis of ancillary ligand 16.

4-Ethylbenzaldehyde (5.1 mL, 37.2 mmol) and piperidine (0.31 mL, 3.14 mmol) were dissolved in 50 mL MeOH. 2,3-Butandione (1.63 mL, 18.6 mmol) in 15 mL MeOH was added dropwise and the reaction mixture was heated to reflux overnight. The reaction mixture was allowed to cool to room temperature. As no precipitation occured, the reaction mixture was concentrated and cooled in an ice bath, when a precipitate formed. The precipitate was filtered off and washed with cold MeOH to yield compound **16a** as light yellow-golden solid (820 mg, 2.57 mmol, 13.8%). Compound **16a** (599 mg, 1.88 mmol), 1-(2-oxopropyl)pyridinium chloride (1.29 g, 7.57 mmol) and NH_4OAc (1.16 g, 77.1 mmol) were dissolved in 50 mL EtOH and heated to reflux overnight. The reaction mixture was allowed to cool to room temperature, a precipitate formed. The precipitate was filtered off and washed with cold MeOH and diethyl ether. Ligand **16** was isolated as beige-yellow solid (352 mg, 0.897 mmol, 47.7%).[84]

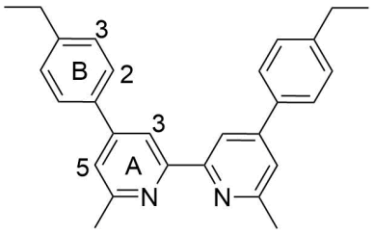

Scheme 65: Structure of ligand 16 with atom labelling for NMR assignments.

^{1}H NMR (600 MHz, $CDCl_3$) δ/ppm 8.46 (s, 2H, H^{A3}), 7.70 (d, *J* = 7.7 Hz, 4H, H^{B2}), 7.39 (s, 2H, H^{A5}), 7.33 (d, *J* = 7.6 Hz, 4H, H^{B3}), 2.76 – 2.68 (m, 10H, H^{CH2+Me}), 1.29 (t, *J* = 7.6 Hz, 6H, $H^{Me(Et)}$).

^{13}C NMR (151 MHz, $CDCl_3$) δ/ppm 158.5 (C^{A6}), 156.7 (C^{A2}), 149.5 (C^{A4}), 145.3 (C^{B4}), 136.3 (C^{B1}), 128.6 (C^{B3}), 127.3 (C^{B2}), 121.0 (C^{A5}), 116.7 (C^{A3}), 28.8 (C^{CH2}), 25.0 (C^{Me}), 15.7 ($C^{Me(Et)}$).

ESI-MS *m/z* 393.18 $[M + H]^+$ (calc. 392.23).

7.5.3 [Cu(**15**)$_2$][PF$_6$]

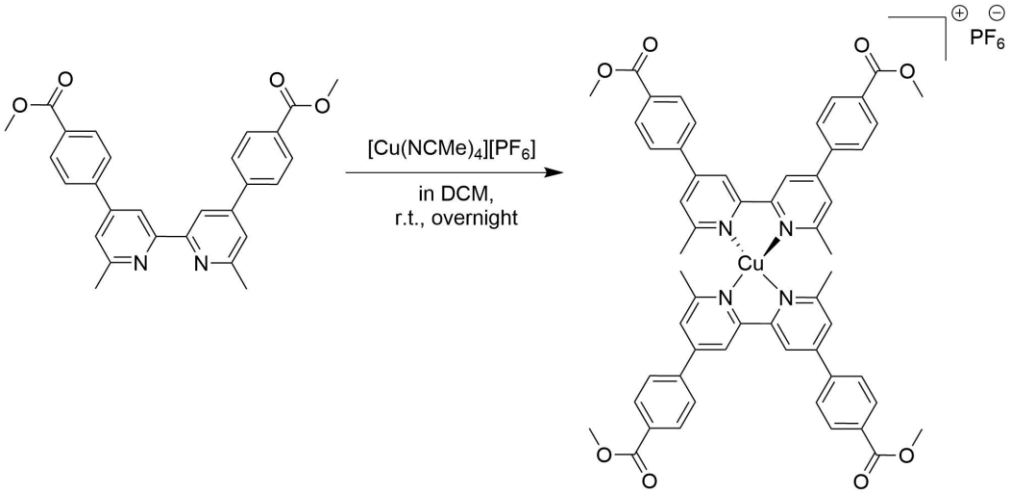

Scheme 66: Synthesis of [Cu(15)$_2$][PF$_6$].

Ligand **15** (350 mg, 0.774 mmol) and [Cu(NCMe)$_4$][PF$_6$] (144 mg, 0.387 mmol) were dissolved in 25 mL CH_2Cl_2 and stirred overnight at room temperature. The solution was filtered, the solvent was removed under reduced pressure and the resulting dark red solid was washed several times with diethyl ether to yield [Cu(**15**)$_2$][PF$_6$] as dark red solid (321 mg, 0.288 mmol, 74.5%).

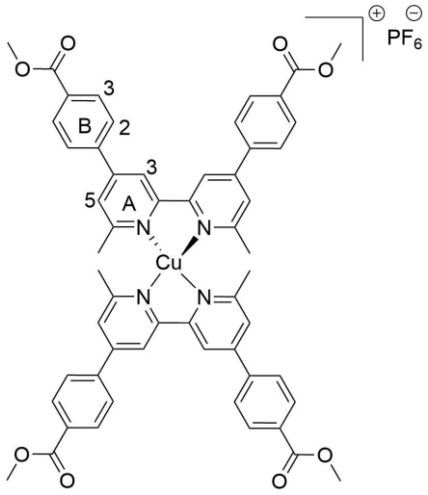

Scheme 67: Structure of [Cu(15)$_2$][PF$_6$] with atom labelling for NMR assignments.

^{1}H NMR (600 MHz, $CDCl_3$) δ/ppm 8.44 (s, 4H, H^{A3}), 8.23 (d, *J* = 6.7 Hz, 8H, H^{B3}), 7.90 (d, *J* = 7.2 Hz, 8H, H^{B2}), 7.73 (s, 4H, H^{A5}), 3.97 (s, 12H, H^{OMe}), 2.40 (s, 12H, H^{Me}).

^{13}C NMR (151 MHz, $CDCl_3$) δ/ppm 166.5 ($C^{C=O}$), 157.9 (C^{A6}), 152.1 (C^{A2}), 149.8 (C^{A4}), 141.2 (C^{B1}), 131.4 (C^{B4}), 130.7 (C^{B3}), 127.4 (C^{B2}), 124.4 (C^{A5}), 117.7 (C^{A3}), 52.4 (C^{OMe}), 25.5 (C^{Me}).

ESI-MS *m/z* 967.24 [M-PF$_6$]$^+$ (calc. 967.28).

7.5.4 [Cu(**16**)$_2$][PF$_6$]

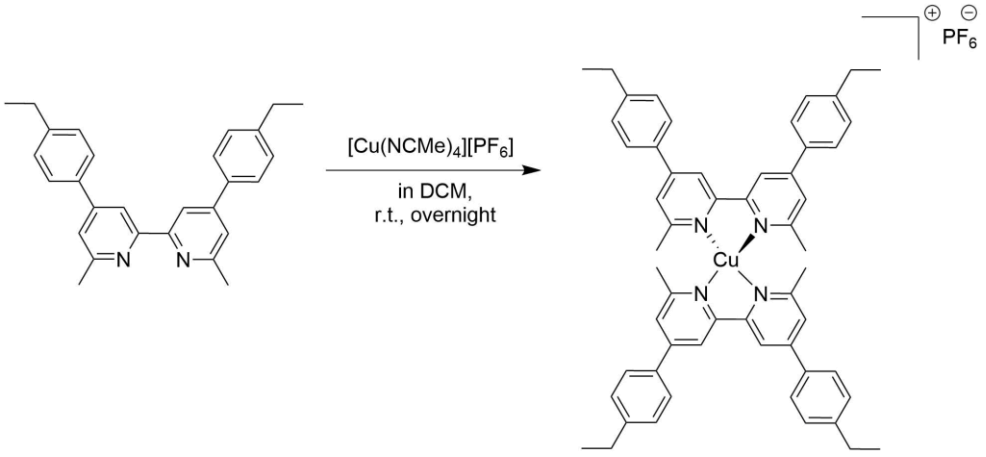

Scheme 68: Synthesis of [Cu(16)$_2$][PF$_6$].

Ligand **16** (251 mg, 0.64 mmol) and [Cu(NCMe)$_4$][PF$_6$] (119 mg, 0.32 mmol) were dissolved in 25 mL CH_2Cl_2 and stirred overnight at room temperature. The solution was filtered, the solvent was removed under reduced pressure and the resulting dark red solid was washed several times with diethyl ether to yield [Cu(**16**)$_2$][PF$_6$] as dark red solid (250 mg, 0.252 mmol, 78.6%).

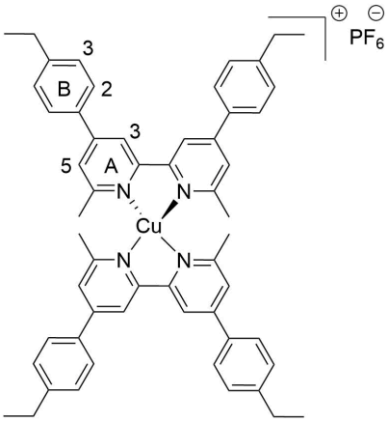

Scheme 69: Structure of [Cu(16)$_2$][PF$_6$] with atom labelling for NMR assignments

^{1}H NMR (600 MHz, $CDCl_3$) δ/ppm 8.36 (s, 4H, H^{A3}), 7.73 (d, *J* = 7.3 Hz, 8H, H^{B2}), 7.67 (s, 4H, H^{A5}), 7.41 (d, *J* = 7.3 Hz, 8H, H^{B3}), 2.75 (q, *J* = 6.9 Hz, 8H, H^{CH2}), 2.37 (s, 12H, H^{Me}), 1.31 (t, *J* = 7.4 Hz, 12H, $H^{Me(Et)}$).

^{13}C NMR (151 MHz, $CDCl_3$) δ/ppm 157.6 (C^{A6}), 152.3 (C^{A2}), 150.8 (C^{A4}), 146.8 (C^{B4}), 134.5 (C^{B1}), 129.2 (C^{B3}), 127.3 (C^{B2}), 123.7 (C^{A5}), 117.2 (C^{A3}), 28.9 (C^{CH2}), 25.6 (C^{Me}), 15.6 ($C^{Me(Et)}$).

ESI-MS *m/z* 847.31 $[M\text{-}PF_6]^+$ (calc. 847.38).

Chapter 8

Chapter 8 All copper dye-sensitized solar cells

8.1 Motivation

As demonstrated in Chapter 3, the choice of the anchoring ligand plays a fundamental role enabling a proper binding of the heteroleptic copper(I) dye on the TiO_2 surface and with this an efficient charge injection. Furthermore as shown in previous chapters the selection of the ancillary ligand used to assemble the heteroleptic copper(I) based dyes on the electrodes surface in DSCs is of high importance in terms of the overall cell performance. In addition to these two principal components in DSCs the electrolyte is crucial in enabling an efficient transport of the electrons in order to regenerate the dye to facilitate a persistent energy source. The standard electrolyte used in DSCs, also used in earlier chapters of this thesis, is an I^-/I_3^--based electrolyte. Changing the type of the electrolyte can further improve the performance of the cell. It is known that the combination of copper(I) based dyes with a Co^{2+}/Co^{3+}- based electrolyte is beneficial.[55] Also other redox couples in liquid electrolytes, quasi-solid state or solid state electrolytes are of high interest and known to be promising alternatives to the I^-/I_3^--based electrolyte.[56,100,57] In addition, use of a Cu^+/Cu^{2+} redox mediator in electrolytes has shown promising results.[101,102,103,104,105,106,107,108,109,110,59] Besides an increase in the open-circuit voltage by using bis(diimine)copper complexes as the redox couple, another advantage is that the ligands in the homoleptic copper complexes of the redox mediator could possibly be able to regenerate the heteroleptic copper(I) dye.[75,83]

Based on these findings, this chapter will give a short insight into DSCs containing copper(I) complexes of the type $[Cu(\mathbf{1})(L_{ancillary})]^+$ as sensitizers and Cu^+/Cu^{2+} redox shuttles as the electrolyte. The work in this chapter was done in collaboration with Mariia Karpacheva, Cedric Wobill and Frederik J. Malzner, all in our research group. Therefore this chapter gives just a brief overview of results without going into synthetic or analytical details. The findings obtained by the investigation of this new strategy presented here is important for the work reported in Chapter 9.

8.2 Ligands and complexes

Scheme 70 shows the **ALP1** anchoring ligand (**1**)[75] used to assemble the heteroleptic dyes adsorbed on the TiO_2 the surfaces. The synthesis of this anchoring ligand (**1**) was presented in the experimental section of Chapter 3 and DSC performances using **ALP1** (**1**) in heteroleptic bis(diimine)copper(I) dyes with various ancillary ligands was shown in earlier chapters of this thesis. The structure of the ligands used as ancillary ligands in the dyes and in homoleptic copper(I)/(II) redox shuttles in the electrolytes are shown in Scheme 71.

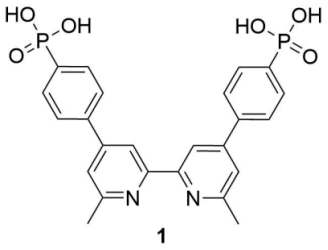

1

Scheme 70: Structure of the ALP1 anchoring ligand (1).

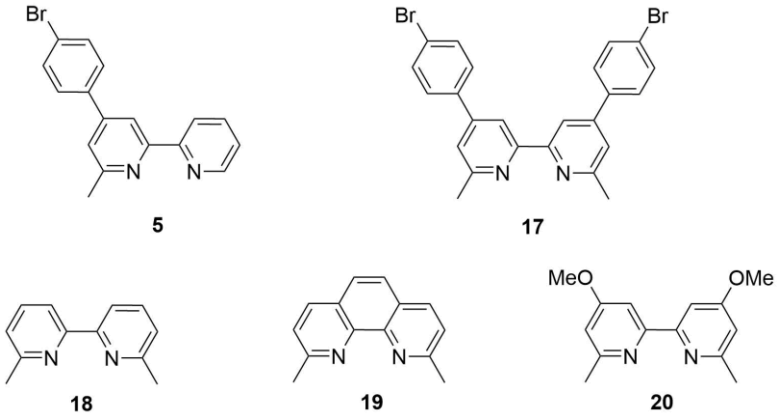

5 17 18 19 20

Scheme 71: Structure of ligands 5 and 17-20 used as ancillary ligands in the dyes and in homoleptic copper(I)/(II) redox couples in the electrolytes.

In Scheme 72 the homoleptic copper(I) complexes used in the dye bath solutions to get the heteroleptic copper(I) complexes $[Cu(\mathbf{1})(L_{ancillary})]^+$ ($L_{ancillary}$ = **5** or **17**-**20**) adsorbed on the electrode surfaces are shown.

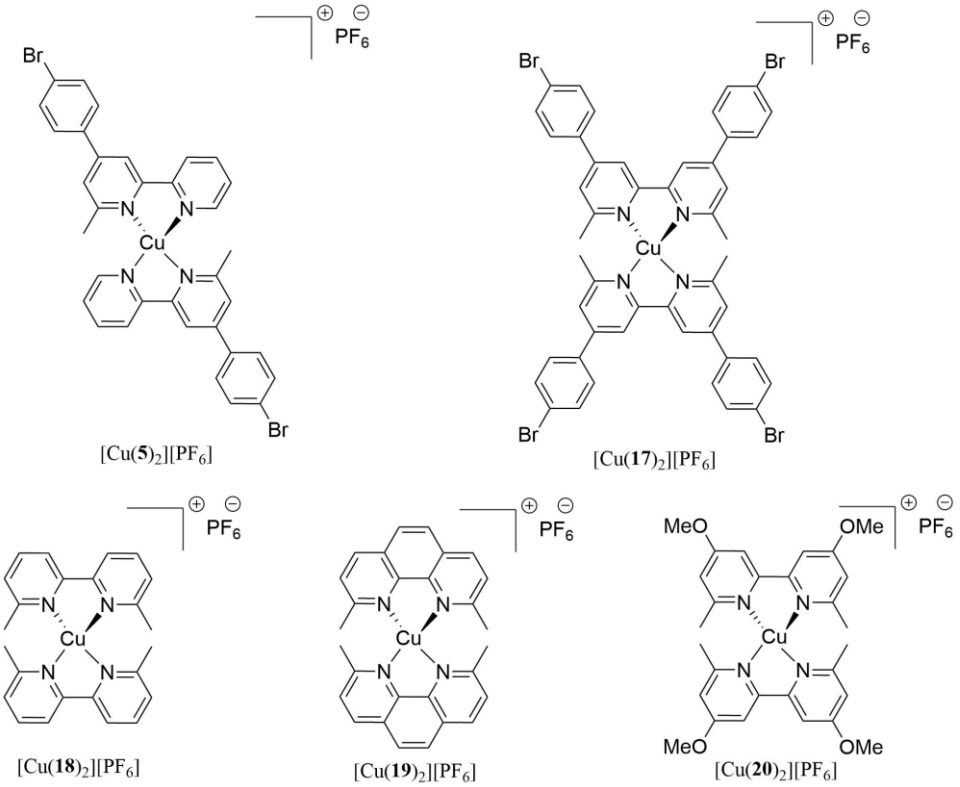

Scheme 72: Structure of the homoleptic copper(I) complexes $[Cu(L_{ancillary})_2][PF_6]$ ($L_{ancillary}$ = 5 or 17-20) used in the dye bath solutions.

In order to functionalize the TiO_2 surfaces of the electrodes with the heteroleptic dyes $[Cu(L_{anchor})(L_{ancillary})]^+$ the ´surface-as-ligand, surface-as-complex´[47] (SALSAC) strategy (Figure 37) was used. The **ALP1**[46] (**1**) anchoring ligand (Scheme 70) was used in combination with the ancillary ligands **5** or **17**-**20** (Scheme 71) to assemble the heteroleptic dyes adsorbed on the TiO_2 surface. The DSCs containing these dyes were compared to a N719 reference cell.[91]

8.3 Results

8.3.1 Solid state absorption spectra

For the solid-state absorption measurements, the copper(I) dyes were assembled with the ´SALSAC´[47] strategy on transparent home-made TiO_2 electrodes to give $[Cu(\mathbf{1})(\mathbf{5})]^+$, $[Cu(\mathbf{1})(\mathbf{17})]^+$, $[Cu(\mathbf{1})(\mathbf{18})]^+$, $[Cu(\mathbf{1})(\mathbf{19})]^+$ and $[Cu(\mathbf{1})(\mathbf{20})]^+$adsorbed on the electrode surfaces. The detailed procedure for screen-printing of the TiO_2 electrodes is given Section 2.2.2. The home-made TiO_2 electrodes were immersed in a 40 mM aqueous $TiCl_4$ solution at 70 °C for 30 min, rinsed with milliQ water and HPLC EtOH, dried in a stream of nitrogen and sintered at 500 °C for 30 min. After cooling, the electrodes were soaked in a 1.0 mM DMSO solution of anchoring ligand **1** for 24 h, washed with DMSO and EtOH and dried. The anchoring-ligand functionalized electrodes were then immersed into 0.1 mM CH_2Cl_2 solutions of the different homoleptic copper(I) complexes $[Cu(L_{ancillary})_2][PF_6]$ ($L_{ancillary}$ = **5**, **17**-**20**) for 3 days. After soaking in the dye bath solutions, the electrodes were taken out, washed with CH_2Cl_2 and dried in a stream of nitrogen. Figure 74 shows the background corrected and normalized solid-state

absorption spectra of the electrodes functionalized with the heteroleptic copper(I) complexes. The MLCT absorption maxima of the transparent TiO_2 electrodes functionalized with $[Cu(\mathbf{1})(\mathbf{17})]^+$ or $[Cu(\mathbf{1})[L_{ancillary})]^+$ ($L_{ancillary}$ = **5** or **18**-**21**) appeared at λ_{max} 485 nm and λ_{max} ~ 465 nm, respectively (Figure 74). The symmetrical ancillary ligand **17** substituted with 4-bromophenyl in the 4,4´-positions of the bpy unit showed the lowest absorption (Figure 74 light blue curve), followed by the dmphen (**19**), the 4,4´-di-methoxy-dmbpy (**20**) and the dmbpy (**18**) ancillary ligand. Interestingly the highest absorption in the solid-state spectrum was measured for the asymmetrical analogue of ligand **17**, ancillary ligand **5** (Figure 74 dark blue curve).

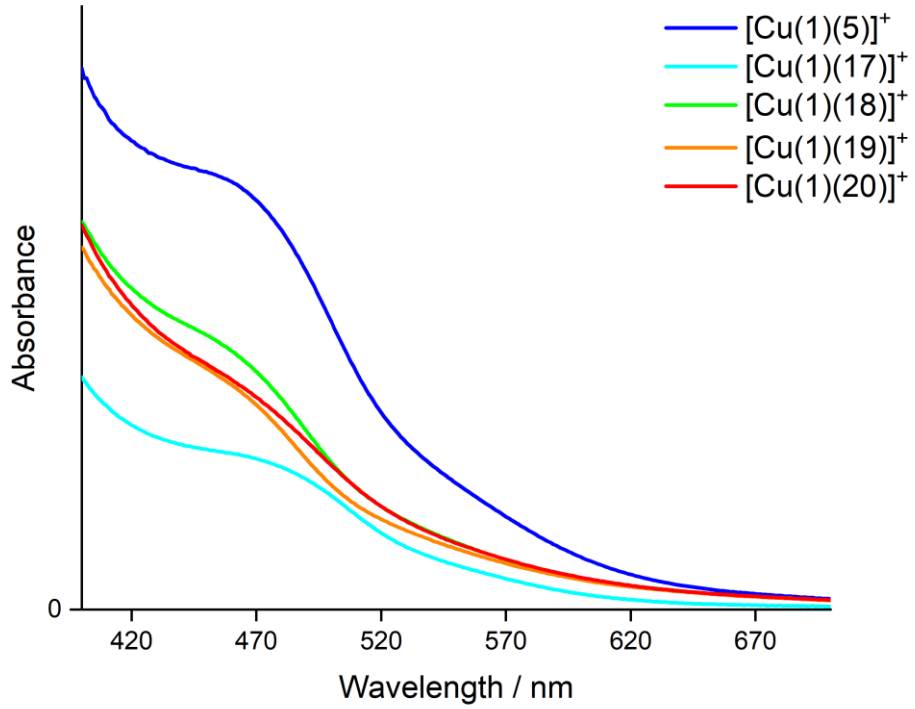

Figure 74: Solid-state absorption spectra of TiO_2 functionalized with $[Cu(1)(L_{ancillary})]^+$ ($L_{ancillary}$ = 5 or 17-20).

8.3.2 DSC performances

The heteroleptic copper(I) dyes were adsorbed on the electrode surfaces using the ´SALSAC´[47] strategy as mentioned in the last section for the solid-state absorption measurements to prepare the dye functionalized working electrodes for the DSCs. In contrast to the home-made TiO_2 electrodes used for the solid-state absorption measurements in the last section, the electrodes for building the solar cells had an additional scattering layer. Each functionalized electrode was assembled with a commercial Pt counter-electrode using a thermoplast hot-melt sealing foil. The electrolyte between the electrodes was introduced by vacuum-backfilling before the DSCs were sealed. Duplicate DSCs were prepared for each dye to confirm reproducibility of the performance parameters.

8.3.2.1 Electrolyte compositions

The copper electrolytes used in this chapter were composed of the homoleptic complexes $[Cu(L_{ancillary})_2][PF_6]$ and $[Cu(L_{ancillary})_2][PF_6]_2$ ($L_{ancillary}$ = **5** or **17**-**20**). The solvent for the electrolyte was MeCN, 4-*tert*-butylpyridine (TBP) and $LiPF_6$ were used as additives. The homoleptic copper(I) and copper(II) complexes were mixed in a 5:1 ratio, due to solubility problems of the complexes in MeCN the concentrations of the salts were different. Table 24 shows the electrolyte compositions used in this chapter.

Table 24: Compositions of the copper- electrolytes.

Electrolyte	$[Cu(L_{ancillary})_2][PF_6]$ / mol dm^{-3}	$[Cu(L_{ancillary})_2][PF_6]_2$ / mol dm^{-3}	4-*tert*-Butylpyridine / mol dm^{-3}	$LiPF_6$ / mol dm^{-3}
$[Cu(\mathbf{5})_2]^{+/2+}$	0.10	0.02	0.5	0.1
$[Cu(\mathbf{17})_2]^{+/2+}$	0.02	0.004	0.5	0.1
$[Cu(\mathbf{18})_2]^{+/2+}$	0.20	0.04	0.5	0.1
$[Cu(\mathbf{19})_2]^{+/2+}$	0.20	0.04	0.5	0.1
$[Cu(\mathbf{20})_2]^{+/2+}$	0.20	0.04	0.5	0.1

8.3.2.2 Solar cell measurements

The solar simulator measurements of the DSCs were performed in a fully-masked mode with an average area size of 0.06012 cm^2 (with a standard deviation of 1%) to avoid the influence from scattered light.[79,80] All DSCs with dyes $[Cu(\mathbf{1})(L_{ancillary})]^+$ and the electrolytes $[Cu(L_{ancillary})_2]^{+/2+}$ ($L_{ancillary}$ = **5** or **17**-**20**) were measured on the day of assembling (day 0), day 1 and day 3, but only the results of day 0 are presented here. A DSC containing N719 was prepared and measured as a reference. For a better comparison of the different dye and electrolyte combinations the relative efficiencies with respect to N719 set to 100%[72] were calculated (Table 25). The lowest cell performance was measured for DSCs with dye $[Cu(\mathbf{1})[\mathbf{17})]^+$ in combination with $[Cu(\mathbf{17})_2]^{+/2+}$ with an efficiency of 0.33% and values for the short-circuit current density (J_{SC}) of 1.10 mA/cm^2 and the open-circuit voltage (V_{OC}) of 558 mV (Figure 77 and Table 25). Changing both the dye and the electrolyte to the smaller ligand **5** resulted in a slight increase in the DSC performance to 0.61%. The change to dye $[Cu(\mathbf{1})(\mathbf{5})]^+$ in combination with $[Cu(\mathbf{5})_2]^{+/2+}$ yielded increased values in J_{SC} and V_{OC} of 1.96 mA/cm^2 and 662 mV, respectively (Figure 77 and Table 25). Although the relative efficiencies of the DSCs with dye $[Cu(\mathbf{1})(\mathbf{5})]^+$ and the electrolyte $[Cu(\mathbf{5})_2]^{+/2+}$ are low, yielding values of 11.1 and 11.5% relative to N719 set to 100%, this combination benefits from open-circuit voltages higher than those for N719 (Figure 77 and Table 25). Changing the dye from $[Cu(\mathbf{1})(\mathbf{5})]^+$ to $[Cu(\mathbf{1})(\mathbf{18})]^+$ and $[Cu(\mathbf{1})(\mathbf{19})]^+$ with the better performing electrolyte $[Cu(\mathbf{5})_2]^{+/2+}$ yielded no increase in the DSC performance parameters (ff = 43 – 52%, J_{SC} = 1.61 – 1.97 mA/cm^2 and η = 0.54 – 0.64%) but the V_{OC} values for these dye-electrolyte combinations remained high (Figure 77 and Table 25). Unfortunately

one DSC containing dye $[Cu(\mathbf{1})(\mathbf{18})]^+$ with electrolyte $[Cu(\mathbf{5})_2]^{+/2+}$ did not yield any performance (Table 25). Varying the electrolyte to $[Cu(\mathbf{18})_2]^{+/2+}$ resulted in a slight increase J_{SC} and V_{OC} with values of 1.99 – 2.43 mA/cm^2 and 624 – 784 mV, respectively, for all the dyes (Table 25). Nevertheless the fill factors (45 – 67%) and the overall cell performance remained low (Table 25). The highest overall efficiencies with this electrolyte were measured in combination with dyes $[Cu(\mathbf{1})(\mathbf{19})]^+$ and $[Cu(\mathbf{1})(\mathbf{20})]^+$ yielding 18.3% for both cells, relative to N719 set to 100%. For electrolyte $[Cu(\mathbf{19})_2]^{+/2+}$, the lowest performing dye $[Cu(\mathbf{1})(\mathbf{17})]^+$ was no longer taken into account. The combination of dyes $[Cu(\mathbf{1})(\mathbf{5})]^+$, $[Cu(\mathbf{1})(\mathbf{18})]^+$, $[Cu(\mathbf{1})(\mathbf{19})]^+$ and $[Cu(\mathbf{1})(\mathbf{20})]^+$ with electrolyte $[Cu(\mathbf{19})_2]^{+/2+}$ resulted in higher short-circuit current densities (J_{SC}) yielding values of 2.12 – 3.09 mA/cm^2 (Figure 77 and Table 25). The change to this electrolyte also led to an increase in both, the open-circuit voltages (V_{OC}) and fill factors (ff) with values of 796 – 812 mV and 68 – 74%, respectively (Figure 77 and Table 25). The best performance was measured for the DSC with dye $[Cu(\mathbf{1})(\mathbf{5})]^+$ and electrolyte $[Cu(\mathbf{19})_2]^{+/2+}$ yielding an overall efficiency of 34.3% with respect to N719 set to 100%, and the highest values in J_{SC} = 3.09 mA/cm^2 and V_{OC} = 812 mV (Figure 77 and Table 25). Even the fill factor of this dye electrolyte combination exceeded the value for the N719 reference cell (72% vs. 65%) (Table 25). The change to electrolyte $[Cu(\mathbf{20})_2]^{+/2+}$ resulted in a further improvement of the DSC performances, yielding increased values in the open-circuit voltages of 3.44 mA/cm^2 for dye $[Cu(\mathbf{1})(\mathbf{19})]^+$, 3.85 mA/cm^2 for dye $[Cu(\mathbf{1})(\mathbf{18})]^+$ and 4.01 mA/cm^2 for dye $[Cu(\mathbf{1})(\mathbf{20})]^+$ (Figure 77 and Table 25). The overall cell performances of these combinations were measured to be 33.1%, 37.7% and 38.8%, respectively, relative to N719 set to 100% (Table 25). Figure 76 shows *J-V* curves for the different dye electrolyte combinations and is an expansion of Figure 75.

In Figure 77 the *J-V* curves of DSCs containing dye $[Cu(\mathbf{1})(\mathbf{18})]^+$ in combination with the electrolytes $[Cu(\mathbf{5})_2]^{+/2+}$, $[Cu(\mathbf{18})_2]^{+/2+}$, $[Cu(\mathbf{19})_2]^{+/2+}$ and $[Cu(\mathbf{20})_2]^{+/2+}$ compared to N719 are shown. The curves depict the increase in the open-circuit voltages on changing the electrolyte exceeding the value in V_{OC} for the N719 reference cell (Figure 77). Figure 78 shows an expansion of Figure 77 illustrating the increase in V_{OC} to $\geq$ 645 mV.

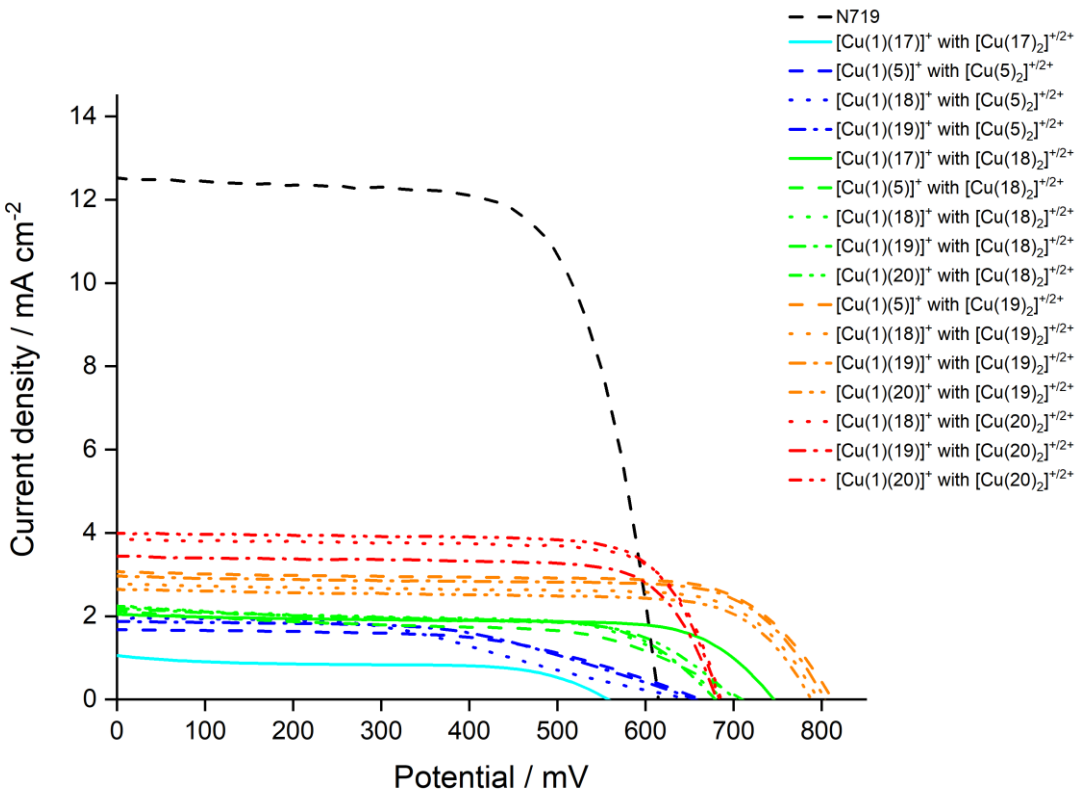

Figure 75: *J-V* curves for DSCs with dyes $[Cu(1)(L_{ancillary})]^{+}$ with the electrolytes $[Cu(L_{ancillary})_2]^{+/2+}$ ($L_{ancillary}$ = 5, 17-20) and N719 with I^-/I_3^- electrolyte measured on the day of cell assembly.

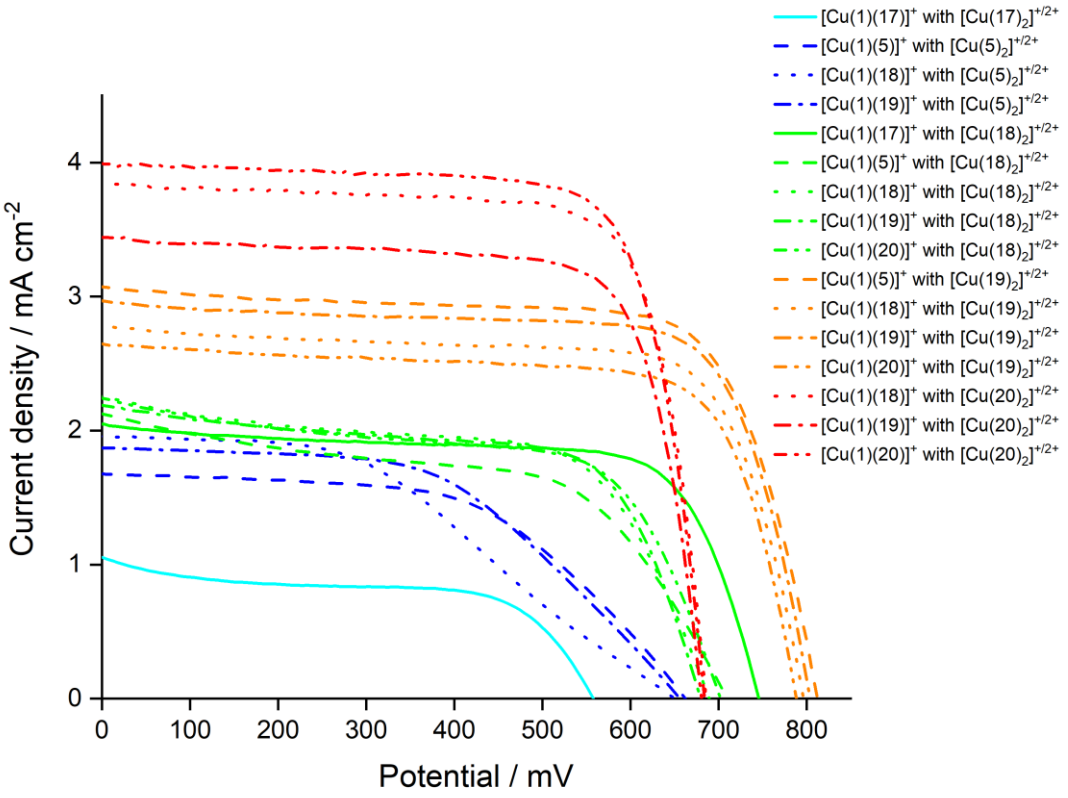

Figure 76: *J-V* curves for DSCs with dyes $[Cu(1)(L_{ancillary})]^{+}$ with the electrolytes $[Cu(L_{ancillary})_2]^{+/2+}$ ($L_{ancillary}$ = 5, 17-20) measured on the day of cell assembly (expansion of Figure 75).

Table 25: Performance parameters for duplicate DSCs with $[Cu(1)(L_{ancillary})]^+$ with the electrolytes $[Cu(L_{ancillary})_2]^{+/2+}$ ($L_{ancillary}$ = 5, 17-20) compared to N719 as reference measured on the day of cell assembly ([a] duplicate cell did not yield any performance).

Dye	Electrolyte	J_{sc}/mA cm^{-2}	V_{OC}/mV	ff/%	η/%	Relative η/%
$[Cu(\mathbf{1})(\mathbf{17})]^+$	$[Cu(\mathbf{17})_2]^{+/2+}$	1.10	558	55	0.33	6.2
$[Cu(\mathbf{1})(\mathbf{17})]^+$	$[Cu(\mathbf{17})_2]^{+/2+}$	0.96	551	49	0.26	4.9
$[Cu(\mathbf{1})(\mathbf{5})]^+$	$[Cu(\mathbf{5})_2]^{+/2+}$	1.69	662	55	0.61	11.5
$[Cu(\mathbf{1})(\mathbf{5})]^+$	$[Cu(\mathbf{5})_2]^{+/2+}$	1.64	659	54	0.59	11.1
$[Cu(\mathbf{1})(\mathbf{18})]^+$	$[Cu(\mathbf{5})_2]^{+/2+}$	1.97	648	43	0.54	10.2
$[Cu(\mathbf{1})(\mathbf{18})]^+$ [a]	$[Cu(\mathbf{5})_2]^{+/2+}$	–	–	–	–	–
$[Cu(\mathbf{1})(\mathbf{19})]^+$	$[Cu(\mathbf{5})_2]^{+/2+}$	1.88	655	52	0.64	12.1
$[Cu(\mathbf{1})(\mathbf{19})]^+$	$[Cu(\mathbf{5})_2]^{+/2+}$	1.61	647	52	0.54	10.2
$[Cu(\mathbf{1})(\mathbf{17})]^+$	$[Cu(\mathbf{18})_2]^{+/2+}$	2.14	784	66	1.12	21.1
$[Cu(\mathbf{1})(\mathbf{17})]^+$	$[Cu(\mathbf{18})_2]^{+/2+}$	1.99	645	67	0.86	16.2
$[Cu(\mathbf{1})(\mathbf{5})]^+$	$[Cu(\mathbf{18})_2]^{+/2+}$	2.15	710	55	0.84	15.8
$[Cu(\mathbf{1})(\mathbf{5})]^+$	$[Cu(\mathbf{18})_2]^{+/2+}$	2.43	624	50	0.75	14.1
$[Cu(\mathbf{1})(\mathbf{18})]^+$	$[Cu(\mathbf{18})_2]^{+/2+}$	2.29	689	60	0.95	17.9
$[Cu(\mathbf{1})(\mathbf{18})]^+$	$[Cu(\mathbf{18})_2]^{+/2+}$	2.20	698	47	0.72	13.6
$[Cu(\mathbf{1})(\mathbf{19})]^+$	$[Cu(\mathbf{18})_2]^{+/2+}$	2.21	679	64	0.97	18.3
$[Cu(\mathbf{1})(\mathbf{19})]^+$	$[Cu(\mathbf{18})_2]^{+/2+}$	2.16	715	55	0.86	16.2
$[Cu(\mathbf{1})(\mathbf{20})]^+$	$[Cu(\mathbf{18})_2]^{+/2+}$	2.27	702	61	0.97	18.3
$[Cu(\mathbf{1})(\mathbf{20})]^+$	$[Cu(\mathbf{18})_2]^{+/2+}$	2.02	668	45	0.61	11.5
$[Cu(\mathbf{1})(\mathbf{5})]^+$	$[Cu(\mathbf{19})_2]^{+/2+}$	3.09	812	72	1.82	34.3
$[Cu(\mathbf{1})(\mathbf{5})]^+$	$[Cu(\mathbf{19})_2]^{+/2+}$	2.90	796	74	1.72	32.4
$[Cu(\mathbf{1})(\mathbf{18})]^+$	$[Cu(\mathbf{19})_2]^{+/2+}$	2.80	796	73	1.63	30.7
$[Cu(\mathbf{1})(\mathbf{18})]^+$	$[Cu(\mathbf{19})_2]^{+/2+}$	2.78	802	73	1.62	30.5
$[Cu(\mathbf{1})(\mathbf{19})]^+$	$[Cu(\mathbf{19})_2]^{+/2+}$	2.98	804	74	1.76	33.1
$[Cu(\mathbf{1})(\mathbf{19})]^+$	$[Cu(\mathbf{19})_2]^{+/2+}$	2.74	803	74	1.61	30.3
$[Cu(\mathbf{1})(\mathbf{20})]^+$	$[Cu(\mathbf{19})_2]^{+/2+}$	2.66	788	73	1.53	28.8
$[Cu(\mathbf{1})(\mathbf{20})]^+$	$[Cu(\mathbf{19})_2]^{+/2+}$	2.12	812	68	1.17	22.0
$[Cu(\mathbf{1})(\mathbf{18})]^+$	$[Cu(\mathbf{20})_2]^{+/2+}$	3.85	686	76	2.00	37.7
$[Cu(\mathbf{1})(\mathbf{18})]^+$	$[Cu(\mathbf{20})_2]^{+/2+}$	3.78	695	75	1.96	36.9
$[Cu(\mathbf{1})(\mathbf{19})]^+$	$[Cu(\mathbf{20})_2]^{+/2+}$	3.44	681	75	1.76	33.1
$[Cu(\mathbf{1})(\mathbf{19})]^+$	$[Cu(\mathbf{20})_2]^{+/2+}$	3.28	6.69	74	1.63	30.7
$[Cu(\mathbf{1})(\mathbf{20})]^+$	$[Cu(\mathbf{20})_2]^{+/2+}$	4.01	684	75	2.06	38.8
$[Cu(\mathbf{1})(\mathbf{20})]^+$	$[Cu(\mathbf{20})_2]^{+/2+}$	3.72	674	61	1.54	29.0
N719	I^-/I_3^-	13.63	602	65	5.31	100

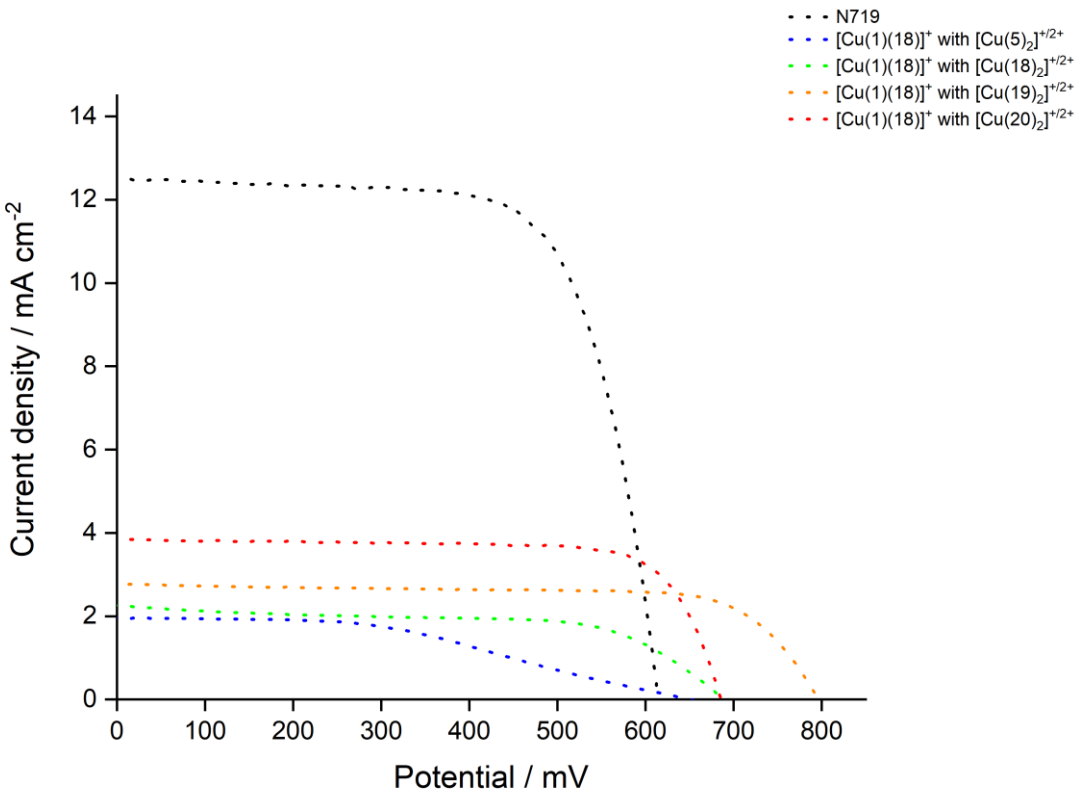

Figure 77: *J-V* curves for DSCs with dyes $[Cu(1)(18)]^+$ and the electrolytes $[Cu(L_{ancillary})_2]^{+/2+}$ ($L_{ancillary}$ = 5, 17-20) and N719 with I^-/I_3^- electrolyte measured on the day of cell assembly.

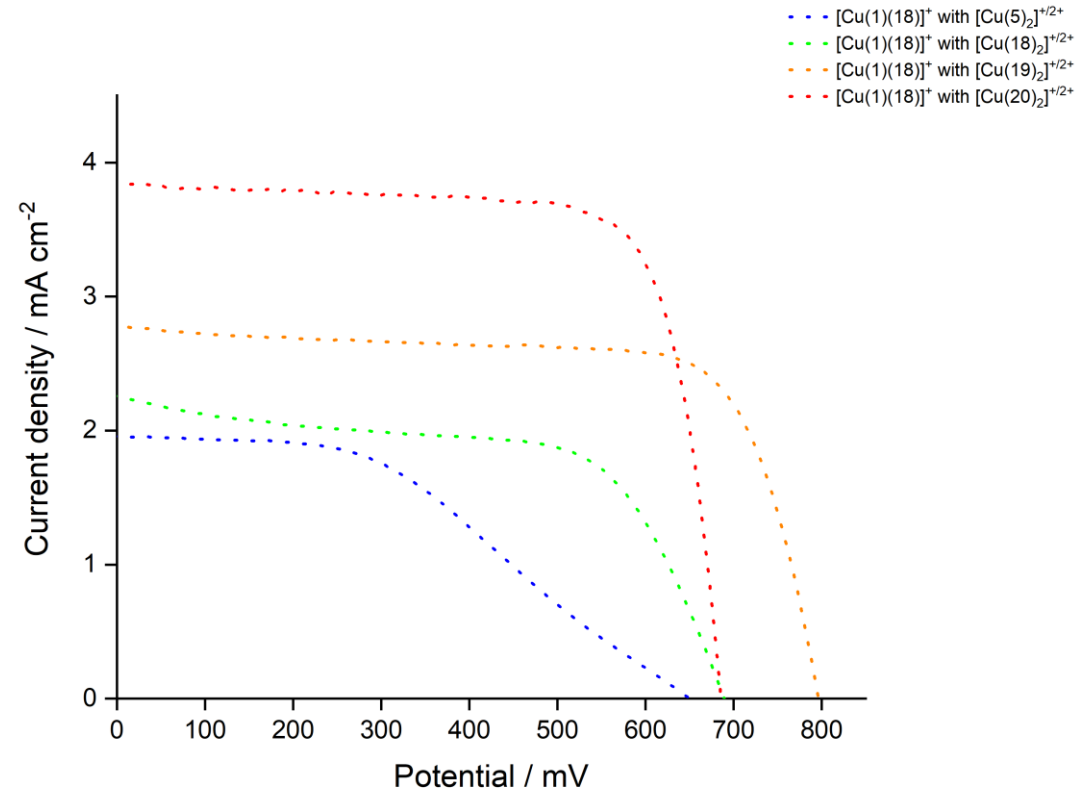

Figure 78: *J-V* curves for DSCs with dyes $[Cu(1)(18)]^+$ and the electrolytes $[Cu(L_{ancillary})_2]^{+/2+}$ ($L_{ancillary}$ = 5, 17-20) measured on the day of cell assembly (expansion of Figure 77).

8.3.2.3 External Quantum Efficiency (EQE) measurements

Figure 79 shows the EQE spectra of the best performing cells with dyes $[Cu(\mathbf{1})(L_{ancillary})]^{+}$ in combination with the electrolytes $[Cu(L_{ancillary})_2]^{+/2+}$ ($L_{ancillary}$ = **18**-**20**). The EQE spectra (Figure 79) reflect the trends in the J_{SC} data from the solar simulator measurements discussed in the last section (Figure 76 and Table 25). On varying the ligand in the electrolyte from **18** to **19** or **20**, the photon to current conversion efficiencies increased almost independently of the dye used in the DSCs (Figure 79). The lower EQE spectra for DSCs with electrolyte $[Cu(\mathbf{18})_2]^{+/2+}$ (Figure 79 green curves) reflect the lower values in short-circuit current density found in the solar simulator measurements for DSCs containing this electrolyte. These cells yielded the lowest EQE_{max} values of 23.8% for $[Cu(\mathbf{1})(\mathbf{18})]^{+}$ at λ_{max} 480 nm, 25.3% for $[Cu(\mathbf{1})(\mathbf{19})]^{+}$ at λ_{max} 470 nm and 26.6% for $[Cu(\mathbf{1})(\mathbf{20})]^{+}$ at λ_{max} 470 nm (Table 26). The EQE_{max} values for DSCs containing electrolyte $[Cu(\mathbf{19})_2]^{+/2+}$ were measured to be 33.6% for $[Cu(\mathbf{1})(\mathbf{18})]^{+}$, 34.5% for $[Cu(\mathbf{1})(\mathbf{19})]^{+}$ and 30.7% for $[Cu(\mathbf{1})(\mathbf{20})]^{+}$ at λ_{max} 490 nm (Table 26). The DSCs with electrolyte $[Cu(\mathbf{20})_2]^{+/2+}$ yielded EQE_{max} values of 34.1, 31.1 and 34.6% at λ_{max} 480 nm on varying the ancillary ligand from **18** to **19** to **20**, respectively (Table 26).

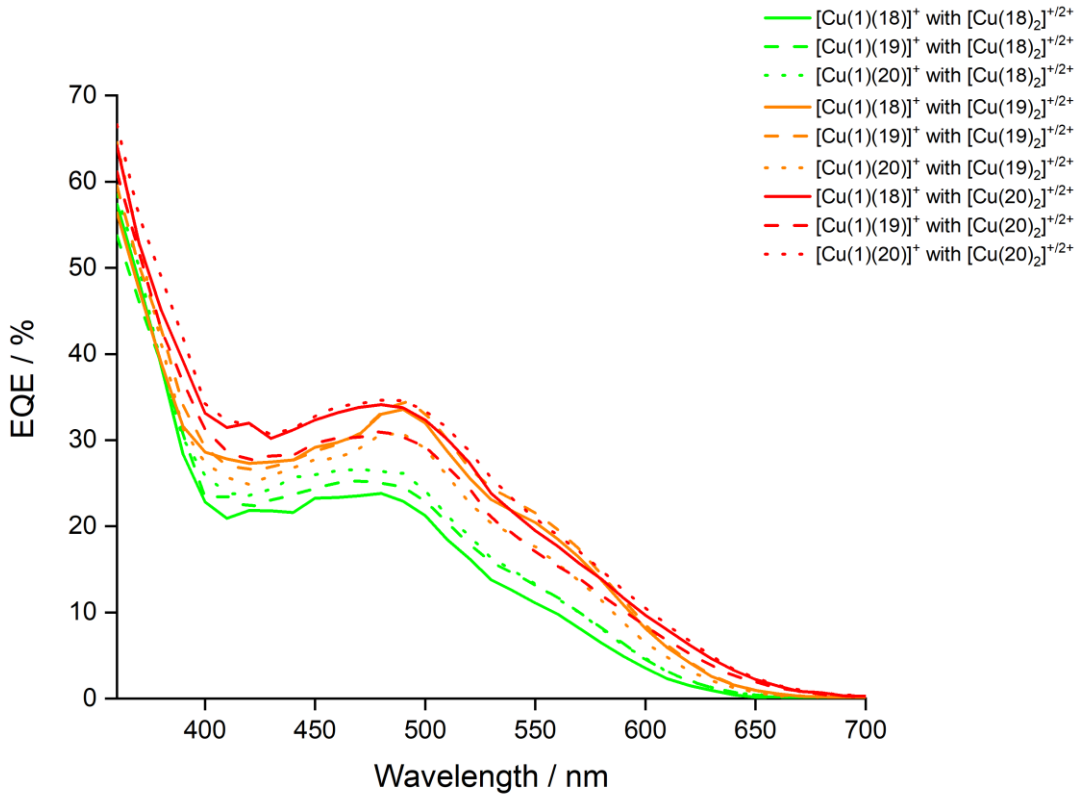

Figure 79: EQE spectra of DSCs with dyes $[Cu(1)(L_{ancillary})]^{+}$ and the electrolytes $[Cu(L_{ancillary})_2]^{+/2+}$ ($L_{ancillary}$ = 18-20).

Table 26: EQE maxima values for DSCs with dyes $[Cu(1)(L_{ancillary})]^+$ and the electrolytes $[Cu(L_{ancillary})_2]^{+/2+}$ ($L_{ancillary}$ = 18-20).

Dye	Electrolyte	λ_{max} / nm	EQE_{max} / %
$[Cu(\mathbf{1})(\mathbf{18})]^+$	$[Cu(\mathbf{18})_2]^{+/2+}$	480	23.8
$[Cu(\mathbf{1})(\mathbf{19})]^+$	$[Cu(\mathbf{18})_2]^{+/2+}$	470	25.3
$[Cu(\mathbf{1})(\mathbf{20})]^+$	$[Cu(\mathbf{18})_2]^{+/2+}$	470	26.6
$[Cu(\mathbf{1})(\mathbf{18})]^+$	$[Cu(\mathbf{19})_2]^{+/2+}$	490	33.6
$[Cu(\mathbf{1})(\mathbf{19})]^+$	$[Cu(\mathbf{19})_2]^{+/2+}$	490	34.5
$[Cu(\mathbf{1})(\mathbf{20})]^+$	$[Cu(\mathbf{19})_2]^{+/2+}$	490	30.7
$[Cu(\mathbf{1})(\mathbf{18})]^+$	$[Cu(\mathbf{20})_2]^{+/2+}$	480	34.1
$[Cu(\mathbf{1})(\mathbf{19})]^+$	$[Cu(\mathbf{20})_2]^{+/2+}$	480	31.1
$[Cu(\mathbf{1})(\mathbf{20})]^+$	$[Cu(\mathbf{20})_2]^{+/2+}$	480	34.6

8.4 Conclusion

This chapter gives a short insight into our first investigation of the combination of heteroleptic copper(I) complexes $[Cu(\mathbf{1})(L_{ancillary})]^+$ ($L_{ancillary}$ = **5** or **17**-**20**) used as sensitizer for DSCs together with homoleptic copper(I)/(II) complexes ($[Cu(L_{ancillary})_2]^{+/2+}$, $L_{ancillary}$ = **5** or **17**-**20**) as the redox couple in the electrolyte. The results in this chapter show that the performances of the cells are dependent of the electrolyte, with increasing overall efficiencies on changing the electrolyte from $[Cu(\mathbf{20})_2]^{+/2+}$ > $[Cu(\mathbf{19})_2]^{+/2+}$ >$[Cu(\mathbf{18})_2]^{+/2+}$ >$[Cu(\mathbf{5})_2]^{+/2+}$ >$[Cu(\mathbf{17})_2]^{+/2+}$. In the same order an increase in the J_{SC} was found to be essentially independent of the sensitizer used in the DSCs. Furthermore, high values in the V_{OC} were found for DSCs with electrolytes $[Cu(\mathbf{20})_2]^{+/2+}$, $[Cu(\mathbf{19})_2]^{+/2+}$, $[Cu(\mathbf{18})_2]^{+/2+}$ and $[Cu(\mathbf{5})_2]^{+/2+}$ outperforming the values for the N719 reference cell with the commonly used I^-/I_3^- electrolyte. The best relative efficiency was measured for a DSC containing dye $[Cu(\mathbf{1})(\mathbf{20})]^+$ in combination with $[Cu(\mathbf{20})_2]^{+/2+}$ in the electrolyte, yielding a value of 38.8% compared to N719 set at 100%.

To conclude this chapter it can be seen that the redox shuttle in the electrolyte has an enormous effect on the cell performance. The electrolytes used in this chapter gave promising results in terms of increasing the open-circuit voltage of the DSCs. Furthermore using the same ligand for both, the heteroleptic copper(I) complex used as dye and the homoleptic analogues in the electrolyte can be beneficial providing a source of the ancillary ligand to regenerate the dye on the surface.[75,83]

At the time that this work was submitted for publication,[58] Dragonetti et al also published a study of the combination of copper(I) dyes (assembled using the HETPHEN approach) and $Cu^{+/2+}$ electrolytes.[59]

Chapter 9

Chapter 9 Tandem dye-sensitized solar cells

9.1 Motivation

As demonstrated in earlier chapters changing and improving the dye or the electrolyte can increase the efficiency of DSCs. Nevertheless bis(diimine)copper(I) dyes still struggle with lower photon to current conversion efficiencies and the lack of photoconversion efficiency at longer wavelength compared to the benchmark ruthenium dye N719, as demonstrated in several EQE spectra in earlier chapters of this thesis. However the results presented earlier are based on DSCs functionalized with only one light-absorbing dye. One strategy to overcome the problem of a low spectral response is the co-sensitization with a second dye absorbing at longer wavelengths to increase the photoconversion efficiency.[53] Another way to incorporate this multi-dye strategy is to change the architecture of the DSC, building devices where both electrodes feature photoactivity, a so-called tandem dye-sensitized solar cell.[11,111,112,113] With the investigation of the copper electrolytes presented in Chapter 8 the first step towards a tandem DSC was completed, because the resulting short-circuit current densities were similar to the values reported for the p-type DSCs[18] studied by Nathalie Marinakis from our research group. This chapter gives a preliminary insight into the tandem DSCs containing a bis(diimine) copper(I) dye to sensitize the n-type TiO_2 photoanode and a NiO photocathode functionalized with a ruthenium based dye[18] or the commercially available **P1**[18] dye in combination with the Cu^{+}/Cu^{2+} redox shuttle reported in Chapter 8 as the electrolyte[58].

The work investigated in this chapter was done in collaboration with Nathalie Marinakis the specialist for p-type DSCs within our research group.

9.2 Ligands and dyes

Scheme 73 shows the **ALP1** anchoring ligand (**1**)[75] used to assemble the heteroleptic dyes adsorbed on the TiO_2 surfaces. The synthesis of this anchoring ligand (**1**) was presented in the experimental part of Chapter 3 and DSC performances using **ALP1** (**1**) in heteroleptic bis(diimine)copper(I) dyes with the same ancillary ligands used in this chapter were presented in Chapter 8. The structure of the ancillary ligands used in the heteroleptic copper(I) dyes are shown in Scheme 74. Moreover ligand **19** (Scheme 74) was used as ligand in the homoleptic copper(I)/(II) redox shuttle in the electrolyte[58]. The homoleptic copper(I) complexes of the ligands shown in Scheme 74 were used in the dye bath solutions to get the heteroleptic copper(I) complexes $[Cu(\mathbf{1})(L_{ancillary})]^{+}$ ($L_{ancillary}$ = **18**-**20**) and adsorbed on the TiO_2 surfaces.

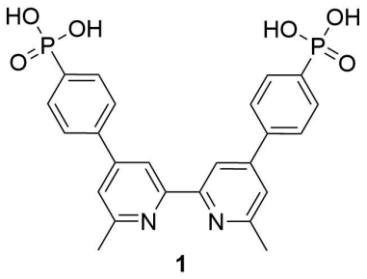

Scheme 73: Structure of the ALP1 anchoring ligand (1).

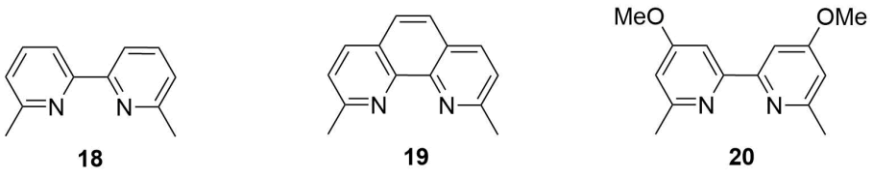

Scheme 74: Structures of ligands 18-20 used as ancillary ligands in the dyes and in homoleptic copper(I)/(II) redox couples in the electrolyte for ligand 19.

In Scheme 75 the structure of the heteroleptic copper(I) complexes $[Cu(\mathbf{1})(\mathbf{18})]^+$, $[Cu(\mathbf{1})(\mathbf{19})]^+$and $[Cu(\mathbf{1})(\mathbf{20})]^+$ adsorbed on the TiO_2 surfaces for the n-type working electrodes are shown.

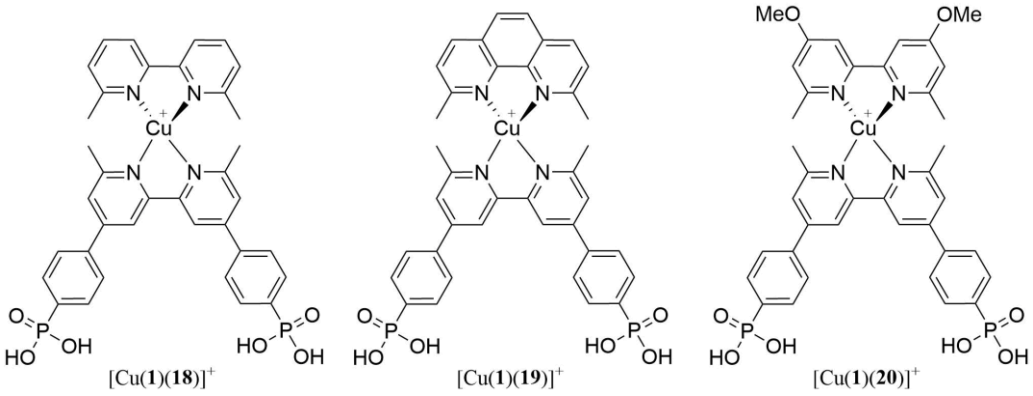

Scheme 75: Structures of the heteroleptic copper(I) complexes adsorbed on the electrode surfaces used as dyes for the n-type working electrodes.

Scheme 76 shows the structure of the dyes **21** and **P1** (**22**) used to functionalize the p-type working electrodes.

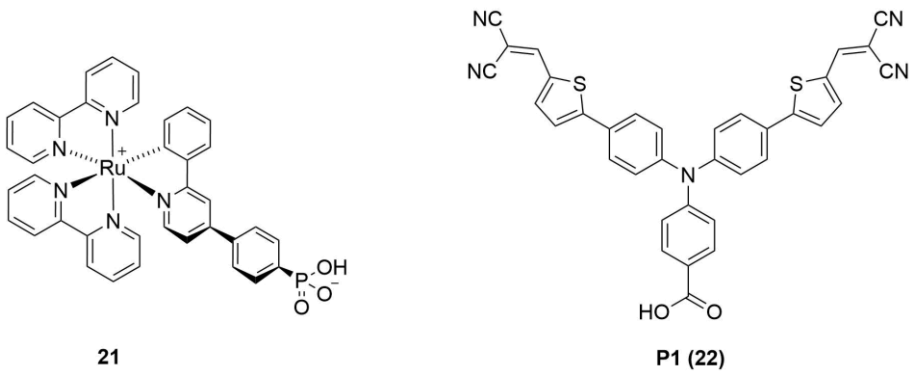

Scheme 76: Structures of the dyes 21 and P1 (22) used to functionalize the p-type working electrodes.

9.3 Electrode preparation

9.3.1 TiO_2 working electrode

The n-type working electrodes for the tandem DSCs were prepared using the screen-printing method described in Section 2.2.2. In order to introduce the electrolyte between the two working electrodes (TiO_2 and NiO working electrodes) by vacuum back-filling after DSC assembling, a hole was drilled into the FTO glass after screen-printing.

9.3.2 NiO working electrode

The NiO working electrodes used as the n-type side for the tandem DSCs were prepared by Nathalie Marinakis using the screen-printing method, similar to the preparation of TiO_2 electrodes described in Section 2.2.2.

The FTO glass plate was cleaned by sonicating in a 2% surfactant solution in milliQ water (Sonoswiss cleaner, SW-C L2) and rinsed with milliQ water and EtOH. After surface activation in a UV-O_3 system (Model 256-220, Jetlight Company Inc) for 20 min, the glass was immersed five times in a 0.5 mM MeCN solution of [Ni(acac)$_2$] and dried in air after each dipping step. A layer of NiO paste (Ni-Nanoxide N/SP, Solaronix) was then screen-printed (90T, Serelith AG, Switzerland) onto the glass plate. The printed plate was placed into an EtOH chamber for 3 min to reduce surface irregularities and then dried at 125 °C for 3 min on a heating plate. This process was repeated to give two layer of NiO screen-printed on the glass substrate. The electrodes were then sintered by gradually heating from room temperature to 350 °C over a period of 30 min, kept at 350 °C for 30 min and allowed to cool to room temperature.[18]

9.4 Results

9.4.1 Solid state absorption spectra

The solid-state absorption spectra of functionalized TiO_2 and NiO working electrodes with dyes [Cu(**1**)(**18**)]$^+$, [Cu(**1**)(**19**)]$^+$, **21** or **P1** (**22**), respectively, are not presented in this chapter. The solid-state absorption spectra for the functionalized n-type[58] and the p-type[17] working electrodes have been published. [Cu(**1**)(**18**)]$^+$ and [Cu(**1**)(**19**)]$^+$ show absorption maxima at ~ 465 nm, and **21** and **P1** (**22**) at λ_{max} ~ 500 and ~ 560 nm and at λ_{max} ~ 525 nm, respectively.

9.4.2 DSC performances

9.4.2.1 Preparation of the dye adsorbed n-type working electrodes

The heteroleptic copper(I) dyes were assembled on the TiO_2 electrodes using the ´surface-as-ligand, surface-as-complex´ strategy[47] (´SALSAC´ strategy) described in section 2.2.5.1, to give [Cu(**1**)(**18**)]$^+$, [Cu(**1**)(**19**)]$^+$ and [Cu(**1**)(**20**)]$^+$ adsorbed on the electrode surfaces. The screen-printed TiO_2 electrodes

were immersed in a 40 mM aqueous $TiCl_4$ solution at 70 °C for 30 min, rinsed with milliQ water and HPLC grade EtOH, dried in a stream of nitrogen and sintered at 500 °C for 30 min. After cooling, the electrodes were soaked in a 1.0 mM DMSO solution of anchoring ligand **1** for 24 h, washed with DMSO and EtOH and dried. The anchoring-ligand functionalized electrodes were then immersed into 0.1 mM CH_2Cl_2 solutions of the different homoleptic copper(I) complexes $[Cu(L_{ancillary})_2][PF_6]$ ($L_{ancillary}$ = **18**-**20**) for 3 days. After soaking in the dye bath solutions, the electrodes were taken out, washed with CH_2Cl_2 and dried in a stream of nitrogen.

9.4.2.2 Preparation of the dye adsorbed p-type working electrodes

The p-type working electrodes were heated at 250 °C for 20 min and then cooled to 80 °C before immersing them into a 0.1 mM EtOH solution of **21** or a 0.3 mM MeCN solution of **P1** (**22**) overnight. After removing from the dye bath solutions the electrodes were washed with EtOH and dried in a stream of nitrogen.[18]

9.4.2.3 DSC assembly

The dye-functionalized n- and p-type working electrodes were assembled using a thermoplast hot-melt sealing foil. The electrolyte between the electrodes was introduced by vacuum-backfilling before the tandem DSCs were sealed. Duplicate tandem DSCs were prepared for each dye to confirm reproducibility of the performance parameters.

9.4.2.4 Electrolyte composition

The $Cu^{+/2+}$ electrolyte used in this chapter was composed of the homoleptic complexes $[Cu(\mathbf{19})_2][PF_6]$ and $[Cu(\mathbf{19})_2][PF_6]_2$. The solvent for the electrolyte was MeCN, 4-*tert*-butylpyridine (TBP) and $LiPF_6$ were used as additives. The homoleptic copper(I) and copper(II) complexes were mixed in a 5:1 ratio. Table 27 shows the electrolyte composition used for the tandem DSCs.

Table 27: Composition of the copper-based electrolyte.

Electrolyte	$[Cu(L_{ancillary})_2][PF_6]$ / mol dm^{-3}	$[Cu(L_{ancillary})_2][PF_6]_2$ / mol dm^{-3}	4-*tert*-Butylpyridine / mol dm^{-3}	$LiPF_6$ / mol dm^{-3}
$[Cu(\mathbf{19})_2]^{+/2+}$	0.20	0.04	0.5	0.1

9.4.2.5 Solar cell measurements

The solar simulator measurements of the DSCs were performed in a fully-masked mode with an average area size of 0.06012 cm^2 (with a standard deviation of 1%) to avoid influences from scattered light.[79,80] The tandem DSCs were irradiated from the n-type side. A DSC containing N719 was prepared and measured as reference. For a better comparison of the different dye combinations, the relative efficiencies with respect to N719 set to 100%[72] were calculated (Table 28). The lowest

performance was measured for tandem DSCs with the n-type dye [Cu(**1**)(**20**)]$^+$ in combination with the p-type dye **21** with an efficiency of 0.96% and values for the short-circuit current density (J_{SC}) of 1.89 mA/cm^2 and the open-circuit voltage (V_{OC}) of 747 mV (Figure 80 and Table 28). Unfortunately one tandem DSC with the dyes [Cu(**1**)(**20**)]$^+$ for the n-type side and dye **21** for the p-type side yielded a very low performance which could come from problems in cell assembly. Changing the n-type dye to [Cu(**1**)(**18**)]$^+$ and the p-type dye to the well-performing **P1** dye, resulted in an increase in the efficiency to 1.34% with a higher value for J_{SC} of 2.62 mA/cm^2 but a slight decrease in the V_{OC} with a value of 711 mV (Figure 80 and Table 28). The overall cell performances of these combinations were measured to be 24.8 and 25.4%, respectively, compared to N719 set to 100% (Table 28). On varying the p-type dye to **21** resulted in a further increase in the efficiency to 1.50% (Figure 80 and Table 28). While this dye combination showed a slight decrease in the J_{SC} to 2.47 mA/cm^2, the value in V_{OC} increased to over 803 mV (Table 28). The change of the p-type dye resulted in a further increase of the overall cell performances yielding values of 26.5 and 28.4%, respectively, compared to N719 set to 100% (Table 28). Changing the n-type dye to [Cu(**1**)(**18**)]$^+$ resulted in the best performing tandem DSC yielding an overall efficiency of 35.0% with respect to N719 set to 100%, and the highest values in J_{SC} = 2.99 mA/cm^2 and V_{OC} = 816 mV (Figure 80 and Table 28). Unfortunately the duplicate tandem DSC with this dye combination did not yield similar high performances (Table 28), which might be a reason of problems in cell assembly. The fill factors (ff) for all tandem DSCs were in a good range of 65-76% (Table 28). Figure 81 shows *J-V* curves for the different dye combinations for the n-type- and the p-type dyes and is an expansion of Figure 80. In Table 29 the performance parameters of duplicate DSCs with dye [Cu(**1**)(**18**)]$^+$ in combination with electrolyte [Cu(**19**)$_2$]$^{+/2+}$ investigated in Chapter 8 are shown for comparison. The V_{OC} of the tandem DSCs presented here are similar to the values of the all-copper cells presented in Chapter 8 (Table 28 and Table 29). The J_{SC} of the tandem cells are slightly lower which also affects the value of the overall efficiencies of the tandem DSCs. The values for the ff are in a similar range (Table 28 and Table 29).

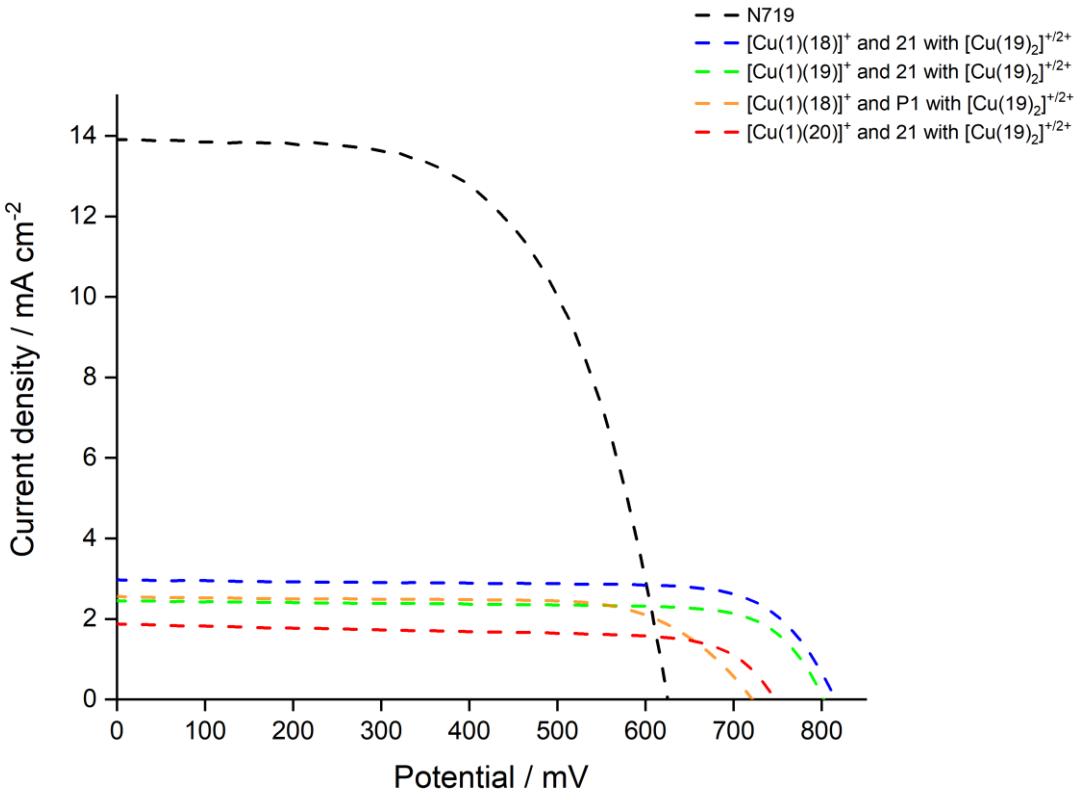

Figure 80: *J-V* Curves for tandem DSCs with n-type dyes $[Cu(1)(18)]^+$, $[Cu(1)(19)]^+$ and $[Cu(1)(20)]^+$ and p-type dyes 21 and P1 (22) with electrolyte $[Cu(19)_2]^{+/2+}$ and N719 with I^-/I_3^- electrolyte measured on the day of cell assembly.

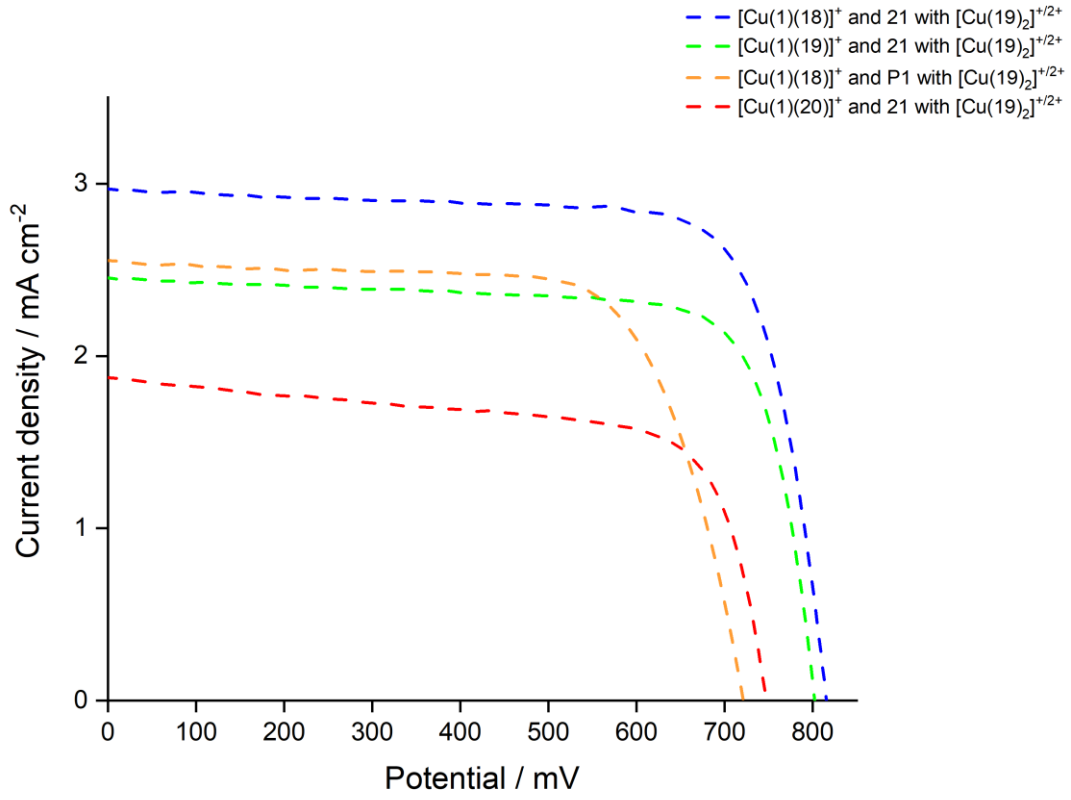

Figure 81: *J-V* Curves for tandem DSCs with n-type dyes $[Cu(1)(18)]^+$, $[Cu(1)(19)]^+$ and $[Cu(1)(20)]^+$ and p-type dyes 21 and P1 (22) with electrolyte $[Cu(19)_2]^{+/2+}$ measured on the day of cell assembly (expansion of Figure 80).

Table 28: Performance parameters for duplicate tandem DSCs with n-type dyes $[Cu(1)(18)]^+$, $[Cu(1)(19)]^+$ and $[Cu(1)(20)]^+$ and p-type dyes 21 and P1 (22) with electrolyte $[Cu(19)_2]^{+/2+}$ compared to N719 as reference measured on the day of cell assembly.

Dye n-type side	Dye p-type side	Electrolyte	J_{sc}/mA cm^{-2}	V_{OC}/mV	ff/%	η/%	Relative η/%
$[Cu(\mathbf{1})(\mathbf{18})]^+$	**21**	$[Cu(\mathbf{19})_2]^{+/2+}$	2.99	816	76	1.85	35.0
$[Cu(\mathbf{1})(\mathbf{18})]^+$	**21**	$[Cu(\mathbf{19})_2]^{+/2+}$	2.43	798	66	1.27	24.1
$[Cu(\mathbf{1})(\mathbf{19})]^+$	**21**	$[Cu(\mathbf{19})_2]^{+/2+}$	2.41	801	73	1.40	26.5
$[Cu(\mathbf{1})(\mathbf{19})]^+$	**21**	$[Cu(\mathbf{19})_2]^{+/2+}$	2.47	803	76	1.50	28.4
$[Cu(\mathbf{1})(\mathbf{18})]^+$	**P1 (22)**	$[Cu(\mathbf{19})_2]^{+/2+}$	2.57	721	70	1.31	24.8
$[Cu(\mathbf{1})(\mathbf{18})]^+$	**P1 (22)**	$[Cu(\mathbf{19})_2]^{+/2+}$	2.62	711	72	1.34	25.4
$[Cu(\mathbf{1})(\mathbf{20})]^+$	**21**	$[Cu(\mathbf{19})_2]^{+/2+}$	1.89	747	68	0.96	18.2
$[Cu(\mathbf{1})(\mathbf{20})]^+$	**21**	$[Cu(\mathbf{19})_2]^{+/2+}$	1.01	645	31	0.20	3.8
N719		I^-/I_3^-	13.93	625	61	5.28	100

Table 29: Performance parameters for duplicate DSCs containing dye $[Cu(1)(18)]^+$ and electrolyte $[Cu(19)_2]^{+/2+}$ measured on the day of cell assembly for comparison with the tandem DSCs.

Dye	Electrolyte	J_{sc}/mA cm^{-2}	V_{OC}/mV	ff/%	η/%	Relative η/%
$[Cu(\mathbf{1})(\mathbf{18})]^+$	$[Cu(\mathbf{19})_2]^{+/2+}$	2.80	796	73	1.63	30.7
$[Cu(\mathbf{1})(\mathbf{18})]^+$	$[Cu(\mathbf{19})_2]^{+/2+}$	2.78	802	73	1.62	30.5

9.4.2.6 External Quantum Efficiency (EQE) measurements

Figure 82 shows the EQE spectra of the tandem DSCs with the n-type dyes $[Cu(\mathbf{1})(\mathbf{18})]^+$, $[Cu(\mathbf{1})(\mathbf{19})]^+$ and $[Cu(\mathbf{1})(\mathbf{20})]^+$ and the p-type dyes **21** and **P1** (**22**) in combination with $[Cu(\mathbf{19})_2]^{+/2+}$ as the electrolyte. In order to show both photon to current conversion efficiencies, the one of the n-type working electrode and the one of the p-type working electrode, the tandem DSCs were measured from both sides. The EQE spectra (Figure 82) reflect the trends of the J_{SC} data from the solar simulator measurements discussed in the last section. The lowest EQE spectrum was measured for the tandem DSCs with $[Cu(\mathbf{1})(\mathbf{20})]^+$ as the n-type dye and **21** as the p-type dye for both working electrodes (Figure 82 red curves and Figure 86). The EQE_{max} values were measured to be 20.6% at λ_{max} 480 nm for the n-type side and 1.2% at λ_{max} 580 nm for the p-type side (Table 30). Changing the n-type dye to $[Cu(\mathbf{1})(\mathbf{18})]^+$ and the p-type dye to **P1** yielded an increase in the EQE spectra (Figure 82 orange curve and Figure 85) which is in accordance with the data from the solar simulator measurements discussed in the last section. The EQE_{max} values of the tandem DSC with this dye combination were 26.1% at λ_{max} 480 nm for the n-type side and 2.3% at λ_{max} 600 nm for the p-type side (Table 30). The EQE spectra of the tandem cell with dyes $[Cu(\mathbf{1})(\mathbf{19})]^+$ and **21** showed a slight increase for the n-type side with a slightly higher EQE_{max} value of 26.8% at λ_{max} 498 nm, but slight decrease for the p-type side EQE_{max} values of 2.1% at λ_{max} 590 nm (Figure 82 green curves, Figure 84 and Table 30). The best

performing tandem DSC also shows the highest photon to current conversion efficiencies in the EQE spectra (Figure 82 blue curves and Figure 83). The tandem DSC with the n-type dye [Cu(**1**)(**18**)]$^+$ and the p-type dye **21** yielded EQE_{max} values of 34.0% at λ_{max} 490 nm and 5.0% at λ_{max} 590 nm, respectively (Table 30). Figure 83 to Figure 86 show the direct comparison of the EQE spectra of the n-type side and the p-type side of each tandem DSCs. The λ_{max} measured in the EQE spectra for the p-type dye **21** and **P1** (**22**) were in accordance with the solid-state absorption maxima for these dyes reported in literature.[17]

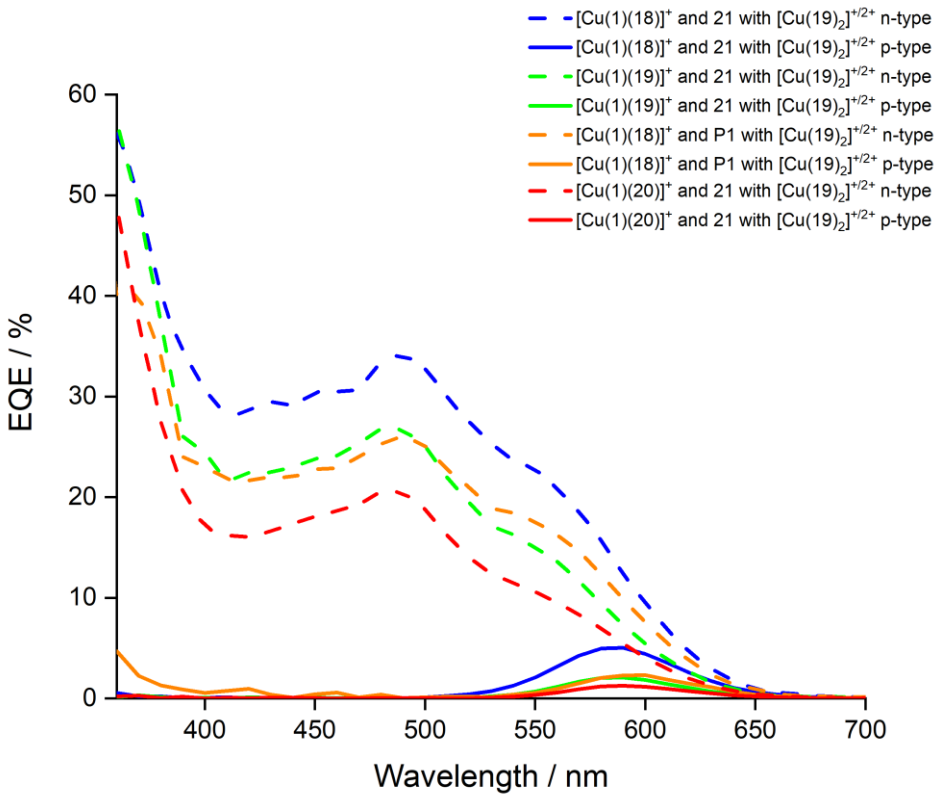

Figure 82: EQE spectra of tandem DSCs with n-type dyes [Cu(1)(18)]$^+$, [Cu(1)(19)]$^+$ and [Cu(1)(20)]$^+$ and p-type dyes 21 and P1 (22) with electrolyte $[Cu(19)_2]^{+/2+}$.

Table 30: EQE maxima values for tandem DSCs with n-type dyes $[Cu(1)(18)]^+$, $[Cu(1)(19)]^+$ and $[Cu(1)(20)]^+$ and p-type dyes 21 and P1 (22) with electrolyte $[Cu(19)_2]^{+/2+}$.

Electrode	Dye n-type side	Dye p-type side	Electrolyte	λ_{max} / nm	EQE_{max} / %
n-type	$[Cu(\mathbf{1})(\mathbf{18})]^+$	**21**	$[Cu(\mathbf{19})_2]^{+/2+}$	490	34.0
p-type	$[Cu(\mathbf{1})(\mathbf{18})]^+$	**21**	$[Cu(\mathbf{19})_2]^{+/2+}$	590	5.0
n-type	$[Cu(\mathbf{1})(\mathbf{19})]^+$	**21**	$[Cu(\mathbf{19})_2]^{+/2+}$	480	26.8
p-type	$[Cu(\mathbf{1})(\mathbf{19})]^+$	**21**	$[Cu(\mathbf{19})_2]^{+/2+}$	590	2.1
n-type	$[Cu(\mathbf{1})(\mathbf{18})]^+$	**P1 (22)**	$[Cu(\mathbf{19})_2]^{+/2+}$	490	26.1
p-type	$[Cu(\mathbf{1})(\mathbf{18})]^+$	**P1 (22)**	$[Cu(\mathbf{19})_2]^{+/2+}$	600	2.3
n-type	$[Cu(\mathbf{1})(\mathbf{20})]^+$	**21**	$[Cu(\mathbf{19})_2]^{+/2+}$	480	20.6
p-type	$[Cu(\mathbf{1})(\mathbf{20})]^+$	**21**	$[Cu(\mathbf{19})_2]^{+/2+}$	580	1.2

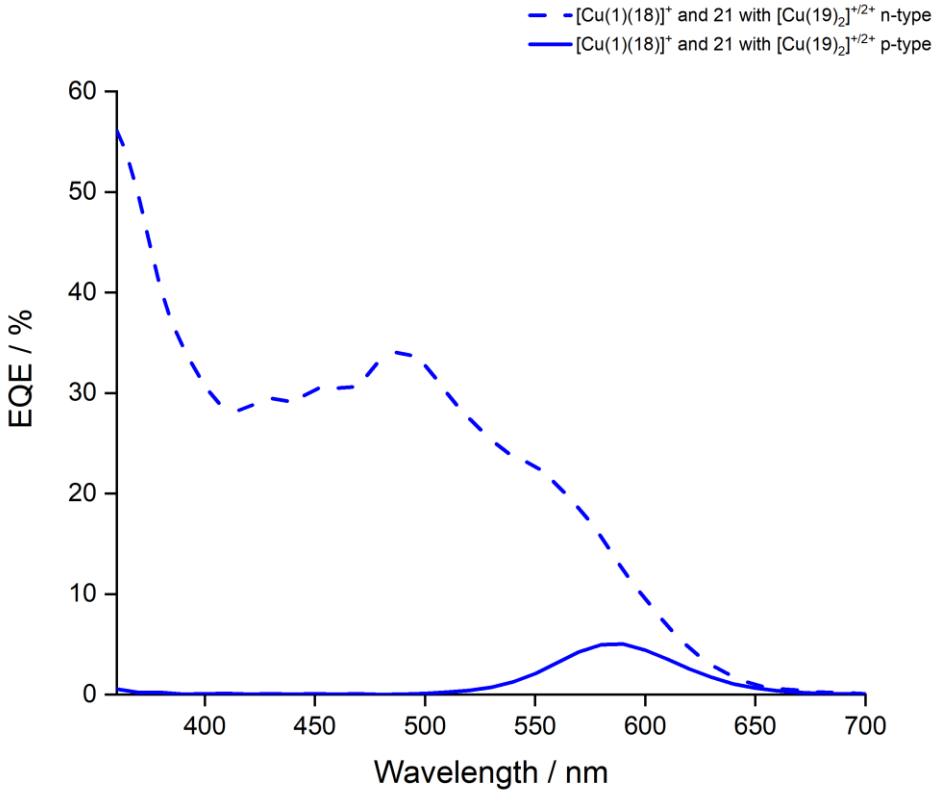

Figure 83: EQE spectra of tandem DSC with n-type dye $[Cu(1)(18)]^+$ and p-type dye 21 with electrolyte $[Cu(19)_2]^{+/2+}$.

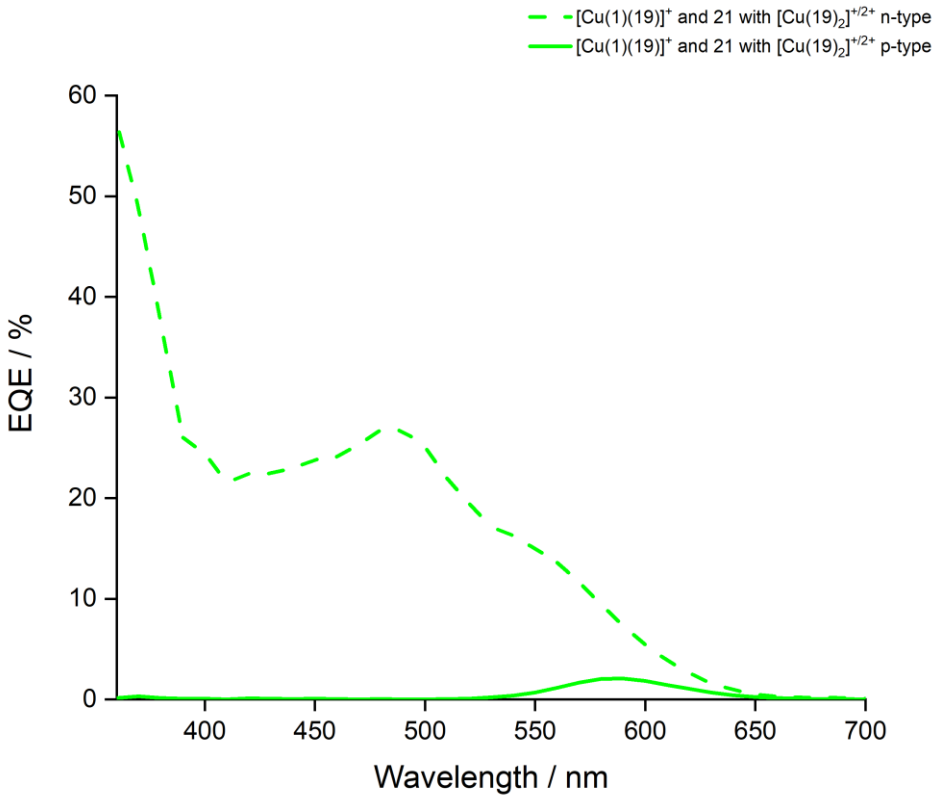

Figure 84: EQE spectra of tandem DSC with n-type dye $[Cu(1)(19)]^+$ and p-type dye 21 with electrolyte $[Cu(19)_2]^{+/2+}$.

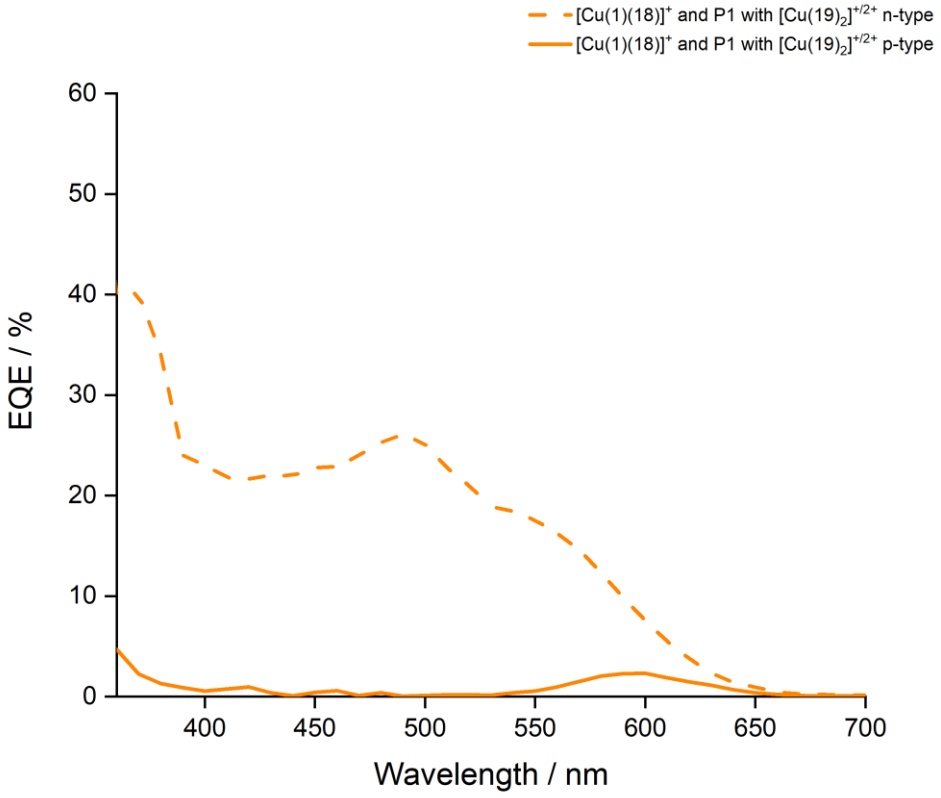

Figure 85: EQE spectra of tandem DSCs with n-type dye $[Cu(1)(18)]^+$ and p-type dyes P1 (22) with electrolyte $[Cu(19)_2]^{+/2+}$.

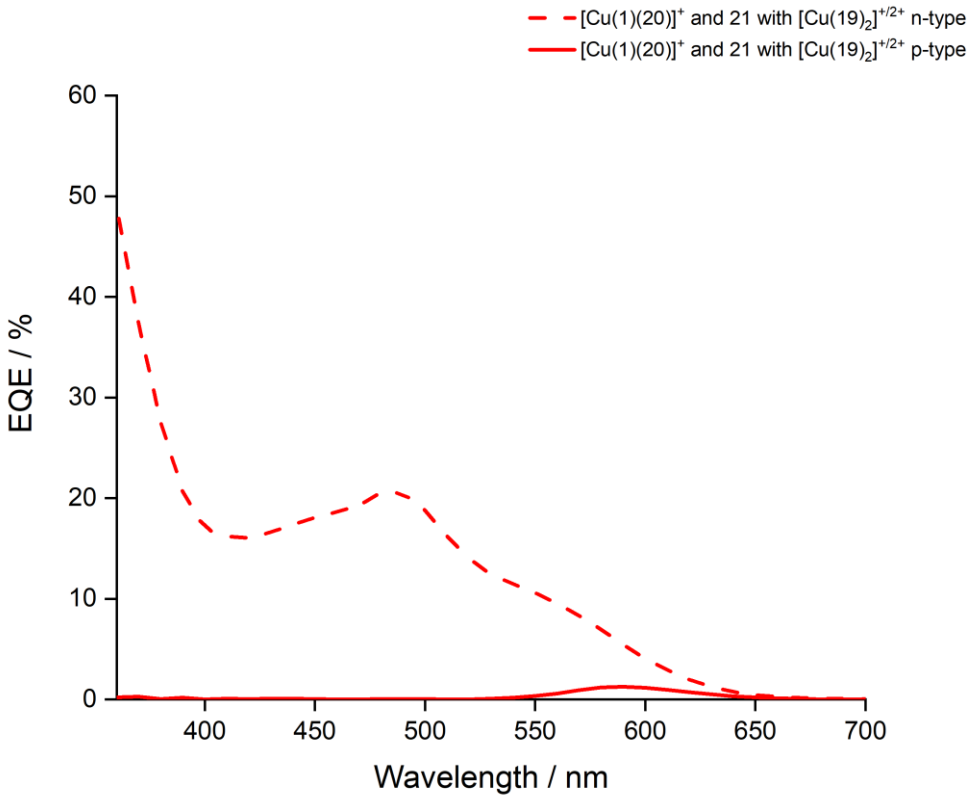

Figure 86: EQE spectra of tandem DSC with n-type dye $[Cu(1)(20)]^+$ and p-type dye 21 with electrolyte $[Cu(19)_2]^{+/2+}$.

9.5 Conclusion

This chapter has described a preliminary investigation of tandem DSCs with bis(diimine) copper(I) dyes for the n-type working electrode, a bpy-based Ru dye (**21**) or the organic dye **P1** (**22**) to functionalize the p-type working electrode in combination with a copper(I)/(II) redox shuttle in the electrolyte. The results in this chapter combine the investigation presented in the last chapter (Chapter 8) with p-type DSCs in order to have two photoactive working electrodes replacing the commonly used Pt counter electrode by a dye functionalized NiO working electrode. Although it was not possible to measure a DSC performance by irradiating from the p-type side, the EQE spectra measured from this side clearly show a photoactive dye being adsorbed on the NiO surfaces. A possible explanation for this is that the tandem DSC behaves like a paddle wheel, where the functionalized NiO working electrode needs the oxidized redox couple, which reduced the oxidized n-type dye, in order to release an electron to the electrolyte and inject a hole in the NiO valence band.

Furthermore the results show that combining an n-type and a p-type working electrode resulted in high values in the open-circuit voltages outperforming the value for the N719 reference cell. Moreover it was shown that it is possible to build an all copper tandem DSCs in which a bis(diimine) copper(II) dye is used to functionalize the NiO surface. Moreover preliminary trials with the copper(II) complex $[Cu(\mathbf{1})(\mathbf{19})]^{2+}$ as dye for the p-type side in combination with $[Cu(\mathbf{1})(\mathbf{19})]^+$ as n-type dye and the

$[Cu(\mathbf{19})_2]^{+/2+}$ electrolyte showed an efficiency of 1.12% with V_{OC} and J_{SC} values of 783 mV and 2.19 mA/cm^2, respectively. The relative efficiencies of duplicate tandem DSCs with this dye and electrolyte combination were 21.2% and 20.3% relative to N719 set to 100%. The EQE_{max} values were measured to be 23.3% at λ_{max} 490 nm for the n-type side and 1.9% at λ_{max} 590 nm for the p-type side.

In order to get the heteroleptic copper(II) complex $[Cu(\mathbf{1})(\mathbf{19})]^{2+}$ adsorbed on the NiO surface, the p-type working electrodes were heated at 250 °C for 20 min and then cooled to 80 °C before being immersed into a 1.0 mM DMSO solution of the anchoring ligand (**1**) for 24 h. After removing from the anchoring ligand solution the electrodes were washed with DMSO and EtOH and dried in a stream of nitrogen. The anchoring-ligand functionalized electrodes were then soaked in a 0.1 mM CH_2Cl_2 solution of $[Cu(\mathbf{19})_2][PF_6]_2$ overnight. The electrodes were removed from the dye bath solution, washed with CH_2Cl_2 and dried in a stream of nitrogen to yield $[Cu(\mathbf{1})(\mathbf{19})]^{2+}$ adsorbed on the NiO surface.

Although these first results for introducing a bis(diimine) copper(II) dye to functionalize the p-type working electrode it has to be mentioned that the homoleptic complex $[Cu(\mathbf{19})_2][PF_6]_2$ that was used as the precursor has yet to be fully characterized.

Further investigation should be done combining more n-type working electrodes with the best performing p-type electrodes. Furthermore it could be interesting to see if concentration or additive changes in the electrolyte could further improve the performances of the tandem DSCs. As assembling the tandem DSCs is not straight forward as both working electrodes have to be aligned exactly on top of each other further investigations should also be done in improving the cell assembly.

Chapter 10

Chapter 10 Summary

In this thesis the anchoring ligands (**1**-**3**) were synthesized, characterized and their performance tested in dye-sensitized solar cells. Furthermore thirteen ancillary ligands (**4**-**16**) and their corresponding homoleptic copper(I) complexes were synthesized and characterized (except for ancillary ligand **14**). The performances of these ancillary ligands were tested in DSCs.

Besides the screen-printing method for the preparation of TiO_2 working electrodes and two different dipping strategies to adsorb the heteroleptic copper(I) dye on the electrode surfaces, the ´surface-as-ligand, surface-as-complex´ strategy (´SALSAC´) and the ´stepwise´ assembly (´SW´) were shown (Chapter 2). Furthermore Chapter 2 shows general analytical characterization methods, the different materials for the DSCs and important characterization methods for the cells.

In Chapter 3, three anchoring ligands **ALP1** (**1**), **PhALP1** (**2**) and the asymmetric **ALP1** (**3**) were investigated in combination with two different ancillary ligand (**7** and **11**) and their performances tested in DSCs. It was found that the **ALP1** (**1**) anchoring ligands performed best although the **PhALP1** (**2**) anchoring ligand with the increased π system shows a broadened spectral response towards the red end of the visible light the sterically demanding anchoring ligand led to dye bleaching. The asymmetric anchoring ligand (**3**) yielded the lowest cell performances and was not further investigated.

In Chapter 4, four asymmetric ancillary ligands (**4**-**7**) and their corresponding homoleptic copper(I) complexes were synthesized and characterized. Their performances in DSCs were tested in combination with the anchoring ligands **ALP1** (**1**) and **PhALP1** (**2**) to further investigate the problem of electrode bleaching mentioned earlier. It was shown that also the smaller ancillary ligands investigated in this chapter suffered from bleaching when combined with the sterically more demanding anchoring ligand **2**. Nevertheless it was possible to regenerate the bleached dyes on the TiO_2 surfaces demonstrating a good binding of the anchoring ligand on the surface.

In Chapter 5, a set of four ancillary ligands (**8**-**11**) substituted with different numbers of methoxy groups on the phenyl-substituents of the 4,4´-diphenyl-2,2´-bipyridines were synthesized and characterized to investigate the effects of electron-donating groups in bis(diimine)copper(I) dyes for DSCs. The ancillary ligands were tested in DSCs in combination with the best performing anchoring ligand **ALP1** (**1**). It was shown that electron releasing groups in the phenyl framework of the ancillary ligand can enhance the photon to power conversion efficiency of DSCs.

In Chapter 6 enhancing the overall cell performance with substituents 4,4´-positions of the phenyl spacer was further investigated. Three ancillary ligands (**12**-**14**) were synthesized and characterized. The idea was to prepare a ligand that can easily be tuned in the 4,4´-positions of the phenyl spacer by undergoing a Schiff-base reaction. Unfortunately the Schiff-base synthesis of 4,4´-di(4-aminophenyl)-

6,6´-dimethyl-2,2´-bipyridine (**13**) with an aldehyde was unsuccessful. Furthermore the homoleptic copper(I) complexes of ancillary ligand **12** and **13** were synthesized and characterized. Two different dipping strategies, the ´SALSAC` strategy and the ´SW´ approach were used to functionalize the TiO_2 surfaces with the heteroleptic copper(I) dyes using anchoring ligand **1** and ancillary ligands **12-13**. DSCs containing these ancillary ligands were assembled and measured. It was shown that a higher lone pair character in the 4,4´-positions of the phenyl spacer or introducing a higher π system in the 6,6´-positions of the bipyridine unit can increase the performance of DSCs.

In Chapter 7 two ancillary ligands (**15** and **16**) and their corresponding homoleptic copper(I) complexes were synthesized and characterized. Both ligands had substituents in the 4,4´-positions of the phenyl spacer to further investigate the findings of previous chapter that substituents in this positions can have a beneficial influence on the cell performance. Furthermore DSCs containing the anchoring ligand **1** and the ancillary ligands **15** and **16** were assembled and characterized.

In Chapter 8, a preliminary study of DSCs containing copper(I) complexes of the type $[Cu(L_{anchor})(L_{ancillary})]^+$ (L_{anchor} = **ALP1** (**1**), $L_{ancillary}$ = **5** or **17-20**) as sensitizer and Cu^+/Cu^{2+} redox shuttles as the electrolyte was shown. DSCs containing different copper(I) dyes and copper(I)/(copper(II) electrolytes were assembled and measured. The investigations presented in this chapter yielded promising results as the open-circuit voltages of DSCs containing heteroleptic bis(diimine)copper(I) dyes and homoleptic copper(I)/(II) redox shuttles in the electrolyte yielded a significant increase in the open-circuit voltages of the cells, outperforming that of N719. The investigations in this chapter were done in collaboration with Mariia Karpacheva, Cedric Wobill and Frederik J. Malzner, all from our research group

In Chapter 9, a preliminary investigation of tandem DSCs was shown. In this chapter the results of Chapter 8 were combined with investigations of Nathalie Marinakis, to build the first tandem DSCs in our research group. The results presented here look promising especially the last findings, opening the possibility to all-copper tandem DSCs.

Chapter 11

Chapter 11 Conclusion and outlook

In this thesis was shown that the **ALP1** anchoring ligand (**1**) performed best. Moreover it was demonstrated that the sterically demanding **PhALP1** anchoring ligand (**2**), having an increased π-system benefits from a broadened spectral response at the red end of the visible light, but resulting in dye bleaching. Nevertheless it the good binding affinity of the phosphonic anchor to the TiO_2 surface could be proven by dye regeneration on the surface. Furthermore it was shown that both, electron releasing substituents in the 4,4´-positions of the phenyl spacer in the ancillary ligand and a higher π system introduced with phenyl substituents in the 6,6´-positions of the bipyridine unit of the ancillary ligand can enhance the performance of copper(I) based dye-sensitized solar cells. In addition to that it was found that homoleptic copper(I)/copper(II) complexes as redox shuttle in the electrolyte can outperform the values in the open-circuit voltage compare to N719, resulting in an all copper dye-sensitized solar cell. Moreover it was possible to build good performing tandem DSCs, where both electrodes are photoactive.

Further investigations are needed in the positions and types of substituents in both the phenyl spacer of the bpy unit and the substituents in the 6,6´-positions of the bipyridine unit of the ancillary ligand to further increase the cell performance. Future work should also concentrate on further studying the ´all copper´ dye-sensitized solar cells as they show promising results in enhancing open-circuit voltages. For the future it is also important to investigate the tandem dye-sensitized solar cells as they are advantageous in terms of sustainability to move away from the rare and expensive Pt counter electrodes, on top of that opening the field of having two photoactive sensitizers being able to both yield photon to power conversion efficiencies.

References

1 P. D. United Nations, Department of Economic and Social Affairs, K. F. and A. (2017). World Population Prospects: The 2017 Revision and Tables. Working Paper No. ESA/P/WP/248, *World Population Prospects: The 2017 Revision*, 2017.

2 BP Statistical Review of World Energy 2017, *BP Statistical Review of World Energy June 2017*, 2017.

3 I. E. Agency, *Global Energy & CO 2 Status Report*, 2018.

4 BP. n.d., Projected global energy consumption from 1990 to 2040, by energy source (in million metric tons of oil equivalent). Statista., https://www.statista.com/statistics/222066/projected-global-energy-consumption-by-source/, (accessed 9 May 2018).

5 R. M. Tuttle and D. V. Becker, *Semin. Nucl. Med.*, 2000, **30**, 133–140.

6 Q. Schiermeier, J. Tollefson, T. Scully, A. Witze and O. Morton, *Nature*, 2008, **454**, 816–823.

7 S. F. M. Bertoz, J. Bisquert, F. De Angelis, H. Desilvestro, F. Fabregat-Santiago, L. K. A. Hagfeldt, S. Ito, K.-J. Jiang, K. Kalyanasundaram, P. V. Kamat, S. J.-E. Moser, M. K. Nazeeruddin, L. Peter, H. J. Snaith, G. Tulloch, S. Uchida and M. G. and S. Y. Yanagida, J.-h. Yum, *Dye Sensitized Solar Cells*, EPFL Press, Lausanne, first edit., 2010.

8 M. A. Green, *Energy Policy*, 2000, **28**, 989–998.

9 D. M. Bagnall and M. Boreland, *Energy Policy*, 2008, **36**, 4390–4396.

10 A. Hagfeldt, *Ambio*, 2012, **41**, 151–155.

11 A. Hagfeldt, G. Boschloo, L. Sun, L. Kloo and H. Pettersson, *Chem. Rev.*, 2010, **110**, 6595–6663.

12 W. Shockley and H. J. Queisser, *J. Appl. Phys.*, 1961, **32**, 510–519.

13 M. Grätzel, *Inorg. Chem.*, 2005, **44**, 6841–6851.

14 M. Grätzel, *Acc. Chem. Res.*, 2009, **42**, 1788–1798.

15 M. K. Nazeeruddin, E. Baranoff and M. Grätzel, *Sol. Energy*, 2011, **85**, 1172–1178.

16 B. Bozic-Weber, E. C. Constable and C. E. Housecroft, *Coord. Chem. Rev.*, 2013, **257**, 3089–3106.

17 F. Brunner, N. Marinakis, C. Wobill, M. Willgert, C. D. Ertl, T. Kosmalski, M. Neuburger, B.

Bozic-Weber, T. Glatzel, E. C. Constable and C. E. Housecroft, *J. Mater. Chem. C*, 2016, **4**, 9823–9833.

18 N. Marinakis, M. Willgert, E. C. Constable and C. E. Housecroft, *Sustain. Energy Fuels*, 2017, **1**, 626–635.

19 A. Morandeira, G. Boschloo, A. Hagfeldt and L. Hammarström, *J. Phys. Chem. C*, 2008, **112**, 9530–9537.

20 B. C. O'Regan and J. R. Durrant, *Acc. Chem. Res.*, 2009, **42**, 1799–1808.

21 C. E. Housecroft and A. G. Sharpe, *Anorganische Chemie*, Pearson Studium, second edi., 2006.

22 A. Hagfeldt and M. Graetzel, *Chem. Rev.*, 1995, **95**, 49–68.

23 S. Valencia, J. M. Marin and G. Restrepo, *Open Mater. Sci. J.*, 2010, **4**, 9–14.

24 S. Ito, T. N. Murakami, P. Comte, P. Liska, C. Grätzel, M. K. Nazeeruddin and M. Grätzel, *Thin Solid Films*, 2008, **516**, 4613–4619.

25 G. J. Meyer, *ACS Nano*, 2010, **4**, 4337–4343.

26 J. R. Mann, M. K. Gannon, T. C. Fitzgibbons, M. R. Detty and D. F. Watson, *J. Phys. Chem. C*, 2008, **112**, 13057–13061.

27 Q. Feng, H. Wang, G. Zhou and Z.-S. Wang, *Front. Optoelectron. China*, 2011, **4**, 80–86.

28 K. Kalyanasundaram and M. Grätzel, *Coord. Chem. Rev.*, 1998, **177**, 347–414.

29 E. Galoppini, *Coord. Chem. Rev.*, 2004, **248**, 1283–1297.

30 C. Anselmi, E. Mosconi, M. Pastore, E. Ronca and F. De Angelis, *Phys. Chem. Chem. Phys.*, 2012, **14**, 15963–15974.

31 A. Yella, H.-W. Lee, H. N. Tsao, C. Yi, A. K. Chandiran, M. K. Nazeeruddin, E. W.-G. Diau, C.-Y. Yeh, S. M. Zakeeruddin and M. Gratzel, *Science*, 2011, **334**, 629–634.

32 S. Anderson, E. C. Constable, M. P. Dare-Edwards, J. B. Goodenough, A. Hamnett, K. R. Seddon and R. D. Wright, *Nature*, 1979, **280**, 571.

33 B. O'Regan and M. Grätzel, *Nature*, 1991, **353**, 737–740.

34 M. K. Nazeeruddin, F. De Angelis, S. Fantacci, A. Selloni, G. Viscardi, P. Liska, S. Ito, B. Takeru and M. Grätzel, *J. Am. Chem. Soc.*, 2005, **127**, 16835–16847.

35 C. Klein, M. K. Nazeeruddin, D. Di Censo, P. Liska and M. Grätzel, *Inorg. Chem.*, 2004, **43**,

4216–4226.

36 C. H. Siu, C. L. Ho, J. He, T. Chen, X. Cui, J. Zhao and W. Y. Wong, *J. Organomet. Chem.*, 2013, **748**, 75–83.

37 S.-W. Wang, K.-L. Wu, E. Ghadiri, M. G. Lobello, S.-T. Ho, Y. Chi, J.-E. Moser, F. De Angelis, M. Grätzel and M. K. Nazeeruddin, *Chem. Sci.*, 2013, **4**, 2423.

38 A. Colombo, C. Dragonetti, A. Valore, C. Coluccini, N. Manfredi and A. Abbotto, *Polyhedron*, 2014, **82**, 50–56.

39 Element Abundances in the upper continental earth crust, https://upload.wikimedia.org/wikipedia/commons/0/09/Elemental_abundances.svg, (accessed 8 May 2018).

40 N. Armaroli, *Chem. Soc. Rev.*, 2001, **30**, 113–124.

41 N. Alonso-Vante, J.-F. Nierengarten and J.-P. Sauvage, *J. Chem. Soc. Dalton Trans.*, 1994, **11**, 1649.

42 S. Sakaki, T. Kuroki and T. Hamada, *J. Chem. Soc. Dalton Trans.*, 2002, 840.

43 T. Bessho, E. C. Constable, M. Graetzel, A. Hernandez Redondo, C. E. Housecroft, W. Kylberg, M. K. Nazeeruddin, M. Neuburger and S. Schaffner, *Chem. Commun.*, 2008, 3717.

44 B. Bozic-Weber, S. Y. Brauchli, E. C. Constable, S. O. Fürer, C. E. Housecroft and I. A. Wright, *Phys. Chem. Chem. Phys.*, 2013, **15**, 4500.

45 B. Bozic-Weber, V. Chaurin, E. C. Constable, C. E. Housecroft, M. Meuwly, M. Neuburger, J. A. Rudd, E. Schönhofer and L. Siegfried, *Dalton Trans.*, 2012, **41**, 14157.

46 B. Bozic-Weber, S. Y. Brauchli, E. C. Constable, S. O. Furer, C. E. Housecroft, F. J. Malzner, I. A. Wright and J. A. Zampese, *Dalton Trans.*, 2013, **42**, 12293–12308.

47 E. Schönhofer, B. Bozic-Weber, C. J. Martin, E. C. Constable, C. E. Housecroft and J. A. Zampese, *Dyes Pigment.*, 2015, **115**, 154–165.

48 A. H. Rendondo, E. C. Constable and C. E. Housecroft, *Chim. Int. J. Chem.*, 2009, **63**, 205–207.

49 F. J. Malzner, S. Y. Brauchli, E. C. Constable, C. E. Housecroft and M. Neuburger, *RSC Adv.*, 2014, **4**, 48712–48723.

50 M. Schmittel and A. Ganz, *Chem. Commun.*, 1997, 999–1000.

51 M. Sandroni, M. Kayanuma, A. Planchat, N. Szuwarski, E. Blart, Y. Pellegrin, C. Daniel, M. Boujtita and F. Odobel, *Dalton Trans.*, 2013, **42**, 10818.

52 M. Sandroni, L. Favereau, A. Planchat, H. Akdas-Kilig, N. Szuwarski, Y. Pellegrin, E. Blart, H. Le Bozec, M. Boujtita and F. Odobel, *J. Mater. Chem. A*, 2014, **2**, 9944–9947.

53 F. J. Malzner, M. Willgert, E. C. Constable and C. E. Housecroft, *J. Mater. Chem. A*, 2017, **5**, 13717–13729.

54 J. Wu, Z. Lan, J. Lin, M. Huang, Y. Huang, L. Fan and G. Luo, *Chem. Rev.*, 2015, **115**, 2136–2173.

55 S. O. Fürer, B. Bozic-Weber, T. Schefer, C. Wobill, E. C. Constable, C. E. Housecroft and M. Willgert, *J. Mater. Chem. A*, 2016, **4**, 12995–13004.

56 M. Wang, C. Grätzel, S. M. Zakeeruddin and M. Grätzel, *Energy Environ. Sci.*, 2012, **5**, 9394.

57 M. Willgert, A. Boujemaoui, E. Malmström, E. C. Constable and C. E. Housecroft, *RSC Adv.*, 2016, **6**, 56571–56579.

58 M. Karpacheva, F. J. Malzner, C. Wobill, A. Büttner, E. C. Constable and C. E. Housecroft, *Dyes Pigment.*, 2018, **156**, 410-416.

59 C. Dragonetti, M. Magni, A. Colombo, F. Melchiorre, P. Biagini and D. Roberto, *ACS Appl. Energy Mater.*, 2018, **1**, 751–756.

60 E. Olsen, G. Hagen and S. Eric Lindquist, *Sol. Energy Mater. Sol. Cells*, 2000, **63**, 267–273.

61 A. Kay and M. Grätzel, *Sol. Energy Mater. Sol. Cells*, 1996, **44**, 99–117.

62 H. Pettersson, T. Gruszecki, R. Bernhard, L. Häggman, M. Gorlov, G. Boschloo, T. Edvinsson, L. Kloo and A. Hagfeldt, *Prog. Photovoltaics Res. Appl.*, 2007, **15**, 113–121.

63 L. Bay, K. West, B. Winther-Jensen and T. Jacobsen, *Sol. Energy Mater. Sol. Cells*, 2006, **90**, 341–351.

64 M. Wang, A. M. Anghel, B. Marsan, N.-L. Cevey Ha, N. Pootrakulchote, S. M. Zakeeruddin and M. Grätzel, *J. Am. Chem. Soc.*, 2009, **131**, 15976–15977.

65 B. Bozic-Weber, E. C. Constable, N. Hostettler, C. E. Housecroft, R. Schmitt and E. Schönhofer, *Chem. Commun.*, 2012, **48**, 5727.

66 H. J. Snaith, *Energy Environ. Sci.*, 2012, **5**, 6513.

67 B. E. Hardin, H. J. Snaith and M. D. McGehee, *Nat. Photonics*, 2012, **6**, 162–169.

68 C. E. Housecroft and E. C. Constable, *Chem. Soc. Rev.*, 2015, **44**, 8386–8398.

69 B. Bozic-Weber, E. C. Constable and C. E. Housecroft, *Coord. Chem. Rev.*, 2013, **257**, 3089–3106.

70 B. Bozic-Weber, E. C. Constable, C. E. Housecroft, P. Kopecky, M. Neuburger and J. A. Zampese, *Dalton Trans.*, 2011, **40**, 12584.

71 B. Bozic-Weber, S. Y. Brauchli, E. C. Constable, S. O. Fürer, C. E. Housecroft and I. A. Wright, *Phys. Chem. Chem. Phys.*, 2013, **15**, 4500.

72 F. J. Malzner, S. Y. Brauchli, E. Schönhofer and C. E. Housecroft, *Polyhedron*, 2014, **82**, 116–121.

73 M. W. Mara, K. A. Fransted and L. X. Chen, *Coord. Chem. Rev.*, 2015, **282**–**283**, 2–18.

74 M. Schmittel, H. Ammon, V. Kalsani, A. Wiegrefe and C. Michel, *Chem. Commun.*, 2002, 2566–2567.

75 S. Y. Brauchli, F. J. Malzner, E. C. Constable and C. E. Housecroft, *RSC Adv.*, 2015, **5**, 48516–48525.

76 B. Bozic-Weber, E. C. Constable, C. E. Housecroft, P. Kopecky, M. Neuburger and J. A. Zampese, *Dalton Trans.*, 2011, **40**, 12584.

77 B. Bozic-Weber, V. Chaurin, E. C. Constable, C. E. Housecroft, M. Meuwly, M. Neuburger, J. A. Rudd, E. Schönhofer and L. Siegfried, *Dalton Trans.*, 2012, **41**, 14157.

78 N. Armaroli, G. Accorsi, F. Cardinali and A. Listorti, in *Photochemistry and Photophysics of Coordination Compounds I*, eds. V. Balzani and S. Campagna, Springer Berlin Heidelberg, Berlin, Heidelberg, 2007, 69–115.

79 H. J. Snaith, *Energy Environ. Sci.*, 2012, **5**, 6513–6520.

80 H. J. Snaith, *Nat. Photonics*, 2012, **6**, 337–340.

81 F. J. Malzner, S. Y. Brauchli, E. Schönhofer and C. E. Housecroft, *Polyhedron*, 2014, **82**, 116–121.

82 M. T. Miller, P. K. Gantzel and T. B. Karpishin, *Inorg. Chem.*, 1998, **37**, 2285–2290.

83 A. Büttner, S. Y. Brauchli, R. Vogt, E. C. Constable and C. E. Housecroft, *RSC Adv.*, 2016, **6**, 5205–5213.

84 F. Kröhnke, *Synthesis*, 1976, **1976**, 1–24.

85 A. Ciupa, P. A. De Bank, M. F. Mahon, P. J. Wood and L. Caggiano, *Med. Chem. Commun.*, 2013, **4**, 956–961.

86 C. Fan, X. Wang, P. Ding, J. Wang, Z. Liang and X. Tao, *Dyes Pigment.*, 2012, **95**, 757–767.

87 G. J. Kubas, *Inorganic Synthesis*, 1990, **28**, 68–70.

88 C. C. Phifer and D. R. McMillin, *Inorg. Chem.*, 1986, **25**, 1329–1333.

89 S. Otto, F. Bertoncin and J. B. F. N. Engberts, *J. Am. Chem. Soc.*, 1996, **118**, 7702–7707.

90 E. C. Constable, C. E. Housecroft, M. Neuburger, I. Poleschak and M. Zehnder, *Polyhedron*, 2003, **22**, 93–108.

91 A. Büttner, S. Brauchli, E. Constable and C. Housecroft, *Inorganics*, 2018, **6**, 40.

92 L. P. Hammett, *J. Am. Chem. Soc.*, 1937, **59**, 96–103.

93 D. H. McDaniel and H. C. Brown, *J. Org. Chem.*, 1958, **23**, 420–427.

94 C. Hansch, A. Leo and R. W. Taft, *Chem. Rev.*, 1991, **91**, 165–195.

95 V.-M. Mukkala and J. J. Kankare, *Helv. Chim. Acta*, 1992, **75**, 1578–1592.

96 A. Boudebous, E. C. Constable, C. E. Housecroft, M. Neuburger, S. Schaffner, A. Listorti, C. Sabatini and F. Barigelletti, *Inorganica Chim. Acta*, 2009, **362**, 1825–1830.

97 J. Hanson, *J. Chem. Educ.*, 2001, **78**, 1266.

98 F. J. Malzner, A. Prescimone, E. C. Constable, C. E. Housecroft and M. Willgert, *J. Mater. Chem. A*, 2017, **5**, 4671–4685.

99 A. Colombo, C. Dragonetti, D. Roberto, A. Valore, P. Biagini and F. Melchiorre, *Inorganica Chim. Acta*, 2013, **407**, 204–209.

100 J. Wu, Z. Lan, J. Lin, M. Huang, Y. Huang, L. Fan and G. Luo, *Chem. Rev.*, 2015, **115**, 2136–2173.

101 S. Hattori, Y. Wada, S. Yanagida and S. Fukuzumi, *J. Am. Chem. Soc.*, 2005, **127**, 9648–9654.

102 M. Brugnati, S. Caramori, S. Cazzanti, L. Marchini, R. Argazzi and C. A. Bignozzi, *Int. J. Photoenergy*, 2007, **2007**, 1–10.

103 Y. Bai, Q. Yu, N. Cai, Y. Wang, M. Zhang and P. Wang, *Chem. Commun.*, 2011, **47**, 4376.

104 M. Freitag, F. Giordano, W. Yang, M. Pazoki, Y. Hao, B. Zietz, M. Grätzel, A. Hagfeldt and

G. Boschloo, *J. Phys. Chem. C*, 2016, **120**, 9595–9603.

105 L. Kavan, Y. Saygili, M. Freitag, S. M. Zakeeruddin, A. Hagfeldt and M. Grätzel, *Electrochim. Acta*, 2017, **227**, 194–202.

106 Y. Saygili, M. Söderberg, N. Pellet, F. Giordano, Y. Cao, A. B. Muñoz-García, S. M. Zakeeruddin, N. Vlachopoulos, M. Pavone, G. Boschloo, L. Kavan, J.-E. Moser, M. Grätzel, A. Hagfeldt and M. Freitag, *J. Am. Chem. Soc.*, 2016, **138**, 15087–15096.

107 A. Colombo, G. Di Carlo, C. Dragonetti, M. Magni, A. Orbelli Biroli, M. Pizzotti, D. Roberto, F. Tessore, E. Benazzi, C. A. Bignozzi, L. Casarin and S. Caramori, *Inorg. Chem.*, 2017, **56**, 14189–14197.

108 J. Cong, D. Kinschel, Q. Daniel, M. Safdari, E. Gabrielsson, H. Chen, P. H. Svensson, L. Sun and L. Kloo, *J. Mater. Chem. A*, 2016, **4**, 14550–14554.

109 M. Magni, R. Giannuzzi, A. Colombo, M. P. Cipolla, C. Dragonetti, S. Caramori, S. Carli, R. Grisorio, G. P. Suranna, C. A. Bignozzi, D. Roberto and M. Manca, *Inorg. Chem.*, 2016, **55**, 5245–5253.

110 M. Freitag, J. Teuscher, Y. Saygili, X. Zhang, F. Giordano, P. Liska, J. Hua, S. M. Zakeeruddin, J.-E. Moser, M. Grätzel and A. Hagfeldt, *Nat. Photonics*, 2017, **11**, 372–378.

111 J. He, H. Lindström, A. Hagfeldt and S.-E. Lindquist, *Sol. Energy Mater. Sol. Cells*, 2000, **62**, 265–273.

112 P. Ho, S. Thogiti, L. Q. Bao, R. Cheruku, K.-S. Ahn and J. Hong Kim, *Sol. Energy*, 2018, **161**, 9–16.

113 H. Choi, T. Hwang, S. Lee, S. Nam, J. Kang, B. Lee and B. Park, *J. Power Sources*, 2015, **274**, 937–942.